ATLAS

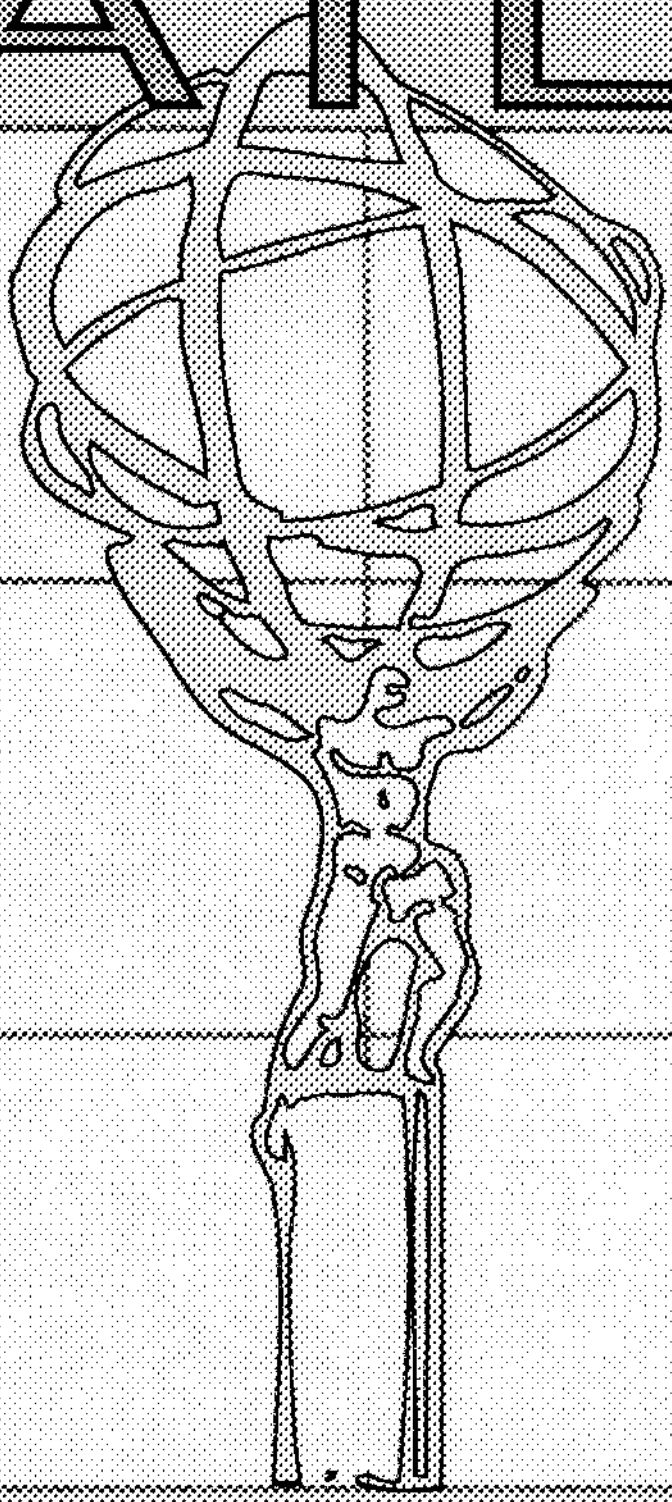

for a
General-Purpose
pp Experiment
at the
Large Hadron Collider
at CERN

CERN/LHCC/92-4
LHCC/I 2
1 October 1992

ATLAS

Letter of Intent
for a
General-Purpose pp Experiment
at the
Large Hadron Collider at CERN

Abstract

The ATLAS collaboration proposes to build a general purpose proton–proton detector for the Large Hadron Collider, capable of exploring the new energy regime which will become accessible. The detector would be fully operational at the startup of the new accelerator. The detector concept, the research and development work under way to optimize the detector design, and its proposed implementation are described, together with examples of its discovery potential.

Members of the ATLAS Collaboration

University of Alberta, Edmonton, Canada
D.Gingrich, G.Greeniaus, P.Kitching, B.Olsen, J.Pinfold, N.Rodning

High-Energy Physics Institute of the Kazakh Academy of Sciences, Alma-Ata, Kazakhstan
E.Boos, E.Khusainov, D.Madigozhin, G.Magonov, N.Nurgozhin, N.Pokrovskij, A.Temiraliev, A.Voronin, B.Zhautykov

NIKHEF, National Institute for Nuclear Physics and High Energy Physics, Amsterdam, The Netherlands
F.E.Bakker, K.Bos, J.Buskens, C.Daum, G.J.Evers, F.Hartjes, J.Homma, G.N.M.Kieft, N.de Koning, R.Kluit, H.Kok, P.A.M.Rewiersma, H.Schuijenburg, J.Schmitz, S.Sman, H.Tolsma, F.Udo, H.van der Graaf, B.van Eijk, J.Vermeulen

LAPP, IN2P3-CNRS, Annecy, France
B.Aubert, A.Bazan, B.Beaugiraud, J.Colas, T.Leflour, M.Maire, M.Moynot, I.Wingerter-Seez, Y.Zolnierowski

Athens National Technical University, Athens, Greece
M.Dris, E.Gazis, S.Maltezos

Athens University, Athens, Greece
G.S.Tzanakos

Institut de Física d'Altes Energies, Universitat Autónoma de Barcelona, Bellaterra, Barcelona, Spain
J.M.Crespo, M.Delfino, E.Fernández, Ll.Garrido, M.Martínez, C.Padilla

Laboratory for High Energy Physics, University of Bern, Bern, Switzerland
K.Borer, G.Czapek, F.Dittus, D.Frei, U.Moser, J.Schacher, K.Pretzl

School of Physics and Space Research, University of Birmingham, Birmingham, United Kingdom
R.Carney, J.D.Dowell, N.Ellis, J.Garvey, R.J.Homer, I.R.Kenyon, T.J.MacMahon, P.M.Watkins, A.T.Watson, J.A.Wilson

University of Bratislava, Bratislava, Czechoslovakia
P.Chochula, M.Grendar, V.Hlinka, K.Holy, R.Janik, P.Kubinec, P.Lichard, L.Luchan, J.Masarik, M.Pikna, P.Povinec, B.Sitar, P.Strmen, I.Szarka, S.Tokar, J.Vanko

Cavendish Laboratory, Cambridge University, Cambridge, United Kingdom
P.P.Allport, J.R.Carter, P.A.Elcombe, M.J.Goodrick, J.C.Hill, D.J.Munday, M.A.Parker

Université Blaise Pascal, IN2P3-CNRS, Clermont-Ferrand, France
Z.Ajaltouni, F.Badaud, N.Bouhemaid, Ph.Brette, M.Brossard, R.Chadelas, J.C.Chevaleyre, M.Crouau, F.Daudon, L.Fredj, G.Montarou, B.Michel, G.S.Muanza, D.Pallin, F.Vazeille

Niels Bohr Institute, University of Copenhagen, Copenhagen, Denmark
H.Bertelsen, H.Bøggild, E.Dahl-Jensen, G.Damgaard, T.A.Fearnley, J.D.Hansen, J.R.Hansen, P.H.Hansen, A.Lindahl, B.S.Nielsen, B.S.Nilsson, R.Møller

Physics Department of the University of Calabria and I.N.F.N., Cosenza, Italy
L.La Rotonda, L.Malgeri, M.Primavera, M.Valdata-Nappi

Institute of Nuclear Physics, Cracow, Poland
K.Cetnar, J.Chwastowski, A.Czermak, S.Gadomski, J.Godlewski, Z.Hajduk, W.Iwański, M.Kajetanowicz, P.Kapusta, B.Machowski, P.Malecki, A.Moszczynski, Z.Natkaniec, K.Pakoński, A.Sobala, M.Turała, J.Zazula

Institute of Nuclear Physics and Techniques, Cracow, Poland
W.Dabrowski, L.Furman, S.Jagielski, K.Jeleń, D.Kisielewska, T.Kowalski, S.Koperny, E.Rulikowska-Zarebska, A.Skoczeń, L.Suszycki, J.Zajac

Institute of Nuclear Research of the Hungarian Academy of Sciences, Debrecen, Hungary
S.Szilágyi

Universität Dortmund, Dortmund, Germany
C.Gössling, B.Lisowski, A.Reichold, V.Sondermann, R.Spiwoks, E.Tsesmelis

Joint Institute for Nuclear Research, Dubna, Russia
G.Alexandrov, G.Alexeev, A.Bannikov, S.Baranov, D.Bardin, S.Bilenky, I.Boguslavskij, G.Chelkov, A.Cheplakov, A.Efremov, R.Eremeev, O.Gavrishchuk, S.Gerasimov, Yu.Gornushkin, I.Gramenitskij, V.Jamburenko, G.Karpenko, M.Kazarinov, B.Khomenko, N.Khovanski, O.Klimov, V.Kotov, T.Kotova, V.Kravtsov, Z.Krumstein, V.Kukhtin, A.Kutov, O.Kuznetsov, E.Ladygin, V.Malyshev, V.Mel'nikov, L.Merkulov, O.Nozdrin, V.Obudovskij, V.Odintsov, A.Olshevski, R.Pose, V.Romanovsky, T.Rudenko, V.Samsonov, M.Shafranov, A.Shalygin, Yu.Sedykh, A.Sissakian, A.Skachkov, A.Solovjev, L.Tkatchev, V.Tokmenin, L.Vertogradov, A.Volod'ko

University of Edinburgh, Edinburgh, United Kingdom
D.J.Candlin, K.J.Peach, A.Walker

Physics Department, Florence University and I.N.F.N., Florence, Italy
L.Carraresi, G.Ciancaglini, M.Colocci, A.Francesco, E.Giorgetti, M.Nuti, L.Palchetti, P.G.Pelfer, S.Sottini, S.Trigari, G.Ventura, A.Vinattieri

Laboratori Nazionali di Frascati dell'I.N.F.N., Frascati, Italy
H.Bilokon, V.Chiarella, M.Curatolo, B.Esposito, G.Tentori, A.Teodoli

Fakultät für Physik, Albert-Ludwigs Universität, Freiburg, Germany
G.Herten, R.Irsigler, R.Kolpin, U.Landgraf, J.Ludwig, W.Mohr, K.Runge, F.Schaefer, M.Webel

European Laboratory for Particle Physics (CERN), Geneva, Switzerland
R.Brenner, A.Dell'Acqua, M.Dodgson, P.Eerola, C.W.Fabjan, A.Franz, D.Froidevaux, O.Gildemeister, P.Jenni, F.Linde, L.Linssen, L.Mapelli, M.Nessi, P.Nevski, L.Poggioli, A.Poppleton, G.Poulard, S.Roe, J.Straver, M.Stravrianakou, R.Voss, V.Vuillemin, P.Weilhammer, J.Wotschack, N.Zaganidis
The CERN group acknowledges the important contributions made to this Letter of Intent by:
F.Anghinolfi, F.Bergsma, M.Campbell, J.L.Chevalley, C.D'Ambrosio*, P.Farthouat, W.Flegel, H.Gerwig, B.Goret, T.Gys*, M.Hatch, C.Hauviller, E.Heijne, P.Jarron, R.Jones, W.Klempt, J.Knobloch, C.Lasseur, P.Lazeyras, L.Leistam, G.Mornacchi, C.Onions, M.Price, W.Richter, E.Rosso, M.Schmitt, G.Stevenson, F.Wittgenstein, W.Witzeling
(* CERN-LAA)

University of Geneva, Geneva, Switzerland
R.Bonino, A.G.Clark, C.Couyoumtzelis, H.Kambara, X.Wu

Department of Physics and Astronomy, University of Glasgow, Glasgow, United Kingdom
A.J.Campbell, A.T.Doyle, A.J.Flavell, D.J.Martin, V.O'Shea, C.Raine, D.H.Saxon, I.O.Skillicorn, K.M.Smith

Institut des Sciences Nucléaires de Grenoble, IN2P3-CNRS, Grenoble, France
J.Collot, D.Dzahini, P.de Saintignon, G.Laborie, G.Mahout, F.Merchez

Israel Institute of Technology, Haifa, Israel
S.Dado, J.Goldberg, N.Lupu

Institute of Experimental Physics, University of Hamburg, Hamburg, Germany
E.Fretwurst, G.Lindstroem, V.Riech

Institut für Hochenergiephysik, University of Heidelberg, Germany
Ch.Geweniger, P.Hanke, E.E.Kluge, A.Putzer, K.Tittel, M.Wunsch

Research Institute for High Energy Physics, SEFT, Helsinki, Finland
I.Hietanen, M.Karppinen

Institut für Experimentalphysik, Innsbruck University, Innsbruck, Austria
P.Girtler, D.Kuhn, G.Rudolph

Universität Jena, Institut für Angewandte und Technische Informatik, Jena, Germany
V.Doersing, A.Reinsch

Department of Physics, Faculty of Science, Kobe University, Japan
M.Nozaki, H.Takeda

Institute of Experimental Physics of the Slovak Academy of Sciences, Kosice, Czechoslovakia
J.Ban, D.Bruncko, E.Kladiva, I.Kralik, L.Sandor

University of Lancaster, Lancaster, United Kingdom
T.J.Brodbeck, F.Foster, G.Hughes, P.N.Ratoff, T.Sloan

Laboratório de Instrumentação e Física Experimental de Partículas, Lisbon, Portugal
A.Amorim, A.Henriques, G.Barreira, A.Maio, A.Gomes, L.Peralta

University of Liverpool, Liverpool, United Kingdom
C.A.Amery, S.F.Biagi, P.S.L.Booth, T.J.V.Bowcock, J.N.Jackson, T.Jones, B.T.King, A.Moreton, J.M.Morton, A.A.Muir, L.E.Sacks, N.A.Smith

Queen Mary & Westfield College, University of London, London, United Kingdom
G.A.Beck, A.A.Carter, E.Eisenhandler, P.Kyberd, M.Landon, S.L.Lloyd, A.J.Martin, D.Newman-Coburn, T.W.Pritchard, G.Thompson

Royal Holloway and Bedford New College, University of London, Egham, United Kingdom
B.J.Green, T.Medcalf, Ll.M.Mir, J.A.Strong

University College, London, United Kingdom
F.W.Bullock, T.W.Jones

Fysiska institutionen, Lunds universitet, Lund, Sweden
T.Åkesson, S.Almehed, H.Carling, V.Hedberg, G.Jarlskog, L.Jönsson, B.Lörstad, U.Mjörnmark, M.Thulesius

Universidad Autónoma, Madrid, Spain
F.Barreiro, L.Labarga

Physics Institute, Mainz University, Mainz, Germany
H.Bluemer, K.Kleinknecht, H.G.Sander

Manchester University, Manchester, United Kingdom
J.Allison, R.J.Barlow, I.P.Duerdoth, J.Foster, R.E.Hughes-Jones, M.Ibbotson, S.D.Kolya, G.D.Lafferty, F.K.Loebinger, R.Marshall, D.Mercer, K.Stephens, R.J.Thompson, T.R.Wyatt

Universität Mannheim, Institut für Informatik 5, Mannheim, Germany
F.Klefenz*, R.Maenner*, K.H. Noffz, R.Zoz
(*informatic experts who sign also the CMS Letter of Intent)

Centre de Physique des Particules de Marseille, IN2P3-CNRS et Université d'Aix-Marseille II, Marseille, France
S.Basa, A.Chekhtman, J.C.Clemens, M.Cohen-Solal, M.C.Cousinou, P.Dargent, P.Delpierre, J.J.Destelle, P.Y.Duval, F.Etienne, A.Falou, D.Ferrato, D.Fouchez, M.C.Habrard, G.Hallewell, A.Le Van Suu, A.Mekkaoui, E.Monnier, T.Monthuy, R.Nacash, E.Nagy, C.Olivetto, R.Potheau, C.Rondot, D.Sauvage, Y.Sun, S.Tisserant, F.Touchard

Research Centre for High Energy Physics, Melbourne University, Melbourne, Australia
R.A.Bardos, G.W.Gorfine, L.P.Guy, G.F.Moorhead, G.N.Taylor, S.N.Tovey

Physics Department, Milan University and I.N.F.N., Milan, Italy
G.Battistoni, G.Bellini, D.Camin, D.Cavalli, G.Costa, L.Cozzi, A.Cravero, M.di Corato, A.Ferrari, F.Gianotti, P.Inzani, L.Mandelli, M.Mazzanti, L.Perasso, L.Perini, P.Sala, M.Sciamanna

Laboratory of Nuclear Physics of the University of Montreal, Montreal, Canada
G.Azuelos, G.Beaudoin, J.C.Cote, W.Del Bianco, P.Depommier, E.L.Florian, H.Jeremie, C.Leroy, B.Lorazo, J.Rioux, J.Roy, P.Roy

Institute for Theoretical and Experimental Physics, Moscow, Russia
A.Artamonov, V.Epstein, P.Gorbunov, V.Jemanov, V.Khovansky, S.Kruchinin, A.Maslennikov, M.Ryabinin, S.Shuvalov, V.Zaitsev, S.Zeldovich, I.Zuckerman

P.N. Lebedev Institute of Physics (FIAN), Moscow, Russia
S.Baranov, M.Belov, E.Devitsin, I.Gavrilenko, A.Komar, S.Konovalov, V.Kozlov, S.Muraviev, L.Popov, S.Potashov, A.Shmeleva, K.Sokolovsky, E.Telyukov, V.Tikhomirov

Moscow Engineering and Physics Institute, Moscow, Russia
V.Bashkirov, V.Bondarenko, B.Dolgoshein, S.Furletov, V.Grigoriev, O.Kondratiev, A.Konstantinov, M.Kopytin, A.Medvedev, S.Pavlenko, A.Romaniouk, S.Smirnov, V.Sosnovtzev

Moscow State University, Moscow, Russia
E.A.Chudakov, P.Ermolov, I.N.Erofeeva, N.Kalinina, D.Karmanov, A.Kulikov, V.Kurochkin, O.Yu.Lukina, M.Merkin, S.I.Lyutov, V.I.Rud, F.K.Rizatdinova, L.N.Smirnova, S.Trusov, A.Voronin, V.Yazkov

Ludwig Maximilian University, Munich, Germany
K.Braune, M.Faessler, A.Staude

Max-Planck-Institut für Physik, Munich, Germany
M.Aderholz, W.Blum, H.Brettel, F.Dydak*, J.Fent, A.Halley, K.Jakobs, C.Kiesling, H.Kroha, E.Lorenz, G.Luetjens, G.Lutz, H.Oberlack, P.Ribarics, Rainer Richter, Robert Richter, P.Schacht, U.Stiegler, U.Stierlin, R.St.Denis, G.Wolf
(* also at CERN)

University of Nijmegen and NIKHEF, Nijmegen, The Netherlands
C.Brouwer, F.J.G.H.Crijns, J.A.Dijkema, W.Kittel, P.F.Klok, A.C.König, W.J.Metzger, C.L.A.Pols, D.J.Schotanus, Th.A.M.Wijnen

Laboratoire de l'Accélérateur Linéaire, IN2P3-CNRS, Orsay, France
C.Arnault, E.Auge, D.Breton, R.L.Chase, J.C.Chollet, P.Delebecque, V.Dubois, A.Ducorps, C.de la Taille, L.Fayard, D.Fournier, A.Hrisoho, L.Iconomidou-Fayard, Ph.Jean, B.Merkel, J.Noppe, G.Parrour, P.Petroff, J.P.Repellin, A.Schaffer, N.Seguin, L.Serin, G.Unal, J.J.Veillet

Oslo University, Oslo, Norway
T.Buran, E.Nygaard, S.Stapnes

Physics Department, Oxford University, Oxford, United Kingdom
J.H.Bibby, J.F.Harris, R.J.Hawkings, A.R.Holmes, P.B.Renton, A.R.Weidberg

Pierre & Marie Curie and Paris VII Universities and IN2P3-CNRS, Paris, France
S.Dagoret, D.Imbault, G.Hansl-Kozanecka, H.Lebbolo, P.Neyman, R.Zitoun

Nuclear Physics and Theory Department, Pavia University and I.N.F.N. Pavia, Italy
G.Ambrosini, P.Cattaneo, C.Conta, R.Ferrari, M.Fraternali, V.G.Goggi, M.Livan, F.Pastore, E.Pennacchio, G.Polesello, A.Rimoldi, V.Vercesi

Physics Department, Pisa University and I.N.F.N., Pisa, Italy
D.Autiero, V.Cavasinni, T.Del Prete, E.Iacopini

Institute of Physics CSAV and Nuclear Centre of Charles University, Prague, Czechoslovakia
J.Bohm, Z.Dolezal, J.Hrivnac, R.Leitner, M.Lokajicek, S.Nemecek, S.Pospisil, V.Simak, M.Smizanska, M.Suk, P.Tas, Z.Trka, S.Valkar, M.Vecko, V.Vrba, I.Wilhelm

Institute for High Energy Physics, Protvino, Russia
V.Ammosov, A.Basilevsky, A.Batalov, S.Belikov, M.Bogoljubsky, A.Borisov, S.Chekulaev, A.Denisov, S.Denisov, A.Dushkin, E.Eremchenko, N.Fedjakin, A.Galjaev, Yu.Gilitsky, V.Golovkin, V.Gorjachev, S.Gurjev, Yu.Gutnikov, Yu.Ivanyushenkov, A.Karyukhin, Yu.Khokhlov, A.Kholodenko, A.Kiryunin, V.Klyukhin, V.Komarov, V.Konstantinov, V.Korotkov, M.Kostrikov, A.Kozhin, R.Krasnokutsky, A.Kriushin, L.Kurchaninov, V.Lapin, M.Levitsky, V.Lipaev, V.Maksimov, S.Medved, E.Melnikov, A.Minaenko, S.Misyura, A.Moiseev, A.Myagkov, V.Onuchin, P.Pitukhin, V.Platonov, Yu.Rodnov, R.Schouvalov, P.Semenov, V.Sergeev, I.Shein, A.Smol, A.Soldatov, A.Solodkov, A.Spiridonov, E.Starchenko, V.Sushkov, V.Sytnik, V.Tikhonov, Yu.Tsyupa, A.Usachev, A.Vasiliev, A.Vorobiev, A.Vovenko, A.Zaitsev, V.Zmushko, I.Zubkov

Coordenação dos Programas de Pós-graduação de Engenharia da Universidade Federal do Rio de Janeiro, Brazil
F.M.L.Almeida, N.O.Bellas, L.P.Calôba, A.Mesquita, A.L.Pereira, J.Sá Borges, J.M.Seixas, M.Souza, Z.D.Thomé, F.Vinci dos Santos, R.Schirru, V.Yoshioka

Physics Department, University 'La Sapienza' and I.N.F.N., Rome, Italy
C.Bacci, P.Bagnaia, F.Ceradini, G.Ciapetti, S.Gentile, F.Lacava, A.Nisati, E.Petrolo, L. Pontecorvo, S.Veneziano, L.Zanello

Physics Department, University 'Tor Vergata' and I.N.F.N., Rome, Italy
R.Cardarelli, A.Di Ciaccio, R.Santonico

Rutherford Appleton Laboratory, Chilton, Didcot, United Kingdom
R.J.Apsimon, D.E.Baynham, R.W.Clifft, C.N.P.Gee, A.R.Gillman, N.A.McCubbin, R.P.Middleton, P.R.Norton, S.P.Quinton, P.Seller, G.J.Tappern, M.Tyndel, C.R.Walters

DAPNIA, Centre d'Etudes de Saclay, CEA, Gif-sur-Yvette, France
J.M.Baze*, H.Desportes*, R.Duthil*, N.Fourches, L.Gosset, C.Guyot, J.Heitzmann, M.Huet, W.Kozanecki, P.Lavocat, C.Lesmond*, J.C.Lottin*, J.P.Lottin, B.Mansoulié, J.P.Meyer, Y.Pabot*, A.Patoux, J.F.Renardy, M.Rouger, V.Ruhlmann, A.Savoy-Navarro, P.Schune, J.Teiger, M.Virchaux, H.Zaccone
(*magnet engineers also involved in the CMS coil design)

Centre for Science and Technology of Russian Academy of Sciences, Saratov, Russia
D.Bandurin, D.Bukatin, V.Dvoeglazov, V.Kikot, Yu.Tukhtuev

University of Sheffield, Sheffield, United Kingdom
F.H.Combley, C.N.Booth, S.L.Cartwright, C.M.Buttar

Siegen University, Siegen, Germany
W.Funk, M.Holder, A.Krentz

Manne Siegbahn Institute of Stockholm, Stockholm, Sweden
P.Carlson, L.Didenko, C.Fuglesang, T.Lindblad, B.Lund-Jensen, J.Söderqvist

Stockholm University, Stockholm, Sweden
C.Bohm, S.Hellman, S.O.Holmgren, B.Hovander, K.Hultqvist, K.E. Johansson, T.Moa, B.Sellden

Institute of Fine Mechanics and Optics, St. Petersburg, Russia
I.Koniakhin, A.Sukhorukov

St. Petersburg Nuclear Physics Institute, St. Petersburg, Russia
V.V.Gromov, V.G.Ivochkin, A.G.Nadtochy, E.M.Spiridenkov, V.L.Stepanov, I.I.Tkach, V.A.Schegelsky

Australian Nuclear Science and Technology Organisation, Sydney, Australia
D.Alexiev, I.J.Donnely, M.Keane, K.E.Varvell

School of Physics and Astronomy, Tel-Aviv University, Tel-Aviv, Israel
G.Alexander, G.Bella, A.Levy, N.Paz-Jaoshvili

International Centre for Elementary Particle Physics and Department of Physics, University of Tokyo, Tokyo, Japan
M.Imori, K.Kawagoe, T.Kawamoto, T.Kobayashi, S.Komamiya, T.Mashimo, T.Mori, M. Morii, S.Orito, M.Sasaki, T.Tsukamoto, T.Yoshida

University of Uppsala, Uppsala, Sweden
N.Bingefors, O.Botner, L.O.Eek, T.Ekelöf, A.Hallgren, K.Kulka

Instituto de Física Corpuscular, Centre Mixto Universidad de Valencia–CSIC, Valencia, Spain
A.Ferrer

University of British Columbia, Vancouver, Canada
R.Howard, D.Axen

University of Victoria, Victoria, Canada
A.Astbury, M.Fincke-Keeler, R.Keeler, M.Lefebvre, C.Oram, P.Poffenberger, R.Sobie, J.White

Institut für Hochenergiephysik, Oesterreichische Akademie der Wissenschaften, Vienna, Austria
R.Frühwirth, J.Hrubec, M.Krammer, D.Liko, I.Mikulec, T.Wildschek

Institute of Experimental Physics, Warsaw University, Warsaw, Poland
H.Abramowicz, K.Charchula, J.Ciborowski, J.Gajewski, M.Krzyzanowski, M.Pawlak

The Weizmann Institute of Science, Rehovot, Israel
A.Breskin, R.Chechik, E.Duchovni, Y.Eisenberg, A.Gibrekhterman, M.Hass, D.Hochman, U.Karshon, D.Lellouch, L.Levinson, G.Mikenberg, A.Montag, S.Tarem, D.Revel

Bergische Universität, Wuppertal, Germany
K.H.Becks, J.Drees, K.W.Glitza, K.Hamacher, S.Kersten, G.Lenzen, B.Sanny, H.Wahlen

Spokespersons:
F.Dydak (DYDAK@cernvm.cern.ch)
P.Jenni (JENNI @cernvm.cern.ch)

Acknowledgements

We warmly acknowledge the important technical design contributions of L. Baisin, M-H. Bovard, E. David, N. Dickson, N. Dudragne, C. Rivoiron and C. Vollerin, as well as early contributions to the detector concept by U. Goerlach.
Our Monte Carlo simulation work has greatly benefitted from the help of R. Brun, F. Carminati, S. Giani and K. Lassila with the GEANT program, and of H. Renshall and E. Jagel with the CSF farm.
We would also like to thank the staff of the Desktop Publishing Service and the CERN Printing Service. In particular we thank S. Leech-O'Neale for her professional proofreading, M. Goossens and A. Samarin for their help with text processing, S. Stillebacher for the cover design, and last but not least D. Klein, M. Mazerand and M. Prost for their efficient administrative work.

Contents

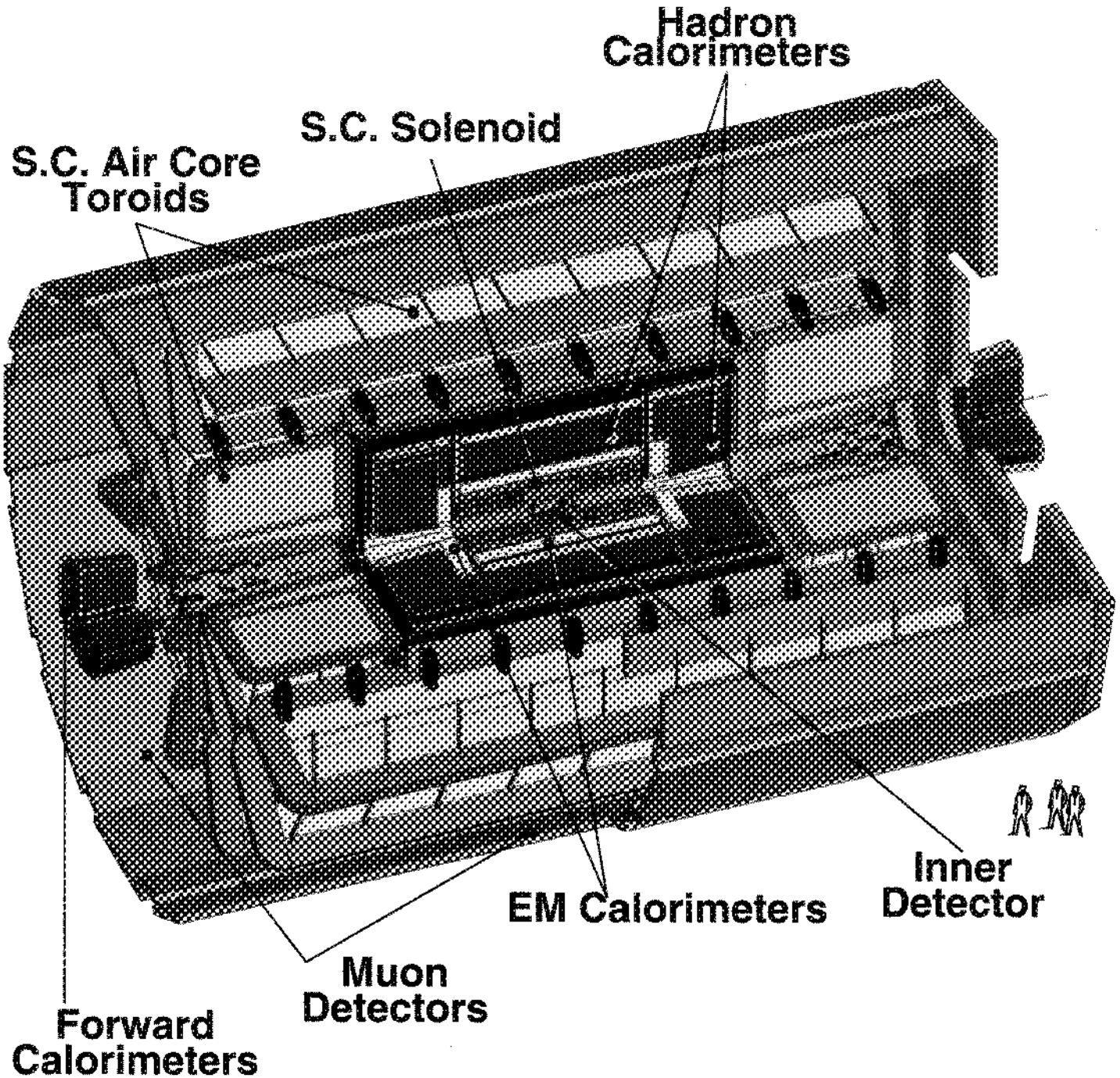

The ATLAS detector (air toroid option)

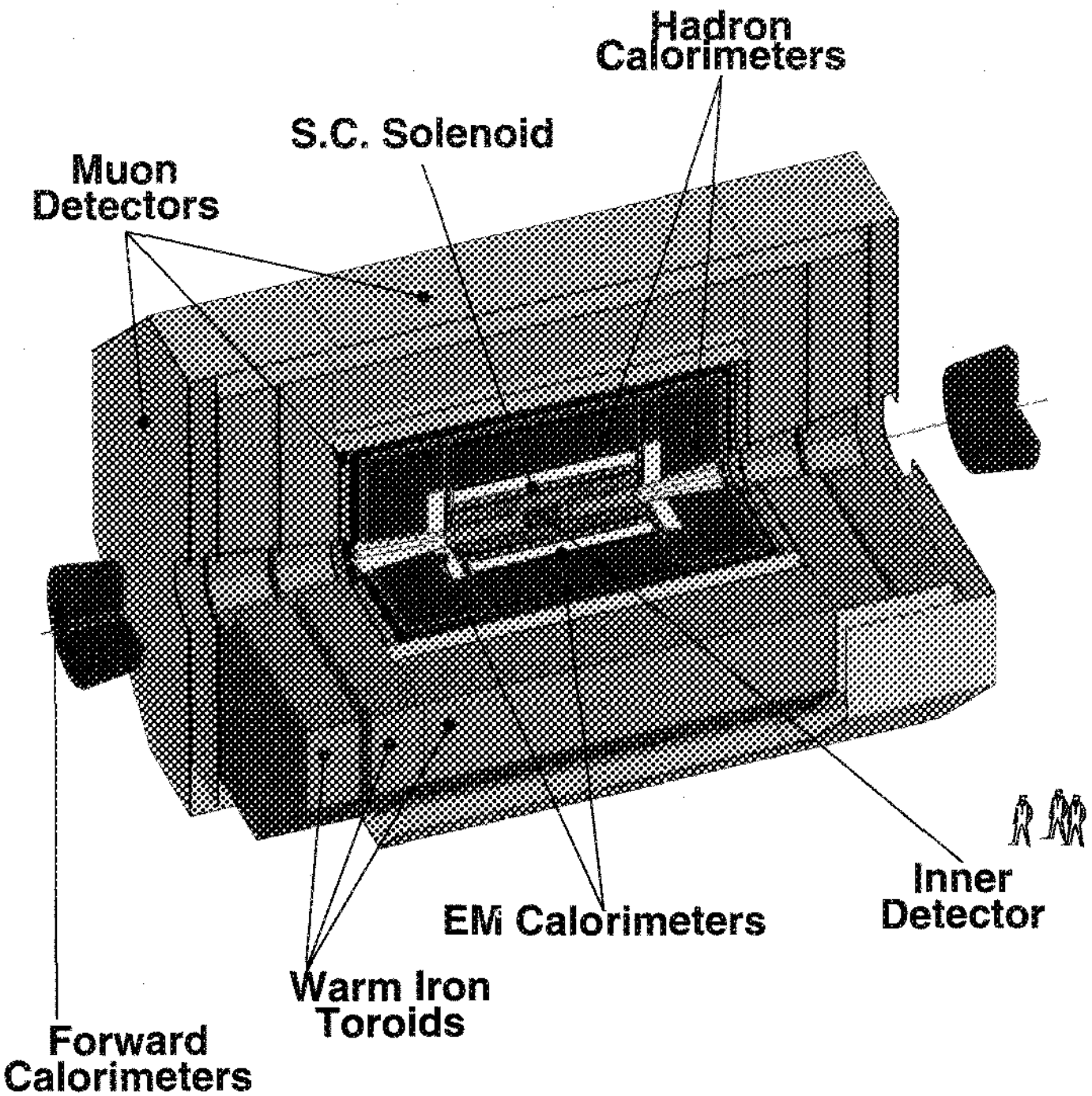

The ATLAS detector (iron toroid option)

1 Introduction and Overview

The ATLAS Collaboration proposes in this Letter of Intent a general-purpose pp experiment which would be operational at the startup of the Large Hadron Collider (LHC) in order to exploit its full discovery potential. The LHC offers a large range of physics opportunities, among which the origin of mass at the electroweak scale is a major focus of interest. The detector optimization is therefore guided by physics issues such as sensitivity to the largest possible Higgs mass range, but also for example by detailed studies of top quark decays, Supersymmetry searches, and sensitivity to large compositeness scales. The ability to cope with a broad variety of expected physics processes also demonstrates most importantly the detector's potential for unexpected new physics.

Many of the interesting physics questions at the LHC require high luminosity, and so the primary goal of the experiment is to operate at the standard high luminosity for LHC of $1.7 \cdot 10^{34}$ cm^{-2}s^{-1} with a detector that provides as many signatures as possible of new physics using electron, gamma, muon, jet, and missing transverse energy measurements.

Emphasis is also put on the performance necessary for physics accessible during the initial lower luminosity running. The experiment will address more complex signatures including tau detection and heavy flavour tags to as high a luminosity as practicable.

Finally, for a restricted set of signatures, the detector is conceived for safe performance even at the highest possible luminosities which could be delivered by the LHC.

1.1 Basic Design Considerations

The Standard Model (SM) Higgs search can be used as a first benchmark for the detector optimization. The search strategies and methods are rather well known from general studies. In order to cover the full mass range above the expected discovery limit at LEP of about $m_H > 80$ GeV one needs sensitivity to the following processes (ℓ = e or μ):

H $\rightarrow \gamma\gamma$ from WH, ZH and $t\bar{t}$ H using a $\ell^{\pm}$ tag,
mass range $80 < m_H < 130$ GeV;

H $\rightarrow \gamma\gamma$ direct production,
mass range $90 < m_H < 150$ GeV;

H $\rightarrow ZZ^* \rightarrow 4\ell^{\pm}$
mass range 130 GeV $< m_H < 2m_Z$;

H $\rightarrow ZZ \rightarrow 4\ell^{\pm}$, $2\ell^{\pm}2\nu$,
mass range $2m_Z < m_H < 800$ GeV;

H $\rightarrow WW, ZZ \rightarrow \ell^{\pm}\nu$ 2 jets, $2\ell^{\pm}$ 2 jets, $2\ell^{\pm}2\nu$, $4\ell^{\pm}$
from WW, ZZ fusion using tagging of forward jets for m_H up to about 1 TeV.

The expected observable cross-sections at LHC are small both for the low ($m_H < 2m_Z$) and very high m_H range, hence the need to operate at high luminosities. Also it is well documented that good mass resolution is important for efficient Higgs searches in the range $m_H < 2m_Z$.

As a second benchmark one may use the search for particles of the Minimal Supersymmetric extension of the Standard Model (MSSM). In addition to signatures similar to the ones for the SM Higgs, one needs sensitivity to processes like:

$A \rightarrow \tau^+\tau^- \rightarrow e\mu$ plus ν's
$\rightarrow \ell^{\pm}$ plus hadrons plus ν's;

$H^{\pm} \rightarrow \tau^{\pm}\nu$
$\rightarrow$ 2 jets.

In particular $H^{\pm}$ searches from the reaction $t\bar{t} \rightarrow H^{\pm}bW^{\mp}b$, are strongly enhanced by b-quark tagging as are t-quark studies in general. These processes are expected to have observable cross-sections even at lower luminosities (10^{33} cm^{-2}s^{-1}).

Other LHC benchmark processes like Supersymmetry (SUSY) and effects of quark compositeness include as further signatures the missing transverse energy (E_T^{miss}) from undetected lightest stable SUSY particles (LSP) and deviations in the jet cross-section from the QCD expectations for very high p_T jets respectively.

These few examples, along with many others, show that sensitivity to a variety of final state signatures is required. The basic design considerations are therefore:

- very good electromagnetic calorimetry for electron and photon identification and measurements, complemented by hermetic jet and missing E_T calorimetry;
- efficient tracking at high luminosity for lepton momentum measurements and for enhanced electron and photon identification, and tau and heavy flavour tagging capabilities at lower luminosity;
- precision muon momentum measurements with stand-alone capability at highest luminosity.

In order to maximize the physics reach and to optimize the exploitation of the LHC it is also important to achieve:

- large acceptance in η coverage;
- triggering and measurements of particles at low thresholds

The performance goals are summarized in Table 1.1. They have been chosen primarily as a result of detailed physics performance studies as well as seeking to stay within cost-effective and feasible technologies which fulfil the essential physics requirements.

1.2 Overall Detector Concept

The magnet configuration has a major influence on the overall detector concept and on how well the performance goals can be met. Careful studies have led us to the conclusion that a toroid muon magnet system complemented by an inner superconducting solenoid offers the best solution:

- almost no constraints on calorimetry and inner detector allowing non-compromised technological solutions;
- a large acceptance and robust stand-alone muon detection system.

At this stage both a superconducting air-core and a warm iron-core magnet are options for the barrel and end-cap regions. Although the superconducting design offers superior performance, further studies of technical feasibility, operational safety and cost implications are needed before a final choice is made between the two magnet options. A combination of a long superconducting air-core barrel toroid with warm iron-core end-cap toroids is also an attractive solution, considering possible large background rates in the forward directions, as well as cost arguments. The open choice for the optimum muon magnet technology does not greatly influence the conceptual layouts of calorimetry and inner detector at this stage. However, in view of its impact on the future detailed design of the overall detector, the decision will be made as early as possible well before the Technical Proposal.

The generic overall detector layout is shown in Fig. 1.1 with a superconducting air-core toroid and in Fig. 1.2 with a warm iron-core toroid, with the corresponding configuration of the muon chambers.

The inner detector is confined to a cylinder of length 6.80 m and radius 1.10 m in a field of 2 T provided by a superconducting solenoid. The thin coil is integrated into the inner cryostat wall of a Liquid Argon (LAr) preshower detector and electromagnetic sampling calorimeter. Hermetic hadron calorimetry for jet and E_T^{miss} measurements is extended from the central region ($\eta = \pm 3$) into the forward regions by separate detectors covering the range $3 < |\eta| < 5$.

The main dimensions are indicated in Figures 1.1 and 1.2. The overall weights are 6 kt and 30 kt for the two toroid options respectively.

1.3 Detector Subsystems

The choice of specific detector subsystems will be based on the results and extrapolations from R&D activities. At this early stage of preparation for LHC instrumentation, it is not yet possible to make a definite selection of the technology in all cases, and further R&D results and design work are needed. Wherever sufficient studies are already available, a baseline design with the preferred technology is presented in this document, with a brief mention of alternative solutions. Decisions on open choices will be made before the Technical Proposal.

A summary of the detector subsystems is given in Table 1.2, with quantitative performance figures in the corresponding chapters.

1.3.1 Calorimetry

The baseline technology for the electromagnetic part is a highly granular LAr sampling calorimeter with Pb absorber, including an integrated preshower detector for γ - π^0 separation. In the barrel region the recently developed 'Accordion' structure is used as baseline design whereas both the 'Accordion' and the 'Thin Gap Turbine' (TGT) structures are currently options for the end-cap regions.

Iron absorbers will be used for the hadron calorimetry. The technology choice is still open and will be made among the options under active investigation with LAr, scintillating fibre or scintillating tile read-out media. Depending on the solution, the central solenoid flux return yoke will be integrated into the hadron calorimeter or surround it.

The separate forward calorimeters have a replaceable read-out medium in order to survive extremely high radiation doses. Ongoing tests with liquid scintillator and with high pressure gas designs will be used to make a selection.

1.3.2 Inner detector

The basic functions of the inner detector, namely precision momentum measurements of leptons and electron (and photon) identification at high luminosity as well as τ and b tagging at lower luminosities, are achieved in the baseline concept by combining three

technologies adapted to the LHC tracking environment.

The interaction region is surrounded by Si micro-strip detectors extending up to a radius of about 35 cm and $|\eta| < 1.5$. Their purpose is to provide an initial high precision track vector and with the innermost pixel layer to give impact parameter measurements. GaAs micro-strip detectors will be used to extend the coverage to larger η where the radiation dose is highest.

At larger radii, pattern recognition and tracking are based on integrated designs of straw tubes with transition radiation detection (TRD) capability and high precision track vector measurements in Si and gas strip and pad detectors. Highly efficient Si tracking is well suited for the very central region ($|\eta| < 1$) whereas radial micro-strip gas counters (MSGC) are well adapted for the forward tracking. The optimization of the inner detector layout is not finalized at this stage, neither in terms of performance nor costs, and alternative layouts are also studied.

1.3.3 Muon detection

In the toroid magnet configuration the muon triggering and identification can be made entirely outside the calorimetry, after a substantial thickness of absorber material, without using the inner detector. This feature, together with the stand-alone momentum measurement capability of the muon system, will allow the safe use of muon signatures up to the highest possible LHC luminosities. Excellent stand-alone performance is achieved for the superconducting air-core option, whereas still adequate, though multiple scattering limited performance is obtained with the warm iron-core option. An independent muon momentum measurement is provided by the inner detector, and the best resolution is reached with a combined measurement in the inner tracking and the muon system.

The superconducting air-core design is based on a twelve-fold symmetry with individual coils providing a field integral of 3 Tm at $\eta = 0$. A sagitta measurement is made with three pairs of superlayers of chambers. The warm iron-core toroid option has 2.5 m of iron magnetized at 1.8 T at $\eta = 0$. Entrance and exit angles are measured with four superlayers of chambers.

Performance tests and design studies are underway to choose among the following high precision chamber technologies: high pressure drift tubes, honeycomb strip chambers and drift chambers with jet cell geometry. Trigger signals are either derived from the same detector or provided by additional resistive plate chambers.

1.4 Construction, Installation and Cost

It is the firm goal of the Collaboration to have the detector fully operational at the start-up of the LHC. It will be installed into a longitudinal experimental hall through a large diameter shaft in large pre-assembled units. Assembly and accesses exploit longitudinal displacements of the end toroids as well as of detector components inside the barrel toroid.

The physics requirements, rather than a fixed cost target, have been the primary design criteria for the detector concept, with the aim however of meeting them with cost-effective and feasible technologies. The ATLAS Collaboration is still at an early stage of cost estimates and optimization. The preliminary material cost of the complete detector is estimated to be in the range 370–450 MCHF depending on the final choices of the detector subsystem options. Scenarios with deferred installation of parts of detector subsystems and the resulting reduced physics performance would have to be considered, should financial or time constraints impose a need for it.

1.5 Layout of the Letter of Intent

The three main subsystems of the ATLAS detector concept, calorimetry, inner detector and muon spectrometer, are discussed first. These chapters are followed by a discussion of the trigger and data acquisition aspects. After that, experimental area, installation, safety and radiation environment are considered briefly in two chapters. The expected physics performance is presented in the final major chapter with examples of processes representative of the physics potential of the proposed experiment. Finally, R&D needs, preliminary costs and schedules, collaboration structure and construction responsibilities are briefly summarized in the last chapter.

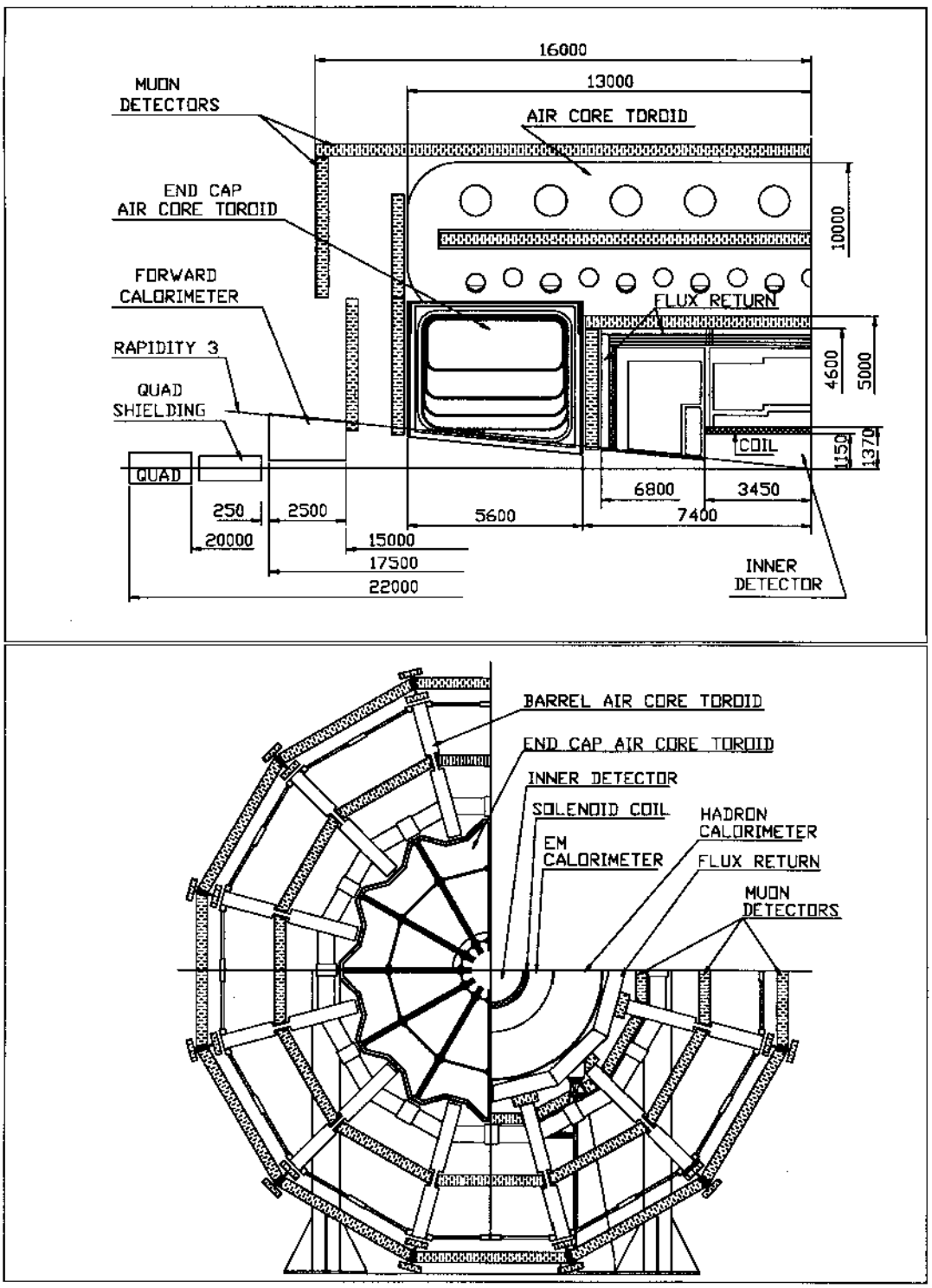

Figure 1.1: *Conceptual detector layout and main dimensions for the version with superconducting air-core toroids*

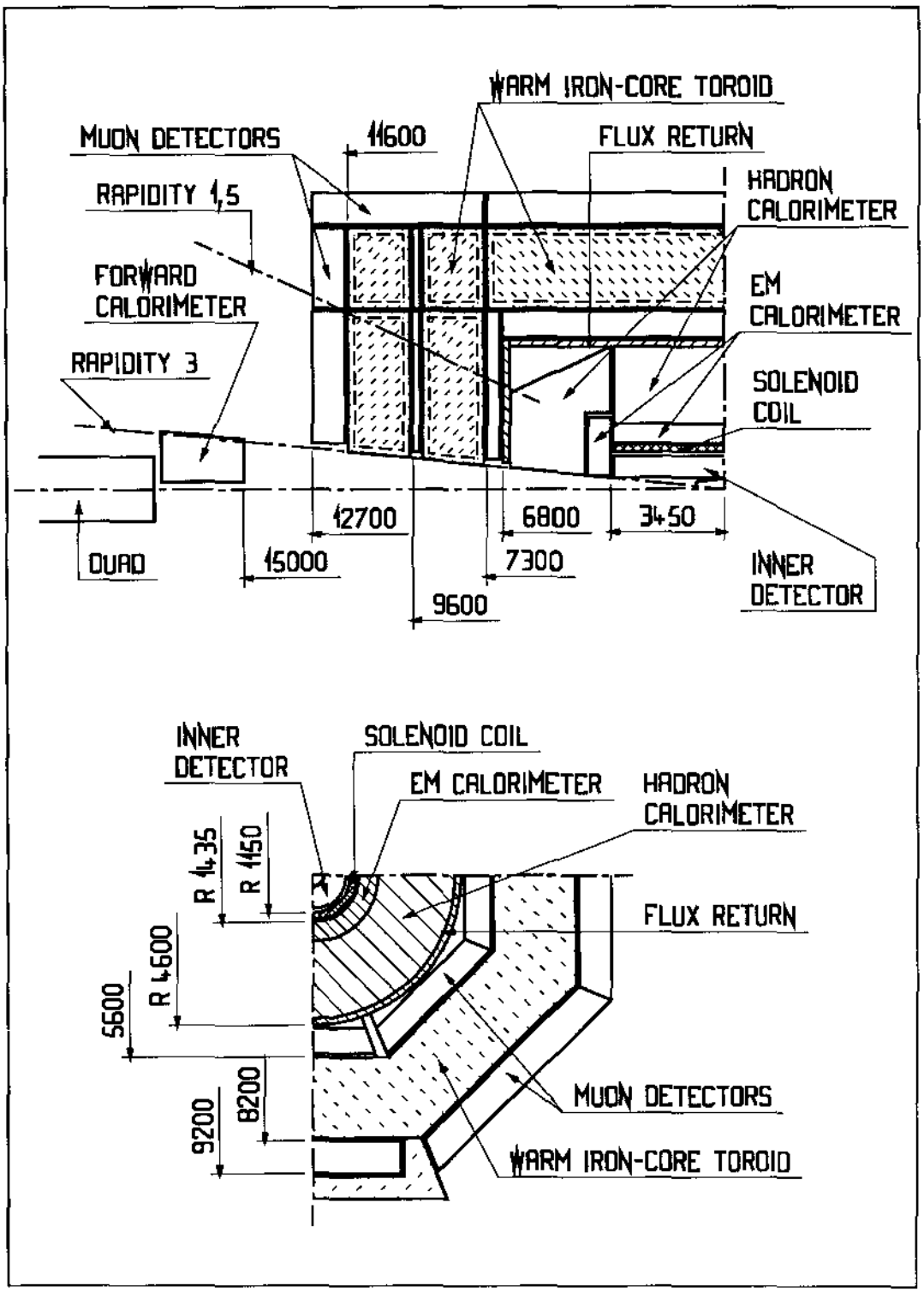

Figure 1.2: *Conceptual detector layout and main dimensions for the version with warm iron-core toroids*

Table 1.1: *Performance goals*

Detector component	Resolution, characteristics	η coverage	
		Measurement	Trigger
Em calorimetry	$10\%/\sqrt{E} \oplus 1\%$	± 3	± 2.5
Preshower detection	Enhance $\gamma - \pi^0$ separation	± 2.5	
Jet and missing E_T Calorimetry			
- barrel and end-cap	$50\%/\sqrt{E} \oplus 3\%$	± 3	± 3
- forward	$100\%/\sqrt{E} \oplus 7\%$	$3 < \lvert\eta\rvert < 5$	$3 < \lvert\eta\rvert < 5$
Inner detector	$5 \cdot 10^{-4} p_T \oplus 1\%$	± 2.5	
	Enhance electron identification	± 2.5	
	τ and b tagging	± 1.5	
Muon detection	20% or better at $p_T = 1$ TeV Stand-alone capability at highest luminosity	± 3	± 2.5

Table 1.2: *Subdetector summary*

Subdetector	η coverage	Baseline design	Alternatives	Comments
Inner detector	± 2.5			
- vertexing	± 1.5	Si pixels	Si micro-strips	Removable at high $\mathcal{L}$
- innermost tracking	± 1.5	Si micro-strips		if necessary
	> 1.5	GaAs micro-strips		
- outer forward tracking	> 1	MSGC and TRD straws		
- outer central tracking	± 1	Si strips and pads TRD straws	MSGC or scint. fibres	Further studies needed to optimize layout
Superconducting solenoid		Integrated in LAr cryostat	Separate cryostat	2 T
Calorimetry	± 5			
- em with preshower				
- barrel	± 1.5	LAr Accordion	LAr TGT	
- end-caps	1.5–3	LAr Accordion or TGT	or scint. fibres	
- hadronic				Possibly a tail
- barrel and end-caps	± 3	LAr, or scintillating fibres or scintillator tiles		catcher calorimeter in case of LAr
- forward	3–5	Liquid scintillator or high pressure gas		
Muon system	± 3			
- magnet	± 3	Superconducting air-core or warm iron-core toroids		
- tracking detectors	± 3	High pressure drift tubes or honeycomb strip chamb. or jet cell drift chambers		
- trigger	± 2.5	Resistive plate chambers	Combined with tracking detector	

2 Calorimeter System

2.1 Introduction

The study of the physics accessible at LHC has led to the following design criteria for the calorimetry system:

- good electromagnetic (*em*) calorimetry for identification and measurement of photons and electrons in the energy range from 7–10 GeV up to a few TeV;
- hermetic jet and missing transverse energy measurement;
- ability to operate and trigger at luminosities in excess of 10^{34} $cm^{-2}s^{-1}$;
- ability to tolerate the radiation level accumulated during at least 10 years of operation.

This leads us to propose a system as shown in Fig. 2.1. Calorimetry covers a rapidity range $|\eta| < 5$ with full coverage of azimuth. The barrel and endcap parts ($|\eta| < 3$) consist of a lead/liquid argon (LAr) electromagnetic (*em*) calorimeter, followed by a hadronic calorimeter, thick enough to contain the very high energy jets which will be produced at LHC. In the forward region ($3 < |\eta| < 5$) where speed and radiation hardness are crucial, a separate detector with somewhat lower performances is used.

The superconducting solenoid, providing the central field, is placed in front of the *em* calorimeter, with its coil being integrated in the cryostat of the barrel calorimeter. The position of the solenoid coil, in front of the *em* calorimeter rather than behind, results from detailed simulation studies. The loss of resolution due to an increase in the dead material in front of the calorimeter is found to be less serious than the disadvantages which would result from the coil being placed behind the *em* calorimeter: shower widening due to the presence of a magnetic field, degradation of the jet energy measurement due to the dead space occupied by the coil, and higher costs.

The choice of the LAr technology for the *em* calorimeter is motivated by:

- the radiation hardness of this technique;
- the significant progress which has recently been achieved in the readout speed by the RD3 collaboration [1];
- the ease of segmenting the calorimeter in small cells to reduce pile-up;
- the stability of the detector response and its uniformity which make energy calibration easier.

It is supported by the successful building and operation of large-scale detectors like H1 [2] and D0 [3].

A preshower detector, located between the cryostat-coil assembly and the calorimeter, serves for particle identification and photon direction measurement. It allows us also to correct for the energy lost in the upstream material.

A lead-fibre *em* calorimeter, following the technique developed by the RD1 collaboration [4], is kept under investigation as an alternative.

For hadron calorimetry, three options are being actively studied: iron-LAr or iron-scintillating fibres or iron-scintillator tiles. The flux return yoke of the solenoidal coil is integrated in the calorimeter structure of the scintillator options. In the case of LAr, the possibility to instrument the yoke outside of LAr as a tail-catcher calorimeter is being investigated.

2.2 Physics Requirements

2.2.1 Electron and photon calorimetry

The search for processes such as the production of the SM Higgs or of a heavy Z′ (see Chapter 8) puts severe requirements on the *em* calorimetry in terms of dynamic range, acceptance, energy resolution, direction measurements and particle identification.

2.2.1.1 Acceptance

The efficiency for the detection of the decay of a low-mass $H \rightarrow ZZ^* \rightarrow 4e$ increases rapidly with decreasing E_T thresholds. On the other hand, very energetic electrons up to ~ 3 TeV need to be measured for a heavy $Z' \rightarrow ee$. The detector should thus be able to cover the energy range from 7–10 GeV up to 3 TeV.

To maintain the acceptance to processes with small measurable rates, like $H \rightarrow ZZ^* \rightarrow 4e$ or $H \rightarrow \gamma\gamma$, measurement and triggering ability should cover the rapidity range $|\eta| \lesssim 2.5$.

2.2.1.2 Energy resolution

The energy resolution of *em* calorimeters can be expressed as the quadratic sum of three terms:

$$\Delta E/E = a \oplus \frac{b}{\sqrt{E}} \oplus \frac{c}{E}.$$

The constant term a, which dominates the energy resolution at high energy, is affected by the quality of the mechanical assembly and of the detection medium, by the uniformity of response and stability with time, and by the cell-to-cell calibration. The depth of the *em* calorimeter also sets a limit to the resolution: the fluctuation on the shower leakage at

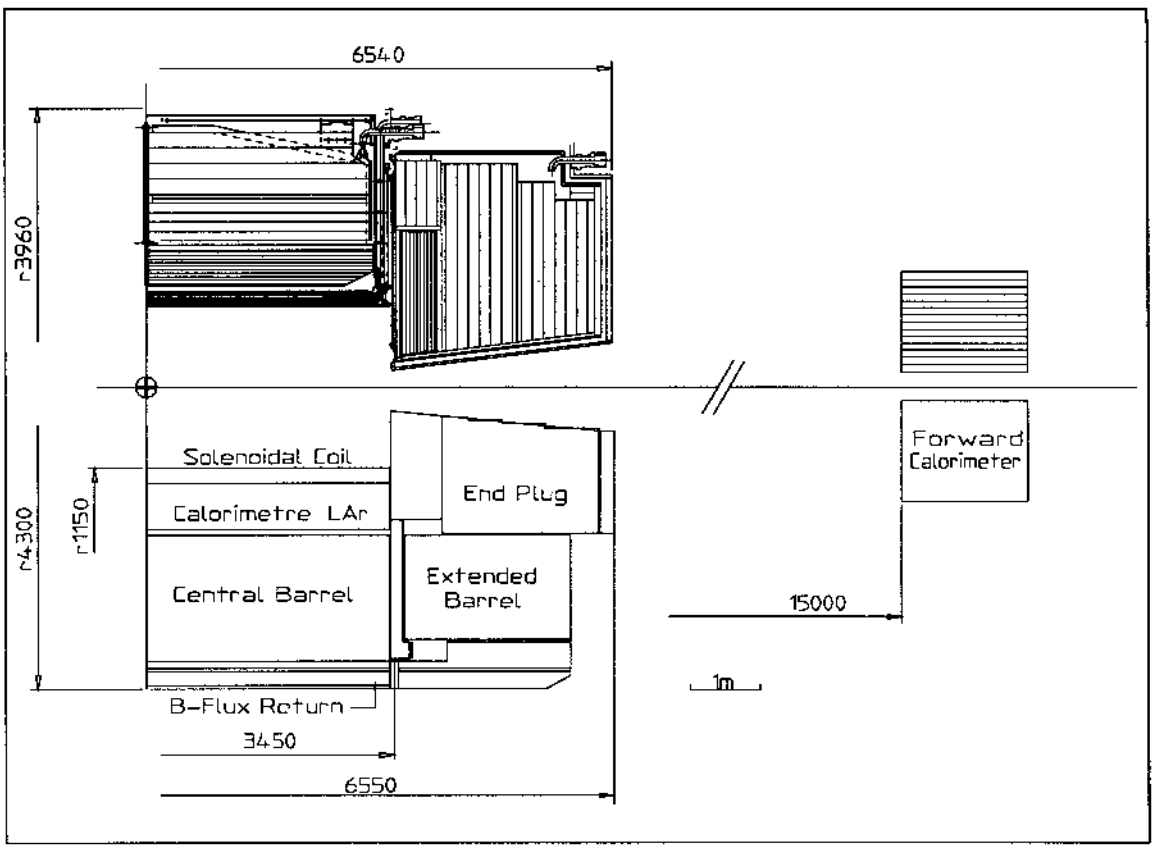

Figure 2.1: *Barrel, end-cap and forward calorimeter. In the barrel and end-cap regions lead-LAr em calorimetry is followed by hadron calorimetry: either iron-LAr as shown in the upper part or iron-scintillator (tiles or fibres) as shown in the lower part of the figure. The separate solenoid flux return (or tail catcher calorimeter) is not shown in the case of the full LAr version.*

the back of a 26 X_0 deep calorimeter is $\simeq 0.5\%$ for a 500 GeV electron [7]. A constant term a of 1% or better is the design goal.

For lower energies, the sampling term b becomes more important. Relevant processes are the low-mass Higgs decays $H \rightarrow ZZ^* \rightarrow 4e$ and $H \rightarrow \gamma\gamma$. With a 1% constant term, a sampling term b of 10% or better is required [8].

Electronics and pile-up noise contribute to the noise term c. The distribution of the probability of having more than a given transverse energy (E_T^{min}) coming from the pile-up of an average of 40 minimum bias events in $\Delta\eta \times \Delta\phi = 0.08 \times 0.08$, the typical cluster size to contain an *em* shower, is shown in Fig. 2.2. The 40 events correspond to the pile-up of 2 bunch-crossings, 15 ns apart, in the sensitive time of a typical detector at full LHC luminosity. The distribution of pile-up energy has an rms of $\sim$ 215 MeV and exhibits large tails affecting the resolution of a very precise *em* calorimeter. To a first approximation, the rms of the pile-up energy increases linearly with the lateral size of the cell while the probability of having events above a certain energy increases much faster, roughly linearly, with the cell area [9]. In order not to be dominated by pile-up effects, the detector should be fast, and have a granularity of typically $\Delta\eta \times \Delta\phi = 0.025 \times 0.025$, such that a 3×3 cell cluster contains more than 95% of the shower energy. Additional contributions to the term c, such as electronics noise, should be kept at or below the pile-up level.

The many Z's decaying to electrons produced at LHC will provide an absolute calibration of the energy scale and a check of the resolution of the calorimeter.

2.2.1.3 Direction measurement

To reconstruct a $\gamma\gamma$ mass at high luminosity, in cases where the event vertex is not known the measurement of the photon direction must come from the

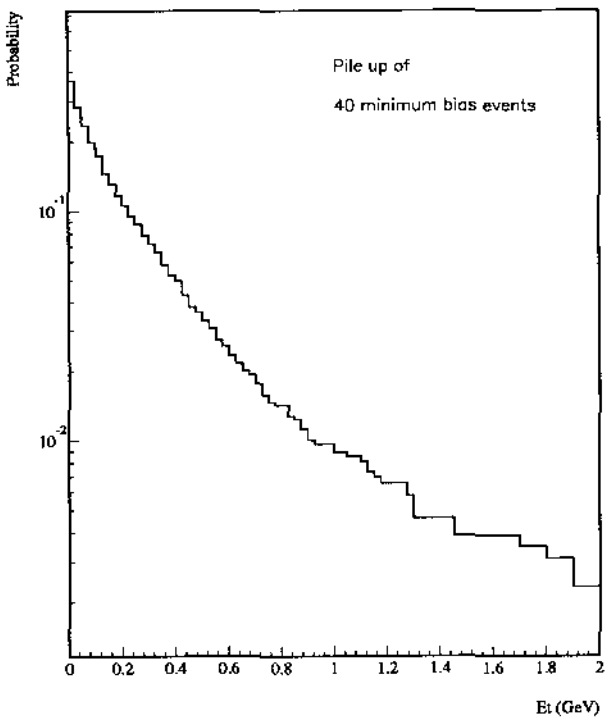

Figure 2.2: *Probability that the transverse energy piled up in an em cluster is larger than E_T, (see text)*

calorimeter. Given an energy resolution of $\frac{10\%}{\sqrt{E}} \oplus 1\%$, an angular resolution of $\Delta\Theta = \frac{100\text{mrad}}{\sqrt{E}}$ or better is sufficient in order not to further degrade the two-photon mass resolution [10]. Such an angular measurement can be obtained with the transverse segmentation given above and an at least 2-fold longitudinal segmentation of the *em* calorimeter. Using in addition the preshower detector will further improve the angular resolution.

2.2.1.4 Particle identification

The dominant background in electron and photon identification comes from jets. Longitudinal and transverse segmentation of the *em* calorimeter give a measure of the shape of the cluster. This is an essential tool in rejecting jet backgrounds [11, 12]. Increasing the transverse segmentation of $\Delta\eta \times \Delta\phi$ from 0.02×0.02 to 0.06×0.06 degrades the jet rejection by a factor of 2 to 3 at trigger level. To veto leakage at the back of the *em* section and to apply isolation criteria, the hadronic calorimeter should also be segmented ($\Delta\eta \times \Delta\phi \sim 0.1 \times 0.1$). A longitudinal segmentation of the hadronic section would reduce the sensitivity of these cuts to backgrounds and to the presence of nearby jets.

Isolated energetic *em* clusters with no high p_T charged tracks pointing to them are photon candidates. The remaining background to photons comes from π^0's. Multi-π^0's are removed using the fine granularity of the calorimeter. To reject single π^0's up to ~ 70 GeV E_T, which is typically what is needed for the $H \rightarrow \gamma\gamma$ search, a very fine grain preshower detector positioned after 3 X_0 of material is required [13].

2.2.2 Jet calorimetry

The jet energy defined by the energy flow in a cone of opening angle $\Delta R = \sqrt{(\Delta\eta)^2 + (\Delta\phi)^2}$ around the jet direction is subject to several uncertainties:

- fragmentation effects which depend on the nature of the jet (light-quark, heavy-quark or gluon);
- the energy carried away by non-interacting particles (ν or μ);
- the amount of energy swept in and out of the cone by the solenoidal magnetic field;
- the pile-up energy from minimum-bias events (5.8 GeV rms in a cone $\Delta R = 0.5$ for an average of 40 minimum-bias events).

With these limitations in mind, several processes have been studied to determine the required performance of the hadron calorimeter.

2.2.2.1 Inclusive jet cross-section

The measurement of the inclusive jet cross-section at LHC will test the validity of QCD by searching for deviations from its expected QCD behaviour, as introduced by quark compositeness (see Section 8.7). The understanding of possible non-linearities of the calorimeter response as a function of energy is the most important issue for such measurements.

2.2.2.2 Jet spectroscopy

Several examples of multi-jet signals are discussed in Chapter 8. They are particularly important for top-quark physics which can be studied in the 10^{33} cm^{-2}s^{-1} luminosity range. In this case pile-up effects are small and the calorimetric jet resolution has a significant impact on the multi-jet mass resolution. The constant term of the jet energy resolution affects in particular the search for high-mass objects such as a heavy Z' decaying into two jets where pile-up effects are negligible, even at high luminosity, as discussed in Section 8.6. A jet energy resolution of

$\frac{\sigma(E)}{E} = \frac{50\%}{\sqrt{E}} \oplus 3\%$ has been adopted as design goal for the barrel and end-cap calorimeters.

Energy leakage at the back of the calorimeter affects the resolution. Simulations show that the resolution does not improve significantly with calorimeter depth beyond $\sim 9\ \lambda$.

In the case of two-jet final states from high-p_T W or Z, e.g. from a heavy Higgs decay, good granularity is important to resolve the nearby jets. Given the fine *em* calorimeter granularity the requirement on the hadronic part is $\Delta\eta \times \Delta\phi \lesssim 0.1 \times 0.1$ as discussed in Chapter 8.

2.2.3 Missing transverse energy

As detailed in Chapter 8, the measurement of E_T^{miss} is important for the search of Higgs and SUSY particles; it also helps in top physics. Figure 2.3 shows that the calorimeter should cover at least four units of rapidity to reduce the Z + jet background in the search for the process $H \rightarrow ZZ \rightarrow \ell^+\ell^-\nu\bar{\nu}$ ($M_H \geq$ 500 GeV) to an acceptable level.

Cracks between active components of the detector (for instance around $|\eta| \simeq 1.4$ and $|\eta| \simeq 3.0$) must be kept small. Energy leakage can also occur in case of a too thin calorimeter. The minimal required calorimeter depth has been chosen by matching the energy leaking at the back of the calorimeter to the irreducible level of energy loss due to prompt neutrinos and muons, using simulations and extrapolations of lower energy data [14]. Energy leakage effects become negligible for a minimum depth of 9 λ in the barrel and 10 λ in the end-caps, even for highest jet energies.

2.2.4 Jet tagging

Jet tagging at high rapidity ($|\eta| \geq 3$) is important to identify WW/ZZ fusion processes where final-state quark jets with an energy of a few TeV are produced in the forward direction. Here a moderate energy resolution $\frac{\sigma(E)}{E} = \frac{100\%}{\sqrt{E}} \oplus 7\%$ is adequate. The transverse granularity should be equal or better than 0.15×0.15.

2.3 Liquid Argon Calorimeter Design

At present, two designs for integrated LAr *em* and hadronic calorimetry are under study:

- the 'Accordion' design, based on test beam results [1] and
- the 'Thin Gap Turbine' (TGT) design [15].

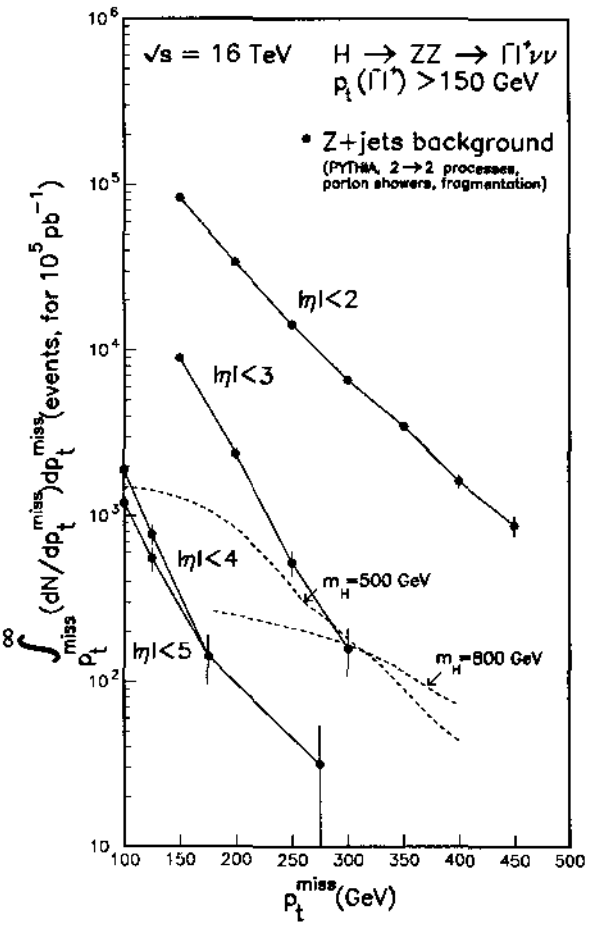

Figure 2.3: *Effect of calorimeter coverage*

For the *em* barrel the Accordion is the baseline design, the TGT an alternative. Both are options for the *em* end-caps.

Prototypes of both *em* and hadron calorimeters with all the features of an LHC detector are being built for the Accordion design for testing at the end of this year.

For the TGT design, an *em* prototype is under construction to be tested in spring 1993.

2.3.1 Overall system aspects

This section describes the system aspects common to both calorimeter designs.

The calorimeter is housed in three large independent cryostats, one for the barrel and one for each end-cap. The proposed design of the cryostats aims at reducing dead material and dead space to a minimum.

The solenoid coil is integrated inside the vacuum of the cryostat, and a liquid argon preshower detector is placed between the coil and the *em* calorimeter. This configuration is optimum in a number of ways:

- The total radial space for the coil and cryostat is only 220 mm.
- The preshower detector is located outside the magnetic field, thus it can achieve its best performance.
- The coil and cryostat walls are used as part of the material for the preshower detector.

The amount of material in front of the calorimeter varies from 1 X_0 at $\eta = 0$ to 2.5 X_0 at the end of the barrel ($\eta \sim 1.4$). Simulations and beam tests have shown that the energy resolution is not degraded by the presence of this material if the energy can be measured in the preshower after 2 and 3 X_0. For γ/π^0 identification, the best thickness for the preshower detector is between 3 and 4 X_0.

The discontinuity between barrel and end-cap calorimeters is minimized by:

- flat and thin end-walls of the cryostats;
- integrating the service lines for the coil into the vacuum of the cryostat;
- placing the feed-throughs for the large number of channels of the *em* calorimeter at the outermost radius of the hadron calorimeter.

For the hadronic part, a transverse segmentation of $\Delta\eta \times \Delta\phi \leq 0.05 \times 0.05$ has been chosen, somewhat finer than required in Section 2.2. This is motivated by considerations of electronics noise and the effectiveness of the software weighting technique in LAr calorimetry [16].

In order to measure the hadron energy leaking out of the LAr calorimeter and to help identify muons among the hadronic debris of high-energy jets or those which have suffered catastrophic energy loss, the iron structure of the return yoke could be instrumented. A possibility is to equip the gaps between the iron plates with plastic streamer tubes with capacitive readout pads and strips parallel to the wires.

The pads read out by analogue electronics are used for hadron energy measurement. The strips track muons through the iron and recognize punch-through.

The position of the transition between precise LAr calorimetry and the tail-catcher would be optimized for performance and cost.

2.3.1.1 The cryostat

The necessity of holding the hydrostatic pressure of the liquid usually leads to having either thick flat walls, or thinner but bulged walls. In the novel cryostat design, as shown in Fig. 2.1, the stainless steel cold wall is tied to the ends of the hadronic calorimeter modules, which allows it to be flat and thin (10 mm). The vacuum is contained by a thin stainless steel wall (8 mm) spaced from the cold wall by insulating pods and an epoxy lattice. A flexible connection between the warm end-wall and the warm tubes allows for relative longitudinal movements of the inner and outer vessels during cool-down. This is provided at the inside and outside radius by two thin (2 mm steel) rings of $\Delta R = 200$ mm, slightly bulged.

Care has been taken to minimize the thickness (in X_0) of the central tubes. The warm tube can easily be made of aluminium (10 mm). However, the use of aluminium for the cold tube is more difficult because of the connection between the aluminium tube and the steel walls. Our proposal is to use a 27 mm aluminium support tube and, for tightness, a 2 mm thick skin of steel welded to the body of the cryostat.

2.3.1.2 The solenoid coil

The solenoid is a single-layer superconducting coil 123 cm in radius and 630 cm in length. The current is 7500 A and the stored energy is 50 MJ. Owing to the small radius-to-length ratio the field homogeneity is good down to very low polar angles, as discussed in the tracking section. The coil is supported at the ends by tie-rods. Horizontal rods hold it in place along the z-axis. The coil connections (He, power, vacuum) run along the end-walls of the calorimeter inside the vacuum. There is a separate vacuum for the coil, in order to reach a lower pressure than in the calorimeter vacuum. This enclosure is closed at its ends by a flexible membrane similar to the one discussed above (see Fig. 2.4).

2.3.1.3 The Cryogenics

The barrel and the two end-caps are contained in three independent vessels. The barrel cryostat contains ~ 120 m^3 of LAr. It is foreseen to have no gas phase inside the main vessel and to use an expansion vessel (12 m^3). Heat exchangers with a liquid nitrogen flow are placed inside the main vessel at the inner and outer circumferences and possibly at locations with high power dissipation. The operation is regulated with respect to the temperature in the main vessel and the pressure in the expansion vessel. In the Accordion design, the power consumption for the barrel is 6.5 kW for radiation losses, 6 kW for the feed-throughs, and 12 kW for the *em* preamplifiers if these are in the argon (the consumption for the preshower electronics is yet unknown, but would not exceed 6 kW). The cool-down time for the barrel calorimeter (1200 t) will be of the order of two months.

The safety aspects of the LAr system are discussed

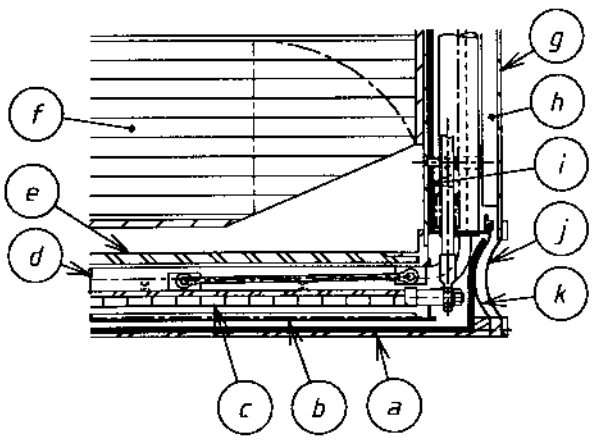

Figure 2.4: *Close-up view of the end-corner of the barrel (longitudinal cut) showing: a) warm tube, b) thermal screen, c) coil, d) He collector, e) cold tube, f) em calorimeter, g) warm end-wall, h) epoxy lattice, i) cold end-wall, j) flexible ring (warm wall), k) flexible ring (coil vacuum separation)*

in Section 6.5.

2.3.2 Fast LAr calorimetry

The operation of calorimeters at LHC imposes unprecedented requirements on the readout speed of the detectors.

During the time ionization electrons drift in the liquid, many events pile-up and may spoil the energy resolution of the detector. This can be overcome, in principle, by exploiting the rapid rise time ($\sim$ 1 ns) of the ionization current in the LAr. In practice this is done by electronic shaping; the price to pay is a worsening of the signal-to-noise ratio. To limit safely the contribution of the pile-up noise, without increasing the electronics noise too much, the peak of the response of the shaping circuit to a δ current pulse t_p^δ must be $\sim$ 20 ns for the *em* calorimeter. The drifting electron signal then would have a peaking time of $\sim$ 40 ns, provided there is no time constant longer than $\sim$ 10 ns in the connections between the detector cell and the preamplifier.

Both LAr designs considered use techniques which attempt to overcome the above-described difficulties. The RD3 collaboration has shown that a fast LAr readout and therefore the use of LAr calorimetry in LHC conditions is indeed feasible. This work is described in the following sections.

2.3.2.1 The Accordion and EST concepts

The RD3 collaboration has recently developed and tested an attractive solution to overcome this difficulty, based on a new calorimeter geometry in which the electrodes and converter plates (separated by honeycomb) have an accordion shape with waves parallel to the direction of the incident particles. Readout towers are naturally defined by cutting the electrodes in longitudinal strips through which the signal propagates to the calorimeter front or back faces. With preamplifiers directly mounted there, no additional cables are needed and the most favourable configuration for high speed, low noise and small crosstalk is reached. At the same time the absence of dead space between towers gives a hermetic detector and allows high granularity.

For hadronic calorimetry, the accordion structure is complemented by the electrostatic transformer (EST) readout scheme in which several argon gaps are connected in series. This allows fast readout of large towers and optimizes the signal-to-noise ratio [17].

2.3.2.2 Test beam results of the Accordion

The feasibility of the Accordion approach to fast LAr calorimetry has been proven by the performance of *em* prototypes extensively tested at the CERN SPS in muon, electron and photon beams [18, 19].

Fast output signals (Fig. 2.5) were observed. Without optimizing the shaper performance, the measured electronics noise was about 70 MeV/channel ($\sim$ 300 MeV contribution to an *em* shower) and the muon signal was at three standard deviations above the noise.

The Accordion geometry gives rise to a small response modulation transverse to the accordion waves (Fig. 2.6). This effect is well reproduced by a Monte Carlo simulation of the calorimeter including the charge collection mechanism; it is contained within 1-2% and can be easily corrected for. The resolution (Fig. 2.7) obtained by reconstructing the electron energy in a 3×3 cell cluster (each cell was 2.5×2.7 cm^2) is: $\frac{\sigma(E)}{E} = \frac{(9.6 \pm 0.3)\%}{\sqrt{E}} \oplus (0.3 \pm 0.1)\% \oplus \frac{0.326 \pm 0.015}{E}$ where E is in GeV and the last term is the contribution of the electronics noise. No degradation in the sampling term is observed due to the fast shaping. The resolution of the cluster position measurement is ~ 5 mm$/\sqrt{E(\mathrm{GeV})}$ in both directions.

2.3.2.3 Integrated LAr preshower detector

A small size (6×6 cm^2) LAr preshower prototype [20] has been tested in front of the projective LAr calorimeter prototype discussed above [19]. It consisted of two 10 mm thick LAr layers, instrumented for x/y readout (granularity 2.5 mm), pre-

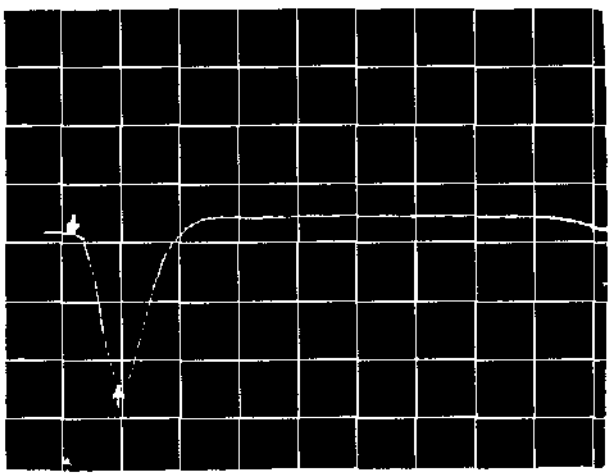

Figure 2.5: *Fast shaped signal from a 60 GeV electron hitting one calorimeter cell. The 400 ns electron drift time is clearly visible. (50 ns × 50 mV per square)*

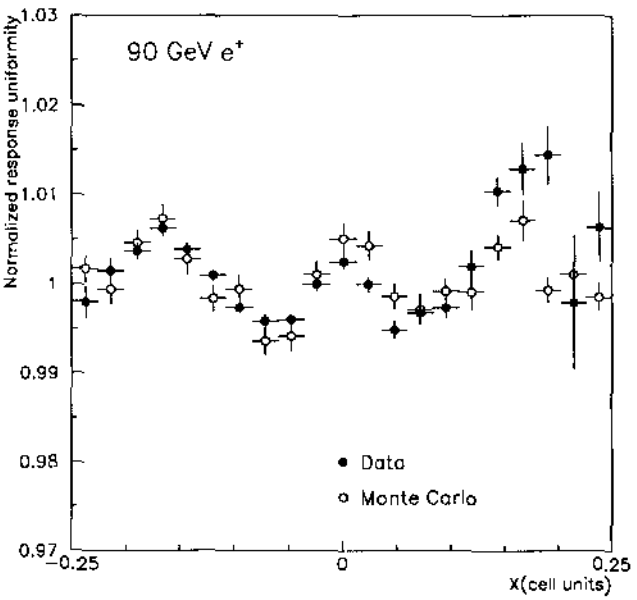

Figure 2.6: *Normalized calorimeter response to 90 GeV electrons along the direction perpendicular to the accordion waves, over half a cell*

ceded by 2.1 X_0 of material and separated by 1.2 X_0 of lead.

A signal-to-noise ratio of about 10 and a space resolution of 340±40 μm were measured with muons.

When the preshower detector is placed in front of the calorimeter the Accordion energy resolution is preserved (Fig. 2.7), provided that the signal released in the active preshower layers is used to recover the energy lost by the electron in the upstream material. The combined preshower–calorimeter system is linear within ±1% in the range 10–200 GeV.

The shower barycentre reconstructed by the preshower detector (resolution ~ 2 mm$/\sqrt{E(\mathrm{GeV})}$) can be combined with the position measured by the calorimeter to determine the direction of the incident particle. The angular resolution achieved with electrons and photons (Fig. 2.8) is better than 5 mrad above 40 GeV. From the longitudinal segmentation of the calorimeter alone, the angular resolution is somewhat worse $\sim$ 8 mrad above 50 GeV. A rejection factor of more than 3 against 50 GeV π^0 for a single γ efficiency of 90% was obtained using results from photon data.

2.3.3 Accordion design

2.3.3.1 The *em* barrel calorimeter

Taking advantage of the Accordion geometry, we present below a design in which the barrel *em* calorimeter has a complete ϕ symmetry, without cracks. The detector is made of 1024 converter plates, all identical, interleaved with multilayer readout Kapton electrodes. Each readout electrode covers a pseudo-rapidity interval of 0.3. For the barrel calorimeter there are 10 different readout electrodes.

For the purpose of assembly and testing, converter and readout electrodes are grouped in 32 modules each containing 32 converter plates. Each converter plate is 6.4 m long and about 45 cm wide and is built from 1.8 mm thick lead sheet clad with two layers of 0.2 mm thick stainless steel. In order to work with a constant argon gap (2 × 1.9 mm) and a constant sampling fraction in depth (24%), plates are folded with a varying angle from 76° at the inner radius (1.43 m) to 103° at the outermost radius. In order to keep the variation of the effective absorber thickness with η at an acceptable level, the amount of lead in the electrodes is decreased for $|\eta| > 0.9$ from 1.8 mm to 1.2 mm. The effective radiation length of the calorimeter is 18 mm.

The readout electrodes are divided, along η, in 12 strips spanning the same η interval, chosen to be 0.025. In the azimuthal direction a similar granularity (0.0245) is obtained by ganging together 4 adjacent strips. The readout is divided in three longitudinal sections, typically 8 X_0 each. For the purpose of limiting the channel count, the last section would have a coarser granularity (0.05 × 0.025).

All modules are precisely positioned in a stainless

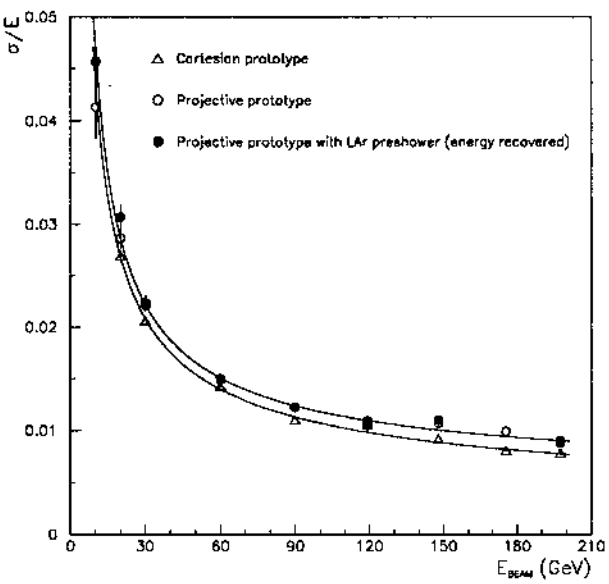

Figure 2.7: *Energy resolution of Accordion prototypes versus electron energy*

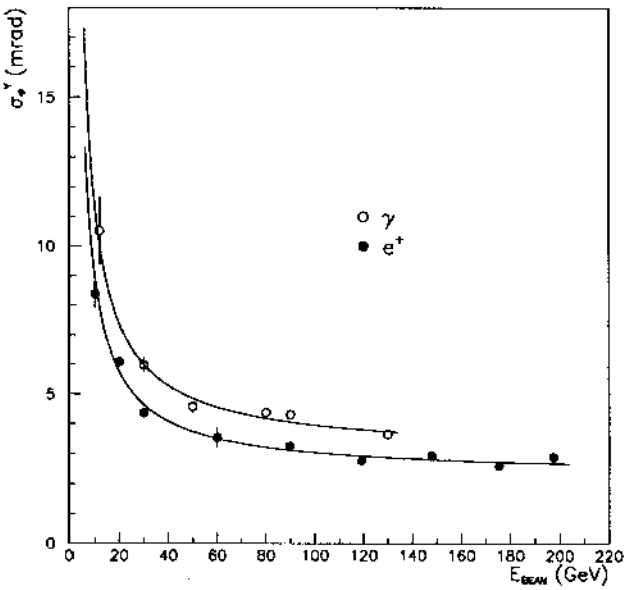

Figure 2.8: *Angular resolution of the combined preshower-calorimeter system (in the η direction)*

steel cylinder reinforced by flanges at each end, and tied to a set of rings at the inner radius. Vertical mounting is foreseen. Preliminary estimates of deformations indicate that, under the calorimeter load ($\sim$ 100 t), the 1 cm thick cylinder would sag longitudinally by about 1 mm. Converter plates close to the horizontal plane would also sag under their weight, by about 0.6 mm. However, such a deformation, being continuous from vertical to horizontal positions, would maintain the gap constant within narrow tolerances (0.05 to 0.1 mm).

A detector of similar geometry, 2 m long and spanning 27° of azimuth is currently being assembled (beam tests in autumn 1992) by the RD3 collaboration. Figure 2.9 shows a schematic view of the converter and readout electrodes of this prototype, and Fig. 2.10 is a picture of the prototype taken during assembly.

2.3.3.2 Preshower detector

The *em* calorimeter is preceded by a preshower section of high granularity, integrated in the LAr. Using tapered material the total thickness of the preshower detector, irrespective of η, is chosen to be 3 X_0. The readout is organized in two 'shells' of ministrips, perpendicular to each other and located after 2 and 3 X_0 for the ϕ- and η-shell respectively. The granularity chosen is 0.002×0.1. The detector would be built in modules, tied to the corresponding calorimeter module. The precision mounting system of the calorimeter should allow position measurements in both the calorimeter and the preshower detector with an absolute accuracy of about 0.2 mm. The geometry of the detector, locally, follows closely the recently tested prototype, except for longer strips (12 cm). A sketch is shown in Fig. 2.11.

The most challenging problem with the preshower detector concerns the readout which should combine radiation resistance, low noise and low power dissipation while maintaining a large enough dynamic range. A R&D programme, within the framework of RD3, has recently been approved [21].

2.3.3.3 The *em* end-cap calorimeter

Each end-cap is made of two coaxial wheels, cut at a radius of about 700 mm ($\eta = 2.3$). Each wheel is ϕ symmetric, without cracks, and made of accordion-shaped electrodes with a folding angle which varies from about 70° at the inner radius to 110° at the outer radius. The converter electrode structure (lead–stainless steel sandwich) must be adjusted to give the detector a constant thickness (in X_0) as a function of radius. The larger wheel has 768 converter plates, leading to the same granularity as the barrel: 0.0245×0.025. In the inner wheel there are only half the number of plates, and the granu-

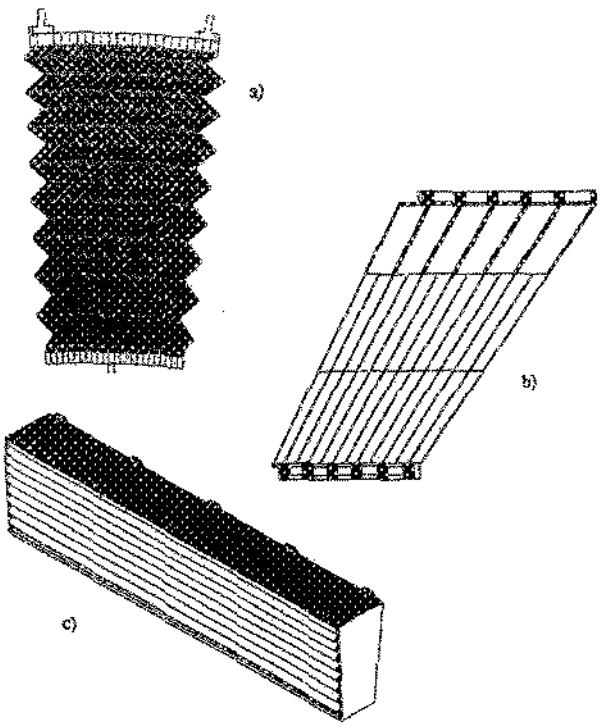

Figure 2.9: *(a) Transverse view of the em prototype module, with radial dimensions of 1.43–1.95 m (b) a Kapton readout electrode (c) perspective view of a 2 m long module*

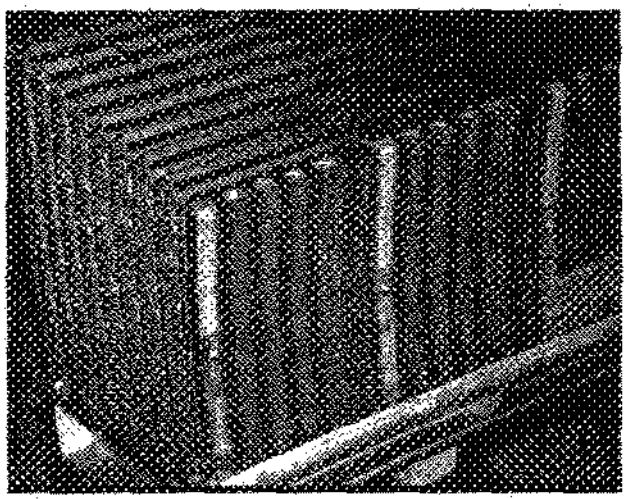

Figure 2.10: *Picture of the em Accordion prototype under construction (stack of two modules)*

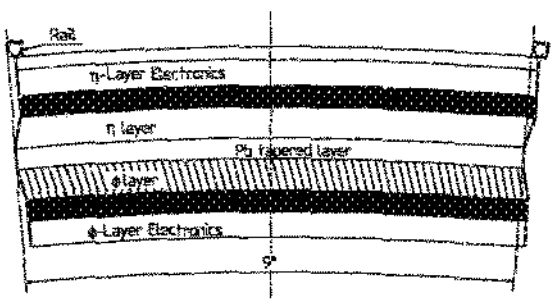

Figure 2.11: *Structure and sketch of a preshower module*

larity would be half. A preshower detector, using two layers of ministrips, as in the barrel, would sit in front of the calorimeter. The granularity would be kept constant at typically 3 mm × 10 cm.

The number of channels is summarized in Table 2.1. The power dissipation of electronics and the location of the feedthroughs are given in Section 2.3.1.

2.3.3.4 The hadron calorimeter

The barrel hadron calorimeter is made out of accordion-shaped stainless steel plates (12 mm thick) with the folds along the z-axis, as in the *em* part. The total thickness including the *em* calorimeter is $\sim 9\ \lambda$ at $\eta = 0$. The hadronic part is divided into projective cells with an area of $\Delta\eta \times \Delta\phi = 0.05 \times 0.05$ and in depth into two modules of two samplings each, see Fig. 2.12. In order to allow fast readout with a good signal-to-noise ratio the electrodes are connected in the EST series-parallel mode.

The structure contains two types of 12 mm thick plates: ground and readout plates, both folded in an accordion shape. The angles of the accordion change with radius, and single folds are curved in order to keep the argon gap constant at 2.5 mm. To implement the EST concept, the readout plates are cut to form the readout cells. Then the pieces, separated by insulating material, are re-assembled as a tile and clad with Kapton, for insulation, and a resistive coating connected to high voltage. In the inner (outer) two samplings, a calorimeter module is obtained by assembling 5 (7) readout plates between 2 ground plates (Fig. 2.12). The central readout piece of each cell is connected to a preamplifier, reading out 6 (8) argon gaps, in a 2 parallel × 3 series way (2 parallel × 4 series). As for the *em* calorimeter preamplifiers are located at the front and back faces

Table 2.1: *Main characteristics of the Accordion design. In the end-cap section, had0 denotes the calorimeter which surrounds the em section.*

		t_p^0 ns	noise MeV/cell	X_0	channels
	PS1	40	0.2 mip	2	92 200
	PS2	40	0.2 mip	1	92 200
B	em1	20	70	8	30 700
A	em2	20	70	8	30 700
R	em3	20	90	>8	14 300
R				λ	
E	had1	80	80	1.3	6 600
L	had2	80	100	1.6	6 100
	had3	80	200	2.4	5 400
	had4	80	220	2	4 600
				X_0	
	PS1	40	0.3 mip	2	39 400
E	PS2	40	0.3 mip	1	39 400
N	em1	20	60	8	12 500
D	em2	20	60	8	12 500
-	em3	20	90	9	6 300
C				λ	
A	had0	80	200	2.3	900
P	had1	80	160	2.3	2 600
	had2	80	160	2.3	2 600
	had3	80	150	2.3	2 400
	had4	80	150	2.3	2 200

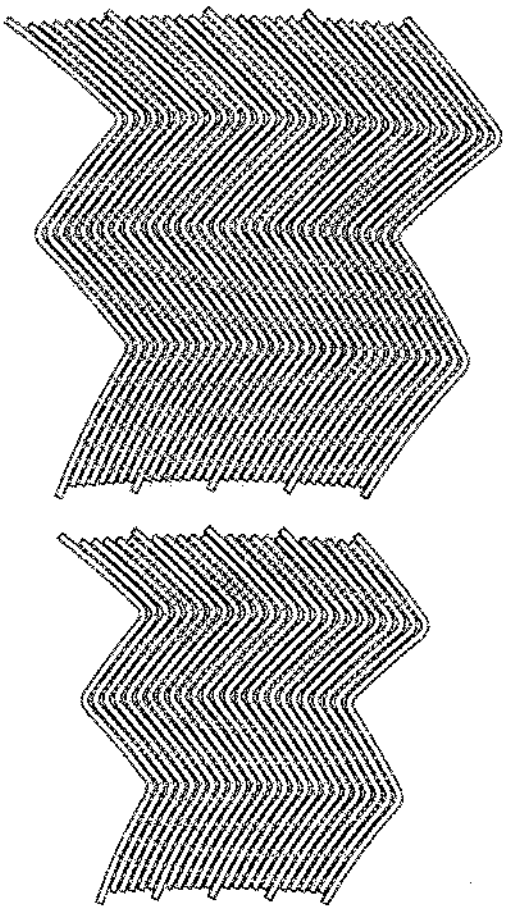

Figure 2.12: *Profile view of a sector of the accordion hadron calorimeter; 4 barrel modules are shown. The radial dimensions are $r_i = 2.08$ and $r_o = 3.60$ m*

of each module. 128 such modules form a complete ring without any azimuthal cracks.

The end-cap hadron calorimeters have a depth of 11 λ (*em* included). The granularity is identical to the barrel except at high rapidity, the smallest size of a cell being $\sim 8 \times 8$ cm^2. Each end-cap is made by 4 wheels in depth. Each wheel is divided into 4 sectors in ϕ. Each of these sectors is built around a straight accordion structure, with folds parallel to the median plane of the sector. Hence the cells are projective only in this plane. Pseudo-projectivity in the other direction is achieved by merging cells through the 4 wheels in depth.

2.3.3.5 Front-end electronics

Three solutions are now being developed in parallel for the front-end electronics. In the first two, charge preamplifiers (using MESFET GaAs [22] or JFET silicon [23] transistors) are directly mounted on the calorimeter and used at LAr temperature. They would be exposed to radiation. The third scheme, a current preamplifier, uses bipolar transistors located outside of the calorimeter cryostat, connected to the calorimeter cells by 50 Ω cables [24]. In all three cases, the noise spectral density is smaller than 0.6 nV/$\sqrt{\text{(Hz)}}$ consistent with test beam results (see Section 2.3.2).

Several tests of radiation resistance have been done by the RD3 Collaboration. Some Si and GaAs preamplifiers have received at room temperature a flux of $4.5 \cdot 10^{14}$ n/cm^2 and a dose of 23 kGy - corresponding to the dose to which the barrel calorimeter would be exposed in more than 20 years running at full design luminosity. Measurements with a peaking time t_p^0 of 20 ns show that the noise increased by less than 10% for Si preamps (Fig. 2.13) and by 40% for GaAs preamps. The rise-time deterioration was less than 2 ns. Some measurements were done (also at room temperature) with a ^{60}Co source at a dose of 600 kGy (corresponding to more than two years in the end-

cap). The noise increased by a factor 2 for GaAs preamps and by a negligible factor for Si preamps. It is planned to repeat these measurements at LAr temperature.

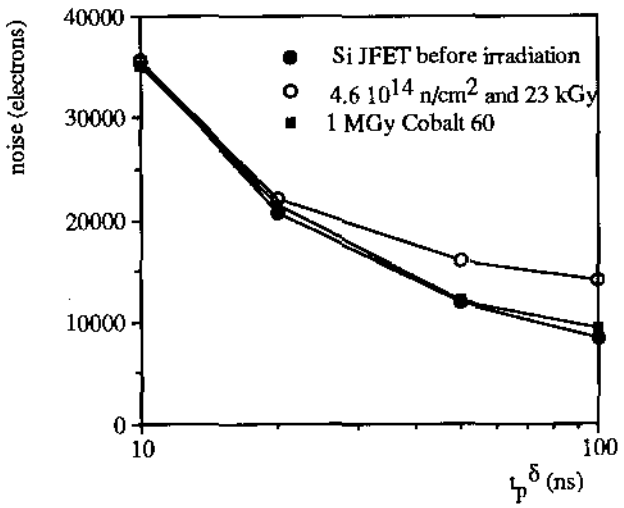

Figure 2.13: *Electronics noise increase under severe irradiation as a function of shaping time*

The calibration system aims at a precision of $\sim$ 0.2%. A first design with active elements at LAr temperature, and a second one with only precision resistors inside the cryostat are being developed in the RD3 Collaboration. Both will be tested in the autumn of 1992.

For the preshower detector, $\sim$ 200 000 electronics channels have to be built and operated in a limited volume. Several solutions for the front-end preamplifiers are under study [21], such as an extrapolation of CMOS monolithic chips which were designed [25] for silicon detectors. Solutions with Si JFETs or GaAs transistors are also envisaged using for instance the new radiation-hard DMILL technology [26]. The use of optical links is being evaluated; in particular light emitting diodes or modulators working in the cold, such as the ones being developed by the RD23 Collaboration [27].

2.3.4 TGT design

In the following the 'Thin Gap Turbine' (TGT) design of a LAr calorimeter is presented, as an alternative to the 'Accordion' concept. The basic arrangement of the TGT calorimeter is shown in Fig. 2.14 and its design goals are listed in Table 2.2. A detailed description of the TGT calorimeter is given in [28] and the related R&D proposal [15].

The distinct features of the TGT design are:

- the thin LAr double-gap of 2 × 0.8 mm;
- the flat absorber plates, arranged at 45° with respect to the incident particles;
- the small independent modules;
- the integrated preshower and position detector;
- VLSI electronics with a high degree of multiplexing in the cold.

Table 2.2: *Design goals of the TGT calorimeter*

	Electromagnetic	Hadronic
$\Delta E/E$	$(\gamma)\ \frac{9.5\%}{\sqrt{E}} \oplus 0.5\%$	$\sim \frac{50\%}{\sqrt{E}} \oplus 2.0\%$
$\Delta\eta \times \Delta\phi$	0.025 × 0.020	0.05 × 0.04
Signal uniformity	±0.5 %	±2 %

The thin LAr gap allows for a short charge collection and signal processing time ($\sim$150 ns) and safety against high-voltage problems (operational voltage $\leq$800 V).

The absorber and readout planes are arranged at a constant angle with respect to the particle direction chosen to be 45°. This guarantees uniform energy response and constant energy resolution over the entire η range.

The simple and modular mechanical structure eases design and construction, with a potential cost reduction. Each readout element ($\sim$ 60 × 40 cm^2) is a separate mechanical and electrical entity which can be tested independently prior to installation. The independence of the TGT elements offers a large flexibility of the pad segmentation (both longitudinally and transversally). It allows for the integration of a preshower detector and a strip detector for the precision measurement of position at its optimal location in the *em* shower.

The readout electronics consists of amplifiers which are integrated as VLSI chips on the readout board in the LAr, and of summing amplifiers and shapers on the outside of the calorimeter. The latter form the signals from the readout channels and perform a non-linear compression of the signal. The trigger signals are derived from the summing amplifiers. It is foreseen to locate integrated pipelines and a high degree of multiplexing in the LAr. Thus the number of signal cables leaving the cryostat and thereby the number of feed-throughs will be reduced to a minimum.

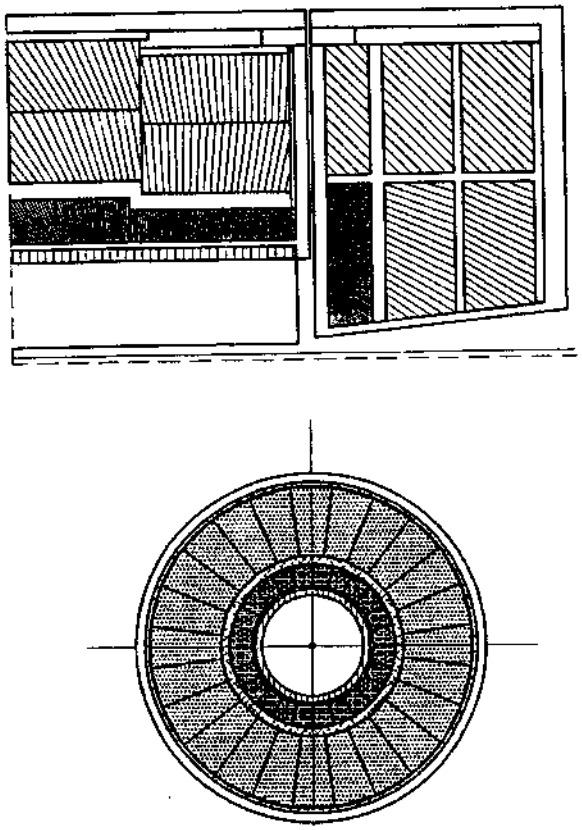

Figure 2.14: *Basic arrangement of the TGT calorimeter; lines show the orientation of the modules*

2.3.4.1 Layout of the calorimeter system

The overall layout of the integrated *em* and hadron calorimeter TGT design is shown in Fig. 2.14. The same cryostat dimensions as for the 'Accordion' design are assumed. The TGT design then allows for a somewhat larger amount of absorber material to be housed inside the cryostat ($\sim 9.6\lambda$ in the barrel).

The azimuthal segmentation was chosen to be 24-fold, adjacent radial units being rotated in ϕ by half a segment (see Fig. 2.14). The basic mechanical unit is a wheel of 24 identical calorimeter modules, mechanically stable and self-supporting. It is positioned on rails in two azimuthal places. The tower building electronics is located at the perimeter of the wheels. There will be 10 separate wheels, four in the barrel and three in each end-cap. The overall weight of the calorimeters is 3000 t. The cryostat and cryogenics have been described in Section 2.3.1.

2.3.4.2 The *em* calorimeter design

Lead is used as the absorber material for the *em* calorimeter. The total thickness is 28 X_0 at η=0.

Because of the 45° angle between the impact direction of a particle and the readout board orientation, the longitudinal segmentation is correlated with the η - segmentation. Five longitudinal segments (two larger segments at the shower maximum) yield a precise angular reconstruction of γ's and a good e/π separation. The thickness of one readout cell defines the minimal bin size in η. Depending on θ, up to four readout cells are added to form one η-bin. Beyond a depth of $\sim$ 22 X_0 there is only one segment, with the lateral granularity reduced by a factor of 2. To correct for energy losses in the passive material in front of the *em* calorimeter (preshower detector), the pad board extends beyond the absorber plates by $\sim$ 20 mm.

The readout cell is designed for fast signal transport and to avoid direct cross-talk. The total thickness of the readout cell (Fig. 2.15) is 16.0 mm, corresponding to 0.89 X_0. The sampling ratio is 8.9%. One readout cell contains four absorber plates, two outer stainless steel plates (2.0 mm) and two inner lead-plates (1.6 mm). The lead-plate is coated with 0.1 mm stainless steel sheets. Rivets keep the mechanical structure fixed, spacers between absorber plates define a double liquid argon gap of 2×0.8 mm with high precision. Three pad boards collect the deposited charge and are directly connected to a multilayer board which carries the amplifiers and the calibration inputs. The amplified signals are fed to a summing board, located close to the outer end of the multilayer board (see Fig. 2.15). An example of a pad structure, including the strip pattern, is shown in Fig. 2.16. The segmentation in depth is given by the η binning; up to 30 readout cells define one η-channel. The total dead area due to the electric connections and the rivets/spacers (HV guard zones) is below 1% on average. The pad board (copper-clad G10 board, 0.5 mm) is coated with a layer of high resistivity connected to high voltage.

Additional strips, located within the second longitudinal segment (Fig. 2.16), improve the angular resolution of single γ's and offer good π^0 rejection. One of the three pad boards has θ-strips (see board (a) in Fig. 2.16) while the two others carry ϕ-strips (board (b) in Fig. 2.16). Five strips (3.5 mm wide, length corresponding to $\Delta\phi = 0.06$) cover the acceptance of one readout cell. The relevant projected θ-strip width is thus 2.5 mm. The pad board (b) has ϕ-strips with every second strip ganged to one channel for a distance of $\Delta\phi = 0.06$. This 'double-comb structure' thus yields two ϕ-channels for a distance of $\Delta\phi = 0.06$. The third pad board has a similar structure, but shifted by half a ϕ-strip width. A local

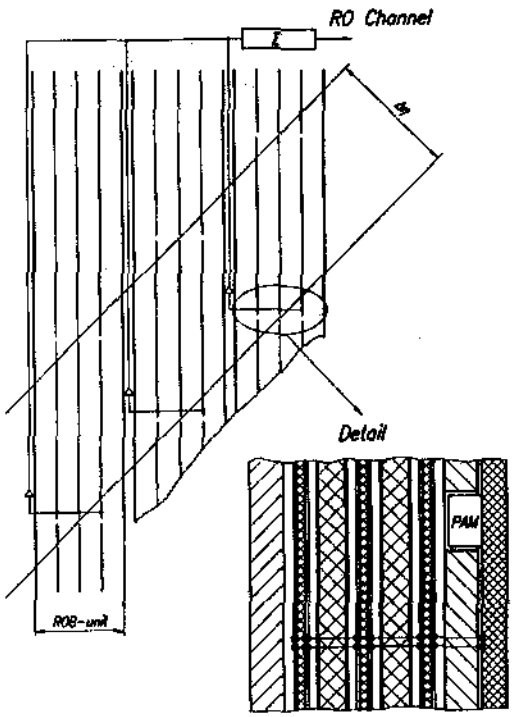

Figure 2.15: *Principle of readout structure and readout cell in the em calorimeter*

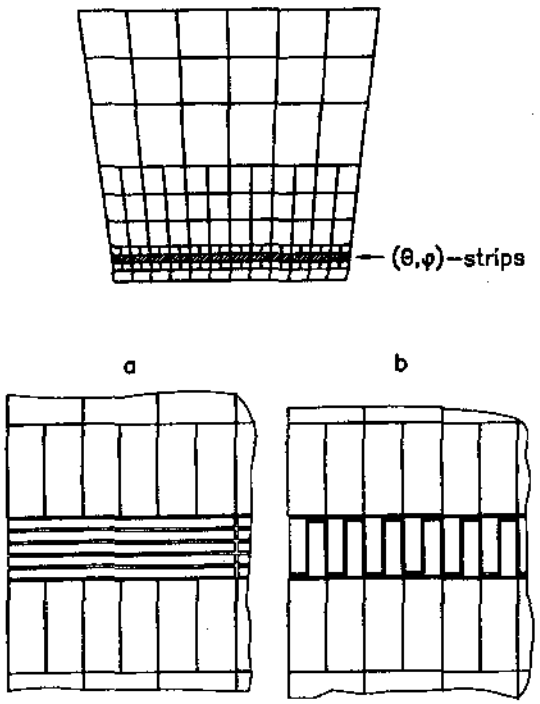

Figure 2.16: *Schematic layout of a pad board of the em calorimeter including the strip detector*

ϕ-resolution of 3.7 mm is obtained, but with ambiguities at the scale of 4 ϕ strips. To resolve these ambiguities, a finer ϕ-segmentation for the neighbouring longitudinal segment is required: $\Delta\phi = 0.01$ instead of 0.02. Adding the strips to the segmentation of the *em* calorimeter, we estimate an angular θ-resolution of 4–5 mrad for a γ of 50 GeV.

2.3.4.3 The hadron calorimeter design

The hadron calorimeter has 10 mm thick stainless steel plates, arranged in two layers, each 3.9 λ deep. The lateral granularity is given in Table 2.2 and the longitudinal segmentation is eightfold. The rather fine longitudinal and lateral segmentation of the hadron calorimeter is mainly required to apply the 'π^0-weighting technique' [16] in order to achieve compensation.

The readout cell is located in the gap between two absorber plates and is formed by two stainless steel plates (2 mm) with a pad board in the centre and a double liquid argon gap of 2 x 0.8 mm. The signals are amplified and summed in close similarity to the *em* design. The thickness of the readout cell is 7.8 mm, it corresponds (including the 10 mm absorber plate) to 0.09 λ (0.83X_0). The sampling ratio is 1.9%.

2.3.4.4 The TGT electronics

The electronic chain has to be designed with a large number of amplifiers (227 000 VLSI-chips) and readout channels (1 080 000) in mind. The chain of readout electronics for the TGT calorimeter consists of three basic building blocks: an amplifier unit, a summing, shaping and pipeline unit, and a level-2 pipeline and multiplexing unit.

The amplifier unit is located on the multilayer board of each independent readout cell. Several amplifiers are grouped into one VLSI chip, the number ($\sim$16) depending on the position in the calorimeter. A first chip is in production.

In the summing, shaping and pipeline unit the signal for the readout channels is formed by first summing over the amplifier signals of different readout cells. It is then shaped by a fast deconvolution filter. A pulse width of $\sim$ 20 ns is expected. For each bunch crossing the result of the deconvolution is nonlinearly compressed to the required resolution. It is then stored into a switched capacitor pipeline which is long enough to take care of the latency of the level-1 trigger. Sixteen channels are grouped into one chip. After a level-1 trigger signal, the information of the corresponding bunch crossing is transferred to the pipeline and multiplexing unit without stopping the filling of the level-1 pipeline. In parallel, the shaped

signals of the 16 channels are summed to form an input signal to the level-1 calorimeter trigger.

Several of these chips are positioned on a summing and merging board which is located in the LAr at the outside of the calorimeter stack. Experience with a similar chip was gained in the H1 experiment [29].

The design goal for power consumption is 20 mW per readout channel. This leads to a total power consumption of 9 kW in each of the end-caps and of 27 kW in the barrel cryostat.

2.4 Hybrid Calorimetry Designs

In comparison to the *em* calorimeter, the requirements for the hadron calorimeter are less stringent. Also the radiation level is lower by a factor of ~ 5. With a LAr *em* section in front, hybrid solutions are being investigated, with the goal of obtaining a good performance and a fast readout at lower cost.

2.4.1 Scintillating tile hadron calorimeter

Scintillator tile calorimetry with wavelength shifter (WLS) readout is a relatively simple and well-established technique. Reading out the tiles with WLS-fibres leads to excellent hermeticity and requires only a small overall photodetector surface. Usually the tiles are positioned about normal to the traversing particles. Simulations indicate that behind

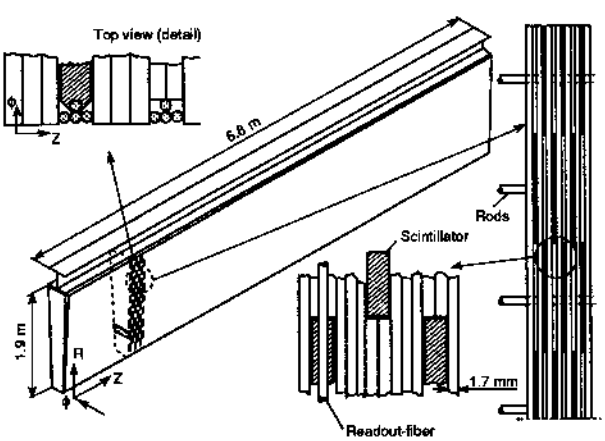

Figure 2.17: *Structural layout of a barrel module of the scintillating tile calorimeter*

the *em* calorimeter (1.8 λ) the orientation of the tiles relative to the direction of the primary particles does not affect the energy resolution for hadrons or jets provided they are staggered in depth. In the proposed layout (Fig. 2.1) the tiles are orientated normal to the beam line in the barrel and normal to the radial direction in the end-plug. This greatly simplifies the mechanical construction and the assembly procedure and contributes to cost reductions.

2.4.1.1 Design

The central barrel part [30] consists of 64 sector modules of 6.8 m length (Fig. 2.17). The absorber is a compressed stack of thin punched iron sheets leaving staggered slots for the insertion of 3 mm thick trapezoidal scintillator tiles of 10 to 20 cm height. The tiles couple on both ϕ edges to 1 mm WLS-fibres running straight in the radial direction to light detectors mounted on the outside face of the module. The ϕ granularity corresponds to the module width ($\Delta\phi$ = 0.1). The granularity in η is 0.1 as well. In depth a 4-fold segmentation is chosen such that pointing towers can be formed from the rectangular $r \times z$ cells (Fig. 2.18). The individual cells of each tower may ei-

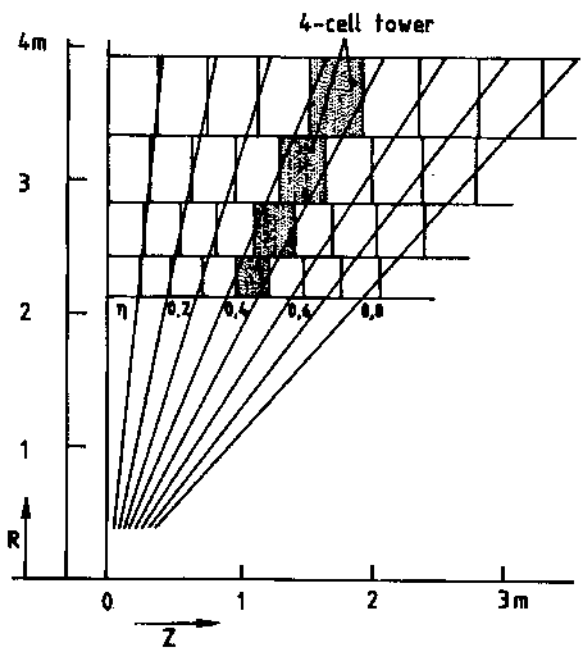

Figure 2.18: *R-z segmentation of the scintillating tile barrel calorimeter*

ther be read out independently or partially combined by common light detectors. Independent readout of the two edges of the tiles allows for offline correction of the light attenuation. Optimum light collection is achieved by inserting the fibres into grooves in the 3 mm wide faces of the tiles and by cutting their outside edges at 45°. Tiles are injection-cast into their final shapes.

Each of the recessable end-caps consists of an extended barrel part for 2 m$< R <$ 3.5 m, structured like the central barrel, and a plug part for $R <$ 2 m. The plug consists of 32 sector modules (Fig. 2.19).

Absorber plates and staggered scintillator tiles are

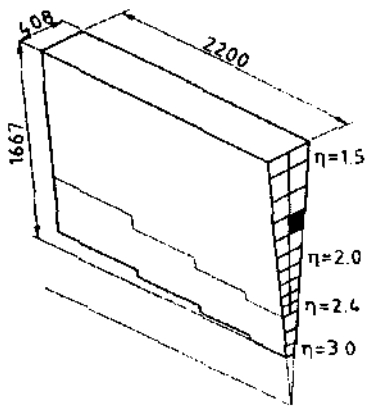

Figure 2.19: *A scintillating tile calorimeter end-cap module showing the r–ϕ segmentation*

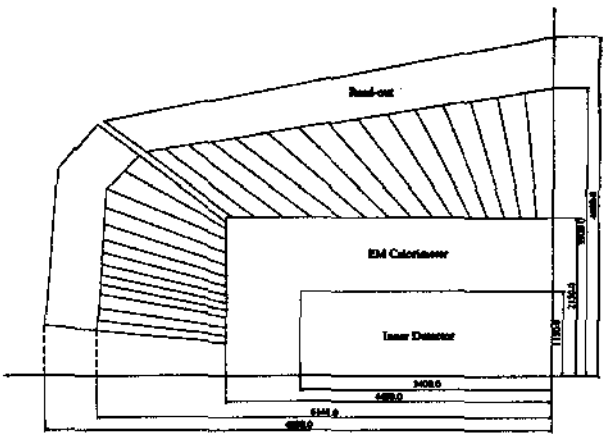

Figure 2.20: *General layout of the scintillating fibre hadron calorimeter*

stacked in the radial direction with the WLS-fibres running parallel to the beam axis. The granularity varies from $\Delta\eta \times \Delta\phi = 0.1 \times 0.1$, for $|\eta| < 2.4$, to 0.2×0.2 for $2.4 < |\eta| < 3$. This small inner part, which is most exposed to radiation, may easily be made exchangeable.

2.4.1.2 Readout channels

The total number of readout channels with two light detector elements per cell is $\sim$ 24 000. This number can be reduced by partially combining the readout of the layers of each tower (e.g. layer 2 and 3) and/or by reducing the granularity of the 4^{th} layer.

2.4.1.3 Radiation damage

The dominant radiation effect for polystyrene-based materials with radiation-hard dopings is the increase of light absorption in the scintillator tiles and a smaller increase in the WLS fibres [31]. No visible effects are expected up to doses of a few kGy. Around 10% signal reductions will occur after about 10 kGy. Given the doses discussed in Chapter 7 no effects are expected in the barrel for more than 30 years of operation. An annual recalibration in the end-cap will probably be needed for $|\eta| > 2.4$.

2.4.2 Scintillating-fibre hadron calorimeter

2.4.2.1 Design

The detector consists of scintillating fibres embedded in an absorber matrix and running longitudinally along the axis of projective towers. The performances of this technique for hadron calorimetry have been demonstrated by extensive test-beam studies by the SPACAL and RD1 Collaborations [32, 33]. Their approach provides a very high degree of uniformity and hermeticity, with an attractive solution to a segmented readout in a projective geometry. A particular advantage of this technique is the direct collection of scintillating light, without the mechanical and optical complications of more conventional techniques. In this way a large light yield can be obtained.

Figure 2.20 illustrates the design of the hadron calorimeter. Scintillating fibres are arranged longitudinally in a regular pattern inside a laminated iron absorber. The calorimeter is mechanically organized into 60 'orange' slices, covering the pseudo-rapidity region $|\eta| < 3$. The projectivity in ϕ is ensured by a 'staircase' geometry (Fig. 2.21) allowing a constant sampling ratio. Each sector is divided into towers, the projectivity in η being provided by using shorter fibres. The proposed design is mechanically stable and features low material and manufacturing cost. With the iron plates running parallel to the central solenoid axis, the proposed option provides a fully integrated magnetic flux return. In order to ensure the flux return continuity, the extraction of cables and cryogenics from the central detectors is obtained by allowing a non-projective crack between the barrel and the end-caps in a limited number of modules (see Fig. 2.20).

With a passive-to-active material ratio of 20:1, appropriate for compensation, and 3 mm fibres arranged with a pitch of 12 mm, the calorimeter has a fully instrumented depth of 10 λ. The limited amount of scintillator volume is very cost effective from the point of view of both fibre cost and photodetector surface. Each tower corresponds to 0.1×0.1 in $\Delta\eta \times \Delta\phi$. Since the readout granularity is indepen-

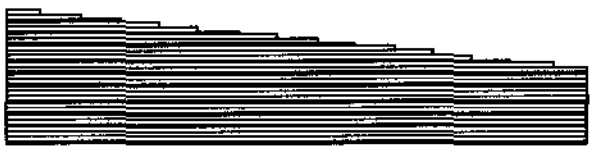

Figure 2.21: *Sketch of a scintillating fibre calorimeter module; r-ϕ view showing the staircase geometry*

dent of the mechanical modularity a finer granularity could be easily achieved, if required. Reading out shorter fibres separately could also provide a pseudo-longitudinal segmentation.

The high degree of modularity of the proposed design makes it very suitable for industrial fabrication. A preliminary engineering study with cost estimates including supports and installation has been carried out by industry [34].

2.4.2.2 Radiation damage

In the hadron calorimeter the radiation problem is much less critical than in the *em* part (see Section 2.4.4). One expects a degradation of 1% in the hadron resolution after 10 years running, in the rapidity range $2.5 < |\eta| < 3$. The corresponding light loss would be $\sim 10\%$. An even smaller effect is expected from damage due to neutrons.

2.4.3 Calibration, light detectors and R&D

Several similar questions and developments have to be addressed for the two hadron scintillator calorimeter options.

2.4.3.1 Calibration

Experience with previous scintillator calorimeters has shown that a combination of several methods [35] can be used to achieve an uncertainty of less than 2%.

- Radioactive sources: RD1 is testing movable Cs sources to monitor the calibration and to evaluate possible effects of radiation damage, particularly in *em* modules.

- Energy flow: This method measures the average energy deposited from all pp interactions into all cells and can be used to monitor the calorimeter response, and, using ϕ symmetry, to transfer the absolute calibration of a few sample modules in a test beam to the full calorimeter. It is envisaged that the measurements can be performed during normal runs by integrating the photodetector dc-currents as a function of the luminosity.

- Light flasher system: Monitor short-term fluctuations of the photodetector sensitivity.

2.4.3.2 Light detectors

The RD1 Collaboration is investigating new light detectors as an alternative to conventional photomultipliers. Among these devices, Avalanche Photo-Diodes (APD) and Proximity Focused Hybrid Photodiode Detectors (PFHPD) [36] look very promising because of large dynamic range, low sensivity to magnetic fields and small sizes. In PFHPD, the dynode chain is replaced by a silicon detector in close proximity ($\sim$ 1.5 mm) to the photocathode. A large electrical field ($\sim$ 10 kV) is applied between both electrodes. The main features of this light detector are a gain of up to a few thousand varying linearly with the applied high voltage, a power consumption close to zero and a multipixel capability. The APDs also offer an internal gain up to a few hundred. Recent advances in fabrication technology have resulted in commercially available low-noise devices with sensitive areas up to 180 mm^2.

2.4.3.3 R&D efforts

Pre-prototype calorimeter modules of both options will be constructed to assess the performance in a test beam. As an important part of the R&D for a hybrid calorimeter, an engineering design of a cryostat for the stand-alone *em* LAr calorimeter with its feedthroughs is needed.

2.4.4 Lead/Fibre *em* calorimeter alternative

The lead/fibre technique is also kept as an alternative to the LAr designs for the *em* calorimeter.

2.4.4.1 Design

The basic design consists of a matrix made up of grooved extruded lead plates stacked together and soldered with a low melting point alloy, in which 1 mm diameter scintillating fibres are embedded. The lead-to-fibre ratio is 1.8/1 in volume. The fibres sticking out of a module are bunched together and coupled via a light mixer to a light detector (see previous section). This technique allows for a large flexibility in segmentation. It is $\Delta\eta \times \Delta\phi = 0.04 \times 0.04$ in the basic design, but can be reduced later using focusing readout. The projectivity in η and ϕ is ensured by a 'staircase' geometry (Fig. 2.22). The modules are arranged in orange slices and tilted by 6° in ϕ. The support is made by an outer shell taking the forces ($\sim$ 300 t) via a honeycomb structure at the back of the modules.

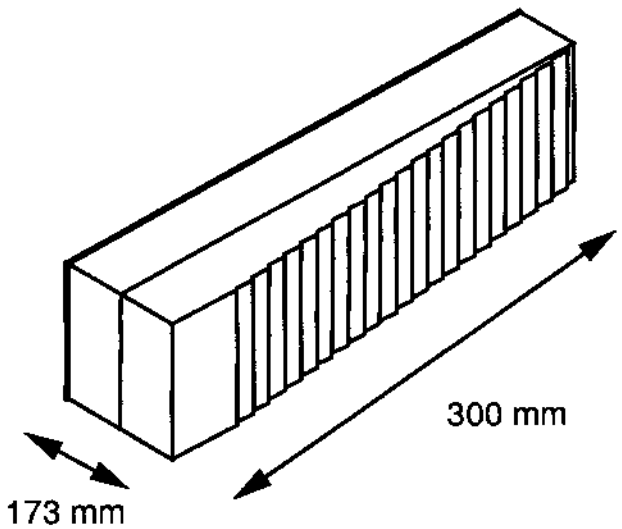

Figure 2.22: *Sketch of a module of the em scintillating fibre calorimeter*

2.4.4.2 Performance

We review here the most significant results on electron response as obtained by the SPACAL and RD1 collaborations [32, 33]. The energy resolution is $10.9\%/\sqrt{E} \oplus 1.1\%$. A small crack effect has been seen at the boundary between modules. The non-uniformity inside a module is $\simeq 2\%$ and is now understood to be a mechanical problem. The impact point resolution scales as $\sigma_{x,y} = 4\,\mathrm{mm}/\sqrt{E} + 0.1\,\mathrm{mm}$. The signals are fast, allowing a satisfactory response in 30 ns collection time.

2.4.4.3 Radiation damage

Both the light emission and transmission of the fibres are affected by irradiation from *em* showers. We use the experimental measurements [37] on the damage to commercial fibres increased by a factor 2 to account for low dose rate effects. Table 2.3 shows the number of years of running at LHC (for an integrated luminosity of 2×10^5 pb^{-1} per year) which would result in an increase of 0.8% of the energy resolution and the annual light loss.

These conservative numbers, obtained with today's fibres, show that the problem of radiation damage is critical only in a small region of the end-caps where a replacement of the fibres would be affordable.

2.4.4.4 Preshower detector

RD1 is also testing a preshower detector based on the thin, high-gain wire chambers used for OPAL [38]. With dedicated electronics yielding a good sensitivity to minimum-ionizing particles and allowing for a high-rate environment, this technique could represent a cheap and efficient alternative.

Table 2.3: *Radiation effect on scintillators for hybrid calorimeters for an integrated luminosity of* 2×10^5 pb^{-1} *per year (see text)*

$\lvert\eta\rvert$	Years	Annual light loss (%)
0.0–1.5	14	0.4
1.5–2.0	6	1.1
2.0–2.5	1	5
2.5–3.0	0.5	14

2.5 Forward Calorimetry

The main challenge for a forward calorimeter design is the high radiation dose it must withstand up to 1 MGy/year at $|\eta| = 5$, for an integrated luminosity of 10^5 pb^{-1}. This implies the use of radiation-hard materials and an appropriate protection of readout electronics, as well as a protection (or replaceability) of parts that cannot be made radiation hard. Simulations show that the hadronic energy resolution and the lateral granularity are not critical parameters for forward calorimetry. Because of the high occupancy, fast response is of more importance. The main design parameters of the forward calorimeter are listed in the Table 2.4. Currently, two options are under consideration: liquid scintillator [39] and high-pressure gas ionization calorimetry. In both cases the replacement of the active medium is foreseen.

Table 2.4: *Forward calorimeter design parameters*

Fiducial coverage	$3.0 < \lvert\eta\rvert < 4.5$
Energy resolution	$\leq 100\%/\sqrt{E} \oplus 7\%$
Time response	$\leq$30 ns
Distance from I.P.	15 m
Depth	2 m (10 λ)
Outer radius	190 cm
Readout channels per side	1000

At the highest LHC luminosities, the innermost part of the forward calorimeter ($|\eta|$ >4.0) could, if necessary, be protected by a passive 15 X_0 plug to absorb primary γ's causing the main radiation damage. The corresponding deterioration of the energy resolution will have little effect on most E_T^{miss} signatures above $\sim$ 100 GeV.

Mechanically, the forward calorimeter will be built as two identical stand-alone retractable units.

2.5.1 Liquid scintillator option

The advantages of this technique are fast response and low noise. Conceptually, the calorimeter module consists of a sealed 200 × 6 × 6 cm^3 absorber matrix instrumented with thin glass tubes and filled with circulating liquid scintillator. Glass is known to be radiation-hard while liquid scintillators can stand a dose of about 100 kGy (in some cases up to 600 kGy [40]). The photodetector housing is attached to each module equipped with a light-guide mixer to transport the light from the tubes. The lateral size of the module is determined by the considerations of photocathode area, liquid flow uniformity, the module mechanics and weight. The calorimeter unit is composed of 3000 such modules, arranged in layers, with half a module staggering and held by a 380 cm diameter cylindrical steel support. The beam pipe comes through a hollow insert with an inner diameter of 30 cm. The calorimeter unit will weigh about 200 t and contain about 5 m^3 of liquid scintillator. Signals from the modules are combined into patterns varying from a single module at the highest η to 7 modules at $|\eta| \leq 3.5$ to form readout cells of $\Delta\eta \times \Delta\phi \simeq 0.15 \times 0.15$.

We have built prototype modules with lead and iron absorbers, 50 cm long and 6.2 × 6.2 cm^2 wide, containing 56 3.6 mm glass tubes arranged in a hexagonal pattern with 8.2 mm spacing and filled with methylnaphtalene-based scintillating liquid. The modules were exposed to 5 GeV test-beam particles. Figure 2.23 shows some of the observed signal distributions. The measured energy resolution $\sigma(E)/E$ is 23% for electrons at $\theta_Z > 3°$ and 51% for pions [41]. The latter would correspond to $\sigma(E)/E \simeq 30\%$ in the case of full hadronic shower containment. The construction of full-scale prototypes and the testing of them in high-energy beams is envisaged in a future R&D programme.

2.5.2 High-pressure gas ionization option

This technique is expected to be radiation hard. The calorimeter geometry is similar to the one described above. The design involves high-pressure gas ionization tubes parallel to the beam, with 2 mm gap between the inner tube wall and the outer surface of the central rod. The gas mixture 95% Ar + 5% CF_4 at 20–100 atm will be used. The signals from all charge collection rods in one 10 × 10 cm^2 module are combined into a single readout cell. Several prototype modules with different tube parameters and spacing are currently under test [42].

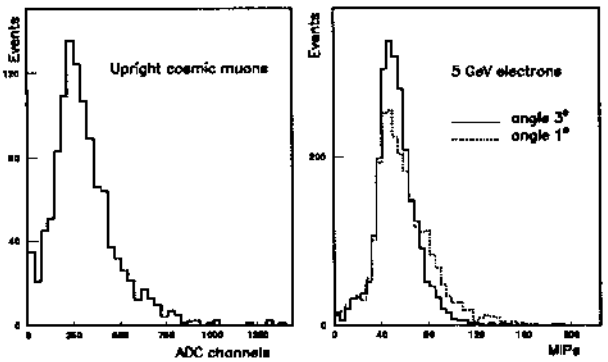

Figure 2.23: *Response of the liquid scintillator module to minimum ionizing particles (MIP) and electrons*

An alternative design involves planar absorber plates with pad readout, embedded in a high-pressure gas volume [43].

2.6 Readout Electronics

This section deals with the readout electronics which is nearly independent of the calorimeter option finally chosen. As usual for calorimeters, the readout electronics has to provide data to the level-1 and level-2 trigger processors. In addition, several new requirements have to be met:

- the number of channels is large ($\sim 10^5$);
- the dynamic range from a high-mass $Z' \rightarrow 2e$ to the acceptable quantification noise limit is $\sim 50\,000$;
- the linearity and stability of the response must be better than 1%;
- the information has to be pipelined with the complication introduced by the above items.

Several approaches for the digitization and readout of the data are currently being investigated. One possible scheme has been already presented in Section 2.3.4.

Another possibility is the FERMI (Front-End Readout MIcrosystem) [44], a digital implementation of the front-end and readout electronic chain for calorimeters. It is based on dynamic range compression, a high-speed ADC, a programmable pipeline/digital filter chain, local storage and trigger functions. FERMI also acts as the interface to the Trigger and DAQ systems.

Digital pulse-shaping for calorimetric purposes is also being studied by the RD12 collaboration which reported the successful operation of an 8-bit digital filter at 60 MHz [45]. A 16-bit demonstrator is foreseen by the end of this year.

Still another approach uses an extension of the analogue CMOS pipeline developed for the RD2 Collaboration [46]. Owing to the large dynamic range, two (12-bit) pipelines are needed in parallel. A limited number of electronic channels (in particular fast analogue summing circuits and ADCs) would be needed to feed the level-1 trigger processor.

2.7 Calorimeter Performance

A large simulation effort has been undertaken and is still going on to assess the performance of the proposed calorimeter systems including as much as possible the known imperfections due to the integration of the calorimeters in a large detector system. The simulation results are backed up by results obtained in test beams by the R&D teams.

As an example, Fig. 2.24 shows the expected energy resolution for a 60 GeV transverse energy γ as function of η in the LAr Accordion barrel calorimeter. For a 120 GeV mass Higgs the average photon transverse energy is $\sim$ 60 GeV independent of η (after kinematical cuts). All effects due to electronics noise, pile-up, dead material (coil and cryostat) have been included [10].

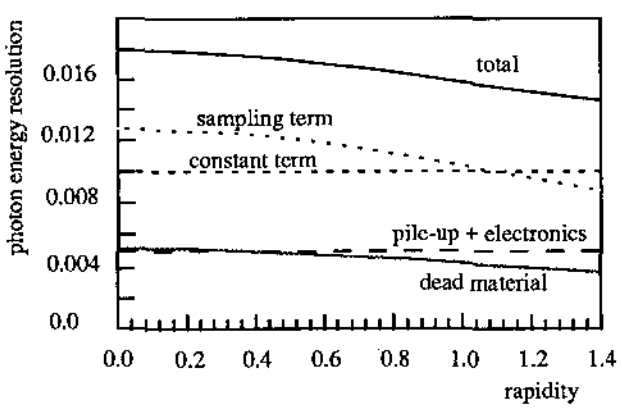

Figure 2.24: *Energy resolution for a 60 GeV E_T photon as a function of rapidity*

The ability of the calorimeter to select electromagnetic clusters for photons and electrons has been simulated [10]. Above 20 GeV, a rejection factor of $\sim$ 1000 against jets can be achieved by requiring a cluster of *em* energy in an area of 0.1×0.1 and rejecting those which deposit more than 10 GeV in the surrounding *em* and all hadronic calorimeter cells over an area of 0.18×0.18. This selection maintains an efficiency for photons and electrons of 95% even in the presence of pile-up at $1.7 \cdot 10^{34}$ cm^{-2}s^{-1} luminosity.

The performance of the various options for the hadron calorimeter are being studied with GEANT 3.15. All the hadronic models present in this version have been tested (NUCRIN, GHEISHA, FLUKA). Differences of up to a factor of 1.2 in the value of the sampling term in the energy resolution are found. This underlines the importance of beam tests to accurately measure the performance of a detector.

For the hybrid options, complete simulations have been performed using the FLUKA model, which reproduces experimental data from the SPACAL and RD1 Collaborations in the case of fibres, and from the ZEUS Collaboration for tiles. In the LAr/fibre case, light-quark jets from 40 to 1000 GeV have been passed through the combined calorimeter system, in the absence of a magnetic field. The resolution is well described by a straight line: $30\%/\sqrt{E} + 2\%$. A similar study has been pursued for the LAr/scintillator tile option where, due to the simple geometry, a full simulation within the detailed, complete detector environment was possible. The resolution values are fitted best with $27\%/\sqrt{E} + 2\%$. In the case of the full liquid argon solution (TGT), jets in the 50–1000 GeV energy range have been simulated using the GHEISHA model (backed up by results obtained with the H1 calorimeter) and the π^0-weighting technique [16]. This predicts an energy resolution of (30–35)$\%/\sqrt{E} \oplus 2\%$. In all cases, no source of systematics has yet been included. For single hadrons, the results are worse by typically 20%.

The performance of the forward calorimeter has been simulated for jet tagging. The E_T resolution is found to be 9% for jets with an energy of 750 GeV measured in a cone with $\Delta R = 0.5$.

The effect of cracks in the calorimeter was studied using GEANT simulations of charged-pion and photon showers in the regions between the barrel and end-cap calorimeters and also between the end-cap and forward calorimeters. This study was performed in the case of the full LAr calorimeter design described in Section 2.3.3.

The expected average energy response as a function of η, for charged pions and photons is shown in Fig. 2.25 (a) for the barrel/end-cap and in (b) for the end-cap/forward cracks. From Fig. 2.25a, we conclude that energy losses in the barrel/end-cap crack are small. However, for $1.40 < |\eta| < 1.45$, the *em* calorimeter resolution is degraded significantly, implying that in the case of searches for $H \rightarrow \gamma\gamma$ or $H \rightarrow ZZ^* \rightarrow 4e$ decays, a fiducial cut is needed to exclude photon or electron candidates in this region.

Figure 2.25b shows that a large fraction of the shower energy may be lost in the passive material of the end-cap calorimeter cryostat. The im-

pact of these losses on E_T^{miss} measurements is discussed in Chapter 8, both for $H \rightarrow ZZ \rightarrow \ell\ell\nu\overline{\nu}$ and squark/gluino searches. Despite the currently crude and non-optimized design of this region, the impact of this crack on E_T^{miss} measurements is expected to be small.

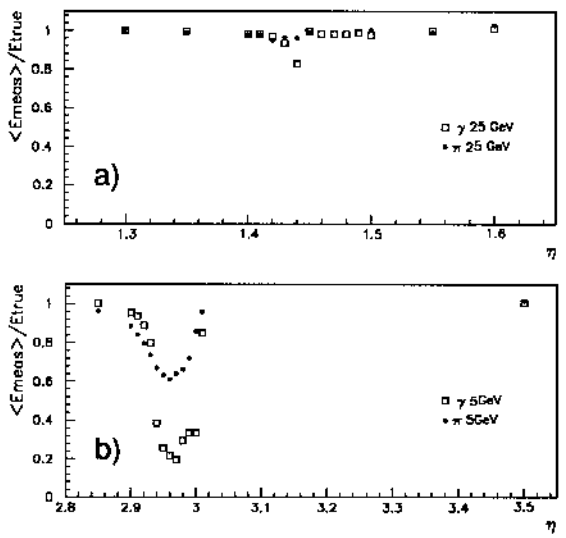

Figure 2.25: *Relative energy response near crack regions (see text)*

References

[1] B. Aubert et al. (RD3 Collaboration), Liquid Argon Calorimetry with LHC-Performance Specifications, CERN/DRDC/90-31 (1990).

[2] W. Braunschweig et al. (H1 Calorimeter Group), Report DESY 88-073 (1988); Report DESY 89-022 (1989).

[3] M. Abolins et al., Nucl. Instrum. Methods **A280** (1989) 36.

[4] The RD1 Collaboration, Status report, CERN/DRDC/91-50 (1991).

[5] *Proceedings of the Second International Conference on Calorimetry in High Energy Physics*, Capri, 1991, edited by A. Ereditato (Singapore, World Scientific, 1992).

[6] *Proceedings of the Large Hadron Collider Workshop*, edited by G. Jarlskog and D. Rein (Aachen, 4-9 October 1990) CERN 90-10/ECFA 90-133.

[7] C. Hearty, Effect of Electromagnetic Calorimeter Thickness on Resolution, in [5], p. 257; and Note SDC-91-00084 (1991);

L. Serin, RD3 note 35.

[8] C. Seez et al., in [6], Vol. I, p. 474.

[9] Y. Zolnierowski, Study of pile-up from minimum-bias events, ATLAS note, CALO-NO-014.

[10] L. Fayard and G. Unal, EAGLE note, PHYS-NO-001.

[11] J.P. Repellin, Electron detection in LHC calorimeters, in [6], Vol. III, p. 402.

[12] J.C. Chollet and J.P. Repellin, Simulation and study of electromagnetic jets, in [5], p. 348.

[13] G. Unal, EAGLE note CALO-NO-009.

[14] J. Krüger, Length of calorimeters and effect of absorbers in front of calorimeters, in [6], Vol. III, p. 306.

Y. Zolnierowski, Study of the effects of the calorimeter thickness on jets energy measurement, ATLAS note, CALO-NO-012.

[15] C. Berger et al., A Highly Segmented and Compact Liquid Argon Calorimeter for the LHC, CERN/DRDC 92-41, DRDC/P44 (1992).

[16] H1 Calorimeter Group, W. Braunschweig et al., DESY 89-022 (1989).

[17] J. Colas, M. Pripstein and W.A. Wenzel, Nucl. Instrum. Methods **A294** (1990) 583.

[18] B. Aubert et al. (RD3 Collaboration), Performance of a Liquid Argon Accordion Calorimeter with Fast Readout, CERN-PPE/92-46 (1992), submitted to Nucl. Instrum. Methods.

[19] B. Aubert et al., Performance of a Liquid Argon em Calorimeter with a Cylindrical Geometry, CERN-PPE/92-129 (1992), submitted to Nucl. Instrum. Methods.

[20] B. Aubert et al., Performance of a Cold Preshower Detector Integrated with a Liquid Argon Accordion Calorimeter, RD3 note # 31, to be submitted to Nucl. Instrum. Methods.

[21] RD3 Collaboration, R&D for a Liquid Argon Preshower, CERN/DRDC/92-40 (1992).

[22] D.V. Camin, G. Pessina and E. Previtali, Front-End in Gallium Arsenide, in Proc of the 5th Pisa meeting on Advanced Detectors Isola d'Elba (Italy), May 1991, to be submitted to Nucl. Instrum. Methods.

[23] B. Yu and V. Radeka (editors), SSC Detector R&D at BNL, BNL52244 (1990).

[24] R.L. Chase, C. de la Taille, S. Rescia and N. Seguin, Transmission lines between detector and Front-End Electronics in LAr Calorimetry, submitted to Nucl. Instrum. Methods.

[25] P. Aspell et al., Nucl. Instrum. Methods **A315** (1992) 425.

[26] E. Beuville et al., DMILL Collaboration, CERN/DRDC/92-31, DRDC/P42 (1992).

[27] J.D. Dowell et al., RD23 Collaboration, CERN/DRDC/91-41, 91-42 (1991).

[28] H. Brettel, J. Fent, H. Oberlack and P. Schacht, Conceptual Design of a 'Thin Gap Turbine' calorimeter for the LHC, MPI Munich Report 92-15 (1992).

[29] U. Schoeneberg, J. Fent, B.J. Hosticka, H. Oberlack, G. Zimmer, CMOS Readout Electronics for Operation at Cryogenic Temperatures, IEEE J. Solid State Circ. **24** (1989) 718–722 and Nucl. Instrum. Methods **A288** (1990) 191.

[30] O. Gildemeister, F. Nessi-Tedaldi and M. Nessi, An economic concept for a barrel hadron calorimeter with iron scintillator sampling and WLS-fiber readout, in [5], p. 199.

[31] P. Bonamy et al., Radiation damage in scintillating plates and fibres, DPhPE 91-03 (1991).

[32] D. Acosta et al., Nucl. Instrum. Methods **A314** (1992) 432; Nucl. Instrum. Methods **A316** (1992) 184; and references therein.

[33] RD1 Collaboration, in [5], pp. 135, 139.

[34] Ansaldo Componenti, Manufacturing Feasibility Study, September 1992.

[35] A. Beer et al., Nucl. Instrum. Methods **A224** (1984) 360.

[36] S. Basa et al., CCPM/92-003.

[37] D. Acosta et al., Nucl. Instrum. Methods **B62** (1991) 116.

[38] C. Beard et al., Nucl. Instrum. Methods **A286** (1990) 117.

[39] A. Artamonov et al., in [5], p. 207.

[40] S. Golovkin et al., *LHC Workshop,* May 1992, Protvino (Russia).

[41] A. Artamonov et al., EAGLE note CALO-NO-015.

[42] A. Batalov et al., EAGLE note CALO-NO-010.

[43] S. Denisov et al., Gas Ionization Calorimetry, submitted to Nucl. Instrum. Methods.

[44] G. Goggi and B. Lofstedt, Digital Front-end Electronics for Calorimetry at LHC, in [6], Vol. III, p.190.

S. Berglund et al., Status Report on the FERMI Project, CERN/DRDC/92-26 (1992).

[45] J. Altaber et al., Status Report on the RD12 Project, CERN/DRDC/92-10 (1992).

[46] D.J. Munday et al., RD2 Collaboration, CERN/DRDC/90-27 (1990).

3 Inner Detector

3.1 Physics and Performance Targets

In this section, we briefly review the requirements set on the inner tracking detector by the physics at LHC. We discuss both the high luminosity requirements, which are the main goals to be achieved, and the desired performance at initially lower luminosities, for which the inner tracker is expected to play a major role in extracting interesting physics (see Section 8).

3.1.1 Performance goals at nominal high luminosity

3.1.1.1 Reconstruction of high-p_T charged tracks The inner tracking system should efficiently reconstruct isolated high-p_T charged tracks, and in particular those of electrons and muons. The pattern recognition should be as insensitive as possible to pile-up, and should reconstruct these tracks as efficiently as possible. At very low transverse momenta, electron and muon identification becomes increasingly difficult, and therefore the goal of the inner tracking system is to identify electrons and muons down to transverse momenta of 7 to 10 GeV. The acceptance for a possible four-lepton signal from Higgs decay, for $m_H < 150$ GeV, is quite sensitive to this lower p_T threshold.

3.1.1.2 Electron identification In contrast to existing hadron colliders, where the isolated electron to jet ratio at transverse momenta of order 40 GeV is about 10^{-3}, this ratio is expected to be much lower at LHC, of the order of 10^{-5}. The expected calorimeter rejection of hadronic jets, while retaining a high efficiency for electrons, is of order 10^3. The inner tracking system must therefore bring an additional rejection of 10^2 to 10^3 in order to reduce the jet backgrounds to less than 10% of the inclusive isolated electron signal. These jet backgrounds consist mainly of π^0 mesons, which carry most of the jet energy and are not matched to a high-p_T charged track, but also of electron pairs from Dalitz decays of π^0/η mesons or conversions of photons from π^0/η decays, and of high-p_T charged hadrons yielding an electromagnetic shower in the calorimeter. Most of these backgrounds can be rejected by simple tracking algorithms requiring the presence of a charged track matching the calorimeter cluster position, and with momentum matching its energy. Such tracking algorithms provide sufficient rejection at the level-2 trigger to bring the single electron trigger rate down to a manageable level whilst retaining a good efficiency for electrons from W decay (see Section 5). The possibility of a level-1 track trigger was considered and its physics potential was not judged sufficiently rewarding to warrant its implementation.

3.1.1.3 Lepton momentum measurement The inner tracking system should provide a measurement of the electron charge sign up to momenta of 500 GeV. This is dictated mainly by the need to reject opposite-sign dileptons from $t\bar{t}$ decays, when searching for a possible excess of same-sign dileptons which might arise from high-mass same-sign W boson pair production. In the case of a possible asymmetry measurement in Z' decay, where the Z' mass is in the TeV range, a more modest electron momentum resolution would be sufficient, since each event is known to contain an electron–positron pair. At low momenta, the inner tracking system can provide the most accurate estimate of electron and muon momenta.

3.1.1.4 Reconstruction of low-p_T tracks near a high-p_T lepton candidate The rejection of various dangerous backgrounds can be greatly improved if the inner tracking system is able to reconstruct low-p_T charged tracks in the vicinity of a high-p_T lepton candidate track:

- Requiring that no such charged track be found within a limited cone around the lepton candidate, additional rejection is obtained against backgrounds from non-isolated leptons originating from b-decay. Two good examples are the $Zb\bar{b}$ and $t\bar{t}$ to 4-lepton backgrounds to a possible signal from an intermediate mass Higgs boson decaying to four leptons.
- The reconstruction of low-p_T partners of electrons from Dalitz decays or conversions provides additional rejection against these backgrounds to prompt electron signals.
- Finally, in the search for Higgs decays into two photons, hard photons from electron bremsstrahlung may be a major source of background if the Higgs boson mass is close to the Z mass. In this case, the identification of the low-p_T electron from which the hard bremsstrahlung occurred is again a powerful tool to reject such backgrounds.

3.1.2 Performance goals at lower luminosity

At the lower LHC luminosities expected at start-up (10^{32} to 10^{33} cm^{-2}s^{-1}), the inner tracking detector will be a powerful tool in studying the rich and diverse physics expected from the very large samples of top-quark decays, which should be collected even at these lower luminosities. In addition, it is hoped that the abundant rates of b-quarks expected at LHC may

lead to a rich field of B-physics, such as CP-violating decays of B^0 mesons, which will still be a topic of intense interest at the end of the century.

3.1.2.1 Identification of jets originating from b-quark decay Tagging of b-quarks will be a powerful tool to reduce combinatorial background from light-quark jets when reconstructing the top-quark mass, or to reject backgrounds from processes other than top-quark production when searching for new and/or rare top-quark decays such as $t \rightarrow bH^+$ decays.

We note here that b-tagging at LHC for luminosities below 10^{33} $cm^{-2}s^{-1}$ is expected to result in single-hit and impact-parameter resolution requirements similar to those for LEP and the Tevatron, since the b-quark energies and therefore the charged particle multiplicities inside b-quark jets are similar. For these reasons, it is expected that silicon micro-vertex detectors similar to those used at LEP and the Tevatron, but with sufficient speed and radiation hardness, should yield similar performance in terms of b-quark tagging efficiency and light-quark background rejection.

3.1.2.2 Identification of hadronic τ decays Hadronic τ decays are of particular interest to identify a possible signal from charged Higgs decay or from a pseudoscalar Higgs expected in some SUSY models. The use of a micro-vertex detector combined with the possibility of reconstructing tau decays will provide a useful tool to reject the much more abundant backgrounds from light-quark jets, which cannot be sufficiently reduced using calorimetric cuts alone.

3.1.2.3 Reconstruction of CP-violating B-decays The expected rates of triggered and reconstructed $B_d^0 \rightarrow J/\psi K_s^0$ decays are quite large at LHC. The inner tracking detector should be able to reconstruct leptonic J/ψ decays down to low lepton momenta, and more importantly reconstruct K_s^0 decays to charged pions. The precision with which the B_d^0 mass can be reconstructed will also be an important tool to reject backgrounds from the more abundant $B_d^0 \rightarrow J/\psi K^*$ decays.

3.1.3 Summary of performance requirements

The design goals for the inner tracking system are briefly summarized below:

- efficient track finding over a pseudo-rapidity range of ± 2.5 for isolated electrons and muons with transverse momentum above 7 to 10 GeV;
- momentum accuracy of 20 to 30% for $p_T = 500$ GeV over this pseudo-rapidity range;
- efficient reconstruction of charged tracks with $p_T > 1$ GeV in a localised area around a high-p_T lepton candidate track;
- good efficiency for tagging hadronic b-quark and τ decays at as-high-as-possible luminosity;
- the possibility of unambiguously reconstructing exclusive final states from B-meson decays;
- enhanced electron identification for overall physics performance and level-2 triggering;
- control of the amount of material for minimizing radiation length causing conversions and energy loss of electrons due to bremsstrahlung.

The Inner Detector has to be designed to perform robustly up to the highest LHC luminosity, $1.7 \cdot 10^{34}$ $cm^{-2}s^{-1}$.

3.2 General Operating Conditions

3.2.1 Tracking volume

The inner tracker will occupy the space inside the inner vacuum shell of the solenoidal coil. The length of the tracking volume is 6.8 m and its radius is 1.06 m (see Section 1). The 2 T solenoidal field is uniform over the central part. Because of the finite coil length the field integral decreases at the end of the tracking volume; thus the momentum resolution is degraded by $\sim$ 20% in this region (i.e. for tracks with $|\eta| > 1.9$).

3.2.2 Flux of charged particles and occupancies

The charged particle flux at an LHC luminosity of $1.7 \cdot 10^{34}$ $cm^{-2}s^{-1}$ is $N \approx 2 \times 10^9/r^2$ $cm^{-2}s^{-1}$ at a radius of r cm with respect to the beam axis. Particles with a transverse momentum $p_T \leq 0.3$ GeV are trapped in the sensitive area of the inner detector by the 2 T solenoidal field in a radius of 1 m; they loop inside the Inner Detector and contribute to the occupancy.

A small flux of charged particles will result from 'backsplash' from the neutron moderator, the coil and the calorimeter - it will add more hits to the detectors and increase the occupancy. This is under study.

3.2.3 Neutron albedo

The neutron flux above 100 keV in the cavity of the Inner Detector, coming from a Pb-LAr electromagnetic calorimeter and, for example, a Fe-LAr hadron calorimeter has been calculated [1] and it is expected to be in the range 1.7 to 6 $\times 10^{13}$ n cm^{-2} for an integrated luminosity $\mathcal{L} = 10^{41}$ cm^{-2}. These neutrons

are a potential source of radiation damage. To reduce this flux the Inner Detector will be surrounded by a moderator of 5 cm polyethylene (nCH_2) or equivalent. The neutron fluxes expected in this case are in the range $1.7 - 2.7 \times 10^{12}$ n cm^{-2} (see Section 7).

3.3 Tracking System

3.3.1 General considerations

The design goals for the tracking detector are listed in Section 3.1. No single tracking detector satisfies all these requirements, and the best features of several detector techniques are used. Figure 3.1 shows the baseline option for the full tracking detector. In the barrel region two design concepts, A and B, representative of existing studies and used for optimization, are shown. The overall tracker design is still evolving and, therefore, different options are considered. The required momentum reconstruction accuracy for charged lepton tracks implies a measurement precision of < 20 μm for the inner tracker, and < 60 μm at the calorimeter entrance. The detectors have to be fast and they have to stand the expected levels of occupancy. They also have to survive and operate in high fluxes of charged and neutral particles. So far the best match to these requirements is provided by solid-state detectors (Si and possibly GaAs) and microstrip gas chambers (MSGC). These detectors are shown in Fig. 3.1. At small radii, in the barrel part, silicon microstrip [2] and pixel [3] detectors give precision tracking information. In the forward direction GaAs detectors [4] are used to increase the acceptance for high-resolution track measurement (the choice of GaAs is dictated by the high radiation levels in this region). At larger radius the required accuracy is provided by silicon pad and strip detectors [5] or MSGCs [6]. Scintillating fibres are also considered as an alternative [7].

The high-precision measurements can be supplemented by measurements of accuracy $\simeq 150$ μm per hit using a multi-layer straw drift tube array. This kind of tracker has the additional advantage of being able to be used as a Transition Radiation Detector (TRD) for electron identification [8].

Efficient pattern recognition of high-p_T charged leptons with a low ghost-track rate demands a few layers of high-granularity detectors (Si, MSGC; i.e. 'vector tracking'), and/or a large number of detector planes on the track (TRD/T; i.e. 'continuous tracking'). Each pattern recognition method gives good results, even in the stand-alone case for the concepts A and B (see Section 3.5). Both low occupancy and continuous tracking elements are useful for the recognition of low-p_T conversion partners, or the secondary decays of long-lived particles (for example K^0's).

An essential aim of the inner tracking detector is the efficient identification of isolated electrons, with a rate of fake signatures small compared with the true isolated electron rate. The dominant background sources to electrons are from Dalitz decays or external π^0 conversions, and hadrons. Electrons are identified by the reconstruction of a high-p_T track pointing to the electromagnetic preshower/calorimeter cluster and transition radiation. More details on rejection of fake electrons can be found in Sections 3.5.

Electron and photon candidates are defined by the level-1 trigger from isolated electromagnetic energy depositions in the em calorimeter. The Inner Detector can contribute efficiently to the level-2 trigger as shown in Section 5.

3.3.2 Layout of tracking system

3.3.2.1 Detectors The inner tracker system consists of the elements described separately in Section 3.4. In order of increasing radius they are (see Fig. 3.1):

1. The Silicon Tracker/Vertex (SITV) detector which covers the pseudo-rapidity region $|\eta| < 1.5$ and consists of two layers of double-sided silicon microstrip detectors, which are placed at radii 20 and 30 cm to give precise tracking information. An additional layer of pixel detectors is placed at a radius of about 10 cm to give accurate and unambiguous measurements and to ensure good pattern recognition for primary and secondary vertex finding. As an alternative a layer of double-sided strip detectors can be used. The forward region is covered by GaAs detector rings to improve the momentum measurements beyond $|\eta| = 1.8$.

2. Rings of MSGC counters at radii from 40 to 50 cm with azimuthal strip orientation and 15 mrad stereo provide accurate track measurements for $|\eta| > 1.5$.

3. For radii greater than 50 cm the tracking system includes two parts:

   • The end-cap part ($\theta > 45°$, $0.9 < |\eta| < 2.5$) consists of a TRD/tracker arranged as a number of $r\phi$ layers of 4 mm straw drift tubes with radiator foils in between ($50 < r < 100$ cm). The outer MSGC rings extend radially between $r = 84$ and 100 cm and are interleaved with the TRD/tracker 'wheels'. In the forward direction, three full MSGC disks at z between 330 and 340 cm extend radially from $r = 40$ to 100 cm.

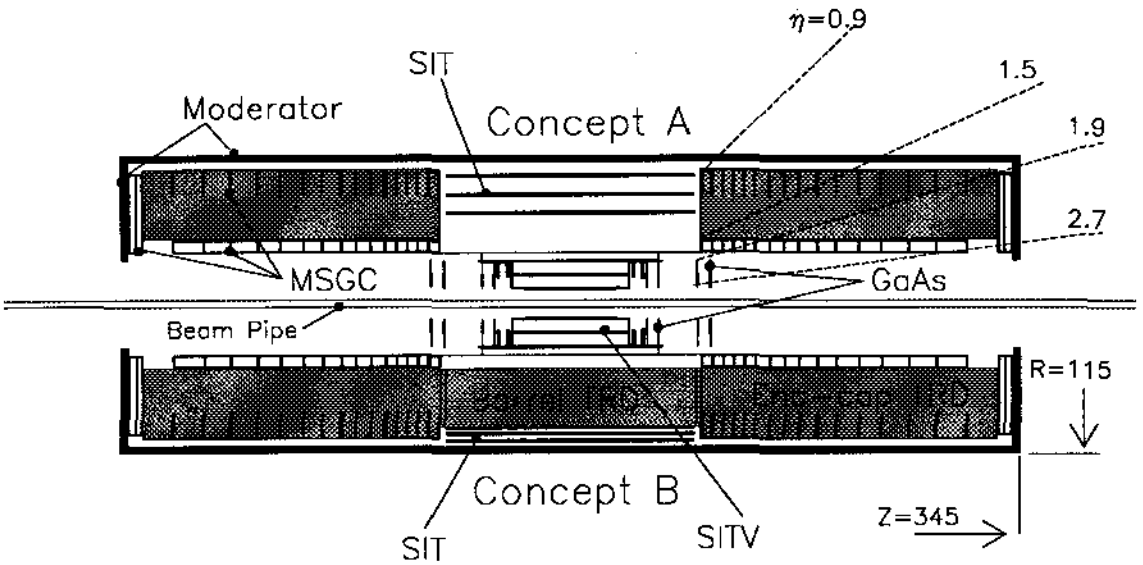

Figure 3.1: *Layout of the Inner Detector with two design concepts; concept A above and B below the beam line (dimensions in cm)*

• In the barrel part ($\theta < 45°$, $|\eta| < 0.9$), variants of two tracking concepts are being considered. Concept A consists of a silicon tracker (SIT) with an axial strip orientation. Four strip layers between radii $r = 70$ cm and $r = 100$ cm provide ϕ-measurements, while two pad layers provide good space-point pattern-recognition capability. Concept B consists of a barrel TRD/tracker with axially oriented straw drift tubes ($60 < r < 95$ cm) for pattern recognition and particle identification, and six layers of the SIT at $r > 95$ cm.

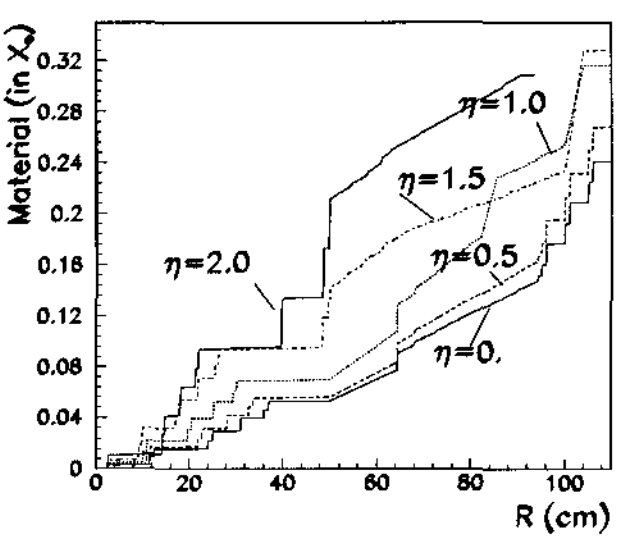

Figure 3.2: *Radial distribution of the material density for the inner tracker (concept B)*

To match the precision of the tracking detectors (20–60 μm) a rigid and stable mechanical construction is needed. The material of the Inner Detector contributes to multiple scattering, conversion of photons and bremsstrahlung of electrons. Hence, the material content should be minimized, especially at small radius, where these effects are most critical. Figure 3.2 shows the radial distribution of material as a function of pseudo-rapidity for concept B.

3.3.2.2 Readout electronics The on-detector front-end electronics must be of high density and satisfy many constraints:

• high reliability and fault tolerance;

• good radiation tolerance (up to 100 kGy or more);

• minimal power dissipation, while maintaining maximal on-detector functionality (including possible digitisation of analogue signals);

• 2 μs pipeline buffers for analogue or digital signals corresponding to the maximum latency of the level-1 trigger;

• minimal readout dead time (< 1%);

• good stability to eliminate the need for time-dependent calibration constants;

• easy testing and monitoring.

Candidate front-end chip developments are noted in specific detector subsections; both analogue (SITV, SIT) and binary (TRD/T, MSGC) front-end developments are being pursued. In all cases, data will be stored on-chip until a level-1 decision is taken,

following which only relevant data will be transferred. The baseline design foresees a readout architecture consistent with present technology; groups of chips (typically 10–20) would be arranged on detector boards, with the data from each chip transferred to a board buffer before transfer off the detector by an optical fibre. Preliminary studies of average data rates indicate that transfer rates of $\approx$ 100 Mb/s over such fibres are sufficient. The final number of parallel read-out boards will be determined from an optimization of occupancy and readout speed to achieve minimal dead time. More ambitious opto-electronic readout schemes including analogue readout [9] are also being considered, and their suitability depends on future technical development. Input clock, trigger and calibration signals will be common to all tracking detectors [10].

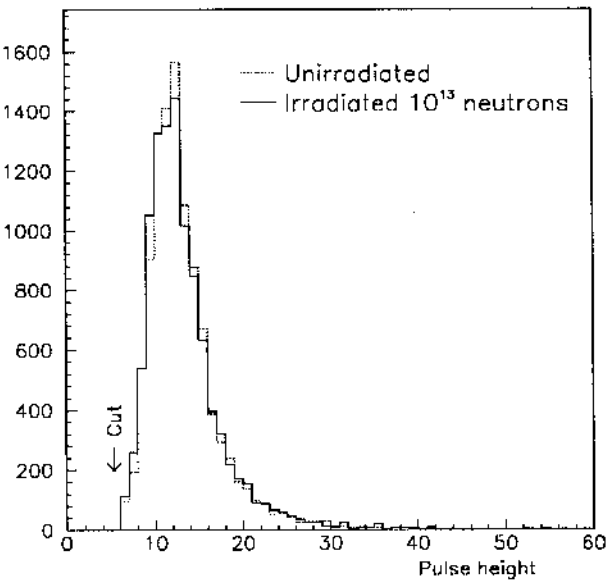

Figure 3.3: *Landau distributions from Si counters before and after irradiation with* 10^{13} *neutrons* cm^{-2} *(five LHC years at* $r \sim 100$ *cm)*

3.3.3 Radiation resistance

In silicon detectors, neutrons as well as other particles damage the crystal structure causing an increase of the leakage current and consequently an increase of noise [11]. A further consequence is a change of the effective doping concentration [12] which affects the operating voltage. Charged particles and gammas also create ionization in dielectric materials, which may accumulate to significant levels and influence the electrical field in the material beneath [13]. It has been shown that silicon strip and pad detectors can work in neutron fluences up to 10^{14} n cm^{-2} [5] or higher [12] and radiation doses up to 100 kGy [12, 13]. Most of the phenomena are understood, but the performance depends strongly on the specific design. A careful choice of the operating conditions is currently the subject of several R&D projects [5]. The result of recent measurements is shown in Fig. 3.3 [13].

GaAs detectors are less well understood but they have operated at fluences up to $10^{14} - 7 \cdot 10^{14}$ n cm^{-2} and radiation doses up to 200 kGy [14].

Gaseous detectors are sensitive mostly to charged particles and are much less sensitive to hard photons and neutrons. We have verified that the TRD/T proportional tubes operate without significant degradation up to a charge deposit above 5 C/cm [15, 16]. We are actively involved in the development of radiation-hard MSGCs through the RD28 collaboration [17], (see also [18]).

The components of the Inner Detector will be equipped with VLSI electronics, which has to withstand the same level of radiation as the detectors. Standard technologies of industrial electronics have insufficient radiation hardness. However several technologies exist which are radiation hard and which are now becoming available at a cost of about 2–3 times that of the standard ones. Leading examples are MOS devices, which are favoured from the point of view of low power, high density and wide range of applications. Radiation-hard MOS electronics is offered by several companies[1]. Transistors and analogue circuits from these companies have been tested up to 50 kGy [19, 20] and some of the VLSI digital devices have been operating up to 500 kGy [21]. Another possible choice is bipolar or JFET technology, which is less frequently used as it has more limited design possibilities but which is inherently more radiation resistant. Such devices have been tested up to doses of 100–200 kGy [22]. Again, several R&D projects are being pursued to demonstrate the applicability of these different technologies to front-end electronics of particle detectors [23].

The remaining materials used for the detectors and electronics (epoxy resins, Kapton, Mylar, ceramics, etc. - with the exception of Teflon!) are much less sensitive to radiation and moderate or severe damage starts above 0.1–1 MGy [24].

[1] UTMC and Harris in USA, Thomson and ABB HAFO in Europe.

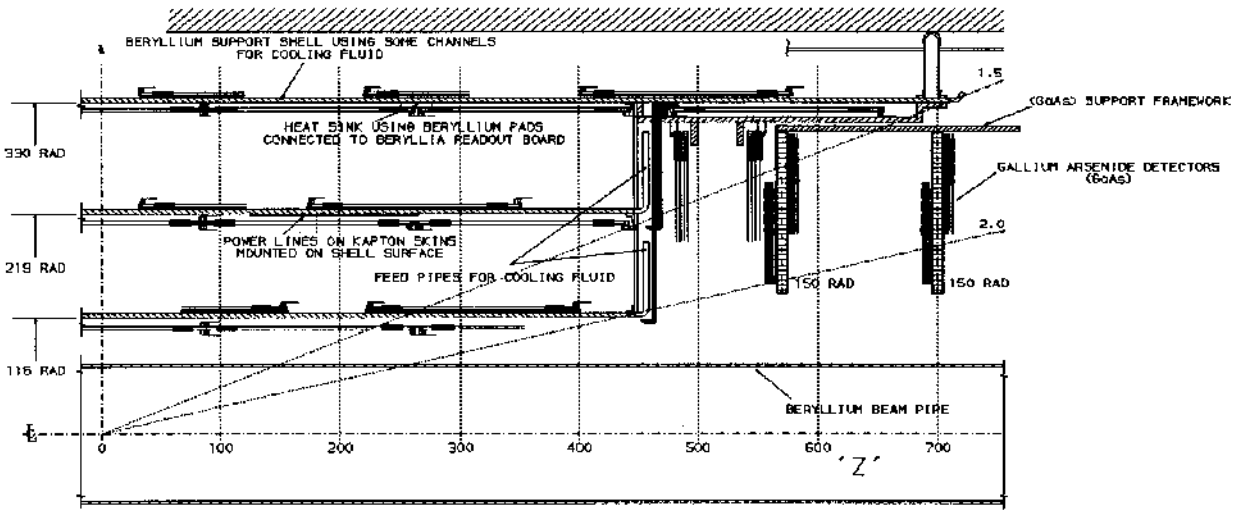

Figure 3.4: *SITV conceptual design*

3.4 Description and Performance of Proposed Technologies

3.4.1 Silicon Tracker/Vertex (SITV)

Precise measurements close to the interaction point allow the measurement and identification of primary and secondary vertices as well as improving the overall momentum measurement. Studies have shown that a measurement precision of 10–20 μm at radii of 10–30 cm is required to satisfy these goals [25, 26].

Because of the high resolution required and the severe conditions near the interaction point (high track densities and radiation levels) the most appropriate technology is silicon micropattern detectors, in the form of strips and/or pixels, with the following features:

- high spatial resolution: precisions of 5–10 μm have been achieved in large-scale collider applications [27];
- high speed: the full charge collection time is about 20–30 ns, for detectors of thickness 300 μm with most of the charge collected in the first 5–10 ns [28];
- good two track separation: typically 150 μm or twice the readout pitch [29];
- high radiation resistance (see Section 3.3.3).

There are currently several MOS and bipolar full custom readout chips being designed with the necessary speed and radiation resistance to satisfy the needs of the LHC. Of particular interest to the SITV is the RD20 front-end chip, which consists of a low-noise preamplifier (45 ns peaking time), an analogue delay buffer (ADB) and an analogue pulse shape processor (APSP), to restore the time tag of the interactions by deconvolution of the CR - RC shaped pulse. Prototypes of the amplifier, the ADB and the APSP chips exist and have been tested successfully. The results indicate that a signal-to-noise ratio (referred to the charge of a minimum-ionizing particle on one strip) of better than 15:1 can be maintained over the entire lifetime of the experiment [13, 30]. Radiation-hard versions of this electronics are currently being produced[2].

The conceptual design for the SITV is presented in Fig. 3.4. The detector consists of three cylindrical layers of silicon micropattern detectors at radii between 10 and 30 cm plus several forward disks of similar detectors. The η coverage is ± 1.5 units of rapidity and could be extended at additional cost. The most relevant numbers related to this design are presented in Table 3.1.

The inner layer's main function is to allow the tagging of short-lived particles, b's and τ's (see Section 3.5) especially at the lower luminosities expected at the start of LHC operation. The layer consists of silicon pixel detectors with a spatial resolution of 15 μm in $r\phi$ and about 60 μm in z, which will allow the reconstruction of the impact parameter of stiff tracks with a resolution of about 25 μm. As an alternative a layer of double-sided microstrip detectors with a high resolution in $r\phi$ and z directions could be used. The two-dimensional readout of pixel detectors simplifies pattern recognition and the small sizes of individual diodes would be an advantage under the harsh radiation conditions. To ensure complete coverage and redundancy this shell will be constructed out of two layers of detectors (a 'superlayer'). Pixel

[2]Harris and ABB HAFO.

Table 3.1: *SITV components and performances* ($\mathcal{L} = 1.7 \cdot 10^{34}$ cm^{-2}s^{-1})

Layer	Type of detector	# of Si detectors	Diode size *in* mm^2	# readout channels	Resolution in $r\phi$	Resolution in $z(r)$	Occupancy
Inner	pixels	372	0.05 × 0.2	$8 \cdot 10^7$	15 μm	60 μm	< 0.1%
Middle	strips	804	0.05 × 60	$1.9 \cdot 10^6$	15 μm	1 mm	< 1%
Outer	strips	1632	0.1 × 60	$2.0 \cdot 10^6$	15 μm	1 mm	< 1%
Forward	pixels/strips	400	0.05 × 0.2	$2 \cdot 10^7/8 \cdot 10^5$	15 μm	0.06/1 mm	< 1%

detectors are being developed by the RD19 collaboration [31] and radiation-hard electronics[3] is under development [23].

Taking into account expected doses and presently known limits on radiation resistance, one could expect that, after several years of operation at high luminosity, detectors and/or electronics could fail. For this reason the inner layer is designed to be removable and can be exchanged if necessary.

The outer layers serve mostly to improve the precision of the momentum measurement. They will be built from single- and double-sided silicon microstrip detectors, with dimensions chosen on the basis of allowed occupancies, leakage currents and signal-to-noise ratio, as well as to maximize the production yield and hence minimize the cost. As the performance of silicon detectors depends very much on the design and the operating conditions, a systematic study of single- and double-sided silicon strip detectors (especially their behaviour under radiation), fabricated by a selection of manufacturers using different processes and different sources of silicon, is underway in the RD20 collaboration [13]. Detectors of 60 mm length and widths between 30 and 60 mm are currently considered. The readout pitch is 50–100 μm. For the z-coordinate a combination of small stereo angle (10–20 mrad) and orthogonal strips is considered to ensure both accurate coordinate measurement and good pattern recognition. Again, for redundancy reasons, the shells are built as double 'superlayers'. The final choice of the number of layers will be made on the basis of cost, stand-alone track-finding capabilities and alignment. Studies on these subjects are in progress.

Because of the large number of sensitive elements, data reduction and sparsification will be done locally at the detector. The data from one or more detectors will be read out serially on a single optical fibre.

The forward disks will be constructed out of silicon strip and pixel detectors. The current preference is for pixels, due to their better pattern recognition capability and potentially better radiation resistance, but microstrip detectors of 50 μm pitch could also be used.

One of the principal difficulties faced in such a high-granularity detector with a corresponding high density of electronics is cooling. The SITV detector will dissipate about 10–15 kW of power in a small volume. Furthermore the operating temperature should be lower than the ambient temperature (close to 0°C) in order to reduce detector leakage currents and the temperature gradient across a single wafer should not be larger than a few °C. A number of options are under study - liquid cooling, evaporative cooling and gas cooling, which all seem capable of removing the heat. Each technique leads to a different mechanical construction and to a different distribution of introduced material [32]. A choice will be made only after full-scale prototyping and detailed simulation studies.

For the construction of the support cylinders we plan to use beryllium and/or carbon-carbon composites: thin sheets of material separated by distance/support ribs [13].

3.4.2 Gallium Arsenide detectors (GaAs)

The technology for making microstrip detectors from gallium arsenide (GaAs) is currently being developed by the RD8 collaboration [4]. The main advantage of GaAs is its radiation hardness (see Section 3.3.3). Microstrip detectors have been routinely made with a signal-to-noise ratio of $\sim 7:1$ in a test beam using AMPLEX readout [33]. While this is already acceptable, it is hoped that the performance will improve in the near future.

We propose to install GaAs microstrip detectors to improve the momentum resolution in the range $|\eta| > 1.8$ where the radiation levels are largest. The detectors will be in the form of wheels, centred on the beams, covering the radial region $15 < r < 25$ cm and positioned at z values of $z_1 = 57 - 70$ cm and $z_2 = 96 - 109$ cm from the interaction region (see Fig. 3.1 and Fig. 3.4).

The wheels will be covered by GaAs microstrip detectors in the form of tiles 53 × 23 mm^2 with microstrips of pitch 60 μm. The tiles overlap each other

[3] Thomson SOI and DMILL.

to make a hermetic detector. Each wheel consists of two layers with the radial microstrips offset from each other by an angle of 1° for small-angle stereo reconstruction. This provides a spatial resolution of 20 μm in $r\phi$ and an angular resolution of ± 2 mrad in θ.

Monte Carlo studies show that the occupancy of such a system at a luminosity of 1.7×10^{34} cm^{-2}s^{-1} is $< 1\%$ per readout channel.

3.4.3 Silicon Tracker (SIT)

The outer barrel tracker (SIT) in conjunction with the SITV detector provides precision momentum measurements for charged particles in the central rapidity region, space-point measurements for efficient pattern recognition in a high-multiplicity environment, and a fast, efficient, level-2 tracking trigger.

To demonstrate a practical realisation of silicon technology for LHC detectors, extensive developments at the material and electronics levels have been made by the RD2 collaboration [5].

The concept A design shown in Fig. 3.1 consists of six detector layers at radii $r = 70 - 100$ cm. The active length of each detector layer is $\pm$ 95 cm, therefore covering about $\pm$ 1 unit of rapidity in the central region. Each double layer is mounted on a thin but rigid carbon-fibre support cylinder. This support cylinder, designed to match the thermal properties of silicon detectors, will enable the precision mounting of independent 'mother boards' or modules containing typically 10–20 silicon detectors that are fully assembled and tested outside the detector. These modules overlap in ϕ (Fig. 3.5 (a)) to provide hermetic coverage. As already demonstrated by CDF and the LEP experiments, an alignment precision of < 10 μm on individual boards can be achieved.

Two types of detectors will be mounted on the mother boards. Single-sided strip detectors (60 mm length by 50 mm width) will consist of 256 strips of 195 μm pitch aligned to give a ϕ measurement with a precision of 60 μm. Four layers will be equipped with these detectors. Two layers will be equipped with detectors of the same size, but with a pad layout of 10–20 mm^2 in the present design giving a z precision of 300 μm. The final pad dimensions will be minimized subject to constraints of cost and the density of low-power electronics. A number of possible layouts for each mother board are now being studied [34] and one such layout is shown in Fig. 3.5 (b). Each motherboard is attached to the support cylinder by a thin graphite frame. Each layer will contain 3500 detectors and 450 000 readout channels.

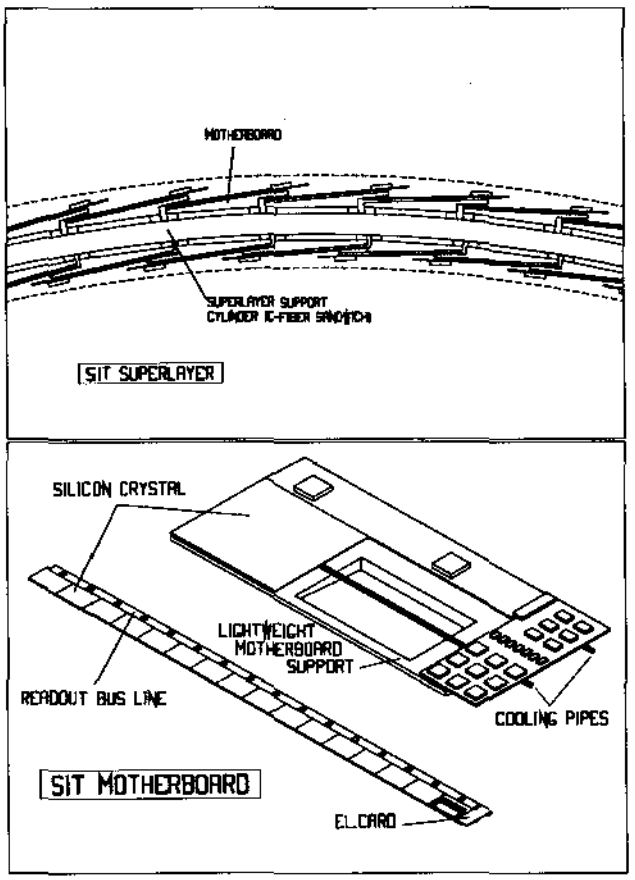

Figure 3.5: *Possible layout of an SIT 'superlayer' (top) and a 'motherboard' (bottom)*

The RD2 collaboration has measured radiation effects in silicon detectors [35] (see also Section 3.3.3). By operating the detectors at a temperature of 0–5 °C, the leakage current after 10 years LHC operation is expected to remain below 2 μA due to bulk damage, with a detector depletion voltage of < 150 V. Given this result, the design aim of a signal-to-noise ratio of 10 is achievable for minimum-ionizing particles. Prototype detectors have performed as expected in beam tests, both before and after irradiation.

Cooling is also essential for the dense VLSI electronics chain mounted on the detector. It will be provided by circulating an inert fluorcarbon compound (Fluorinert FC72) through cooling pipes built into each module (see Fig. 3.5 (b)). The pipes have an internal cross-section of 1 mm^2, and make direct contact with silicon detectors and electronics. Prototype tests [34] have shown that the cooling power meets the design requirements.

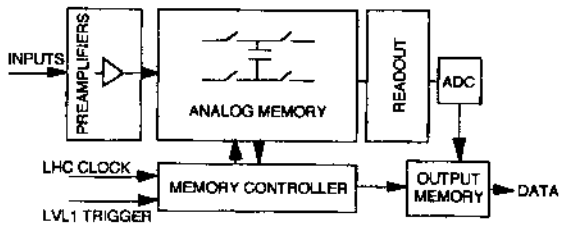

Figure 3.6: *Example of the front-end readout architecture*

The current design foresees analogue front-end electronics based on the HARP architecture [36] and further developed in the RD2 project [37] - see Fig. 3.6. The target for a 64 (or 128)-channel chip is to achieve, using a 2 μs 'pipeline', a signal-to-noise ratio for minimum-ionizing particles of 10 (for 10 years of operation), 8-bit resolution and a power consumption of < 5 mW per channel. Current R&D goals are to develop the integrated functionality of this architecture, and in parallel to reach design performance levels. Considerable progress has already been made. A chip with 32 channels, each with a fast low-noise preamplifier, a 64-cell analogue memory, and common control logic has been designed and fabricated. A three-counter silicon telescope was equipped with this pipeline electronics and tested in a particle beam. The test showed satisfactory operation and full chip functionality [37, 38].

This electronics is foreseen for both the pad and strip detectors. However, in the case of pad counters as part of an optimization of maximum detector granularity at reasonable cost and low power consumption, the possibility of binary electronics is being investigated. Data from several chips are collected serially and transferred by light fibre to the level-2 triggers and the off-detector trigger and DAQ system (see Section 5 and [39]).

Studies to implement this design with radiation-hard technologies[4] are in progress [23].

The pattern recognition and electron identification capabilities of this detector are excellent because of the high detector granularity ($< 0.5\%$ mean occupancy at high luminosity for events selected by the level-1 trigger after taking into account charge sharing) and its ability to provide space-point reconstruction. The results of extensive Monte Carlo studies are presented in Section 3.5. Even in the vicinity of jets, the mean maximum counter occupancy remains $< 5\%$.

[4] Thomson SOI, Harris and DMILL

3.4.4 Microstrip Gas Counters (MSGC)

Microstrip gas counters (MSGCs) are strong candidates for high-precision tracking detectors at LHC. All groups involved in R&D on MSGCs in preparation for LHC experiments have recently formed the joint RD28 project [17].

A MSGC consists of an insulating substrate covered by a thin metal film on which long, narrow cathode and anode strips are etched [40, 41].

Tests with various prototype detectors have shown that minimum-ionizing particles can be observed with a typical spatial resolution of 30 μm and a two-track resolution of 300 μm in the direction perpendicular to the strips. Ions produced in the avalanche process are captured quickly due to the short distance (50 μm) to the nearest cathode strip, thus allowing these detectors to be operated at rates up to a few hundreds of kHz per mm^2.

The MSGC geometry can be specifically adapted to meet the LHC operating conditions; only the resolution is slightly affected. The minimum track length in the counter gas has to be at least a few mm to approach 100% detection efficiency. This track length must on the other hand be minimized to obtain a short charge collection time. Therefore the drift gas applied should both have a high primary ionization density and high drift velocity. One promising gas mixture is 60% dimethyl ether with 40% CO_2 which has a primary ionization density of 47 cm^{-1} and an electron drift velocity of 69 μm/ns at a field strength of 10 kV/cm. Using a 2 mm gas gap, the charge collection will take only 30 ns. This gas mixture has more attractive features, such as a $> 10^4$ gas amplification, a very small transverse diffusion coefficient ($\sigma_T = 50\ \mu\text{m}/\sqrt{\text{mm}}$ [42]) and a modest Lorentz angle at high magnetic fields ($\Phi_L \approx 16°$ at $B = 2$ T).

An optimal resolution is achieved using analogue readout of the strip signals. A coarse position measurement can be done using a digital readout. With a small transverse diffusion in the drift gas, only one or two strips will have a hit when a particle crosses at normal incidence. For an anode pitch of 200 μm, a resolution of 44 μm is measured using digital readout. The corresponding efficiency is 98.4 % at a threshold of 8 $\times$ noise [41].

MSGC strip signals are of the order of 20 000 e$^-$ and can therefore be read out with available preamplifiers. Currently, prototype tests are made using the MX5 chips developed for Si microstrip counters. The readout chips that are being developed by RD2 [29] and RD20 [28] match all criteria to be used for analogue readout of MSGCs at the LHC. One candidate for a digital readout chip is the FASTPLEX chip now under development [43]. Data reduction and sparsi-

fication will be done locally. The data of a group of detectors will be transmitted via an optical fibre to the DAQ system.

Various substrate materials and metallisations are being investigated. A good substrate candidate is borosilicate glass with a thickness of 150 μm and aluminium strips. A support structure of carbon fibre composite has been built and equipped with dummy detectors. The smallest MSGC unit is a double counter which will consist of two facing substrates with a cathode plane in between. This double counter has an effective thickness of 550 μm glass or 0.43% of a radiation length for particles incident along a normal on the plane.

In the end-cap detectors counters will be assembled in large rings or disks (see Fig. 3.7). The average thickness of one MSGC wheel, including supports, readout, overlap, cooling etc., is estimated to be 1.5% X_0. The minimum size of an individual double-counter is 10 × 10 cm^2 with 2 × 512 anode strips. The strips will run radially but for a small stereo angle of about 15 mrad. They will be mounted to have 25% overlap with their radial neighbours giving on average three measurements per 2 crossed wheels.

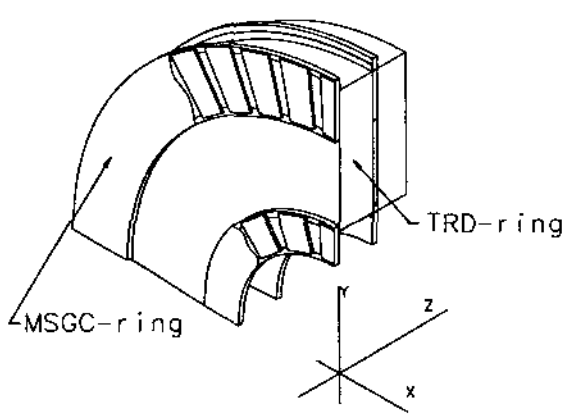

Figure 3.7: *Layout of MSGCs in the end-cap detector*

In the forward part of the Inner Detector MSGCs and TRD/Ts are interleaved, as described in Section 3.3.2. A combined design is under study to minimize support material.

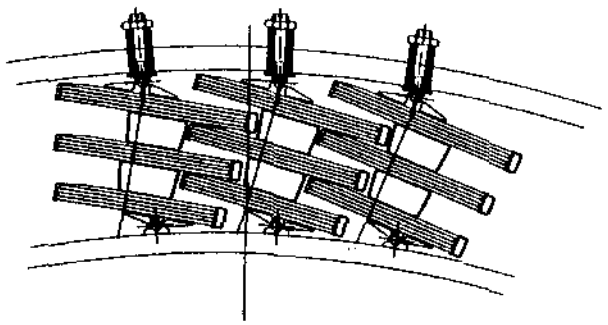

Figure 3.8: *Possible layout of MSGCs at large radius in the barrel part*

MSGCs also provide an alternative technology for precision tracking in the barrel region. The groups involved are studying several substrates including SiO_2 [44], and intend to develop MSGCs with double-sided readout, to measure also the second coordinate of a hit. Such detectors may be used in the barrel at a radius of about 46 cm with 200 μm anode spacing for the ϕ coordinate and 0.5 mm u and v strips oriented at $\pm 10°$. The space-point accuracy is expected to be $\sigma_{r\phi} \sim 40$ μm and $\sigma_z \sim 600$ μm (at $\eta \sim 0$). A second part has been designed for a radius of about 94 cm with an anode pitch of 300 μm and 1 mm wide u/v strips. The space-point accuracy is expected to be $\sigma_{r\phi} \sim 60$ μm and $\sigma_z \sim 1.2$ mm (at $\eta \sim 0$). A possible layout is shown in Fig. 3.8.

3.4.5 TRD/Tracker (TRD/T)

3.4.5.1 The role of the TRD/Tracker The TRD/T plays a major role in:

- Efficient pattern recognition over the pseudo-rapidity range ± 2.5 at the highest LHC luminosities for charged tracks with $p_T > 0.5$ GeV.
- Particle identification over a wide rapidity range, namely, the efficient detection of electrons with the rejection of hadrons (using transition radiation), and γ-conversions and Dalitz-pairs (by finding the partners). It is also possible to identify high-energy muons (> 100 GeV).
- Providing level-2 trigger information to identify tracks of $p_T > 10$ GeV, as discussed in Section 5.

The TRD/T stand-alone momentum resolution is $\Delta p_T/p_T = 8 \times 10^{-4} \times p_T$ for the pseudo-rapidity range ± 1.9, using drift-time information [48].

3.4.5.2 Overview of the TRD/Tracker system The TRD/T is a straw drift-tube detector with 4 mm diameter Kapton straws spaced on average 8 mm apart. The free space between straws is filled

with polypropylene foils or foam which produce transition radiation photons.

The end-cap TRD/T is positioned radially between 0.5 and 1.0 m and from 1.0 to 3.3 m in $|z|$, with radial straws of 50 cm length and $2 \times 130 \cdot 10^3$ readout channels (see Fig. 3.1 in Section 3.3).

The barrel part (concept B), with axial straws of total length less than 190 cm, is divided into two halves with independent readout ($2 \times 55 \cdot 10^3$ readout channels), positioned radially between 0.6 and 0.95 m, with a pre-radiator between 0.5 and 0.6 m.

The barrel and end-cap parts cover $|\eta| < 0.9$ (integrated with SIT) and $0.9 < |\eta| < 2.5$ (integrated with MSGC), respectively. The barrel-part radiator consists of polyethylene foam (density of 0.05 g/cm^3) [45]. The radiator for the end-cap part consists of 15 μm thick polypropylene foils; the density of foils and straws along z is adjusted in order to keep the average number of straws crossed by the particle between 40 and 70 and the total material thickness of TRD/T at the level of 7 to 10% X_0 over the full η-range. The total amount of TRD/T material (with the mechanics and electronics) is included in Fig. 3.2.

Substantial progress relating to straw properties, performance and design of the TRD/T has been made within the RD6 collaboration [46] over the last two years. We summarize below the most important results from prototype measurements, detailed Monte Carlo simulations and engineering design.

3.4.5.3 Straw tube and radiator properties Detailed studies of many types of straws and radiators have led us to choose multilayered Kapton welded straws (Kapton + welded layer + Al + carbon) and CH_2 foam or foils with a high transition radiation yield [16, 45]. Direct measurements in a nuclear reactor (0.8 MGy of ionization dose + 2×10^{15} neutrons cm^{-2}) indicate that straw and radiator components will operate stably for more than 20 LHC years [15, 16].

Studies of different gas compositions demonstrate that a gas mixture consisting of 70% Xe + 20% CF_4 + 10% CO_2 has a high drift velocity (60 μm/ns) [16, 46], efficient protection against spurious discharges (up to gas gains of 1.5×10^4), and shows no gain loss for a collected charge of more than 5 C/cm corresponding to more than six LHC years [16]. In the 2 T field, the total drift time is between 35 and 40 ns. The decrease of the gas gain due to space charge effects is within 3% for the highest LHC luminosities.

Measurements using a neutron source showed that expected LHC neutron fluences provide a negligible contribution to the straw occupancy (due to proton recoils, neutron capture etc.) [46].

3.4.5.4 Prototype measurements A TRD/T prototype containing 1000 straws embedded in a polyethylene foam has been built and tested with and without a magnetic field (B = 0.78 T), using a two-threshold readout scheme with fast signal shaping (7 ns rise-time). The combined use of a low threshold, 0.2 keV, for tracking and drift time measurements, and a high threshold, $\sim$ 5 keV, for transition radiation detection, was evaluated [47].

- A track is measured with an accuracy of 28 μm (180 μm) in position and 0.12(0.45) mrad in angle with (without) drift time measurements. Using drift time information, the position accuracy per straw is measured to be 140 μm, giving a momentum resolution $\Delta p_T/p_T = 4 \times 10^{-3}\ p_T$ for $\int Bdl = 0.2$ T·m, which agrees with the stand-alone momentum resolution quoted above, if extrapolated to the TRD/T at LHC [47, 48].

- The rejection, R, against hadrons has been measured for different energies and straw occupancies. For example, for 30 GeV pions, $R = 500$ for low straw occupancy, and $R = 30$ for the expected 20% straw occupancy at LHC [46, 47].

3.4.5.5 Expected performance Extensive MC simulations based on the test beam measurements have been performed to simulate as realistically as possible the TRD/T performance at LHC. The expected occupancy per straw is $\sim$ 20%, as shown in Table 3.2, but the effective occupancy is significantly reduced (by a factor $\sim$ 3) with the drift time measurement, at the expense of losing 10% of the hits. The transition radiation hit occupancy due to pile-up is $\sim$ 2%. The expected electron/hadron identification performance is shown in Fig. 3.9. The plot presents the pion efficiency for $p_T = 20$ GeV and as a function of η for different luminosities and an electron efficiency of 90 %. A rejection factor of 10 to 100 is provided by the TRD/T at the highest luminosity in addition to the calorimeter and E/p matching. The TRD/T performance in terms of tracking and overall electron identification is described in Section 3.5.

3.4.5.6 Full scale prototype design As described in ref. [8, 46], the RD6 collaboration is designing a full-scale engineering prototype of a wheel of the endcap TRD/T. This wheel contains 16 planes of 600 radial straws and the detailed design of all components is now complete. In addition a 30° azimuthal sector of several wheels is also being built, such that it fits in the magnet used for test beam measurements,

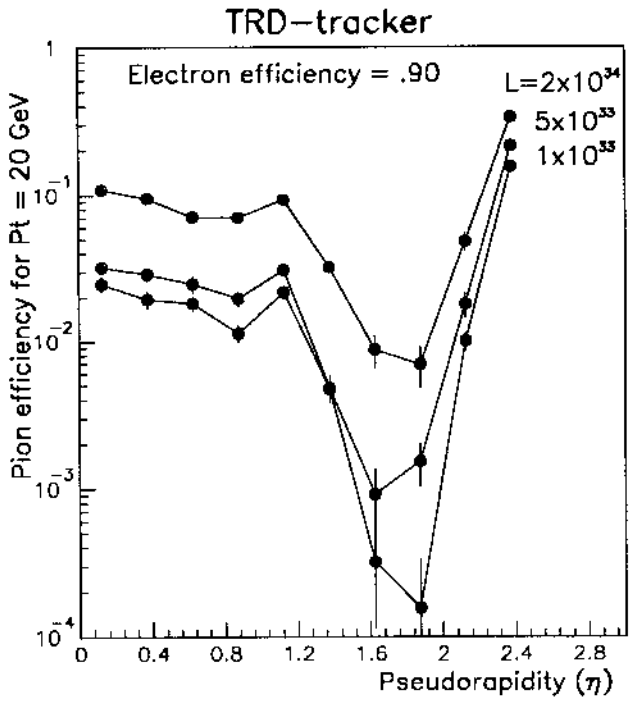

Figure 3.9: *Hadron rejection of TRD/T detector versus η*

and will be equipped with ASIC electronics with LHC functionality (except for the drift time measurement and radiation hardness). The data will be read out via HIPPI into VME commercial modules [49], and will also be used to test a hardware implementation of a level 2 TRD/T trigger (see Section 5). Both the full-scale engineering prototype and the sector prototype with its electronics will be tested towards the end of 1993.

3.4.6 Scintillating fibre outer tracker

Scintillating fibres may provide an interesting alternative technology for the outer barrel tracker. The device considered here follows the work of the RD7 collaboration [50] and uses bundles of 60 μm diameter doped polystyrene fibres in a 1.7 μm cladding. Glass capillaries filled with liquid scintillator [51] are also studied.

The outer tracker would consist of four layers of straight 0° and 6° oblique (u, v) fibres each layer 4 mm thick, mounted on a thin carbon-fibre cylinder. For this configuration, the spatial resolution is better than 60 μm (and limited by the optoelectronic chain), the two-track separation is 80 μm, and the occupancy at a luminosity of 1.7×10^{34} cm^{-2}s^{-1} is well below 1%. Pattern recognition is enhanced by the vector obtained from the two ϕ measurements.

The fibres are arranged in two half barrels, each read out at the centre by optoelectronic delay tubes coupled to the fibres by a fibre-optic plate. This arrangement compensates for light attenuation in the fibres by providing a longer path length in the fibre at larger distances from the tube. The bundles of fibres are rearranged at the ends to match the annulus of the fibres to the circle of the tube face. The two halves of the fibre system overlap so that there is always a good triplet (ϕ, u, v) for tracks around 90°. With the photocathode used in the tests, the average number of photoelectrons per millimeter depth of fibre is three. For 16 mm of fibres the number of opto-electronics tubes required for the whole system is 140.

Electrons liberated from the tubes' photocathodes are drifted slowly up and down the tube, preserving the space and time precision of the image, until, on receipt of a trigger level-1 'yes', the tube selects the right 15 ns bucket and accelerates the electrons to a silicon pixel device at the end of the tube. The pixel size is 60 μm in azimuth (matched to the fibre size) and 600 μm in radius. The signal is eventually read out and the tracking information is available for a level-2 trigger. The in-built pipeline is a distinct feature of this tracker. At present, the tube delay is 1 μs. Developments must be made to extend the tube delay to 2 μs.

A further advantage of the fibre tracker is its fast response. Successive bunch crossings do not mix in the detector, hence the occupancies are very small and ghosting of tracks is very much reduced. One should also consider the very low power consumption (no heat from fibres, pixels active only when level 1 set). The fibres have been tested and are radiation-hard to 5 kGy, sufficient for several years of LHC operation.

3.5 Performance of Proposed Layout

3.5.1 Introduction

A summary of the principal characteristics of the proposed Inner Detector is shown in Table 3.2.

The occupancy of the components of the Inner Detector has been calculated at nominal luminosity, including the effect of loopers, δ-rays and secondary interactions, and is presented in Fig. 3.10 and Fig. 3.11.

In the barrel region it was assumed that SITV silicon detectors have elements with areas shown in Table 3.1. The SIT has strips of the same length every 200 μm. The TRD/T straws are 95 cm long with a diameter of 4 mm. For the SITV a clustering factor

Table 3.2: *Characteristics of the proposed tracker*

Detector	SITV	GaAs forward	SIT concept A	TRD/T barrel	MSGC end-cap	TRD/T end-cap
No.Elements	$4.2 \cdot 10^6 (10^8)^*$	$8 \cdot 10^5$	$2.7 \cdot 10^6$	$1.1 \cdot 10^5$	$5 \cdot 10^6$	$2.6 \cdot 10^5$
Hits/Track	6	4	6	40	4 - 6	40
Occupancy(1,2)	0.1 - 1%	< 1%	< 0.1%	25/2.5%	< 1.5%	20/2%
Rad. Length(3)	6%	5%	8%	12%	7.5%	12%
Resolution ($r\phi$)(4)	15	20	60	150	45	150
Resolution (η) (5)	1(0.06)*	2	2	-	3	30

(1) Occupancy per element for $B = 2$ T and $\mathcal{L} = 1.7 \cdot 10^{34}$ cm^{-2}s^{-1}
(2) For the TRD/T the first figure refers to a low threshold (0.2 keV deposited energy per straw), the second to a high threshold (5 keV per straw).
(3) Radiation length of total sub-detector at normal incidence.
(4) Resolution in $r\phi$: in μm per measurement.
(5) Resolution in η: in mm in the z-direction for barrel detectors, and in the r-direction for forward detectors.
* The numbers in brackets are for pixel detectors.

of 2 was added, and similarly 1.5 for the SIT. For the TRD/T events were integrated over two bunch crossings. To include the effect of conversions a realistic amount of material was taken for the beam pipe and the detectors.

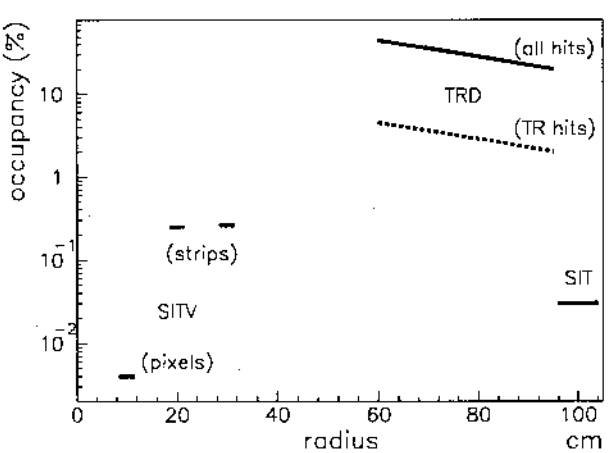

Figure 3.10: *Occupancy for the barrel detectors at $\eta = 0$ as a function of radius (20 minimum-bias events per bunch crossing). The upper and lower curves for the TRD/T are for the low and high threshold respectively*

In the forward region the response of MSGCs to charged particles was simulated and the events were integrated over 30 ns (two bunch crossings). The material of the other detectors has been included. The number of hits in 200 μm pitch radial strips between 40 and 50 cm and between 84 and 100 cm has been calculated as a function of z (see Fig. 3.11).

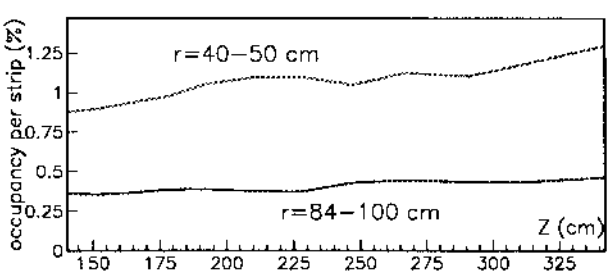

Figure 3.11: *Occupancy for the forward detector in radial strips as a function of radius and position along the beam (for 40 minimum-bias events in two bunch crossings)*

The Inner Detector reconstructs tracks and vertices and identifies electrons. It measures momenta and impact parameters of the tracks. The relevant performance questions are therefore:

- pattern recognition capability;
- momentum resolution;
- electron identification and rejection of QCD jets;
- impact parameter resolution;
- level-2 trigger capability.

The large coverage in polar angle requires the Inner Detector to have a break in the geometry to avoid small angles of incidence. This break is at 45° i.e. $|\eta| \simeq 0.9$, and divides the Inner Detector into a barrel part and two end-cap parts.

Two concepts of the barrel part were studied to get experience and understanding of the different factors that influence its performance. Concept A uses a small number of layers of highly granular detectors, and concept B also uses a barrel TRD/T to give many measurement points along the track and transition radiation information.

3.5.2 Efficiency of pattern recognition and ghosts

The inner tracker searches for tracks in trigger roads defined by either the muon detector or by the electromagnetic calorimeter. The sizes of these roads are $\Delta\eta \times \Delta\phi = 0.03 \times 0.04$ and 0.20×0.06 for a 10 GeV muon and electron respectively. The figures of merit are the track-finding efficiency and ghost frequency in these roads. Simulations were performed for the more difficult case of electron candidates. Below we present results from studies for the two different barrel concepts and for the end-cap detector.

3.5.2.1 Barrel detector with SITV and SIT

The SIT design used for simulations is similar to that of concept B, except that no TRD information was recorded. As shown in Fig. 3.1, 4 strip layers (200 μm × 50 mm) and 2 pad layers (9 mm × 1 mm) are arranged between radii 95 cm and 105 cm. Four strip layers of granularity 50 μm × 50 mm have been simulated for the SITV. For all the simulations, an average of 60 minimum-bias events were superimposed on the high-p_T track candidate. This gives a higher occupancy than expected from beam-beam events, in order to allow for extra unassociated hits, as have been seen at existing hadron colliders. Track segments are initially reconstructed independently in the inner and outer detector layers, using a road defined within 4 cells of an electromagnetic cluster centroid. Possible track segments (of $p_T > 0.25\ E_T^{cal}$ or 20 GeV) are then combined in a global fit including the vertex and calorimeter cluster positions. A helix fit is made for all tracks, and a special 'electron' fit for electron candidates includes a possible bremsstrahlung 'kink'. Table 3.3 summarizes the performance obtained [53] for muons using a helix fit with quality $\chi^2 < 5/n_{df}$, and for electrons using an 'electron' fit. The contribution to this inefficiency from bremsstrahlung effects is between 2.5 and 4%, with an additional 1.5% due to assumed layer inefficiencies. The effect of pile-up is negligible, the fake track rate is <0.2% (90%CL). The results of Fig. 3.12 for 10 GeV electrons indicate a significant improvement in the efficiency by using the electron fit.

Table 3.3: *Performance of the barrel detector with SITV and SIT* ($\mathcal{L} = 1.7 \cdot 10^{34}$ cm^{-2}s^{-1})

$\|\eta\|$	0		1.2	
Momentum [GeV]	10	100	10	100
Efficiency e [%]	96	97	94	96
Efficiency μ [%]	98.5	98.5	98.5	98.5
Fake tracks * [%]	< 0.2	< 0.2	< 0.2	< 0.2

* within trigger roads.

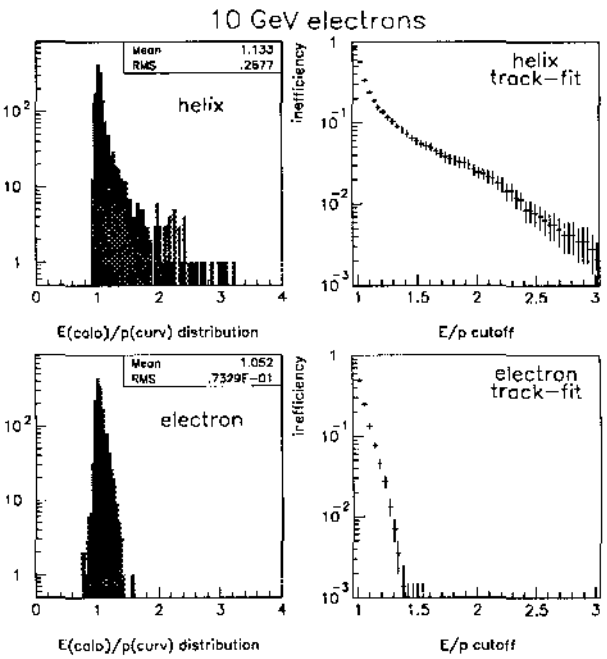

Figure 3.12: *E/p for 10 GeV electrons with a helix fit (top) and the electron fit (bottom), and the inefficiency of E/p cuts including the effect of pile-up*

3.5.2.2 Pattern recognition with TRD/T

In the 2 T magnetic field, tracks originating from the vertex, with $p_T > 0.5$ GeV, appear as almost straight lines in the (ϕ, r) plane for the barrel TRD/T and as straight lines in the (ϕ, z) plane for the end-cap TRD/T. Given the large number of hits per track (40 to 70), an efficient and simple global pattern recognition can be performed, with low fake-track rate, even for tracks with p_T as low as 0.5 GeV at the highest LHC luminosities, despite the high straw occupancy. The found tracks can then easily be extrapolated to the precision measurement layers, in order to reduce further the fake track rate and to provide a polar angle measurement in the barrel part.

The performance of the TRD/T global pattern recognition was simulated for isolated muons and electrons, and for the minimum-bias pile-up as a function of luminosity up to 6×10^{34} cm^{-2}s^{-1} [52]. The

efficiency for reconstructing isolated muon and electron tracks in the presence of pile-up is shown in Table 3.4, for p_T = 20 and 100 GeV. The electron reconstruction efficiency at low momenta is somewhat lower than that for muons due to bremsstrahlung. Also shown in Table 3.4 is the probability to observe a fake track from minimum-bias pile-up, facing an electromagnetic calorimeter cluster ($\Delta\eta \times \Delta\phi = 1.0 \times 0.06$ in the barrel and 0.20 × 0.06 in the end-cap).

Table 3.4: *Performance of the TRD/T pattern recognition ($\mathcal{L} = 1.7 \cdot 10^{34}$ cm^{-2}s^{-1})*

	barrel		end-cap	
p_T [GeV]	20	100	20	100
Efficiency μ [%]	> 99	> 99	> 99	> 99
Efficiency e [%]	96	98	96	99
Fake tracks * [%]	< 0.3		< 0.05	

* within road as explained in text

Figure 3.13 (barrel TRD/T) and Fig. 3.14 (end-cap TRD/T) show the total number of fake tracks expected over the full geometrical acceptance as a function of luminosity, for p_T > 2 GeV and 10 GeV. Also shown are the expected rates for real tracks from minimum-bias events, which, for low transverse momenta, are significantly higher than the fake-track rates. Figure 3.14 also shows, for p_T > 10 GeV, the expected improvement due to drift time measurements, which significantly reduce the effective occupancy.

In addition we expect the silicon/MSGC detectors to reduce even further these fake-track rates and we therefore conclude that the overall pattern recognition capabilities of the Inner Detector are sufficient to achieve the goals described in Section 3.1.

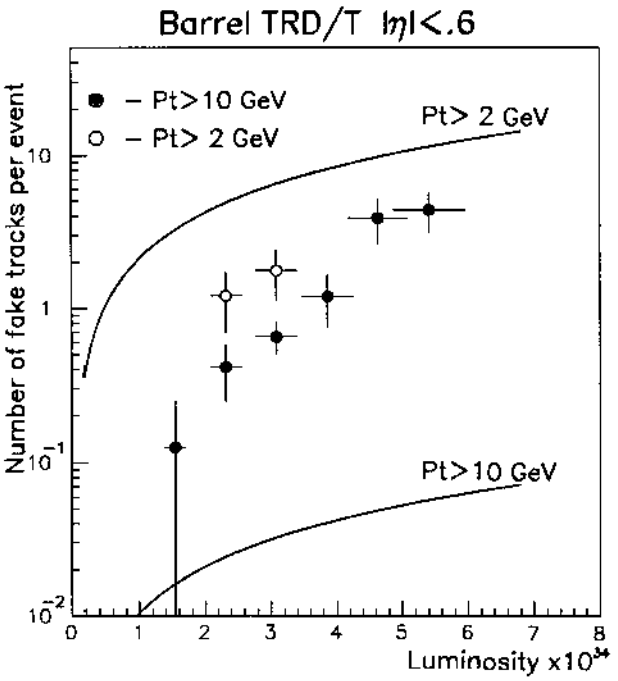

Figure 3.13: *Number of fake tracks per event in stand-alone TRD/T barrel detector versus luminosity (the solid curves give expected rates from minimum-bias events)*

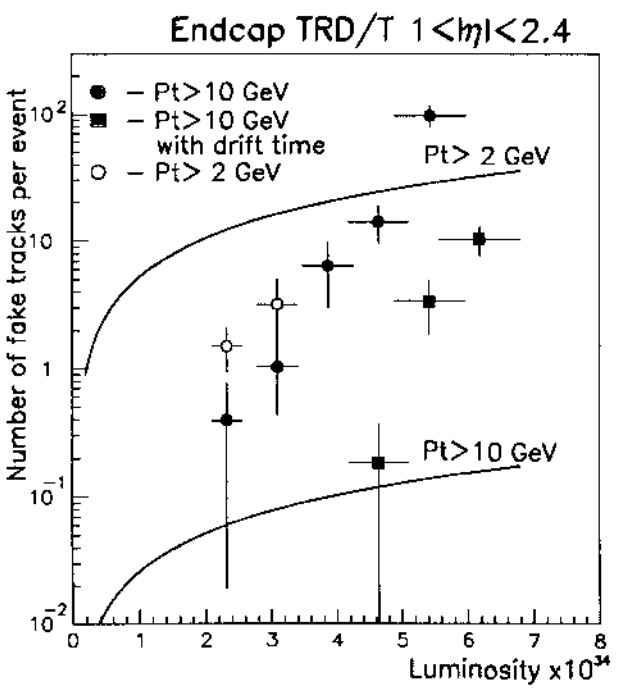

Figure 3.14: *Number of fake tracks per event in stand-alone TRD/T end-cap detector versus luminosity (solid curves as above)*

3.5.3 Momentum resolution

For the proposed Inner Detector, the momentum resolution is mainly determined by the track vector detectors measuring the sagitta and end point. Here, the resolution of the transverse vertex is assumed to be $\sigma = 20$ μm. Four η-bands can be distinguished where different subdetectors have the role of measuring p_T:

- $0.0 < |\eta| < 0.9$: SITV-SIT
- $0.9 < |\eta| < 1.5$: SITV-MSGC
- $1.5 < |\eta| < 1.9$: MSGC-MSGC
- $1.9 < |\eta| < 2.7$: GaAs-MSGC

Figure 3.15 shows the transverse momentum resolution as a function of η, for tracks with $p_T = 100$ and 500 GeV, using a realistic field map. The momentum resolution can be supplemented by the TRD/Tracker as mentioned in Section 3.4.5.1.

The resolutions of each detector superlayer are slightly degraded to account for alignment uncertainties: the SITV and GaAs detectors are assigned an $r\phi$ resolution of 20 μm/superlayer, the inner MSGC 45 μm, the SIT and outer MSGC detectors 60 μm.

The scaled transverse momentum resolution, $\Delta p_T/p_T^2$ is better than 5×10^{-4} at $|\eta| < 2$ and degrades to $\sim 10^{-3}$ at $|\eta| = 2.5$. At low momenta multiple scattering dominates with a contribution of between 1 and 1.5% to $\Delta p_T/p_T$.

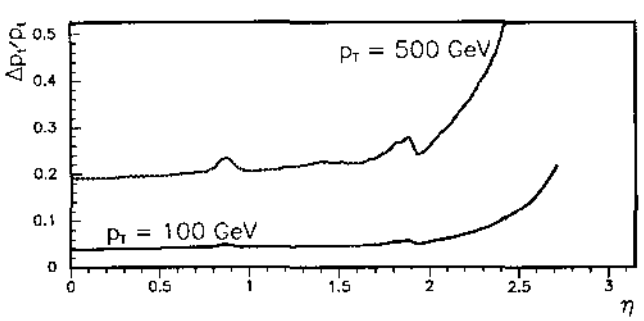

Figure 3.15: $\Delta p_T/p_T$ *as a function of* η *at high* p_T

3.5.4 Electron identification

Electron identification at high luminosity is one of the major tasks of the Inner Detector. With the calorimeter level-1 and -2 trigger algorithms discussed in Section 5, a fraction of $\sim 10^{-3}$ of QCD jets will be selected as electron candidates for p_T^e around 20 to 40 GeV. As indicated in Section 3.1, most of these jets consist of high-p_T π^0/η's, and the additional rejection required to bring them below $\sim 10\%$ of the isolated electrons is in the range $10^2 - 10^3$ (see Fig. 3.16). A good rejection capability of fake electron signatures due to π^0/η Dalitz decays and external photon conversions is therefore essential.

3.5.4.1 Rejection of electron pairs using SITV and SIT Using the pattern recognition algorithm, described in Section 3.5.2.1, which corrects for single hard bremsstrahlung from electrons, an efficiency of $\sim 93\%$, for isolated electrons including pile-up, is obtained. A large sample of π^0/η's was generated following the p_T-spectrum shown in Fig. 3.16. This spectrum is in agreement with that of QCD jets, which are selected as isolated electron candidates by calorimeter cuts. The dark-shaded histogram in Fig. 3.16 represents the events, which have a reconstructed electron track, with $0.9 < E/p < 1.3$ (for $p_T > 20$ GeV the upper bound is increased linearly to 2.0 at 100 GeV), and no reconstructed partner with $p_T > 2$ GeV. For $p_T > 30$ GeV, the background rate after these cuts is about 10% of the true electron rate (Fig. 3.16 and [53]).

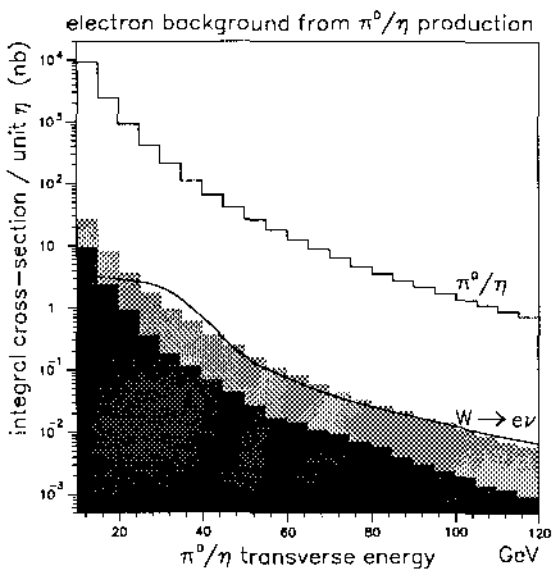

Figure 3.16: *Generated* p_T *distribution of* π^0/η*'s and of isolated electrons from* $W \rightarrow e\nu$*. The light-shaded histogram shows the calorimeter measured* E_T *for electromagnetic clusters with an associated track. The dark-shaded histogram represents electrons passing* E/p *and e-pair cuts (see text)*

3.5.4.2 Rejection of electron pairs using TRD/T As discussed in [8], the TRD/T provides a powerful tool to reject electron pairs, originating from photon conversions both in front of and inside the TRD/T and from Dalitz decays. A simulation similar to that described above, using a sample of π^0/η mesons with $p_T > 20$ GeV, shows that the most dangerous electron-pair background arises from asymmetric Dalitz decays. An overall rejection of ~ 30 against π^0/η Dalitz decays is obtained,

mainly by requiring no reconstructed partner track with $p_T > 0.5$ GeV within a limited solid angle around the electron candidate. The corresponding efficiency for isolated electrons, including pile-up, is estimated to be $94 \pm 2\%$. The rejection against external photon conversions is much higher, ~ 200 in the case of photon conversions in the beam pipe and ~ 100 in the case of photon conversions in the TRD/T itself. We note here that most photon conversions in the Inner Detector material beyond the first sensitive tracking layer can be rejected by requiring a hit in this first layer on the electron track candidate.

3.5.4.3 Study of QCD jet rejection Since this task is most difficult at low transverse momenta, a sample of $\sim$ 500 000 QCD jets was generated, at $\eta = 0$ and with $p_T > 20$ GeV. After full GEANT simulation of tracking and calorimetry, these events were used to study the combined performance of the Inner Detector, using the precision layers of SITV and SIT for momentum reconstruction and E/p matching, and the TRD/T for pattern recognition and hadron rejection [54].

In a first step, 913 of the generated jets are selected as electron candidates, using only calorimeter information. Only those jets with at least one reconstructed track (combining SITV, SIT and TRD/T) with $p_T > 10$ GeV were retained. Only 108 jets remain, since most jets selected by the calorimeter cuts consist of high-p_T π^0's. After requiring a good matching between the calorimeter energy and the track momentum, as measured using the SITV and SIT, and a cut of $E/p < 1.2$, 51 electron candidates remain, corresponding to a fraction of $\sim 10^{-4}$ of the generated QCD jets. These events contain 21 electrons from b-quark decay, 23 charged hadrons, which produced a dominantly electromagnetic shower in the calorimeter, and 7 electrons from photon conversion or Dalitz decay. The efficiency, including the calorimeter selection, is estimated to be $\sim$ 85% (90%) with (without) pile-up from 40 minimum-bias events, for isolated electrons. Some loss of efficiency is caused by bremsstrahlung leading to momentum measurement errors, and could be recovered by the improved version of the 'electron track' fit (see Fig. 3.12).

The high-p_T charged hadrons can be further rejected by a factor better than 10 using the TRD/T and by an independent factor of 2 to 5 using the preshower detector. The electrons from photon conversion or Dalitz decay can be further rejected by a factor 10 to 20, searching for the second electron, as described above separately for the SITV and SIT and for the TRD/T.

3.5.4.4 Conclusions on electron backgrounds We conclude that the potentially dangerous background from asymmetric electron pairs can be reduced to a negligible level with respect to the expected rate from isolated electrons, even for transverse momenta as low as 20 GeV. Furthermore, despite the large uncertainties (arising mainly from QCD and b-quark jet production, jet fragmentation, and calorimeter modelling), we conclude that the background from QCD jets to the expected isolated electron signal can be reduced well below 10^{-5} of the expected QCD jet rate using the combined system.

3.5.5 Impact parameter measurement

Precise vertex measurements of the SITV (see Section 3.4.1) make possible the tagging of short-lifetime particles.

For b-tagging efficiency studies a detector model was developed. Finite detector resolutions and multiple scattering were taken into account. Pattern recognition problems were not yet included at this stage.

An SITV detector giving three pairs of points between radii 10 and 30 cm was assumed, with 20 μm point resolution in $r\phi$. The experience from present LEP experiments indicates that this value already includes a significant safety margin for possible alignment problems. The total radiation length of the SITV at 90° is assumed to be 4.6%.

The impact parameter resolution for 90° tracks is shown in Fig. 3.17(a) as a function of the track momentum. For high momenta, when the multiple scattering contribution is small, the resolution is 27 μm. Figure 3.17(b) shows the dependence of the resolution on η for two track momenta.

The impact parameters of tracks from b and non b-jets differ significantly due to the finite lifetime of B particles as shown in Fig 3.18. Using the SITV resolution one can estimate the b-jet tagging efficiency for $t\bar{t}$ events. The rejection of non-b jets as a function of acceptance for b jets is shown in Fig. 3.19 (solid line).

The efficiency of τ tagging with an impact parameter measurement was also calculated. Leptonic τ decays were studied. Figure 3.19 (broken line) shows the rejection factor against leptons from W decay, as a function of the acceptance for leptons from τ decays. Background leptons from b decays cannot be removed on the basis of an impact parameter cut and isolation criteria have to be used.

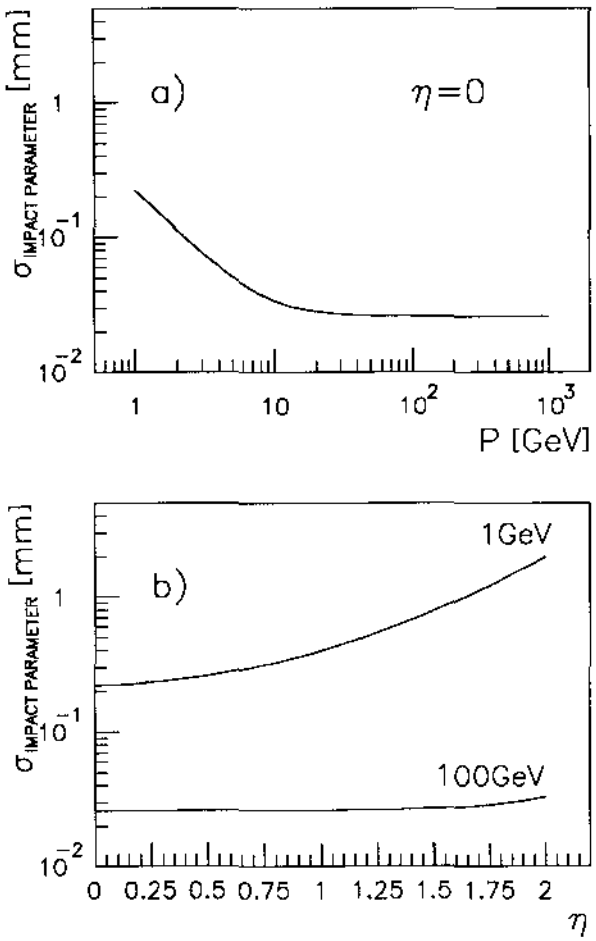

Figure 3.17: *Impact parameter resolution as a function of particle momentum for $\eta = 0$ (a) and as a function of η for 1 GeV and 100 GeV tracks (b)*

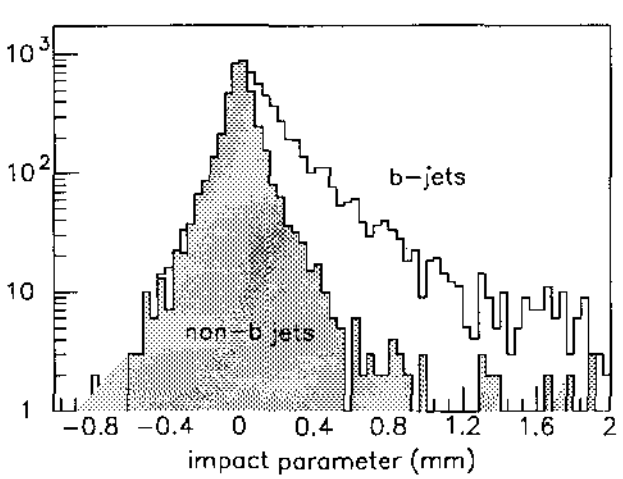

Figure 3.18: *Impact parameter distribution of tracks from b and non-b jets*

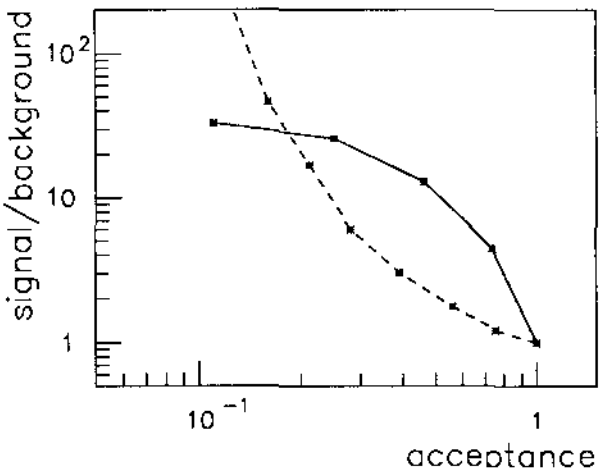

Figure 3.19: *Rejection of non b-jets as a function of b-jets acceptance in $t\bar{t}$ events (solid line). Rejection of W-decay leptons as a function of acceptance for leptons from τ decays (broken line)*

3.6 Installation, Services, Moderator, Alignment

The Inner Detector consists of two concentric cylindrical parts. The inner part up to a radius of 38 cm contains the SITV detector and the GaAs detectors. The outer cylinder from $r = 38$ cm up to the moderator has a barrel SIT and TRD/T detectors and two forward parts with MSGCs and TRD/Ts. The whole Inner Detector and the moderator are suspended from the end flanges of the cryostat which contains the solenoidal coil and the electromagnetic calorimeter.

The presence of many different detector technologies in a relatively small volume requires an integrated design effort. A special working group has been set up for this task.

The inner radius of the cryostat of the barrel calorimeter is 1.15 m and its length is 6.8 m. The moderator has a thickness of 5 cm and consists of a hydrogen-rich material, e.g. polyethylene ($n CH_2$) or water (H_2O). We reserve an additional 2 cm for the support structure of the moderator which is then located between $r = 108$ cm and $r = 115$ cm.

The moderator weighs approximately 3500 kg. The barrel and two forward parts of the outer cylinder of detectors weigh about 500 kg each. The vertex detector and GaAs detectors on each side have each a weight of about 50 kg. The total weight of less than 5500 kg can be suspended easily from the cryostat.

The outer and inner cylindrical parts of the Inner Detector are suspended from rails made of carbon-fibre composites, which are attached to the end flanges of the cryostat. Insertion of the various detector components is rapid by sliding in via the rails.

Each rail has a width of 2 cm and a length of 6.8 m attached only at the ends to the end flanges of the cryostat. The rails reserve an annular slot between $r = 106$ and 108 cm. This slot is to be used for services to the electronics. All connections of services, power, signal cables/optical fibres and cooling, are located at the ends and thus easily accessible.

Very-high-precision position detectors (SITV, GaAs, SIT and MSGC), which have intrinsic resolution between 10 and 40 μm, require special attention. The support structures for these detectors must be maintained with a long-term stability better than their accuracies with a minimum amount of additional material. A large system of such detectors requires a detailed system-engineering study to understand problems such as the design of individual detector modules which must be fully tested and measured, installed and aligned, but still remain exchangeable. A careful planning of the distribution of power lines, signal cables and cooling circuits is essential (they will introduce extra material but also at large currents could give unwanted forces and/or pick-up problems).

The position of the individual elements of the detector can be measured after mounting using standard optical precision stands. The installation and alignment of the detector assemblies on the support rails is performed with standard survey techniques up to a precision of about 100 μm. The final alignment can only be done using tracks down to a level of no more than 10 μm systematic contribution to the resolution. However, a permanent relative monitoring of the detectors with a precision of about 10 μm is needed. Infrared laser diodes and capacitive displacement probes have proven to be useful [55]. Recently, new monitoring methods using optical fibres embedded in the support structure have been developed and brought onto the market.

The problems of installation, maintenance, and alignment *in situ* are recognized and are all under study.

References

[1] G. R. Stevenson et al., CERN-TIS/RP/92-07CF.

[2] E. Belau et al., Nucl. Instrum. Methods **217** (1983) 224.

[3] F. Anghinolfi et al., CERN/ECP-91-29 (1991); W. Snoeys et al., Contribution to 6th European Symp. on Semiconductor Detectors, Milano, Feb. 1992. To be published in Nucl. Instrum. Methods.

[4] RD8 Collaboration, CERN/DRDC 92-12 (1992).

[5] RD2 Collaboration, CERN/DRDC/92-4 (1992).

[6] A. Oed, Nucl. Instrum. Methods **A263** (1988) 351.

[7] RD7 Collaboration, CERN/DRDC 91-55 (1991).

[8] RD6 Collaboration, CERN/DRDC/90-38 (1990); CERN/DRDC/91-47 (1991).

[9] RD23 Collaboration, CERN/DRDC/91-41 (1991).

[10] RD12 Collaboration, CERN/DRDC/92-10 (1992).

[11] H. Dietl et al., Nucl. Instrum. Methods **A253** (1987) 460;
R. Wunstorf et al., CERN 89-10, ECFA 89-124, V.1, 1989, p. 321.

[12] R. Wunstorf et al., Nucl. Instrum. Methods **A315** (1992) 149;
D. Pitzl et al.,Nucl. Instrum. Methods **A311** (1992) 98.

[13] RD20 Collaboration, CERN/DRDC 92-28 (1992).

[14] S. P. Beaumont et al., CERN-PPE/92-51, 1992.

[15] V. Bondarenko et al., CERN-PPE/91-191, 1991.

[16] V. Bondarenko et al., RD6 Collaboration, note 34 (1992).

[17] RD28 Collaboration, CERN/DRDC/92-30 (1992).

[18] RD10 Collaboration, CERN/DRDC 90-40 (1992).

[19] W. Dabrowski et al., Conf. Record of the 1991 IEEE Nucl. Sci. Symposium, Nov. 1991, Santa Fe.

[20] N. Bingefors et al.,Nucl. Instrum. Methods **A316** (1992) 359;
N. Bingefors, et al., Radhard frontend electronics in SOS technology, Paper presented at the Sixth European Symposium on Semiconductor Detectors, Milano, Feb. 24-26, 1992.

[21] J. L. Leray et al., IEEE Trans. Nucl. Science, **NS-37** (1990) 2013.

[22] H. H. Williams, contribution to the Fifth Pisa Meeting on Advanced Detectors: Frontier Detectors for Frontier Physics, La Biodola, Isola d'Elba, May 1991;
N. Cartiglia et al., SCIPP 92/05, March 1992.

[23] RD9 Collaboration, CERN/DRDC/92-15 (1992);
RD29 Collaboration, CERN/DRDC/92-31 (1992).

[24] Radiation Effects at the SSC, SSC Int. Report SSC-SR-1035, Berkeley, June 1988.

[25] A. Poppleton et al., EAGLE note, INDET-NO-001 (1992).

[26] S. Gadomski et al., EAGLE note, PHYS-NO-006 (1992).

[27] A.S. Schwarz, Contrib. to B-factories Workshop, SLAC, April 1992;
M. Caccia et al., Contribution to XXVI Int. Conf. on High Energy Physics, Dallas, Aug. 1992.

[28] S. Gadomski et al., SCIPP 92/02, Feb. 1992;
F. Lemeilleur et al., Conf. Record of the 1991 IEEE Nucl. Sci. Symposium, Nov. 1991, Santa Fe, p. 308.

[29] C. Adolphsen et al.,Nucl. Instrum. Methods **A253** (1987) 444.

[30] S. Gadomski et al., CERN-PPE/92-24 (1992).

[31] RD19 Collaboration, CERN/DRDC 92-5 (1991).

[32] G. Hallewell et al., ATLAS note, INDET-NO-014 (1992).

[33] R. Ansari et al.,Nucl. Instrum. Methods **A279** (1989) 388.

[34] C. Gössling et al., SITP-NO-044 (1992).

[35] F. Anghinolfi et al., Contribution to Sixth European Symp. on Semiconductor Detectors, Milano, Feb. 1992. To be published in Nucl. Instrum. Methods;
F. LeMeilleur et al., Contribution to Conf. on Advanced Technology and Particle Physics, Como, June 1992. To be published.

[36] P. Jarron, Proc. of the Meeting on Fast Triggers, Silicon Detectors and VLSI, CERN, Nov. 1988, p. 420.

[37] D. Munday et al., Contribution to 6th European Symp. on Semiconductor Detectors, Milano, Feb. 1992. To be published in Nucl. Instrum. Methods.

[38] R. Bonino et al., Contribution to the Int. Conf. on High Energy Physics, Dallas, 1992.

[39] H. Verweij et al., SITP-NO-045 (1992).

[40] M. Geijsberts et al.,Nucl. Instrum. Methods **A313** (1992) 377.

[41] M. Geijsberts et al.,Nucl. Instrum. Methods **A315** (1992) 529.

[42] J. Schmitz, NIKHEF-H/92-10, to be published in Nucl. Instrum. Methods.

[43] F. Anghinolfi et al., Proc. of the 14 th Workshop on INFN Eloisotron Project, Nov. 1990, Erice, Italy.

[44] S.F. Biagi et al. Contribution to the Vienna Wire Chamber Conference, February 1992.

[45] RD6 Collaboration, note 33 (1992).

[46] RD6 Collaboration, ATLAS note INDET-NO-18 (1992).

[47] J. T. Shank et al.,Nucl. Instrum. Methods **A309** (1991) 337; Nucl. Instrum. Methods **A317** (1992) 97.

[48] V. Bachkirov et al., RD6 Collaboration, note 32 (1992).

[49] RD6 Collaboration, notes 25 and 29.

[50] C. D'Ambrosio et al., CERN-PPE/92-26; CERN-PPE/92-69.

[51] N.I.Bozhko et al.,Nucl. Instrum. Methods **A317** (1992) 97.

[52] I. Gavrilenko et al., ATLAS note, INDET-NO-16 (1992).

[53] A.G. Clark et al., ASCOT/EAGLE note INDET-NO-015 (1992).

[54] P. Nevski et al., ATLAS note, INDET-NO-17 (1992).

[55] M. Battaglia et al., Nucl. Phys. **B23A** (1991) 448 (Proc. suppl.); P. Aarnio et al.,Nucl. Instrum. Methods **A303** (1991) 233.

4 Muon Spectrometer

4.1 Introduction

The following criteria have been adopted for the conceptual design of the muon spectrometer:

- Very good momentum resolution in the range 10–3000 GeV;
- hermetic coverage and momentum measurement up to pseudorapidities $|\eta| = 3$;
- safe stand-alone operation at luminosities of $\mathcal{L} = 1.7 \cdot 10^{34}$ cm^{-2}s^{-1} and above;
- robust pattern recognition;
- capability of providing an efficient level-1 trigger.

A spectrometer system based on a large toroid magnet has been chosen as the most adequate solution to meet these requirements. The main advantages of this principle have been summarized in the introduction (Chapter 1); at present, both a superconducting air-core and a conventional iron-core magnet are retained as options for the barrel and end-cap regions.

The momentum resolution of such a spectrometer is determined by the following parameters:

- the amount of absorber material in front of the spectrometer, giving rise to energy loss fluctuations;
- the amount of material inside the spectrometer, giving rise to additional energy loss fluctuations and multiple Coulomb scattering;
- the magnetic field integral $\int B\mathrm{d}l$ along the muon track;
- the layout and the spatial resolution of the tracking chambers.

The amount of absorber material is determined by the requirements of the calorimetry and by the necessity to avoid punch-through into the muon spectrometer.

The best performance is achieved with an open superconducting magnet. The design of such a system foresees a large 'barrel' magnet which covers the central region up to $|\eta| = 1.2$ and provides a $\int B\mathrm{d}l = 3$ Tm at $\eta = 0$. The forward regions are covered by two smaller 'end-cap' toroids with $\int B\mathrm{d}l = 8$ Tm at $\eta = 2.8$.

In Section 4.2 we describe the engineering work done to date, it indicates that the superconducting magnets can be safely constructed from present state-of-the-art technology, and within realistic limits on detector volume and cost. A complete design study is being carried out. We have requested an independent review by an international expert panel in order to provide an evaluation of the engineering concept and of the cost estimates.

Should the flux of background particles under small angles exceed the pattern recognition and triggering capabilities of an open spectrometer, the end-cap magnets could be replaced by conventional warm iron toroids as described in Section 4.2.5. At the expense of reduced momentum resolution, such a system provides for additional absorption of hadrons and low-momentum muons, and can accommodate more easily a distributed layout of tracking chambers for improved pattern recognition. It would also lead to significant cost savings.

The option of a toroid magnet based entirely on conventional warm iron technology is described in Section 4.3. This magnet provides similar coverage for momentum measurement and triggering, and increased bending power ($\int B\mathrm{d}l = 4.5$ Tm at $\eta = 0$). However, the resolution of an iron spectrometer is limited by multiple scattering over most of the relevant momentum range and is inferior to the performance of the open system (Section 4.6). Furthermore, the electromagnetic background from radiative energy losses of muons imposes more stringent requirements on the tracking technology.

The layout of the tracking chambers in the spectrometer will depend on the choice of the magnet (Sections 4.2.6 and 4.3.4). For a given magnet design, the momentum resolution of the spectrometer is determined by the intrinsic resolution of the detectors, the mechanical precision of the chamber construction, and the quality of the alignment. In order to achieve adequate resolution for momenta up to 3 TeV, the chambers have to measure track coordinates in the bending plane with an overall accuracy of 100 μm or better.

We have identified three candidate technologies to build large-surface detectors of high accuracy at reasonable cost: high-pressure drift tubes, honeycomb strip chambers, and jet cell chambers. These chambers are well-matched to the comparatively low occupancies which prevail on most of the tracking surface. A great deal of attention is given to the control of systematic effects in the coordinate measurements. All three technologies allow for autocalibration of t_0 and drift velocity. We are evaluating support structures which deform by less than 100 μm and consider the use of thermally stable carbon-fibre materials. Optical alignment will monitor mechanical deformations and will thus ease the demands on stability.

Alternative chamber technologies may be required to cope with the higher rates expected at rapidities $|\eta| \gtrsim 2.5$. This kinematic region corresponds to a small fraction of the total detector surface and could be covered with small-scale variants of the same detectors with reduced cell size, or different types of chambers such as straw tubes or thin-gap cathode strip chambers. A final choice between the different technologies will be made only after a decision on the magnet.

The design of the level-1 muon trigger (Section 4.7) is based on the detection of bending angles in the toroid magnetic field, and on the principle of unambiguous bunch-crossing identification of all spectrometer data. For the technical implementation, a choice will have to be made between a dedicated stand-alone system and an integrated system derived from the tracking chambers. The potential advantage of a stand-alone system is the excellent intrinsic timing resolution which would allow for reliable bunch crossing identification with relatively simple electronics. An integrated system would require a more elaborate signal processing to achieve a similar timing accuracy.

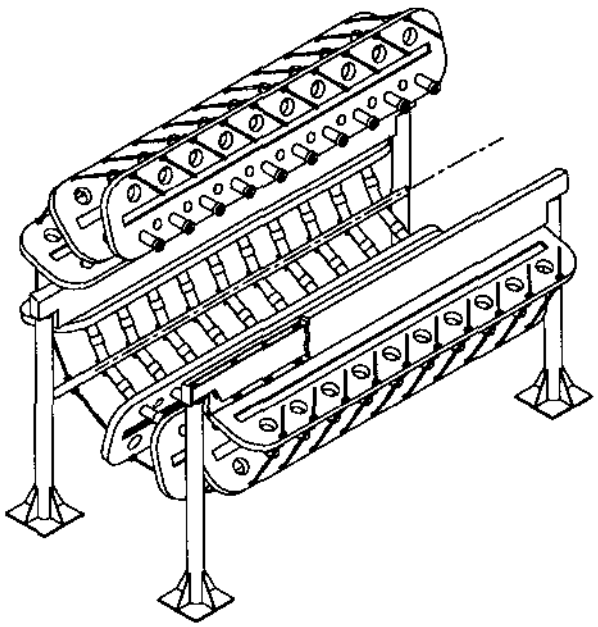

Figure 4.1: *Isometric view of the air-core barrel magnet*

4.2 Air-Core Toroid Magnet

The superconducting air-core toroid system is designed to produce a large-volume field with an open structure giving easy access for the installation of muon detectors. The barrel magnet covering the central region is described in Section 4.2.1 and the superconducting end-cap toroids which complement the barrel at large rapidity are presented in Section 4.2.3. The main parameters of the superconducting magnets are given in Table 4.1. The alternative option of conventional iron magnets for the forward region is described in Section 4.2.5.

4.2.1 Superconducting air-core barrel toroid

An isometric view of the barrel toroid is shown in Fig. 4.1. This magnet [1] consists of 12 separate superconducting coils assembled as an axially symmetrical array around the 10 m diameter calorimeter barrel. Each coil is of a flat 'race track' configuration extending over a surface area of 26 × 5 m^2. The coil is made of two single 'pancakes' wound and clamped rigidly on both sides of a cold solid plate which acts as a central web to contain the internal forces imposed on the conductor (Fig. 4.2).

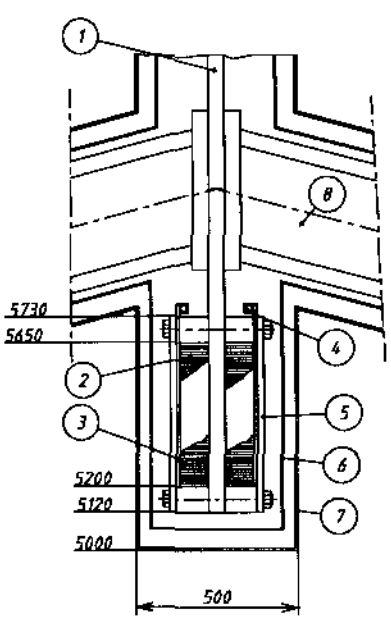

Figure 4.2: *Cross-section of the inner leg of a superconducting coil. 1: central plate; 2: single pancake of 50 turns; 3: Al cooling sheet; 4: liquid helium cooling loop; 5: clamping pieces; 6: thermal shield; 7: vacuum vessel; 8: cold strut.*

The 'pancakes' are made of 50 turns of aluminium-stabilized rectangular conductor of 90 × 8.5 mm^2 cross-section, and are epoxy impregnated in their former together with an aluminium cooling sheet which intercepts and conducts the heat load to a helium pipe running along the entire periphery of the coil. This principle of indirect cooling is particularly well suited for the proposed winding geometry and simplifies considerably the requirements on the cryogenic system.

Each coil is assembled in its own individual cryostat which consists of a stainless steel vacuum vessel made of welded panel sheets braced at regular intervals by inner spacers, the usual thermal shields and superinsulation, and internal supports and circuitry. The coils are built as independent units except for the cryogenic and electrical interconnections. Up to this stage, the coil construction can be carried out entirely by industry and the coils can be transported individually to CERN.

The magnetic forces result in a net inward radial force of 670 t on each coil. This force is carried by the structural plate of the coil and is supported by a series of 10 cold struts tied between adjacent coils. In addition, tie rods at room temperature are arranged in a similar pattern at the periphery of the magnet in order to stabilize the structure and to balance small azimuthal forces which may arise from slight asymmetries in construction or from accidentally disturbed current distributions.

The total weight of the barrel magnet is approximately 800 t. Its support system is made of two longitudinal beams tied to the two opposite lines of struts located in the horizontal midplane (Fig. 4.1). These beams extend over the full length of the magnet and rest on four pillars with the interposition of cold-to-warm transition posts. Complete mechanical analyses have been performed on the overall structure and show that stresses and deformations are kept within acceptable limits under all conditions.

Notwithstanding the large size of the individual coils, which will necessitate special tooling, the techniques of fabrication of the winding and other parts of the magnet are well within the state of the art. All coils will be individually tested before installation at normal operating current. This test will verify their electrical and cryogenic performance, whereas the mechanical behaviour of the coils can only be tested in the final field configuration.

For the assembly at the LHC site, the coils will be pre-assembled into four separate modules before they are lowered into the pit. The underground work will consist of the mechanical assembly and cryogenic closures at the four interfaces, and the interconnections with the external cryogenics and electrical supplies.

4.2.2 Magnetic characteristics of the air-core barrel toroid

The field map of the barrel magnet is shown in Fig. 4.3a. The field integral at $\eta = 0$ between the inner and outer magnet radius varies azimuthally by less than $\pm 10\%$. The presence of saturated iron in the return yoke of the solenoid does not alter significantly the field uniformity inside the volume of the air-core toroid. A consequence of the discrete distribution of currents is the presence of stray fields outside the toroid. The variation of the field strength as a function of the radius, in the absence of the return yoke of the central solenoid, is also given in Fig. 4.3b.

4.2.3 Superconducting air-core end-cap toroids

The air-core end-cap toroids [2] are designed to extend the coverage of the superconducting magnet system to $|\eta| = 3$. Like the barrel, each end-cap toroid consists of twelve coils, powered in series. The end-caps fit inside the barrel, the coils of the end-cap fitting between the coils of the barrel at the same radius. In the present design all twelve coils are contained within one large cryostat, see Fig. 4.4. This offers several advantages. The coils can be in close proximity at the inner edge of the toroid, hence the inner radius can be reduced and the rapidity coverage extended. Aside from the likelihood that one large cryostat would be cheaper than twelve separate ones, the design also allows for greater simplicity in the mechanical restraint of the large magnetic forces, in the current and cryogenic connections, and a reduction in heat losses.

The coil windings are distributed radially (Fig. 4.5) to compensate for the $1/r$ dependence of the field in a simple toroid.

The field distribution is shown in Fig. 4.6. This distributed system provides a flexible design lending itself to further optimization. The main parameters of the end-cap toroid are shown in Table 4.1. Each coil consists of a central plate of 20 mm Al alloy with 1 mm of insulation. A coil is wound onto each side of the central plate using a single length of conductor which is the 'Rutherford cable', stabilized by high purity aluminium of 50 × 6.25 mm^2 cross-section. It is wound on formers of Al alloy which remain in place after the winding and act as structural supports for the coil.

Each side of the windings is covered by another 20 mm aluminium alloy plate which provides a sound

Table 4.1: *Main parameters of the superconducting magnet system*

	Barrel magnet	End-cap magnet (per magnet)
Inner free radius of Toroid	5 m	0.5–1.1 m
Outer radius	10 m	5.87 m
Number of coils	12	12
Individual coil overall dimensions	26×5 m^2	$5.04 \times (4.47 - 4.93)$ m^2
Total Ampere-turns	$24 \cdot 10^6$ A	$11 \cdot 10^6$ A
Stored energy	$1.25 \cdot 10^9$ J	$0.21 \cdot 10^9$ J
Peak field at conductor	3.4 T	4.0 T
Net inward force per coil (barrel on)	670 t	273 t
Net inward force per coil (barrel off)	—	620 t
Conductor cross-section	90×8.5 mm^2	50×6.25 mm^2
Operating current	20 kA	20 kA
Critical current at normal operating conditions, $T = 4.5$ K	44 kA	55 kA
Total length of conductor	68 km	18 km
Total weight of conductor	140 t	14.4 t
Total weight of one coil	60 t	11 t
Refrigeration power at 4.5 K	2 kW	100 W
Cool-down time	$\leq$1 month	$\leq$1 month

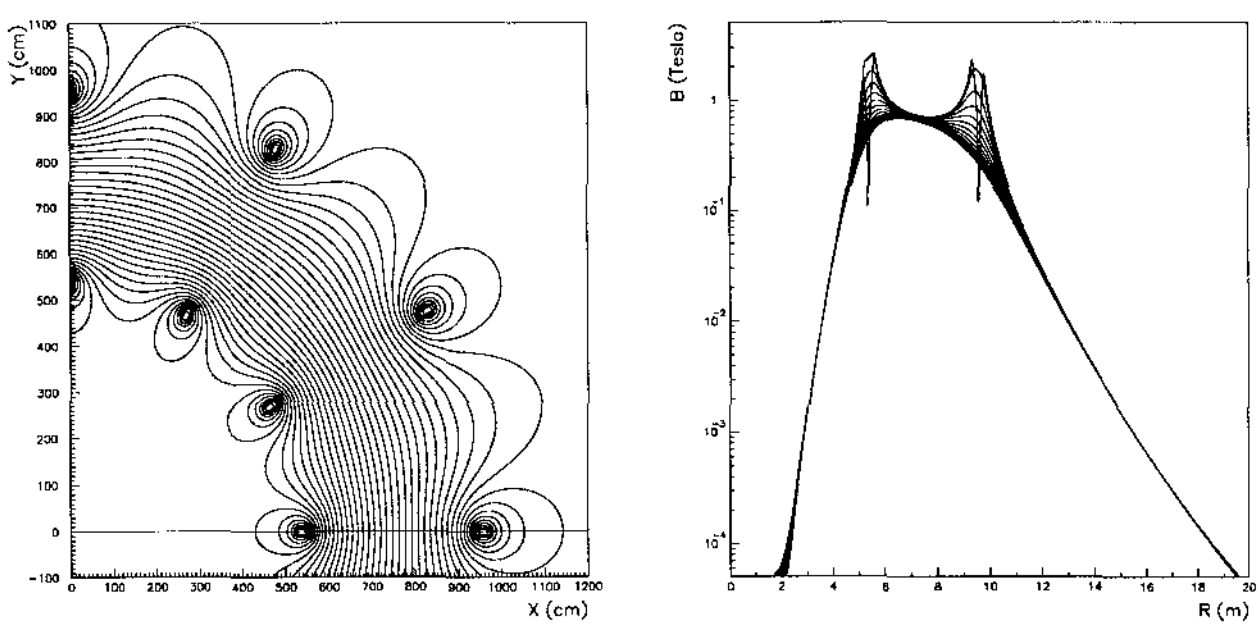

Figure 4.3: *Magnetic field characteristics of the air-core barrel magnet. Left: Field lines in the $x - y$ plane, for constant z; right: Modulus of the magnetic field B as a function of radius r, for various azimuthal angles ϕ.*

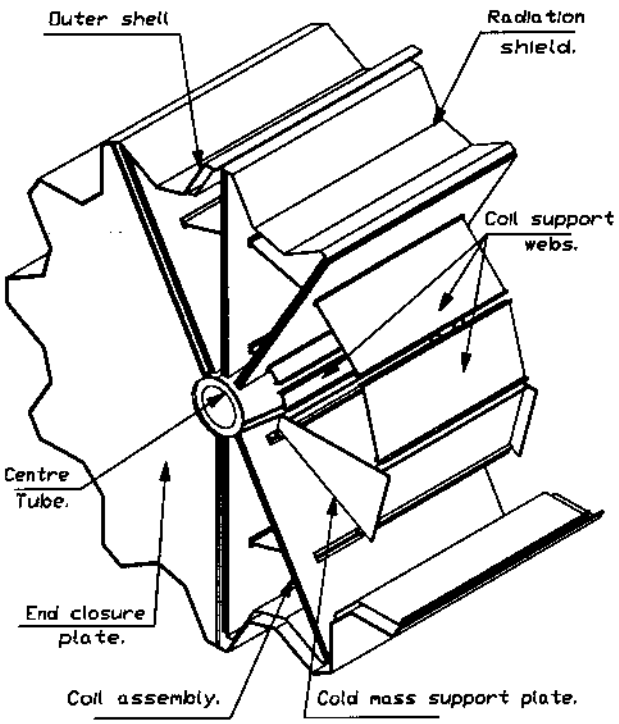

Figure 4.4: *Three-dimensional view of the air-core end-cap toroid*

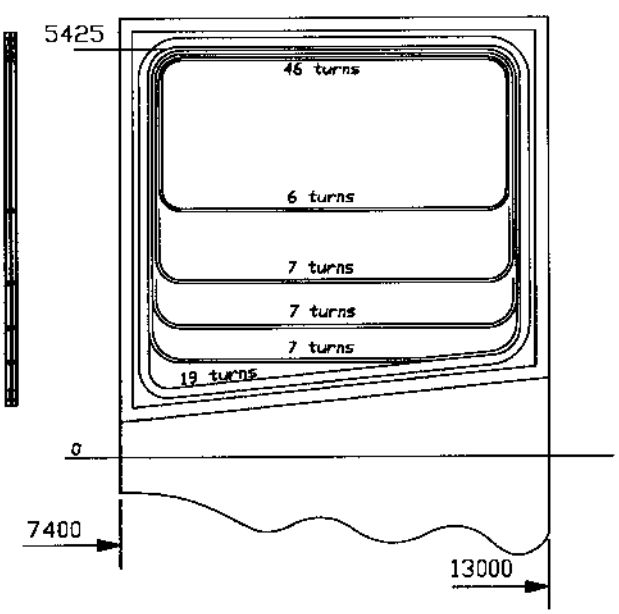

Figure 4.5: *Coil design of the air-core end-cap toroid*

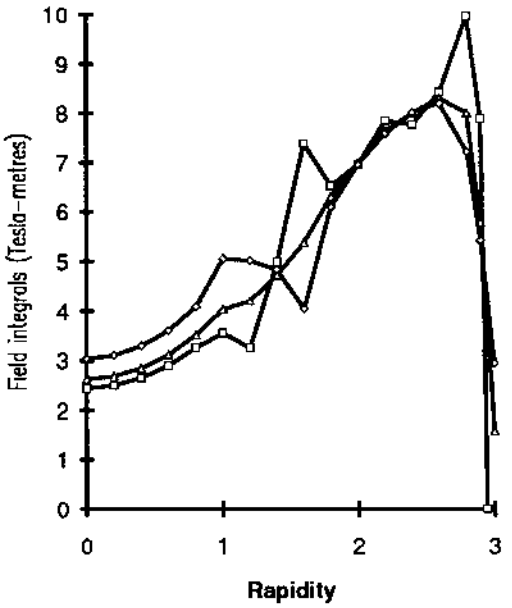

Figure 4.6: *Field integral for the combined air-core toroids as function of pseudorapidity for ϕ angles of (□) 0°, (△) 7.5°, and (◇) 15°*

and rigid double-sandwich structure and a good cooling medium. Each coil is fully impregnated and bonded. Stress analysis indicates that the magnetic forces can be transferred from the coil to the plates through the resin bond, but it is envisaged that dowels will secure the aluminium formers to the central and outer skins for greater security.

The twelve coils are mounted into a single assembly by sets of supports (Fig. 4.4). This serves to make the whole toroid assembly a self-contained rigid cold mass, able to withstand internally the net inward magnetic forces. Only the weight of the cold mass (130 t) needs to be transferred to the outer cryostat. This is achieved by using insulating supports in the central horizontal plane of the toroid, which also ensure that the cold mass remains centred within the cryostat during cool-down. Additional insulated constraints will maintain this central position when the coils are powered.

The design of the cryostat is complicated by the need for a crenellated outer cylinder to let the end-cap coils fit between those of the barrel. It will be prefabricated in industry in large pieces and welded together in the surface building above the experiment. The coils themselves will be manufactured in industry and assembled into a toroid in the same surface building, then inserted into the cryostat and fully tested

prior to installation in the experiment as a complete unit.

4.2.4 Cryogenics

The refrigeration system, common to the barrel and end-cap toroids, is based on a conventional helium refrigerator with a capacity of 2 kW at 4.5 K and 20 kW at 75 K, the latter cooling the thermal shields. At this rating, the refrigerator will be able to cool-down all magnets (700 t cold mass) in one month and will produce liquid helium in steady-state operation as a primary coolant for the heat exchanger of the force-flow system supplying the magnet cooling loops. The 24 cooling loops of the barrel magnet can be fed in parallel by a single pump delivering 72 g/s of helium with a pressure drop of 4 kPa. All possible phases of operation, including quench, have been analysed and will be monitored with a control process by proper valve arrangements. A connection to the general refrigeration sytem of the LHC machine could possibly lead to a significant reduction of the cost of the system together with a shortening of the cool-down time.

4.2.5 Conventional iron end-cap magnets

The preferred solution for a system of conventional forward magnets is an arrangement of twin end-caps which make it possible to place a tracking chamber in between the inner and outer modules. The modules are installed on rollers on the rail system described in Chapter 6 and can be retracted in the beam direction.

Each end-cap module has a length of 2 m in the z direction and weighs $\sim$ 1000 t. It consists of 12 azimuthal sectors, each one equipped with a conventional aluminium coil of about 200 cm^2 cross-section. The weight of one sector is $\sim$ 85 t. In the axial direction, it is made of 9 iron plates of 20 cm thickness each, interleaved with $\sim$ 3 cm thick spacers. The free space between the iron plates allows for the installation of e.g. plastic streamer tubes to detect energy loss from electromagnetic radiation and to help in pattern recognition.

Each module would be pre-assembled on the surface either in two halves and then lowered into the underground area using the 2 x 250 t cranes, or lowered as a single unit by the heavy-load crane (Chapter 6).

The main parameters of the iron-core end-caps are summarized in Table 4.2. If rolled low-carbon steel is used, a current of 276 kAt is required to reach a magnetic field of 1.8 T at a median radius $R_m = 2.9$ m. This contains a contingency of 50% to take into account a possible degrading of the magnetic qualities of the iron due to weldings, different production charges, and possible air gaps. The necessary At can be obtained using conventional aluminium coils of 24 turns each with a water-cooled conductor of 24 x 24 mm^2 cross-section. All coils of one module are powered in series. The small cross-section of the conductor and the approximate size of 4 x 2 m^2 of the coils allow for a production without technological risk.

The field shape in the end-caps has been calculated with the POISSON program. In the azimuthal centre of a sector, it varies radially from 1.97 T at the inner radius of 1 m to 1.73 T at the outside.

Table 4.2: *Parameters of the iron-toroid end-caps (per end-cap)*

Median field	1.8 T
Operating current	960 A
Ampere-turns	2 x 276 kAt
Dissipated power	2 x 200 kW
Stored energy	2 x 2 MJ
Iron weight	2040 t
Conductor weight	13 t

4.2.6 Layout of muon chambers in the air-core magnet system

With the superconducting spectrometer magnet, a muon track is always measured in three 'points'. In the barrel, one point is in front, one behind, and one in the middle of the magnetic field region, the momentum being determined by a sagitta measurement. In the end-caps, one point lies in front, and two lie behind the magnet, the momentum being determined by a point-angle measurement. In practice, each 'point' is represented by a number of chamber layers, forming a superlayer, thus providing a direction in addition to the coordinate.

The arrangement of the chambers in the barrel follows the 12-fold symmetry of the magnet. In Fig. 4.7, the largest chambers appear on the periphery of the magnet where they span the distance of 5.5 m between the cryostats of neighbouring coils; in the beam direction they measure 2 m. The chambers in the middle of the toroidal field region measure 3.7 x 2 m^2 and the inner chambers 2.2 x 2 m^2.

Special attention is given to the problem of insensitive regions between neighbouring chambers. In the barrel, cracks in θ are avoided by staggering the ends of the different layers in each chamber. In ϕ, the dead region between neighbouring chambers is covered by overlapping smaller chambers wherever possible. In

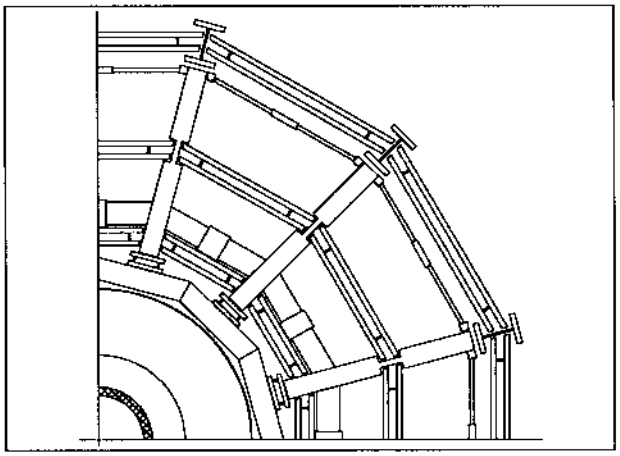

Figure 4.7: *Transverse view of a possible chamber layout in the air-core barrel toroid*

the centre of the field region, the cryostats of the individual coils cause a dead zone of 25 cm, corresponding to 7% of the azimuth. There, the sagitta measurement is replaced by a point-angle measurement using the pair of outer chambers that cover this region of ϕ, decreasing the momentum accuracy by a factor of ~ 2.5.

The chambers of the end-cap spectrometers are installed vertically extending to a radius of ~ 5 m, see Fig. 1.1. They are mounted on the end-cap toroids and move with the toroids in case these are retracted. At larger radii, in the η range where barrel and end-caps overlap, the vertical chambers are fixed to the barrel toroid structure.

4.3 Iron-Core Toroid Magnet

The iron toroid system has been designed as a conventional magnet for the muon spectrometer which can be built and operated at low risk. The proposed construction of this magnet is based on established manufacturing processes which are readily available in European industry. In particular, the handling of the iron plates and the welding methods have been optimized to reduce the cost of manufacturing and assembly. The coils are designed to operate at $\leq$48 V against ground requiring no special insulation.

4.3.1 General layout

The iron structure comprises an octogonal central 'barrel' and two large mobile 'end-caps' as shown in Fig. 1.2. The length of the barrel is chosen to correspond to the total length of the calorimeter section. This has the advantage that the end-cap toroids become totally independent of the central part and that their rail and roller system will not interfere with the active volume of the detector. The end-caps are subdivided into an outer and an inner part, each with its own coil, see Fig. 4.8. The outer part has the same transverse cross-section as the barrel magnet. The main parameters of the magnet are given in Table 4.3.

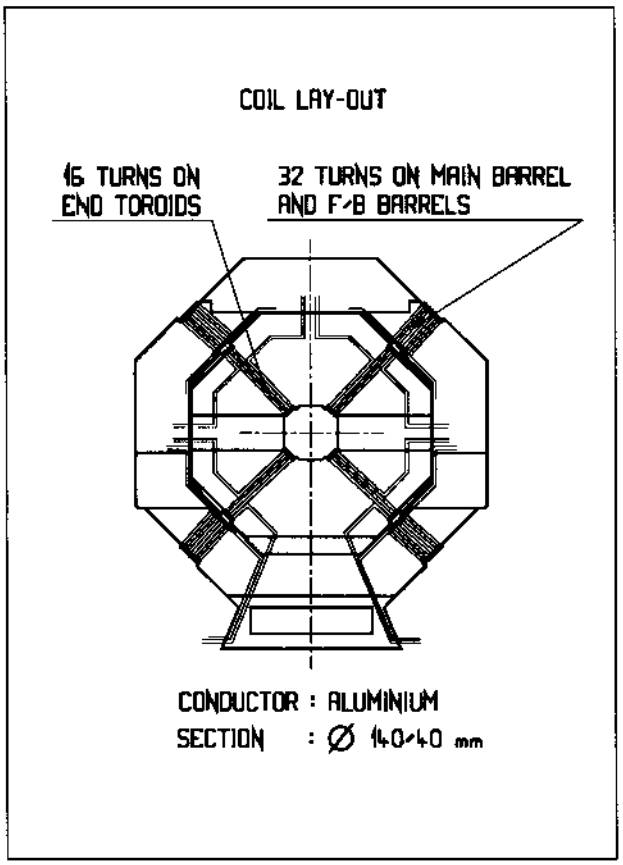

Figure 4.8: *Layout of the coil arrangement of the iron-core toroid; here the end-cap is shown*

It is essential that the end-cap toroids can be easily retracted from the central part for access to the calorimeter and the inner detector. Each end-cap toroid is therefore placed on a roller system and moved horizontally by a hydraulic push-pull traction system. Between the rollers and the load, hydraulic bearing pads will be installed for vertical adjustment. They also provide a possibility to compensate for possible imperfections in the assembly and for small deformations in the foundation. This system can be actively monitored such that each roller unit carries the same load and that the end toroids are correctly aligned after each movement [3].

Table 4.3: *Main parameters of the iron-core magnet system (96% iron filling factor); the figures for the end-caps comprise both sides*

	Barrel	End-cap outer parts	End-cap inner parts	Bus-bars and supports	Total
Turns	32	128	64	—	
Current (kA)	19	19	19	—	
Ampere-turns (MAt)	0.608	2.43	1.21	—	
Dissipated power (MW)	1.1	1.3	1.1	0.2	3.7
Iron weight (t)	12600	6500	5500	1800	26400
Conductor weight (t)	50	60	50	12	172

4.3.2 Magnetic field calculations

Two-dimensional field calculations of the iron toroids have been made with the POISSON program. Assuming the characteristics of normal low-carbon construction steel, 0.608 MAt are required to produce a field of 1.8 T at the 45.4 m long medium line of the barrel. This includes an estimated compensation of $\sim$ 45% for air gaps between the iron plates, permeability degradation in the welded joints, and a possible downgrading of the magnetic quality of the iron. For the outer parts of the end-caps, the same coil arrangement as for the barrel can be used. For the inner end-cap parts, the length of the medium line is 21.6 m and 0.304 MAt are necessary to achieve the same field conditions as in the barrel.

A study [4] of the assembly procedure of the iron and coils has shown that the best location of the coils is in a cut-out in the iron, centred on the 45° symmetry axis. Figure 4.8 shows the details of this arrangement. Field calculations show that in the vicinity of the coils (along the $\phi = 45°$ line) the induction increases to 2.2 T. In the corners of the octagon ($\phi = 22.5°$) the field varies between 1.7 and 1.9 T. The $1/r$ component of the induction is very small ($\sim$ 1%) since the iron is not highly saturated. The fringe field in the muon chamber region varies between 90 and 120 G at the 0° position and between 180 and 600 G at the 45°position.

In order to simplify the construction, the coils and design currents are identical in the barrel and in the end-caps. This arrangement reduces the induction in the outer part of the end-caps to an extent which depends on the relative polarities of the coils in the inner and outer iron toroids. Figure 4.9 shows the radial dependence of the field in the end-cap toroids for the same polarity in the two sets of coils.

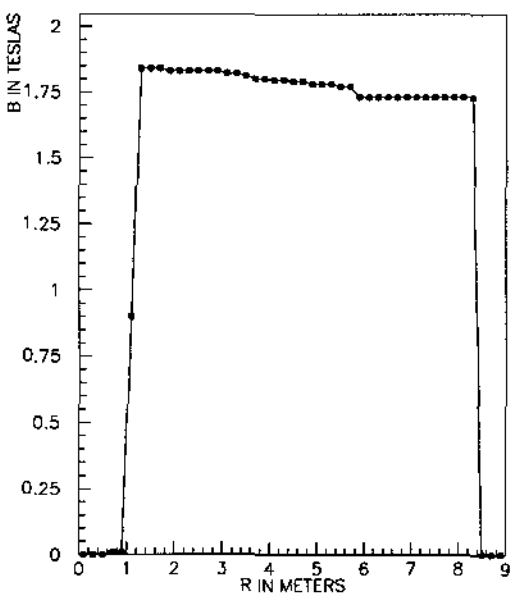

Figure 4.9: *Radial field variation in the iron-core end-cap toroids at $\phi = 0°$ (along the medium plane)*

4.3.3 Design, manufacturing and assembly

The magnet is constructed from 10 cm thick iron plates. Flatness tolerances and production capabilities of European steel mills impose a practical limit of 3.5×5.0 m^2 on the size of individual plates. Flatness tolerances also limit the iron filling factor to 0.96. In order to reduce the assembly work at CERN, plates will be welded together into larger units, the size of which is limited by transport restrictions to 4.1×15.0 m^2.

At CERN the plate units will be assembled into 'blocks' of 500 t maximum weight. The barrel part is divided into six blocks and a separate support structure. The inner and outer part of the end toroids

are also divided into six blocks each. The symmetry of the magnet limits the number of different block geometries to eight (Fig. 4.10).

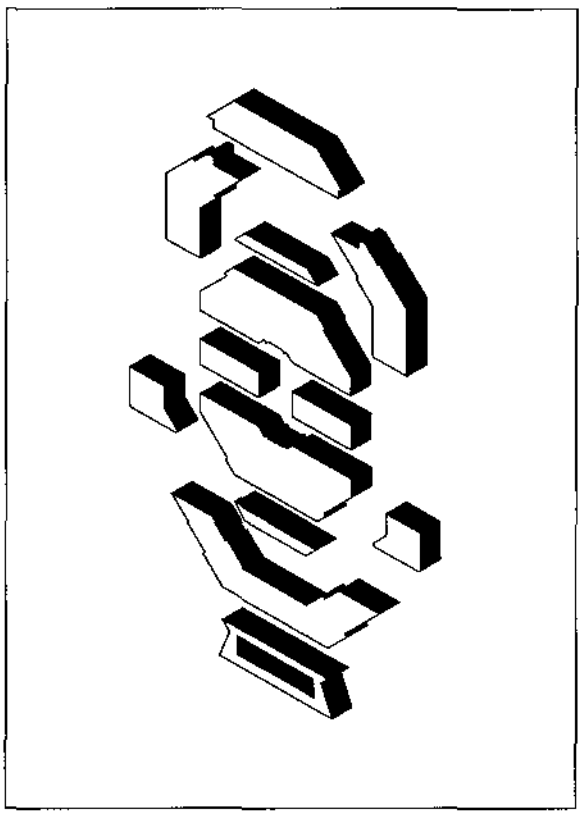

Figure 4.10: *Exploded view of the iron block structure of the end-cap magnet*

The surfaces of the end blocks will probably have to be machined in order to stay within the geometrical tolerances in the axial direction. However, the amount of machining will depend on the initial quality and tolerances of the plates. The gap surfaces between the blocks must be machined in order to allow for a maximum magnetic contact. The mechanical stability of the blocks will be ensured with bolts or welding joints between the plates.

Despite the large weight of the magnet structure, calculations show a very moderate stress situation in the final magnet assembly. The central barrel section will undergo a maximum movement under its own weight of 0.15 mm. The maximum stress value in the magnetized part will not exceed 9 MPa. The highest stress value will occur in the support for the end toroids, where the shape will be adapted to maximize the muon chamber coverage. The calculated peak stress will not exceed 30 MPa.

The coil is made from standard aluminium tube

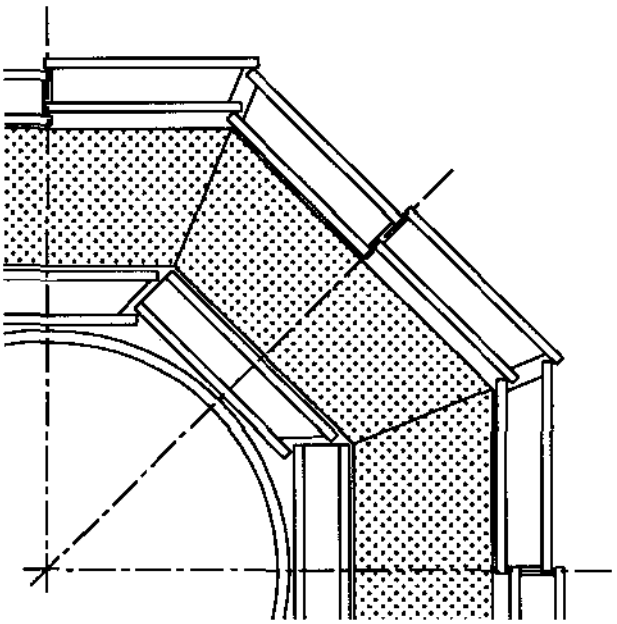

Figure 4.11: *Cross-section through the barrel of the iron-core toroid showing the arrangement of the chamber supermodules*

with an outer (inner) diameter of 140 (40) mm. Because of the low stress, the basic material has a very low specific electrical resistance. The block structure is designed to permit a convenient installation of the coil. The coil elements are prefabricated on the surface and installed in parallel with the blocks. Special 'filler' plates compensate for the difference in radial thickness.

4.3.4 Layout of muon chambers in the iron-core magnet system

In the barrel, the momentum measurement is obtained from the difference in angle between the muon tracks before and after the toroid magnet. For this purpose, two superlayers of tracking chambers are combined with an appropriate support structure into 'supermodules' to provide a lever arm of 80 (100) cm at the inside (outside) of the barrel toroid. The supermodules have a typical surface of 4 m^2 and are staggered to provide adequate overlap as shown conceptually in Fig. 4.11. An isometric view of a supermodule is presented in Fig. 4.12.

The end-caps are equipped with three supermodules in the front, the middle, and behind the toroid. The front and middle supermodules have only a small lever arm and provide a highly redundant point measurement, whereas the last supermodule with 1 m

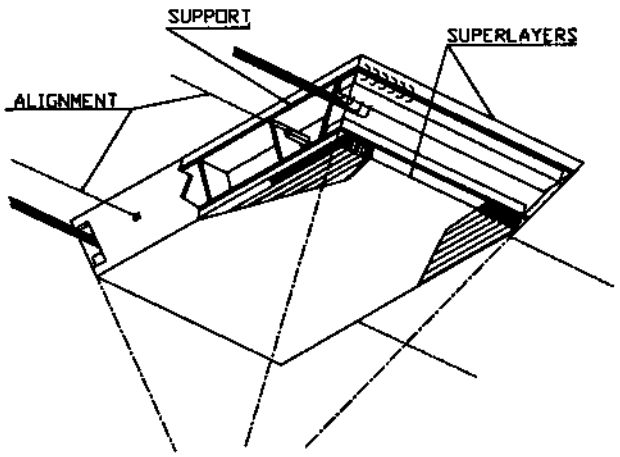

Figure 4.12: *Isometric view of a supermodule with superlayers on both sides of the support structure*

lever arm allows for an angle measurement. The momentum is thus determined from a combined sagitta and angle measurement. In the case where leakage of particles corrupts the measurement in the front supermodule, the momentum can still be obtained from a point-angle measurement in the second and third supermodules.

4.4 Tracking Systems

The tracking chambers provide a coordinate measurement in the bending plane with a resolution of 100 μm or better per superlayer. Adequate redundancy is necessary to achieve robust pattern recognition; tracking behind massive absorbers (e.g. the calorimeter or the iron toroid) requires good two-track separation such that the muon can be reconstructed inside the electromagnetic debris frequently accompanying energetic muons.

In addition to the precision measurement, coarse information on the orthogonal ($r\phi$) direction is needed to help in the pattern recognition and to permit the reconstruction of e.g. high-p_T Z particles. The latter condition imposes a spatial resolution of $\sigma_{r\phi} \simeq 4$ cm. This can be obtained as a by-product from the precision drift chambers or from the stand-alone trigger system.

At present, three tracking technologies are being pursued in all of which the precision measurement is based on drift time determination as described in Sections 4.4.1 to 4.4.3. The final choice will be made after further prototype studies and after the selection of the muon spectrometer magnet.

4.4.1 High-Pressure Drift Tubes (HPDT)

The basic element of coordinate measurement with the HPDT system is a cylindrical tube of 2–3 cm diameter, containing drift gas at a pressure of 2–3 bar. Single wire accuracies well below 100 μm have been achieved with this type of detector [5]. The tube

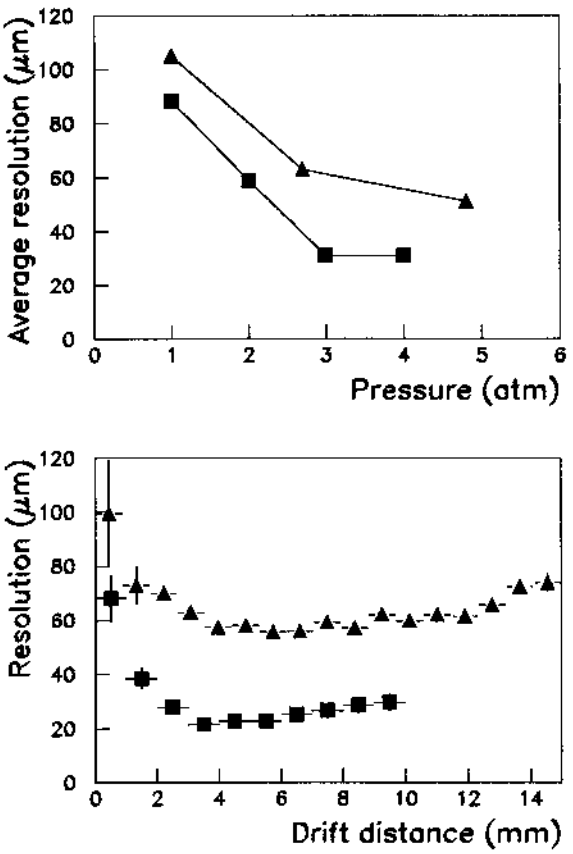

Figure 4.13: *Spatial resolution of high-pressure drift tubes as measured in a muon beam, as a function of (top) gas pressure and (bottom) drift distance for 3 atm pressure: (▲) Ar/C_2H_6 = 70/30, tube diameter D = 30 mm, wire diameter d = 100 μm; (■) $Ar/CO_2/CH_4$ = 45/45/10, D = 20 mm, d = 50 μm*

diameter, the gas mixture and the pressure are being optimized to find a compromise between spatial resolution and occupancy, and may vary as a function of pseudorapidity. Figure 4.13 shows the measured r.m.s. accuracy of two prototypes operating in streamer mode as functions of pressure and drift distance.

The tubes are glued together in flat layers, with three layers arranged in one superlayer. A pair of superlayers is held together by a support structure which separates them by 40 cm (Fig. 4.14). The two

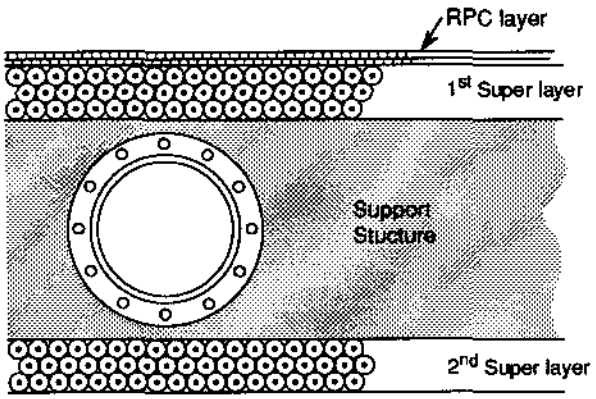

Figure 4.14: *Layout of a 'mattress' of high-pressure drift tubes*

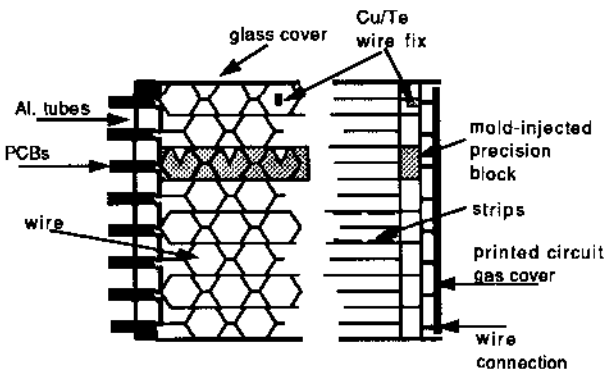

Figure 4.15: *Cross-sections of the Honeycomb Strip Chamber. The left- and right-hand part of the figure are views perpendicular to the wires and to the strips, respectively.*

superlayers and the enclosed structure form a self-supporting unit which is called a 'mattress'. A muon traversing a mattress is thus measured as a vector in up to six points. The overall accuracy, including alignment (Section 4.5), of each superlayer will be $\pm 100\,\mu$m. The track direction will thus be measured to better than ± 0.4 mrad in each mattress to facilitate the pattern recognition. In each superlayer, the three drift times measured for each track allow for a local determination of the drift t_0 and of the bunch crossing time. This information will be used in the level-2 and possibly also in the level-1 trigger.

The size of the mattresses varies according to their radial position in the magnet. All tubes are oriented quasi-parallel to the magnetic field lines of the toroid to measure the coordinate of the track in the bending plane. The coordinate in the $r-\phi$ plane, which has to be known to an accuracy of a few cm, is measured from pick-up electrodes attached to the resistive plate chambers used for triggering. A system of strips orthogonal to the trigger strips will record the $r\phi$ coordinate of muon tracks.

4.4.2 Honeycomb Strip Chambers (HSC)

The HSC consists of a stack of hexagonal drift tubes as shown in Fig. 4.15. The tubes are made from folded polyester foil with a thin copper layer at the inside. Two folded foils are combined in a template and form a layer of hexagonal cells. A glued stack of these layers is a light, rigid and self-supporting block of honeycomb. In each hexagonal cell the sense wire is fixed by means of slotted small copper blocks which, in turn, are positioned by injection-moulded plastic precision blocks. These pieces form an integral part of a layer of cells; they are glued together with the foil at the edge in the template. The chamber is covered by thin plates made of glass, fibreglass or steel to provide for stiffness and to reduce the thermal expansion. By means of a printing and etching process, the conductive layer on the foil is segmented in parallel strips. This allows for a measurement of the second coordinate of the muon track [6].

Figure 4.16 shows the spatial resolution of the drift coordinate of one cell, measured in a prototype with cosmic rays. The resolution is expected to worsen only slightly in strong magnetic fields if a gas with a low Lorentz angle, such as Ar/CO_2, can be used. If small mechanical tolerances are realized and also other sources of systematic errors are small or can be corrected for, an average spatial resolution better than 100 μm per monolayer could be obtained. Because of the poor resolution near the wire, the average resolution would improve with an increased cell size. The maximum drift time is, however, proportional to the square of the radius. This limits the radius because of the expected counting rate and track multiplicity. The optimal cell radius will therefore decrease with pseudorapidity.

After the track reconstruction, the time resolution, being roughly proportional to the spatial resolution and inverse proportional to the local drift velocity, has a value of $\sim$ 10 ns for an Ar/CO_2 mixture of 50/50. A good time resolution is particularly relevant when the HSC is equipped with an integrated level-1 trigger, which is possible due to the staggered layout of the cells. The staggering also provides the possibility of autocalibration of the t_0 and of the drift velocity which is crucial to limit systematic errors.

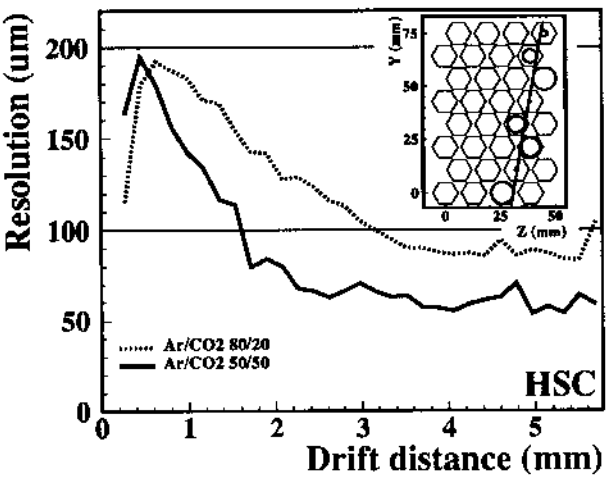

Figure 4.16: *Measured spatial resolution of the drift coordinate as a function of the distance between the track and the wire, for two different gas mixtures*

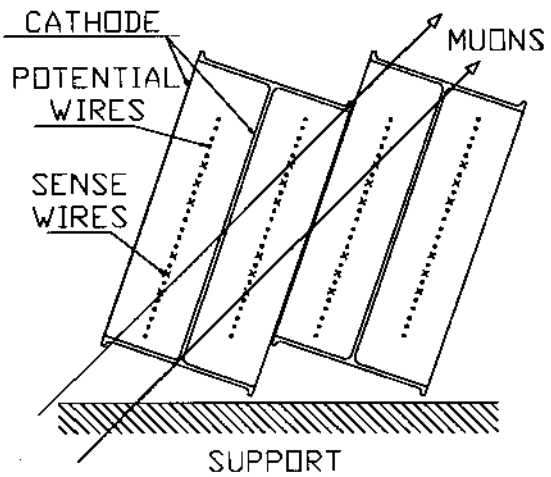

Figure 4.17: *Conceptual layout of one of the jet-cell geometries; the cells are arranged such that muons are measured with at least five out six wires in each superlayer*

4.4.3 Jet Cell Chambers (JCC)

Several types of jet-type multi-wire drift chamber systems have been studied, mostly for use in combination with an iron-core magnet. In a projective geometry like the one proposed in [7], the cells are oriented in such a way that infinite momentum tracks from the interaction point run parallel to the anode wire planes. In another design shown in Fig. 4.17, the anode wire planes are tilted by a constant angle with respect to the direction of infinite momentum tracks [8].

An I-shaped profile made from extruded aluminium provides a mechanical support for two cells and moulded plastic spacers are used to define the wire position. The sides are covered with aluminized Mylar acting as cathode planes. The cells are fixed to a support structure with precision pins.

In the tilted cell option, the chambers are self-calibrating. High-momentum tracks do not give rise to left-right ambiguities. The inclined track geometry also guarantees a large number of measurements in a good drift geometry away from cathode or anode planes. The non-tilted option can be advantageous when two layers of cells are staggered by half a cell width [9].

The maximum drift distance will be determined mainly as a compromise between total number of readout channels, occupancy, and the maximum drift time acceptable in view of the trigger decision time. For a cell width of ± 2 cm, the total number of anode wires will be of the order of 190 000.

A spatial resolution better than 200 μm can be achieved using a non-flammable gas at atomospheric pressure. A possible choice is a mixture of $Ar/CF_4/CO_2$ which has a fast drift velocity and good saturation properties [8]. A study with the GARFIELD program has shown that a double-track resolution of $\sim$ 2–3 mm can be expected. The second coordinate can be measured by a time difference or charge division method with an accuracy of $\sim$ 10 cm per monolayer.

The jet cell chamber system can incorporate a readout to detect high p_T muon tracks for a level-1 trigger decision. Another method utilizes the drift time information within an outer superlayer. Because of the simple configuration of anode wires, the differences between the individual drift times are directly related to the p_T of the track. This provides an adjustable threshold for high p_T tracks. Identification of the bunch-crossing time is possible by using the sum of the drift times in a pair of staggered cells [9]. In the case of the tilted jet cell, hits near the crossing point with the wire plane can be used for the identification. The standard method of triggering using a dedicated additional detector is described in Section 4.7.

4.4.4 Signal processing

The principal function of the muon chamber readout system will be the measurement of drift times with an accuracy of about 1 ns. We present here the con-

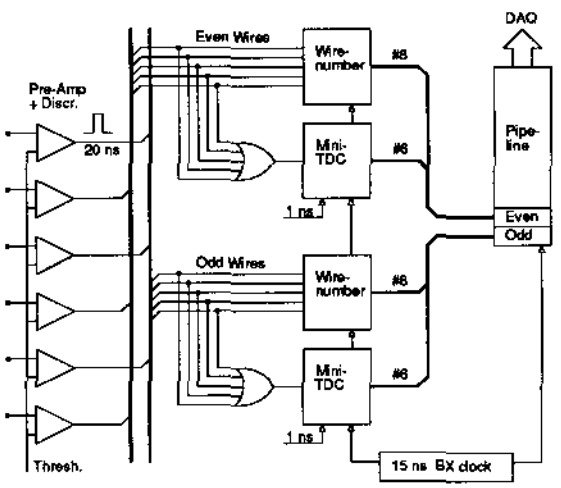

Figure 4.18: *Schematic circuit diagram of wire readout electronics*

cept of a multiplexed digital readout system which we have studied in detail for the HSC option. This or similar concepts can also be adapted to the other two chamber options.

The block diagram of the wire readout is shown in Fig. 4.18. Each wire will be equipped with a preamplifier and discriminator. The discriminator has a one-shot digital output of $\sim$ 20 ns. Preamplifiers, discriminator and one-shot will be grouped in multichannel ASICs.

The leading edge of the discriminator output signal starts a nanosecond counter which is stopped by the leading edge of the BX clock. The mini-TDC thus produces a 'time stamp' for the wire signal relative to the phase of the main clock. Since the occupancy of individual wires is very low, the discriminator outputs from a large number of wires can be 'OR'ed to be served by one mini-TDC. Synchronous with the BX clock, time stamp and wire number are written into the digital pipeline. The rare cases where two or more wires sharing the same mini-TDC have simultaneous hits within 15 to 30 ns are flagged by means of a warning bit.

The pipeline has a capacity of one hit every 15 ns. For the expected occupancies, this is amply sufficient to multiplex typically 256 wires of a monolayer. To cope with muon tracks accompanied by electromagnetic showers, odd and even wires are treated separately, i.e. there will be at least two mini-TDCs per monolayer. The two mini-TDC data streams share the same pipeline by means of interleaving. More refined segmentation and interleaving schemes can be implemented at the expense of additional mini-TDCs. Using this multiplexing scheme, multi-hit capability is shared by all wires served by the same mini-TDC. On the basis of more detailed rate calculations, the option of using a single pipeline for all monolayers in superlayers with low occupancies will also be investigated.

All electronics up to the pipeline is expected to be installed directly on the chambers.

Since all operations are synchronized by the BX clock, the absolute timing of the wire signal can be reconstructed at the exit of the pipeline where the data appear at the pace of one word every 15 ns. The DAQ treats the data according to the level-1 trigger decision: only when a specific BX has resulted in a level-1 trigger does the corresponding data need to be stored for further processing. In this process, the DAQ appends an absolute time stamp identifying the phase of the pipeline.

It should be noted that, except for the pipeline, all of the techniques mentioned above (multiplexing, mini-TDCs etc.) are currently being applied in a test of a large-scale HSC prototype which will start to take data in fall 1992 in the framework of the RD5 project.

Another possibility is offered by the 'Time Memory Cell' (TMC) [10]. This ASIC records digital signals in 1 ns or 2 ns intervals and can be adapted to the mini-TDC and pipeline (Fig. 4.18). It can also be used for the readout of the muon chambers without multiplexing, which may be appropriate e.g. for the chambers at large rapidity.

4.5 Chamber Alignment

Two concepts of chamber alignment have been studied and are retained as possible options until a choice can be made for the magnet. Both rely on optical techniques and are designed for the internal chamber aligment only, i.e. they do not provide alignment relative to the rest of the apparatus. The first method uses light rays oriented radially and pointing to the interaction point ('projective method') [11]; the second method is designed for use with the iron-core magnet and uses light rays running parallel to the beam axis and parallel to the iron surfaces ('parallel method'). In both cases, each muon chamber is assumed to be a stable unit which preserves the accurate internal geometry that has been built into it.

For the alignment we distinguish two domains of precision. To measure the bending of a high-momentum muon in the magnetic field, the highest possible accuracy is required on the relative position of all chambers hit by the same muon track; such

chambers will have to be aligned to a relative accuracy of 50 μm. Less severe are the tolerances in the relative positions of chambers not belonging to the same projective element of the muon spectrometer where an accuracy of ~1 mm is estimated to be adequate.

For the projective method, chambers of successive layers contributing to the measurement of one muon are arranged in a projective geometry such that their corners lie on radial lines pointing to the centre of the interaction region (Fig. 4.19). These lines are

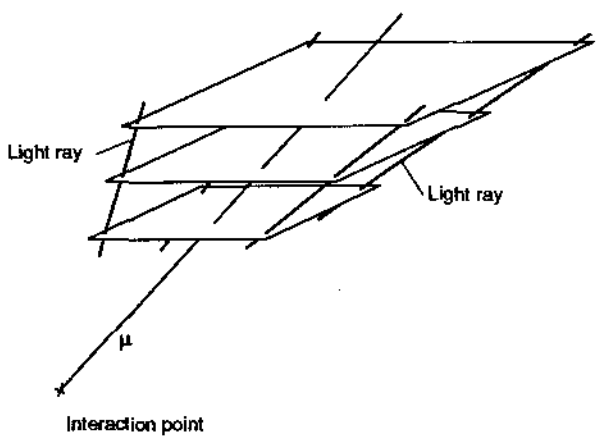

Figure 4.19: *Principle of the projective alignment system*

represented by light-rays simulating infinite momentum tracks. The corners of the chambers carry optical elements measuring the deviation of their actual position from their nominal position on the radial lines. The measured points along the track of a high-momentum muon fall somewhere into the area of each chamber, between its four corners; corrections for these muon points will be derived by linear interpolation between the measured deviations of the corner positions. All linear transformations of the chamber geometry arising from a thermal expansion or from small displacements or rotations in space are automatically corrected by this method.

In one technical implementation, transparent optical detectors are being designed which are similar to silicon strip track detectors; photo currents are produced in 0.3 mm wide strips, thus allowing the position of a laser ray with a diameter of 3 mm to be determined with an accuracy of better than 20 μm. The laser wave-length will be in the infrared where the silicon detectors become transparent.

Another option is the RASNIK system, which is used in the L3 experiment for the alignment of three superlayers [12]. This system could be extended to the alignment of four or more superlayers. The three-station RASNIK focuses a light source with the help of a lens onto a quadrant diode and can detect deviations from straightness with 20 μm precision. The projective alignment method requires unobstructed light paths pointing towards the interaction point; a large number of holes would have to be implemented in the iron-core magnet.

The parallel method is best adapted to an angle-angle momentum measurement in the iron-core magnet. This method foresees axial beams along the full length of the toroid, which guarantee that the chambers inside and outside the iron are parallel to each other; this can be done with an accuracy better than 100 μrad, owing to the large lever arms involved. There are various ways in which this method can be implemented, including half-transparent mirrors for the exact positioning of the light beams, and either quadrant diodes or transparent optical elements for the position measurement.

Finally, particle tracks can also be used for the alignment of the chambers, provided one knows their momenta. This is the case for muons from the decay $Z \rightarrow \mu\mu$, because the Z mass is very well known and their transverse momentum distribution is limited [13]. This method of alignment is particularly important for the determination of the position of the other tracking detectors relative to the muon chambers.

4.6 Momentum Resolution

For both magnet systems, it is assumed that each measurement station consists of two superlayers providing two measurement points (i.e. a vector) per track, with an overall accuracy of 100 μm per point in the direction perpendicular to the wires. The effect of spurious hits from accompanying electromagnetic showers is under study and is not included in the present calculations.

In the air-core toroid, there are three such stations with an average distance of 40 cm between the two superlayers (Section 4.2.6). The momentum determination relies on a sagitta measurement in the barrel and on a point-angle measurement in the end-caps; the corresponding transverse momentum resolution is shown in Fig. 4.20. The accuracy at small momenta is limited by fluctuations of energy loss in the calorimeters and by multiple scattering. In the area of the barrel cryostats which corresponds to ~ 7% of the full azimuth, the measurement relies on a point-angle method and the accuracy at high momentum

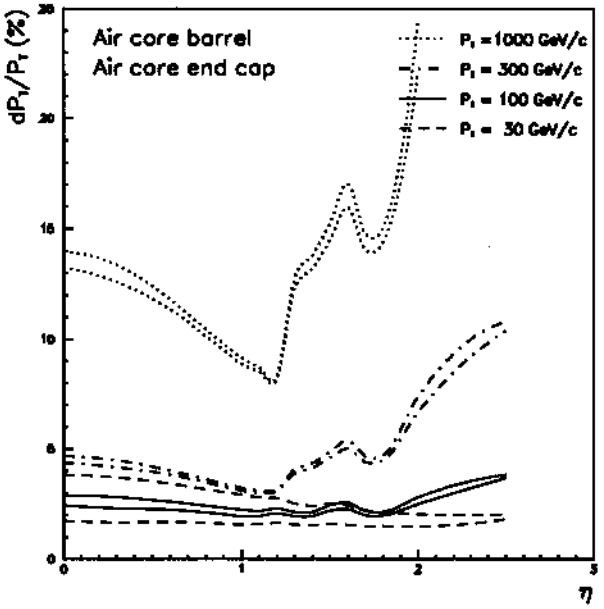

Figure 4.20: *Transverse momentum resolution in the air toroid system, as a function of pseudorapidity. For each p_T, the upper curve shows the resolution of the stand-alone measurement. The resolution shown by the lower curve is obtained when the inner detector is included in the measurement.*

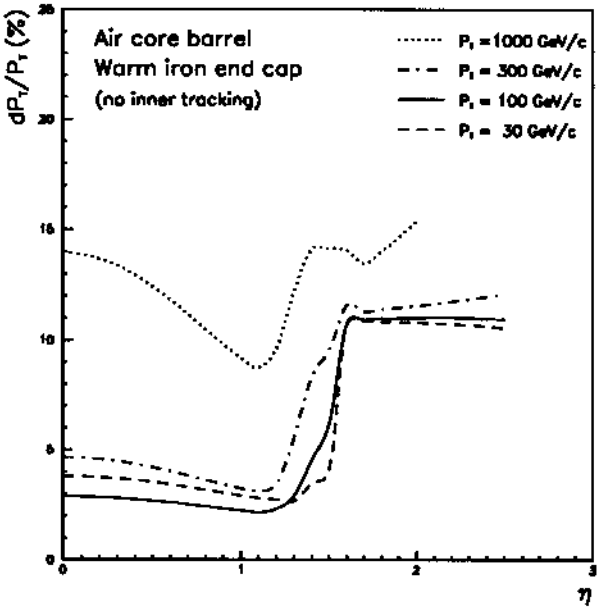

Figure 4.21: *Transverse momentum resolution in the air-core barrel combined with conventional iron end-cap magnets, in stand-alone mode. The resolution in combination with the inner tracking can be read from Fig. 4.20 for small η; at large η, it is very similar to the one shown in Fig. 4.22.*

deteriorates by a factor ~2.5. With the small iron end-caps inserted in the air-core barrel, the number of stations can increase to four and the momentum would be determined from a combined sagitta and angle measurement. The momentum resolution of this configuration is shown in Fig. 4.21 for the stand-alone mode. In all cases, the local vector measurement in each station improves the resolution and the pattern recognition.

With the iron-core toroid magnet, two stations with a larger distance between superlayers (Section 4.3.4) will be used for the barrel to determine the momentum from an angle-angle measurement, and three stations for a sagitta measurement in the end-caps. The transverse momentum resolution of this magnet is shown in Fig. 4.22. Here, the resolution is multiple-scattering limited up to energies of about 500 GeV.

At high momenta, the accuracy can be significantly improved by including a measurement of the z coordinate with a resolution of $\sigma_z \simeq 300$ μm as e.g. achieved in the preshower detector of the liquid argon calorimeter (Chapter 2).

Figures 4.20 and 4.22 also show the resolution when the inner tracking is used in combination with the stand-alone measurement in the muon spectrometer. With the air-core toroid, the improvement is only significant at very low momentum. For the iron toroids, the inner detector resolution is superior for momenta below 400 GeV.

4.7 Muon Trigger

4.7.1 Muon rates

To estimate the rate of charged particles penetrating into the muon detector, we have considered the following processes:

1. decays of pions and kaons in the inner tracking volume ('decays'),
2. decay muons from hadronic showers and hadron leakage from the calorimeter system ('punch-through'),
3. heavy-quark decays: $pp \rightarrow t\bar{t}, b\bar{b}, c\bar{c} + X$
4. vector boson decays: $pp \rightarrow W, Z + X$
5. Drell-Yan pairs: $pp \rightarrow \mu^+\mu^- + X$.

The rates from sources 1 and 2 dominate at very low momenta and thus are responsible for the occupancies

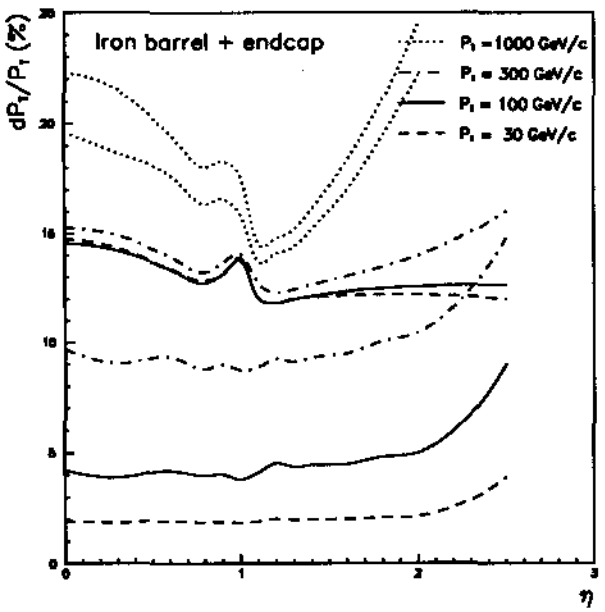

Figure 4.22: *As Fig. 4.20, for the iron toroid spectrometer*

of the muon tracking and triggering system. Sources 3 to 5 dominate the final trigger rate when trigger thresholds of the order $p_T \simeq 10$ GeV are applied.

The decay and punch-through rates have been calculated by combining pion rates from the ISAJET Monte Carlo generator with results of detailed studies of the properties of single pion punch-through. These studies are described in detail in ref. [14] and are based on results of a GEANT simulation of single pions to give the rate, particle nature, momentum and multiplicity of particles leaving the calorimeter system. The results of this simulation were parametrized and used in a fast Monte Carlo program with a simplified geometry of the absorbers. The bending of charged hadrons inside the 2 T solenoid, decay kinematics and muon energy losses were taken into account.

The resulting rates for the nominal luminosity of $\mathcal{L} = 1.7 \cdot 10^{34}$ cm^{-2}s^{-1} are shown in Fig. 4.23 and indicate the flux of muons and charged hadrons exiting the outer calorimeter surface, assuming a total absorption length of 12λ for the barrel and 14λ for the end-caps, well matched to the current detector design.

Uncertainties in the punch-through calculations are determined by our knowledge of the probability of finding a secondary particle with some fraction of the momentum of the incident hadron after the absorber. These uncertainties were estimated to be one order of magnitude, by comparing the probabilities and particle momentum spectra, as obtained in the simulation, with data from the E744 experiment at FNAL [15]. To obtain punch-through rates the formulae from [16] were used which are based on data, up to hadron energies of 400 GeV.

However, the dominant rate is due to hadron decays. These can be simulated more reliably; their uncertainty is estimated to be a factor of two. An additional uncertainty at low momenta arises from the generation of inclusive events and is also of the order of a factor two, due mainly to the uncertainty on the inelastic cross-section at LHC energies. At higher momenta the uncertainty is much smaller. Comparison of the decay rates thus obtained with analytical estimates shows a satisfactory agreement.

The rates shown in Fig. 4.23 indicate that a level-1 muon trigger can be easily implemented in the region $|\eta| < 2$. Beyond $|\eta| \simeq 2.5$ the rate due to background muons becomes large.

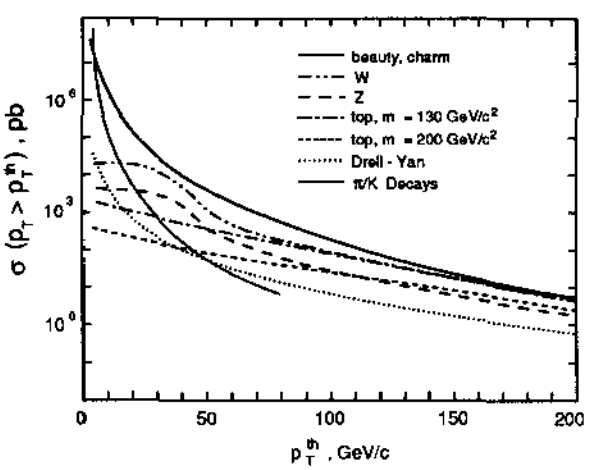

Figure 4.24: *Inclusive muon production cross-sections*

The rates of inclusive muons from sources 3–5 above have also been calculated with ISAJET and are compared in Fig. 4.24 in the form of integrated cross-sections above a transverse momentum threshold [17]. A $p_T \simeq 10$ GeV cut eliminates most of the background. Higher-order QCD corrections are important for the evaluation of heavy-quark production. The ISAJET Monte Carlo incorporates these corrections with the parton shower model. The $b\bar{b}$ and $c\bar{c}$ production cross-sections are predicted, owing to theoretical uncertainties, within a factor 5 [18]. In particular at $p_T = 20$ GeV the ISAJET cross-section is twice as large as the prediction of a full $\mathcal{O}(\alpha_s^3)$ calculation. We are thus confident that the Monte Carlo does not underestimate this background.

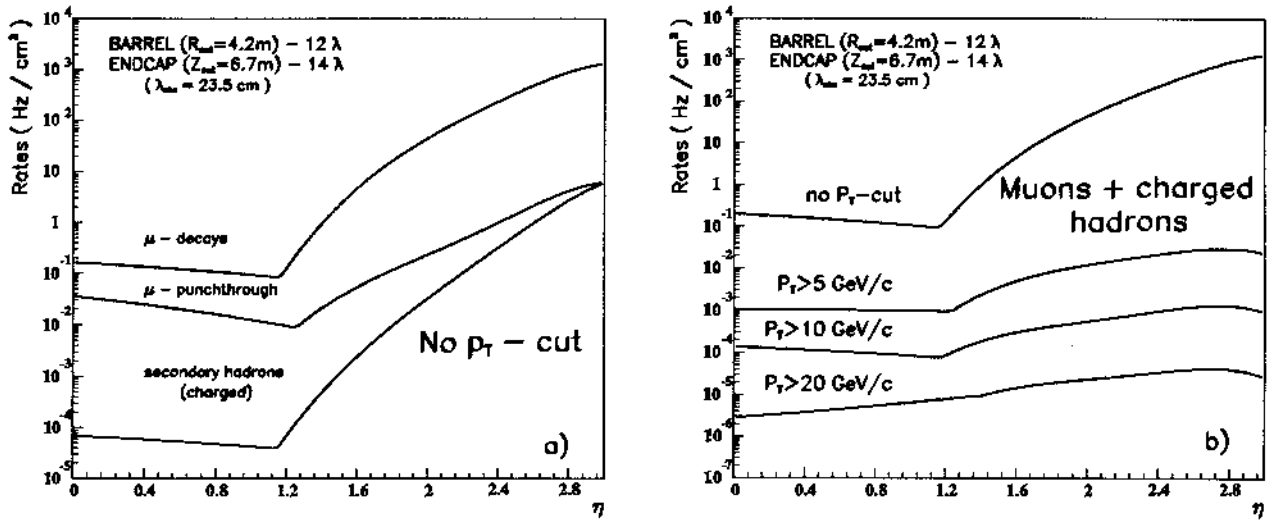

Figure 4.23: *Charged particle rates on outer calorimeter surface: (a) all momenta, (b) for different cuts in p_T*

Muons from semileptonic beauty and charm decays dominate at low values of p_T. Assuming a luminosity $\mathcal{L} = 1.7 \cdot 10^{34}$ cm^{-2}s^{-1}, the corresponding rates are 40 kHz for $p_T > 10$ GeV, 2 kHz for $p_T > 20$ GeV and 200 Hz for $p_T > 40$ GeV.

Figure 4.25 shows the corresponding dimuon production cross-section. Beauty and charm production

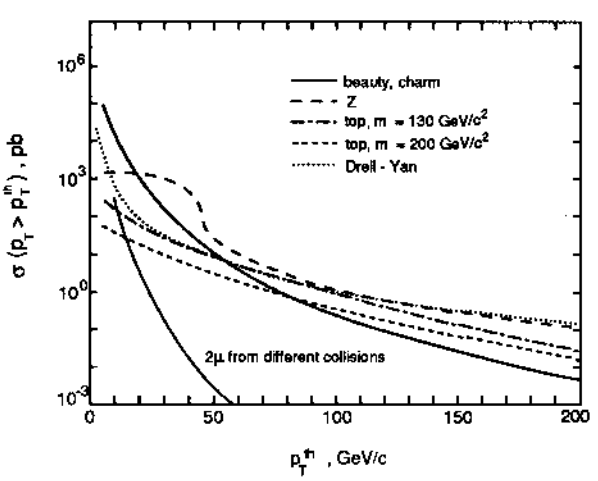

Figure 4.25: *Dimuon production cross-sections*

is still the dominant source at low p_T. For p_T larger than 20 GeV, contributions from Z production and from $t\bar{t}$ processes dominate. At nominal luminosity, the rate of dimuons is $\sim$ 70 Hz for $p_T > 20$ GeV and about 10^8 Z bosons decaying into lepton pairs could be used for calibration of the detectors in one year.

Table 4.4: *Dilepton trigger efficiencies for* $H \rightarrow ZZ \rightarrow \ell\ell\ell\ell$, *for different pseudorapidity coverages*

m_H (GeV)	$\|\eta\| < 2.0$	$\|\eta\| < 2.5$	$\|\eta\| < 3.0$
130	0.25	0.30	0.33
140	0.38	0.43	0.45
160	0.55	0.60	0.61
200	0.68	0.72	0.73
400	0.83	0.85	0.86
700	0.89	0.91	0.91

The effect of the threshold and of the acceptance of the level-1 muon trigger has been studied using the reaction

$$pp \rightarrow H + X,\ H \rightarrow ZZ \rightarrow \ell\ell\ell\ell\ (\ell = e, \mu)$$

as a benchmark process. In Table 4.4 we present the detection efficiency for different values of the Higgs mass and of the pseudorapidity coverages. The trigger requires at least two leptons with $p_T > 20$ GeV, but the other leptons are detected down to $p_T = 10$ GeV in $|\eta| < 3$. The loss in efficiency when decreasing the acceptance of the trigger from $|\eta| < 3.0$ to $|\eta| < 2.5$ is small. We conclude from these results that a trigger acceptance of $|\eta| < 2.5$ is adequate and that an acceptance of $|\eta| < 2.0$ could still be sufficient.

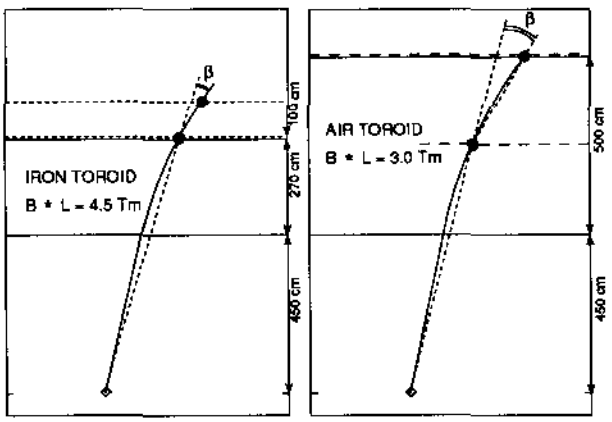

Figure 4.26: *Concept of triggering with toroids; β is the muon exit angle used in the trigger (see text)*

4.7.2 Level-1 trigger

We have designed the level-1 muon trigger to satisfy a number of requirements:

1. Hermetic coverage up to $|\eta| \lesssim 2.5$;
2. A sharp threshold in transverse momentum to ensure an efficient reduction of background muons. The threshold setting should be variable down to 10 GeV;
3. Unambiguous identification of the bunch-crossing, requiring an intrinsic time resolution better than 5 ns;
4. A fast decision time, smaller than $\sim$ 1 μs, to minimize the pipelining of signals.

The above requirements necessitate the use of detectors with large area coverage, good time resolution and flexible segmentation. The detector segmentation should be adequate to obtain the required momentum resolution over the whole rapidity interval covered by the trigger.

The trigger scheme is shown in Fig. 4.26 [19]. Two layers of detectors placed outside of the toroid will measure the angle between the line connecting the centre of the interaction region with the hit recorded on the inner layer, and the muon direction defined by the hits on layers 1 and 2.

For the detector configuration using an iron toroid, this angle is $\beta = 0.8 \times \theta_B \simeq 1.08/p$ (GeV) rad, where θ_B is the bending angle in the toroid. The error due to multiple Coulomb scattering in the iron is $\Delta\beta/\beta = 20\%$, while the error due to finite dimensions of the interaction region is $\Delta\beta \simeq 7.5$ mrad. The above numbers are given for $\eta = 0$. The trigger performance scales with the muon p_T in the barrel.

The same trigger scheme can be used with the air-core magnet. In this configuration, the angle β is smaller due to the lower field integral ($\beta \simeq 0.68/p$ (GeV) rad at $\eta = 0$) but there is no significant effect of multiple scattering. An alternative solution is also sketched in Fig. 4.26. The first trigger layer is placed in the centre of the magnet and the second one at its exit.

The trigger logic is simple and can be the same for the two magnet configurations. A hit in the first layer defines a window on the second layer, centred on the extrapolation of the line interaction point first hit. The width of this window defines the trigger momentum cut-off. This logic can be easily implemented with a system of programmable coincidence matrices defining coincidences between the two detector planes.

A Monte Carlo simulation of this scheme has been performed in both the barrel and the end-caps [19]. The detector planes are segmented into strips that run perpendicular to the beam in the barrel and have a circular shape centred on the beam line in the end-caps. The size of the strips varies between 3 cm and 1 cm in different η regions in order to have a uniform p_T cut-off. In the iron toroid option, the efficiency in the barrel region falls off very rapidly below the nominal threshold of 20 GeV, while the sharpness of the p_T cut at $\eta \simeq 2.5$ is only slightly degraded. The corresponding threshold curves for the air-core toroid option are comparable. The threshold curves for both magnet options are presented in Chapter 5. The selectivity of the muon trigger has been evaluated in the region $|\eta| < 2$ for the iron toroid option, comparing the calculated rate with the one obtained for an ideal sharp cut. The result for a nominal threshold of 20 GeV is that the trigger rate is 8 kHz compared to 2 kHz in the ideal case. For a dimuon trigger at 20 GeV threshold, the rate is 50 Hz. The maximum p_T threshold that can be implemented in such a muon trigger is determined by the strip size, the length of the interaction region and the bending power of the toroidal magnet. One can safely trigger with p_T thresholds up to about 40 GeV in the iron toroid option or 30 GeV in the air-core toroid option.

4.7.3 Implementation of the level-1 muon trigger

The level-1 muon trigger can be derived either from a stand-alone detector system or be integrated with the tracking detectors.

A stand-alone solution has the advantage of providing a fixed response time with almost no jitter and

can be used to monitor all other detectors with cosmic ray muons. An attractive candidate for such a system [20] are Resistive Plate Chambers (RPCs). These are gaseous detectors which combine a good time resolution of a few nanoseconds with a space resolution of a few millimetres [21]. The pick-up electrodes can be shaped in various configurations according to the required segmentation. The propagation time along the transmission line is about 5 ns/m and there is no observable attenuation of the pulses from the induction point to the end of the strip. Studies of the rate dependence [22] have shown that the chambers have good efficiency up to particle fluxes of 50 Hz/cm^2. This would limit the use of RPCs to the region $|\eta| \lesssim 2$.

The proposed trigger can be built with two planes segmented into strips. A system of programmable coincidence matrices is able to make the local trigger decision within 100 ns. A simplified version of such a system built from RPCs is currently used in the WA92 experiment [23] and is also under test in RD5 in a configuration similar to an LHC experiment [22].

The same trigger scheme can be adopted in an integrated system where the trigger signals are derived from the muon tracking chambers. This approach is described in Section 4.4 and would avoid the need for an independent detector for triggering, at the expense of more demanding requirements on the timing performance of the tracking chambers, some compromise on their segmentation and a more complicated processing of the data for the level-1 decision.

References

[1] J.M. Baze, H. Desportes, R. Duthil, C. Lesmond, J.C. Lottin and A. Patoux, Saclay Report DAPNIA/STCM 92/04 (1992).

[2] C.R. Walters, D.E. Baynham, E. Holtom and R.C. Coombs, End Cap Toroid Design Report, Rutherford Appleton Lab. Report, RAL 92065 (1992).

[3] M. Karppinen, SEFT Report, HU-SEFT R 1992-4 (1992).

[4] M.-H. Bovard and C. Vollerin, Proposition de dimensionnement et assemblage des plaques pour la construction d'un aimant toroidal, CERN/PPE Technical Note (1992).

[5] G. Alekseev et al., JINR Rapid Communications 5 (56)-92, Dubna (1992); G. Alekseev at al., ATLAS note MUON-NO-012, in preparation.

[6] H. van der Graaf et al., Nucl. Instrum. Methods **A307** (1991) 220.

[7] Y. Arai et al., SDC note SDC-92-169 (1992).

[8] J.L. Chevalley et al., EAGLE note MUON-NO-005 (1992).

[9] T. Mashimo and S. Komamiya, EAGLE note MUON-NO-004 (1992).

[10] Y. Arai et al., IEEE J. Solid State Circ., **27**, No. 3 (1992) 359.

[11] W. Blum, ASCOT/EAGLE note MUON-NO-007 (1992).

[12] P. Duinker et al., Nucl. Instrum. Methods **A237** (1988) 814.

[13] A. Nisati, ASCOT/EAGLE note MUON-NO-009 (1992).

[14] A. Cheplakov et al., ASCOT/EAGLE note MUON-NO-006 (1992).

[15] F.S. Merrit al., Nucl. Instrum. Methods **A245** (1986) 27.

[16] F. Lacava, ROM-NI 968 (1990).

[17] A. Nisati, in [24], Vol.III, p.442; S. Hellman et al., in [24], Vol.III, p.72.

[18] G. Altarelli et al., Nucl. Phys. **B308** (1988) 724; P. Nason et al., Nucl. Phys. **B303** (1988) 607.

[19] A. Nisati et al., Report Dip. Fis.-INFN-Rome N.I.997 (1992).

[20] F. Ceradini et al., in [24], Vol.III, p. 99.

[21] R. Santonico et al., Nucl. Instrum. Methods **A187** (1981) 377; R. Cardarelli et al., Nucl. Instrum. Methods **A263** (1988) 20.

[22] A. Böhrer et al., RD5 Collaboration, Status report of the RD5 experiment, CERN/DRDC/91-53 (1992).

[23] E. Petrolo et al., Nucl. Instrum. Methods **A315** (1992) 95; C.Bacci et al., Report Dip. Fis.-INFN-Rome, N.I.994 (1992).

[24] *Proceedings of the Large Hadron Collider Workshop*, edited by G. Jarlskog and D. Rein (Aachen, 4-9 October 1990) CERN 90-10 / ECFA 90-133.

5 Trigger, Data Acquisition and Computing

The expected prompt trigger rates (discussed in Section 5.1), the bunch-crossing frequency, and the amount of raw data produced by the detectors determine the basic features of the trigger and data-acquisition system: a multi-level trigger with pipelined front-end readout and a hierarchical data acquisition architecture. The three-level scheme presented here is meant to illustrate functionality rather than implementation aspects of the system. In fact, we are very aware that industrial technological improvements of key components, such as data links, network switches and microprocessors, may make alternative overall architectures possible. Nevertheless, the functional scheme reflects the nature of the expected event selection chain:

- a level-1 trigger with negligible dead time and with the shortest possible latency ($< 2\ \mu s$), making an unambiguous identification of the bunch crossing containing the event of interest;
- a level-2 trigger with programmable algorithms based on local data;
- a level-3 trigger for which the full detector information will be used.

A system will also be provided to monitor the luminosity.

5.1 Event Selection Criteria

The level-1 trigger will be based on combinations of four basic building blocks: muon triggers, electron/photon (e/γ) triggers, jet triggers and missing transverse energy triggers.

We have computed rates for the inclusive trigger elements as a function of the p_T threshold, assuming e/γ and muon trigger coverage within $|\eta|< 2.5$, jet trigger coverage within $|\eta|< 3$, and coverage for the missing-E_T calculation of $|\eta|<5$. The algorithms simulated are the ones described in Section 5.3 for which a level-1 implementation is possible. As shown in Fig. 5.1, the inclusive e/γ and di-jet trigger rates decrease rapidly with increasing p_T threshold. The inclusive muon trigger rate falls from 8 kHz at a nominal p_T threshold of 20 GeV to 2 kHz at 40 GeV. Similar studies have been performed for combined triggers, for example requiring two leptons above a given threshold.

In Fig. 5.2 we present threshold curves for the inclusive level-1 triggers, showing that rather sharp p_T cuts are possible for both calorimeter and muon triggers.

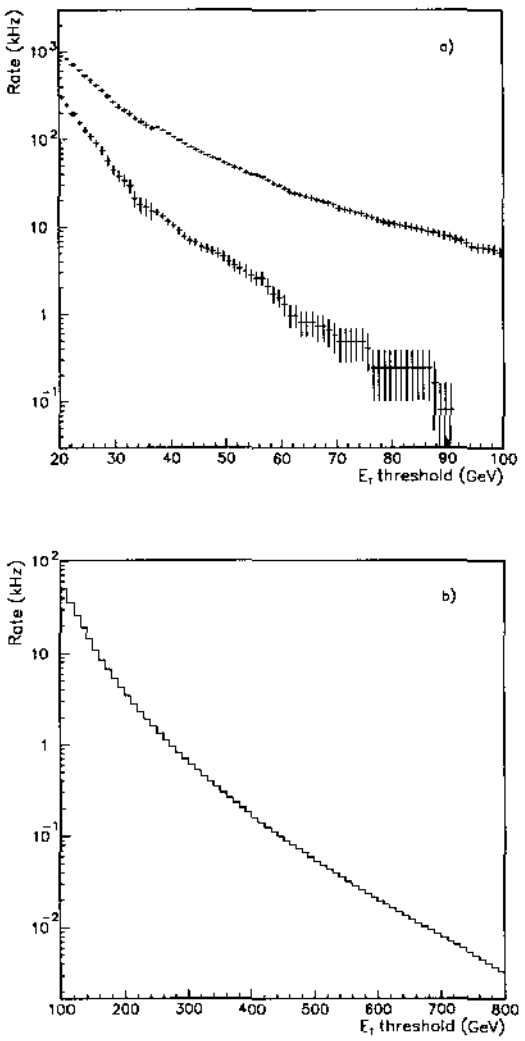

Figure 5.1: *Inclusive trigger rates as a function of p_T threshold for (a) the e/γ trigger (with and without an isolation requirement), (b) the di-jet trigger. The calculation is for $\mathcal{L} = 1.7 \cdot 10^{34} cm^{-2} s^{-1}$.*

A full GEANT simulation was used for the calorimeter-trigger rate and efficiency calculations [1, 2], which allows for the effect of showers being shared between several cells. A granularity of $\Delta\eta \times \Delta\phi = 0.1 \times 0.1$ was used in both the em and hadronic calorimeters. The trigger algorithm described in Section 5.3.2 was simulated, using integer arithmetic with $E_T = 1$ GeV units. Allowance was made for electronic noise and for cell-to-cell calibration differences. High-p_T QCD jet events, generated with PYTHIA, were used to evaluate the trigger rates (the e/γ trigger is dominated by jets with a large fraction of em energy). The efficiency of the isolated-e/γ

trigger was found to be 95% from a simulation of isolated electrons superimposed on an average of 20 minimum-bias events. The muon trigger simulation [3] was performed as described in Section 4.7.

Truly inclusive triggers will not be selective enough to remain efficient for all interesting physics processes, while giving acceptable rates. The level-1 trigger will therefore consist of an 'OR' of some truly inclusive triggers with relatively high thresholds, together with combinations of elementary triggers at lower thresholds. In Table 5.1 we illustrate this scheme by giving efficient[5] trigger conditions for some physics processes of interest (see Chapter 8). In general, the leptons produced in these processes will be isolated (not contained in jets).

We have made calculations for the combination of triggers shown in Table 5.2, which we believe would be efficient for the physics processes which are of interest. The trigger criteria (thresholds, etc.) will be programmable, and those given here are for illustration only. The calculated rates sum to about 60 kHz, which is within the assumed maximum rate into the level-2 trigger of 100 kHz.

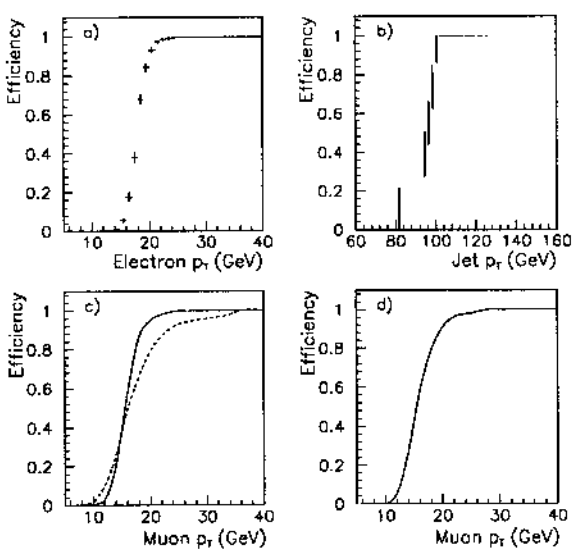

Figure 5.2: *Curves showing the trigger efficiency versus p_T for the following nominal thresholds: (a) p_T = 20 GeV electrons; (b) p_T = 100 GeV jets; (c) p_T = 20 GeV muons (iron toroid) for $|\eta| < 2.0$ (full line) and $2.0 < |\eta| < 2.5$ (dashed line); (d) p_T = 20 GeV muons (barrel air-core toroid).*

[5]In this context 'efficient' means that the trigger selection is sufficiently loose that no threshold effects remain at the level where analysis cuts are expected to be made.

Table 5.1: *Some benchmark physics processes and possible level-1 trigger criteria which are efficient for these signatures.*

Process	Level-1 trigger
Higgs $\rightarrow \gamma\gamma$ ($80 < m_H < 130 GeV$)	2 γ with $p_T >$ 20 GeV
Higgs $\rightarrow 4\ell$ ($120 < m_H < 800 GeV$)	e–e, μ–μ or e–μ with $p_T >$ 20 GeV for both leptons
Higgs $\rightarrow 2\ell + 2\nu$ (very large m_H)	e–e, μ–μ or e–μ with $p_T >$ 20 GeV for both leptons
Top $\rightarrow$ 3 jets + lepton	e or μ with $p_T >$ 40 GeV
Top $\rightarrow$ 2 leptons	e–e, μ–μ or e–μ with $p_T >$ 20 GeV for both leptons
W–Z pairs	e–e, μ–μ or e–μ with $p_T >$ 20 GeV for both leptons
SUSY to jets + E_T^{miss}	$\geq$ 3 jets with $p_T >$ 200 GeV + E_T^{miss} > 200 GeV
SUSY cascade decay to leptons	e–e, μ–μ or e–μ with $p_T >$ 20 GeV for both leptons
Z', W' $\rightarrow$ leptons	e or μ with $p_T >$ 40 GeV
Z', W' $\rightarrow$ jets	2 jets with $p_T >$ 200 GeV

Whether or not the above trigger criteria would also be efficient for any unexpected processes is of course impossible to estimate. However, we note that most conceivable physics signatures which would be discernible above backgrounds are likely to rely on signatures for which the suggested level-1 trigger would be efficient. We emphasize the importance of having a level-1 trigger which is sufficiently powerful and flexible to react to surprises in the LHC environment.

For low-luminosity running, the trigger thresholds can be significantly reduced compared to those given in the Table. In particular, for $\mathcal{L} = 10^{33}$ cm^{-2}s^{-1}, a level-1 inclusive muon trigger threshold of about 10 GeV could be used to select events for beauty physics studies, including CP violation.

5.2 Trigger and Data Acquisition Architecture

The total interaction rate at $\mathcal{L} = 1.7 \cdot 10^{34}$ cm^{-2}s^{-1} will be $\sim 10^9$ Hz. At LHC, bunch crossings will occur at 15 ns intervals giving a rate of 67 MHz, with an average of about 20 overlapping events per crossing.

The level-1 trigger, based on purpose-built electronics, will select interactions at a few $\times$ 10^4 Hz. At higher trigger levels, programmable devices will be used, reducing the rate to a few hundred Hz before full event building with a data rate of the order of 10 Mbytes/s for permanent storage.

Table 5.2: *Level-1 trigger rates at* $\mathcal{L} = 1.7 \cdot 10^{34} cm^{-2} s^{-1}$.

Trigger	Rate
$\geq$ 1 isolated em cluster with $p_T >$ 40 GeV (isolation not required for clusters with $p_T >$ 65 GeV).	31 kHz
$\geq$ 2 isolated em clusters, each with $p_T >$ 20 GeV (loose isolation cut)	16 kHz
$\geq 1\mu$ with $p_T >$ 20 GeV	8 kHz
$\geq 2\mu's$, each with $p_T >$ 20 GeV	67 Hz
$\geq$ 2 jets, each with $p_T >$ 200 GeV	5 kHz

We estimate a latency for the level-1 trigger of < 2 μs, during which data from all detectors will be stored in pipeline memories. The front-end electronics is discussed separately for each subdetector elsewhere in this document. However, in general it contains analogue or digital signal processing, analogue or digital pipeline memory, sparsification logic, digitization (either before or after the level-1 pipeline depending on the detector), local readout buffers and readout control logic common for a group of front-end channels. In addition to detector-specific services such as calibration and test pulses, the front-end readout units will receive a clock signal and a level-1 trigger decision every 15 ns [4]. We recognize that maintaining synchronization at the level of a few ns with such a large number of readout channels distributed over the detector will be very difficult. We are also aware of the importance of minimizing the level-1 latency which strongly affects the cost of the custom-made, analogue and digital pipeline memories.

After a positive level-1 decision, the global level-1 event identifier and possibly other information (e.g. destination addresses or type of event) will be sent to the readout control logic which will tag the data before sending it to the appropriate destination (a level-2 buffer memory and/or a level-2 trigger processor).

The readout and level-2 trigger systems should be able to handle a level-1 rate of up to 100 kHz, corresponding to a total throughput of the order of 10^{12} bits/s. The level-1 deadtime, for example generated by the read-out of those detectors which require data from more than one bunch crossing, stays below 1% with a maximum readout latency of less than $\approx$ 1 ms. We expect the data to be moved off the detector using optical links. The possibility of using analogue optical transmission is under consideration for some detectors [5].

The detectors participating in the level-2 trigger decision should provide local trigger information from 'regions of interest' to the global level-2 trigger processor within $\approx$ 1 ms. The above requirements are dictated by the level-2 trigger latency. The readout system for each detector will have to be tailored to the specific front-end electronics, but the information in the level-2 buffers and processors must be available to the general trigger and data acquisition system.

We are performing computer modelling and simulation of possible architectures to identify solutions giving the required performance for the overall trigger and data-acquisition system.

5.3 Level-1 Trigger

The level-1 trigger system will be based on a number of trigger processors associated with different subdetectors, a central trigger processor which correlates the local results, and a system which distributes the trigger decision together with the LHC clock to the front-end electronics. It will uniquely identify the bunch-crossing to be read out.

The latency of the level-1 trigger has been calculated assuming that the electronics is mounted on or very close to the detector. A realistic estimate of cable lengths between the detectors and the trigger processors requires 50 m or more in each direction, giving a total propagation delay of $\approx$ 500 ns. The trigger processing time is likely to be dominated by the calorimeter trigger for which relatively complicated level-1 algorithms are planned as described below. Including the processing time for the central trigger processor, we estimate that about 60 pipeline steps will be required with 15 ns per step, giving a processing time of 900 ns. Based on these calculations, we believe that a fixed level-1 latency of < 2 μs is realistic.

Level-1 triggering is the subject of an R&D project [6]. More information on level-1 trigger studies performed within ATLAS is available [2].

5.3.1 Muon trigger

The level-1 muon trigger has already been discussed in Section 4.7. It will be based on tracks in the external muon detectors which point back to the interaction region.

The baseline option is to use a dedicated trigger detector based on RPCs which give fast (timing resolution < 15 ns) signals on strips. Very fast digital logic is used to identify patterns of hits in planes of chambers outside the toroid magnet that are consistent with high-p_T muons originating from the interaction region. This logic is programmable allowing the p_T cut to be varied, and several thresholds are foreseen for use in the inclusive muon trigger, multi-lepton triggers and for flagging 'regions of interest' (RoIs) containing lower p_T muons for level-2 analysis.

We are also investigating the possibility of making a level-1 muon trigger based on the precision muon tracking detectors. This would remove the need for an independent detector for triggering, at the expense of more complicated level-1 trigger processing.

5.3.2 Calorimeter trigger

For the calorimeter trigger we envisage a digital trigger processor which will use information from the em and hadronic calorimeters, including those in the forward regions. The trigger will use a reduced granularity ($\Delta\eta \times \Delta\phi \approx 0.1 \times 0.1$) and the sum over all samplings in depth for each of the em and hadronic calorimeters. It will retain events with high-E_T electrons, photons and jets, and large missing E_T.

The digital E_T information will be obtained either from an independent trigger ADC system or from the ADCs of the calorimeter front-end readout if digitization is performed before the readout pipeline as in the proposed FERMI system [7]. Summation (analogue or digital respectively) will be performed to obtain the required granularity.

In the algorithm currently under study, the trigger will look for em clusters contained in pairs of em trigger cells (2×1 or 1×2 cells in $\eta - \phi$), giving a sharp threshold even if the shower falls on a boundary between cells (see Fig. 5.2a). It will also include the option of an isolation requirement based on a 4×4 window, including 12 em trigger cells surrounding the cluster and 16 hadronic trigger cells behind the cluster. Cells with $E_T < 1$ GeV will be ignored in order to reduce sensitivity to pile-up and noise. Simulation studies show that such an isolation requirement reduces the background rate from hadronic jets by about a factor of ten, while having an efficiency for isolated electrons of more than 95% even in the presence of pile-up at $\mathcal{L} = 1.7 \cdot 10^{34}\mathrm{cm}^{-2}\mathrm{s}^{-1}$.

The logic will be programmable allowing the cluster E_T and isolation thresholds to be varied, and several sets of thresholds are foreseen for use in the inclusive e/γ trigger, multi-lepton triggers and for flagging RoIs containing lower-E_T clusters for further study at level 2.

The jet trigger will be based on the E_T sum in overlapping sliding windows, including both the em and hadronic calorimeters. The trigger processor will also calculate the missing transverse energy, using all the calorimeters with $|\eta| < 5$. Several thresholds will be provided, giving the possibility to trigger selectively on processes such as $W \rightarrow e\nu$, which is useful for providing calibration data samples, and SUSY giving jets plus missing E_T.

5.4 Level-2 Trigger

The level-1 trigger will already make a fairly tight selection of events based on the external muon detectors and on calorimetry. Some further reduction in rate will be possible at level 2 by refining these selections using the fine granularity and full resolution information from these detectors. However, additional detectors will have to be used to get the required further background rejection, particularly for the e/γ trigger. Rate reduction at level 2 will also be achieved by requiring additional signatures.

5.4.1 Algorithms

Algorithms for level 2 are still under study, but we expect to use the inner tracking detectors to match high-p_T tracks with calorimeter clusters and preshower hits to provide a highly selective electron trigger. The photon trigger can be refined by using fine-granularity calorimeter and preshower information, and isolation requirements. The muon trigger rate can be reduced by sharpening the p_T threshold using the high-precision external muon tracking and possibly the inner tracking in addition; the rate can be reduced further by applying isolation requirements. The jet trigger threshold can be made sharper using more detailed information from the calorimeters and optimized jet algorithms. Selections on topology and on invariant mass can also be made. For the missing E_T trigger, we see little scope to improve on the level-1 measurement at level 2, although associated signatures such as jets can be refined.

Studies are in progress for level-2 triggers based on a variety of detectors. Two examples of tracking triggers, one based on the outer silicon tracker (SIT) and the other based on the TRD, are described below. A high-p_T track trigger will suppress the background to the electron trigger strongly and can also be used to help to trigger on μ's and τ's, and to veto fake γ's.

The performance of the level-2 electron trigger was studied using full GEANT simulations of large statistics samples of electrons and jets. The level-2 trig-

ger will use the full-granularity information from the calorimeter and preshower detectors (providing more accurate and localized energy thresholds and isolation cuts than at level 1). This will yield an overall rejection factor against jets of $\sim 10^3$. Tracking information will be used to reject most of the remaining events which do not contain a high-p_T track matched to the em cluster.

5.4.2 Trigger based on the SIT detector

The performance of a high-p_T track trigger has been studied for the barrel outer silicon tracker (SIT) in version A of the inner detector layout (see Section 3). This detector covers the central rapidity region. The RoI defined by the level-1 trigger is subdivided into ϕ bins. A sliding window is moved across the RoI, choosing the window width for each layer to give a p_T threshold of about 30 GeV. Candidate tracks must have hits in at least 5 out of the 6 layers. For each such candidate, a straight-line fit is performed on the strip hits, giving an approximate measurement of p_T and a goodness-of-fit measurement (χ^2). The efficiency of the trigger for isolated electrons, requiring only the presence of a high-p_T track in the road, is shown in Fig. 5.3 as a function of p_T. The efficiency for $p_T >$ 40 GeV is 95%, where most of the inefficiency is due to bremsstrahlung before the SIT. Pile-up, simulated by superimposing an average of 20 minimum-bias events on top of the electron events, did not cause a very significant degradation in the performance of the trigger. Further rejection against random hit coincidences can be made with cuts on χ^2, E/p matching and track – calorimeter shower position matching, and a tighter calorimeter selection based on the full granularity. The overall efficiency of the level-2 trigger for electrons with $p_T > 40$ GeV is then 91%.

The rejection power of the level-2 trigger was estimated using simulated jets which passed the level-1 electron trigger criteria with $E_T > 40$ GeV. The rejection power for events which did not contain a high-p_T charged hadron was ≈ 100. The trigger accepts events in which a single high-p_T charged hadron has passed the level-1 electron trigger and so the overall rejection power against jets was only ≈ 35. However, additional rejection power against this class of events can be achieved using the preshower detector. Thus the overall rejection power of the level-2 electron trigger is estimated to be in the range 50–100 while the efficiency for isolated electrons is $\approx 90\%$ [8]. Work is in progress in the RD11 collaboration on the implementation of this trigger algorithm in fast processors.

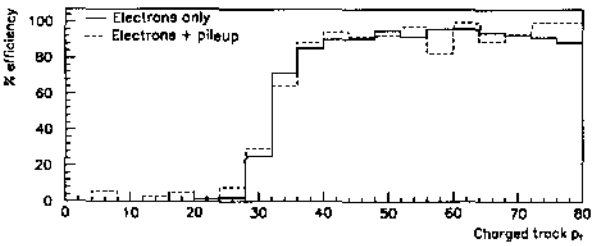

Figure 5.3: *Trigger efficiency versus electron p_T, with (dashed line) and without (solid line) pile-up background.*

5.4.3 Trigger based on the TRD tracker

In the TRD tracker, high-p_T tracks have a simple signature – straight lines – which can be recognized by a histogramming algorithm. Track finding is based on encoding the path of the track in two dimensions, (r,ϕ) or (z,ϕ), in terms of straw and plane numbers, and defining roads in which the numbers of hits are histogrammed. These roads are limited to within an RoI defined by the level-1 trigger.

When all hits in the TRD/T are taken into account, the algorithm selects high-p_T tracks ('tracking' trigger). When only high-energy hits (transition radiation photons) are used, the same algorithm selects only electron tracks ('electron' trigger).

The implementation of this trigger is being investigated in a joint effort between the RD6 and RD11 collaborations. We are investigating the use of parallel processing architectures [9]. These would alternate between a 'reading and reshuffling' mode and a 'histogramming' mode performing the actual track finding.

A Monte Carlo simulation, for $p_T = 20$ GeV at $\eta = 0$ (see Section 3.5.4.3), demonstrates that with the 'tracking' requirement in the level-2 trigger one can expect a rejection factor of 40 against jets which survive the level-1 electron selection and do not contain a signal electron. At this p_T, many of the remaining events contain high-p_T hadrons with an early em shower development. These events will be further suppressed by a factor of 10 by the 'electron' requirement, thus providing a total rejection of $\approx$150 for the level-2 electron trigger, for an electron efficiency of $\approx$90%.

5.4.4 Architectures

Our level-2 trigger studies, which are concentrating on algorithms, will determine the amount of data and

the processing power required for the trigger. Processor and data-link technologies are improving rapidly and we expect to select the best products at the time of implementing the level-2 system. We discuss here a conceptual design of a level-2 architecture based on local feature analysis followed by global event selection. However, we remain open to alternative architectures.

When the level-1 trigger accepts an event, the detector data are transferred from pipelines to buffer memories. Many possibilities are being investigated for the implementation of this readout which will not be the same for all detectors. While the inner detectors have extreme requirements for space, low-power and radiation hardness for their local readout logic, and prefer a relatively simple readout protocol [10, 11], the calorimeters and muon chambers can use more powerful and flexible solutions [12, 13].

We are considering a level-2 trigger system with a latency of $\sim$ 1 ms. Many events will be processed concurrently in this scheme, using a large number of local processors and a farm of global processors. During the level-2 latency, the detector data will reside in digital buffer memories. Given the already low cost of fast digital memory we do not consider the long level-2 latency to be a problem.

A critical point for the level-2 trigger, given the high bandwidth requirements, is giving the local processors access to the detector data which are stored in buffer memories. Our present scheme uses the level-1 trigger to flag RoIs containing candidate electrons, photons and muons. The data from these regions are processed locally to extract features (e.g. to summarize the information about an electron candidate), before performing global processing on all the features from the event. The advantages of this approach are that the rate at which a given RoI has to be analysed is much ($\sim$ 100 times) less than the overall level-1 rate and the volume of data that needs to be processed at level 2 is greatly reduced. Monte Carlo simulations are in progress to calculate typical occupancy numbers for the detectors inside and outside the RoIs, and we are performing simulations of the real-time behaviour of readout systems. The reduction in required bandwidth due to the RoI scheme will have to be balanced against the increased protocol overhead and the complication of distributing RoI information.

We expect to make extensive use of commercial products in the level-2 trigger system which will be integrated with the data-acquisition system (described below). The level-2 system must contain data links and networks to allow local processors to access detector data stored in the buffer memories and to transfer data (features) from local to global processors. Several possibilities are under consideration, including switching networks and special purpose routers [10, 12, 13, 14]. For the processing hardware, it may be appropriate to adopt different processors for different subdetectors although these must be combined into a coherent level-2 trigger system. Possibilities range from general-purpose processors to special-purpose programmable processors. The choice will be made closer to the time of implementation.

5.5 Level-3 Trigger, Event Building and Data Acquisition

The data from all detectors will be read out from local memories for events accepted by the level-2 trigger and the resulting full events will be sent to the level-3 trigger system. The level-3 trigger will then perform the final event selection and data reduction prior to permanent recording on mass storage. Event selection for physics analysis, and for calibration and alignment (e.g. samples of W and Z leptonic decays) will be started at level 2 and refined at level 3. We envisage the possibility of doing partial event readout for some types of trigger, for example calibration triggers or a high-mass jet-pair trigger for new particles decaying to jets.

For a level-2 rejection of ≈ 100, bandwidths of a few Gbytes/s are necessary for full event building. Traditional bus-based event builders are, therefore, ruled out even assuming the availability of new-generation standards, such as Futurebus+. Alternative architectures, implementing a high level of parallelism, have to be adopted. Point-to-point links combined with cross-bar switches and switching networks seem to be suitable candidates. We expect that products being developed in the telecommunication industry will provide an adequate solution.

The final number of parallel readout channels will have to be determined by balancing complexity against speed. Modelling and simulation studies are necessary to optimize the architecture and to develop event building algorithms. A multi-processor data acquisition prototype is being developed [15], integrating commercial VME-based RISC processors running a real-time UNIX operating system (LynxOS) supporting distributed applications. A RISC-processor-based HIPPI/VME interface is used as a high bandwidth (50 Mbytes/s) data-transfer module. The system is being designed with scalable features and a development path to higher bandwidth buses, such as VME64 and Futurebus+. It constitues a scaled-down prototype of an LHC-like data acquisition system. We are also following the development of a

different acquisition architecture, based on the new Scalable Coherent Interface standard [16].

Once the full events have been built, they will be routed to the level-3 trigger system which will consist of a farm of general-purpose processors of sufficient power to allow sophisticated algorithms to be run. We expect to run the full offline analysis algorithms, to reduce the event rate to manageable levels for mass storage. Present estimates indicate a total processing power for the level-3 farm of a few times 10^5 Mips (Mega instructions per second). There are many obvious advantages in running the same analysis software online and offline, for example a safer and easier estimate of trigger biases, and a more efficient use of human and computer resources.

The necessity of having a uniform programming environment, the complexity of the online system and the long time scales involved in the project make it essential that adequate software development and application environments are adopted. Modern software engineering and programming language technologies are needed for reliable software design, code generation and maintenance. The integration of commercial software will provide the most cost-effective solutions in many areas. Operating System standardization is needed to preserve the software investment in the long term, giving platform independence for the most effective use of computer technology advances. The applicability of these concepts to data-acquisition systems is currently being investigated in the RD13 project, with particular emphasis on the evaluation of Real-time UNIX as candidate for a common operating system throughout the online environment. This would also guarantee full online–offline software portability.

5.6 Offline Computing Requirements

In the short term (i.e. in the preparation of the technical proposal) we will intensify our Monte Carlo studies in order to approach a final detector design. We estimate that the computing time required at CERN will be of the order of 500 000 hours (CERN units) of which 90% can be on the CSF farm with the remaining 10% on the IBM.

The medium-term requirement will be governed by further Monte Carlo studies, program development, and a build-up of computing facilities for data reduction and analysis. We shall rely on the expertise at CERN in providing library packages and in coordinating the software development.

In the long term, the requirements for data storage, computing power and computing infrastructure will exceed those of current experiments by several orders of magnitude. The data volume (raw data, DST, and Monte Carlo) is estimated to be several hundred Tbytes/year. A hierarchical system of data storage and access is essential.

The computing power needed for first-pass reconstruction at LHC is estimated to be three orders of magnitude larger than that available on currently installed online reconstruction farms. In 1999 it can be expected that the increase of computing power of processors will compensate for a good part of higher demand, such that a system of about 100 processors will fulfil the task.

Most analysis and program development will be done on clusters of workstations. In an experiment with more than 1000 physicists, a few hundred workstations will be installed at CERN and in the other laboratories. The necessary infrastructure (file servers, high-speed networking, and manpower for system management) will have to be provided.

References

[1] S. Hellman et al., EAGLE note DAQ-NO-004.

[2] N. Ellis et al., ATLAS note DAQ-NO-005.

[3] A. Nisati and M. Torelli, EAGLE note MUO-NO-002.

[4] J. Altaber et al., CERN-DRDC-90-62; 92-10.

[5] J.D. Dowell et al., CERN-DRDC-91-41.

[6] N. Ellis et al., CERN-DRDC-92-17.

[7] B. Lofstedt et al., CERN-DRDC-90-74; 92-26.

[8] R.J. Hawkings et al., ATLAS note INDET-NO-013.

[9] M.v.d. Guchte et al., CERN-DRDC-90-56 and 92-11 and CERN-ECP-92-7.

[10] R.K. Bock et al., RD6 note 27.

[11] F.Anghinolfi et al., RD2 Collab., 3rd Como Conference, June 1992.

[12] FEAST: Studies being performed jointly between RD16 (FERMI) and RD11 (EAST).

[13] J.R. Hansen, EAGLE note DAQ-NO-003

[14] J. Christiansen et al., CERN-DRDC-92-14

[15] R. Bonino et al., CERN-DRDC-90-64; 92-13.

[16] A. Bogaerts et al., CERN-DRDC-91-45.

6 Experimental Area and Installation

6.1 Requirements and Logistics

The overall arrangement of the experimental area and the installation scenario are mainly governed by the large dimensions and possibly large weight of the proposed detector.

The limitations in road or rail transport to CERN define the dimensions and weight of the individual pieces that can be pre-assembled outside CERN. The final assembly of the magnet and essentially all detectors (except for the inner detector assembly) will, therefore, take place at the experimental zone. It is also assumed that the total installation time for the detector will be limited to not more than two years. This implies that large prefabricated units will have to be prepared in the surface hall and installed into the experimental hall, with a minimum of assembly work inside the experimental cavern.

The maximum unit weight of most sub-assemblies has been limited to 500 t such that they can be handled by coupling two 'standard' 250 t cranes. In case heavier units have to be handled it is foreseen to install a temporary crane capacity of 2500 t. A study involving industry has shown that this is possible [1].

6.1.1 Experimental area

Several different geometries for the layout of the experimental area have been studied. The most cost-effective civil-engineering layout and the most suitable shape for the detector installation seems to be a single large access shaft geometry, see Figs. 6.1 and 6.2.

The experimental hall is made up of the access shaft, with a diameter of 33 m, and two forward alcoves of 26 m diameter. The latter provide space for withdrawing the end-cap toroids and the installation of muon chambers. The total length of the cavern is 44 m.

Additional space is provided to allow the forward calorimeters and the shielding of the low β quadrupoles to be pushed into a shielded area during maintenance work.

The exact layout of the area will depend on the final detector configuration. In the air-core toroid version the access shaft is longitudinally offset by 5–6 m. In addition a smaller diameter 'garage' area on one side of the hall is foreseen to serve during major access operations, see Section 6.2.1.

The access shaft must be covered by a mobile radiation shield, as indicated in Fig. 6.2. This shielding can be integrated into the floor of the surface hall.

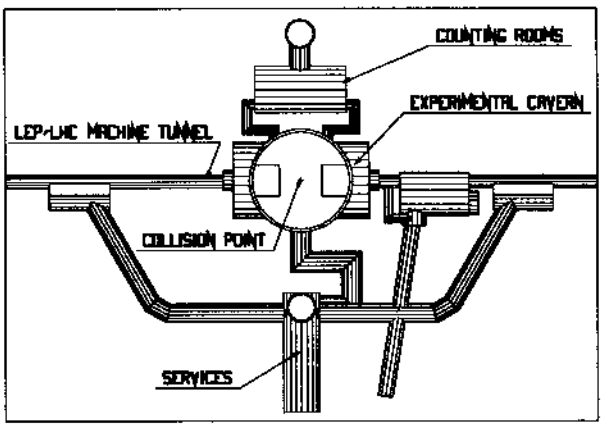

Figure 6.1: *Plan view of the experimental area; here shown for the iron-core toroid scenario*

Further down, in the access shaft, a second obstruction is made by a ventilation cover, which separates the underground cavern from the access shaft volume. This ventilation cover will also serve as an effective safety barrier for the people working underneath.

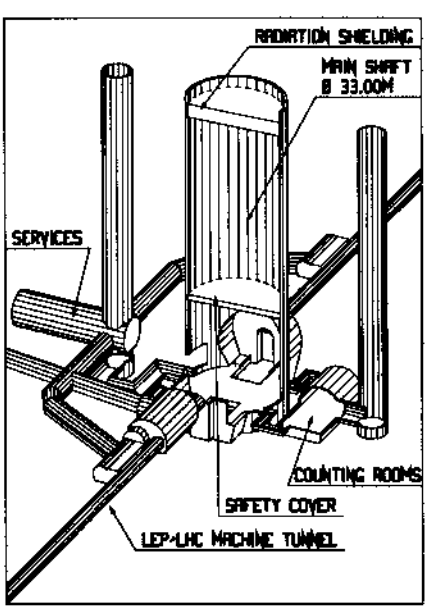

Figure 6.2: *Isometric view of the experimental area*

The access to the LHC service tunnel, which bypasses the experimental area at the inside of the LHC ring, is made via a separate access shaft. The main cavern is linked to the service area by a chicane which will be used for cooling, ventilation and power installations. The additional shaft will also serve as a

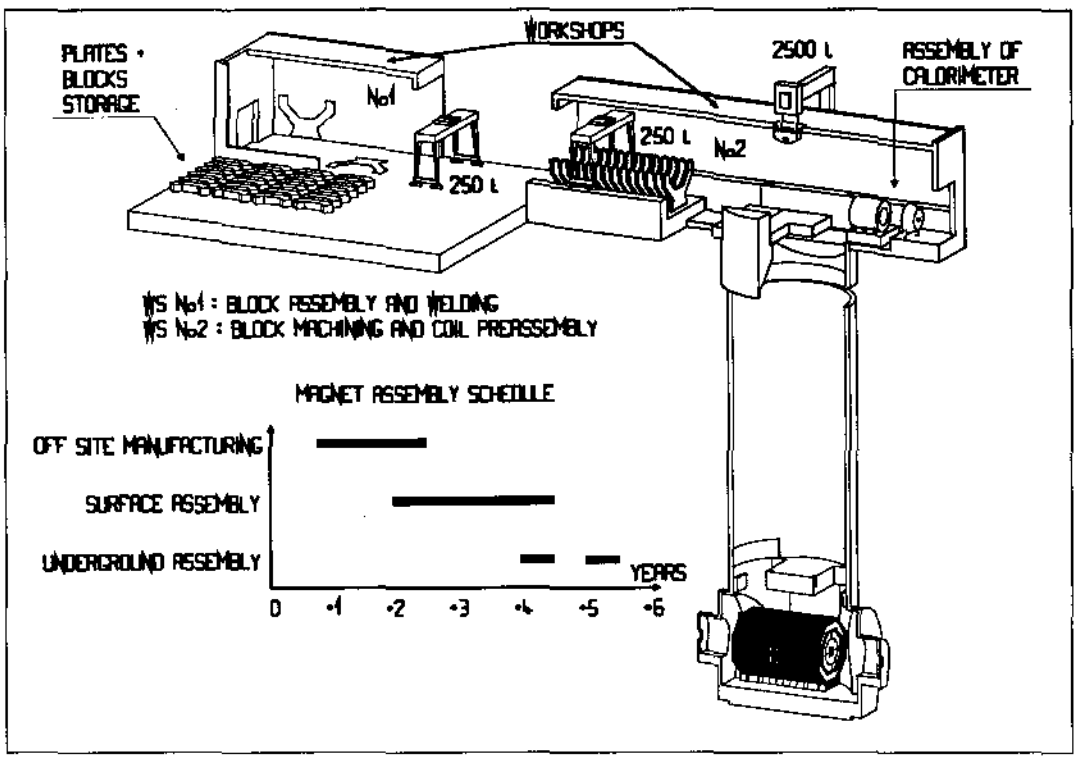

Figure 6.3: *Layout of the manufacturing and assembly of the iron core magnet on the CERN site*

second exit in case of an emergency.

The side opposite to the LHC by-pass is reserved for an underground electronics cavern with its own 9 m diameter dedicated access shaft, and a special cavern for storage of liquid argon. The electronics cavern is linked to the experimental cavern via two access chicanes. These chicanes are placed in such a way that a 'blockhouse', accessible during LHC operation, can be installed inside the experimental hall, providing space for about 40 electronics racks.

The experimental cavern will be equipped with a crane, installed just below the ventilation separation, allowing the manipulation of smaller loads.

It has been demonstrated [2] that this type of experimental area could be built in Point 7 and, with some minor modifications, also in Point 1.

6.1.2 Beam line

The last machine elements before the experiment are the superconducting low-β quadrupoles at 20 m distance from the interaction point. To shield these magnets, 2 m long copper collimators will be installed before them, leaving about ± 17.5 m free space around the interaction point for the detector.

The design of the beam vacuum chamber is mainly conditioned by the requirements set by the inner detectors. A valve, situated at about 8 m from the interaction region [3], separates the vacuum chamber in two sections: a central thin-wall section and a forward thick-wall section. The thin-wall section is composed of a ± 1 m long beryllium section followed by a 7 m long undulated stainless-steel section. The external aperture (including flanges) of the thin-wall section is limited to a diameter of 140 mm in order to facilitate the installation of the vertex detector. The isolation valve will allow the forward section of the vacuum chamber to be removed during e.g. displacement of the end-cap toroids, without deteriorating the vacuum in the central part.

6.1.3 Surface area layout

The assembly of the toroid and the various detector units in conjunction with a limited total installation period will imply the construction of a rather large surface hall, 180 m long and 30 m wide. An example of how such a hall may look in the iron-core toroid scenario is given in Fig. 6.3. The hall is placed asymmetrically around the main installation shaft, thereby creating two distinct assembly regions. One side is reserved for the assembly and construction of the toroid

and the other side is used by the various detector assemblies and the mobile platform for the calorimeter units.

The surface area will be equipped with two 250 t travelling cranes, capable of moving the largest magnet modules, when coupled together. In addition two 60–70 t cranes are needed. To lower heavier detector elements into the underground area, a temporary, fixed crane with a capacity of approximately 2500 t will be installed over the access shaft.

The part of the hall which serves for the magnet construction is needed at least $2\frac{1}{2}$ years before the installation of the first detector elements. It could be a temporary construction, which is no longer needed once the magnet is installed. The part covering the access shaft will only be constructed once the civil engineering of the experimental area is completed.

6.2 Installation and Access

To limit the installation time in the cavern, all large detector elements will be partly or fully assembled in the surface area and lowered into the underground area in as large as possible units.

In particular, it is thought to be a considerable advantage if the three parts of the calorimeter could be lowered as complete and tested units using the temporary crane installation mentioned above.

The installation procedure depends on the final detector choice.

6.2.1 Air-core toroid version

The air-core toroid will be pre-assembled on the surface into four sub-units of three coils each, none weighing more than 250 t. The sub-units will then be lowered in the underground area, moved to the interaction point and interconnected.

Once the barrel is in place, the muon chamber installation can start.

The calorimeter modules and the end-cap toroids are not tied to the barrel toroid structure. They are supported by two rails, running parallel to the beam line through the air-core barrel over the full length of the cavern. The end-cap toroids as well as the calorimeter units, once fully assembled, will be lowered onto the rails and pushed into their final positions. A single 250 t crane is sufficient to lower the air-core end-cap toroids, to lower the calorimeter end-caps the 2500 t crane may be needed. Figure 6.4 shows a view of the installed detector in the hall.

Owing to the open magnet structure, access to the muon chambers and electronics located outside the calorimeters is easy and fast, provided passages and gangways are integral parts of the installation.

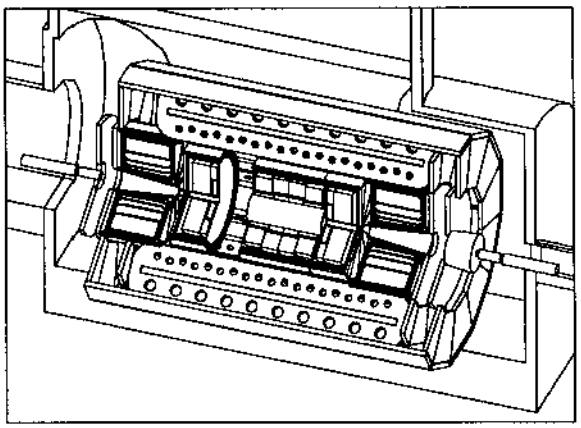

Figure 6.4: *Isometric view of the installed detector (air-core toroid version) with one of the end-cap toroids in retracted position*

Access to the electronics of the calorimeters and the inner tracking detectors, can be provided by retracting the end-cap toroids and end-cap calorimeters, respectively, by a few metres, as shown in Fig. 6.4. These operations could be achieved on a time scale of typically one day, and could be envisaged for a 1–2 week access period.

A more general access scenario is based on a complete withdrawal of the end-cap toroids by several metres into the alcoves, see Fig. 6.5. This implies that

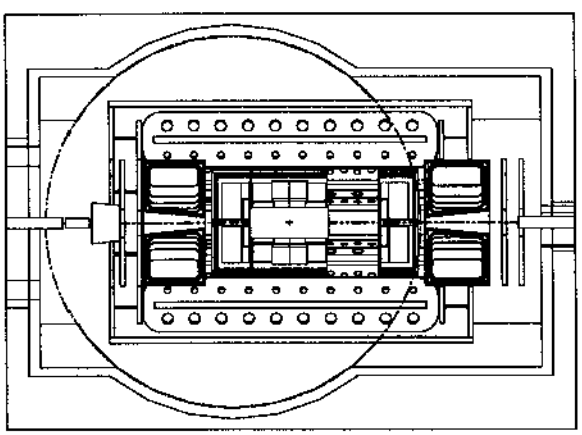

Figure 6.5: *Access position for the air-core toroid with the calorimeter end-cap and the end-cap toroid retracted on one side*

the forward calorimeters and the quadrupole shielding are displaced and that the low-β quadrupoles can partially overlap with the end-cap toroids. In this position all inner tracking detectors can be, if necessary,

removed.

For the removal of calorimeter units or end-cap toroids to the surface a shutdown of typically one year is needed. This intervention requires removal of part of the beam elements on one side of the interaction region and makes use of the 'garage' cavern extension mentioned in Section 6.1.1.

6.2.2 Iron-core toroid version

In this case, the installation sequence is conditioned by the installation of the magnet. The iron plates, delivered by industry, will be welded together into blocks of $\leq$500 t, machined, and stored for final installation as shown in Figure 6.3. First the lower part of the barrel toroid is assembled underground making use of the 2 × 250 t overhead crane. Thereafter, the calorimeter barrel can be placed on its supports directly in its final position. The upper part of the magnet can now be installed and completed with the pre-assembled coil elements.

An alternative is to install the calorimeter after the completion of the barrel part of the magnet, by pushing it into the central cavity.

The end-cap toroids are separate units and independent of the barrel part. Once the moving systems for the end-cap toroids are installed the iron units can be placed directly in place with the 2 × 250 t crane.

The installation of the muon chambers for the end-cap toroids, in particular the vertical chamber planes, will be more difficult than in the central region due to more restrictive crane coverage. This part of the installation sequence will, therefore, require special lifting tools.

The end-cap sections of the calorimeter can be installed independently of the presence of the end-cap toroids. A table is placed on the same rail system as the end-cap toroids, between the barrel and the end-cap toroids in their recessed position. The calorimeter units are then placed on the table and pushed into the inner cavity. Figure 6.6 shows an isometric view of the fully assembled detector in the cavern.

Most of the electronics of the calorimeters and the inner tracking detectors will be placed such that they can be reached without retracting the end-cap calorimeters.

A fast access, with a time scale of typically one day, can be achieved by withdrawing the end-cap toroids by about 2 m to provide access to the back of the calorimeter end-caps, as shown in Fig. 6.6.

The general access scenario is based on a complete withdrawal of the end-cap toroids by 7.75 m into the alcoves, see Fig. 6.7. It implies that the forward calorimeters are displaced and that the low-β quadrupoles can partially overlap with the end-cap

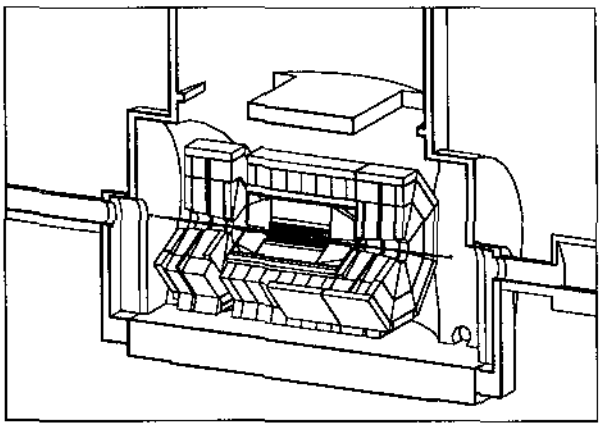

Figure 6.6: *Isometric view of the installed detector (iron-core toroid version) with one of the end-cap toroids in partially retracted position*

toroids. In this position all inner tracking detectors can be reached and, if necessary, removed. The removal of calorimeter units to the surface is also possible in this position but would require a shutdown of typically one year.

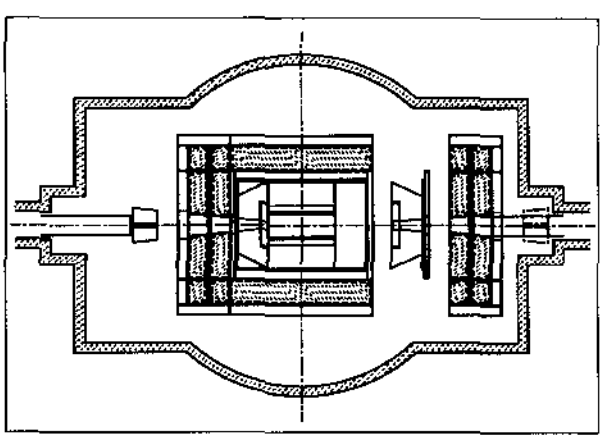

Figure 6.7: *General access position for the iron-core toroid with the calorimeter end-cap and the end-cap toroid displaced on one side*

6.3 LEP–LHC operation

Several ways of providing for the difference in height between the LEP and LHC beam have been studied.

If a solution could be found to bring the LEP beam at the LHC interaction points to approximately the height of the proton beam, only the inner tracking

detector would have to be removed to let the LEP beam pass.

In case this proves to be technically impossible, one solution would be to remove the inner detectors and the complete calorimeter with the possibility of bringing part or all detectors to the surface. This would allow for maintenance work during the time when LHC is not running.

An alternative is to remove the calorimeter end-caps and the central detector, which would liberate a cylindrical cavity of 2.3 m diameter, and to lower the complete barrel part of the detector by approximately 30 cm. Since it is very likely that the barrel part of the toroid will be placed on jacks for alignment purposes, this solution would not introduce much supplementary hardware. Raising the detector by the full distance between the LEP and LHC beams of 1.3 m is technically feasible, however, more expensive.

In the end-cap regions the solution depends on the finally chosen detector option. In case of air-core toroids, the easiest is to lower them to the ground of the cavern or to bring them to the surface. In case of an iron-core end-cap, a hole could be provided by removing special insert plugs. In both cases, it will be necessary to remove some of the muon chambers.

6.4 Schedule and Costs

6.4.1 Detector installation

Following the installation scenario developed in Section 6.2 an estimate has been made of the time needed to install the complete detector in the experimental cavern. The magnet construction and installation time estimate is based on industrial production capacity and the proposed surface assembly arrangement. For the rest of the installation, only the mechanical work has been considered, given the proposed crane capacities. All aspects of making the detector operational have been left out.

For the air-core toroid, a total of $6\frac{1}{2}$ years is needed for design, fabrication and installation. The construction and delivery of the superconducting coils is expected to take 5-$5\frac{1}{2}$ years. A further year is needed for testing of the individual coils, the pre-assembly on the surface and their installation underground. The complete detector installation is estimated to take 18 months.

For the iron-core toroid, 4 years will be needed before the installation date, $2\frac{1}{2}$ years of which would be in the surface assembly building. The underground installation is estimated to take 8 months for the barrel part and 6 months for the two end-caps. The total installation time for the iron-core version is 15 months for the barrel and an additional 9 months for the two end-caps.

6.4.2 Infrastructure costs

The cost of the infrastructure includes the installations that can be defined as common to several sub-detectors or specific extensions to the basic installation of the experimental area. Table 6.1 gives an estimate of these costs, extrapolated from the experience with the LEP detector installation.

The costs for civil engineering and surface area buildings as well as for permanent crane installations, cooling, ventilation, and electricity distribution have not been included in Table 6.1.

Table 6.1: *Infrastructure cost estimate*

Detector component	MCHF
Area infrastructure	6.5
Vacuum chamber	0.5
Area control	0.5
Installation/counting rooms	7.5
Manpower for installation	3.5
Total	18.5

6.5 Safety

6.5.1 General safety considerations

The general safety aspects of the large-hole geometry have been discussed with CERN TIS division [4]. No objection was made to the proposed geometry, since the necessary ventilation separation between the underground cavern and the large access shaft will provide adequate protection.

For the liquid argon used in the calorimeters, a 200 m^3 storage tank will be provided in a separate cavern. Its volume is sufficient to house all the argon of the calorimeters. Such a tank gives more flexibility for normal operation, and could be used as a dump for the argon in case of an emergency, thus adding to the safety of the system.

The LAr system itself has been designed to be safe under the worst possible accident, i.e. a complete breakdown of the vacuum of the barrel cryostat. The connection between main vessel and expansion vessel is of sufficient diameter (400 mm for a single pipe) to allow the liquid, pushed by the appearance of bubbles, to flow to the expansion vessel without increasing the pressure in the main vessel significantly. Then the expansion vessel acts as a phase separator, with safety valves in the gas phase opening above 1.5 atm., connected to a chimney (Ø 350 mm) for venting to

the outside atmosphere. The impact on environmental safety of venting all argon to the atmosphere has been examined and found to be negligible. This study takes into account that under the neutron flux at LHC part of the ^{40}Ar will be activated as ^{41}Ar, a β and γ emitter with a half-life of 110 min.

The large gas volume in the muon chambers (600–1500 m^3, depending on chamber technology) necessitates the use of non-inflammable gases, such as argon, Freon and carbon dioxide. These gases are toxic only in very high concentrations and the principal safety hazard is asphyxiation in confined volumes inside the detector. It is regarded as relatively easy to monitor the general air quality of the cavern and to install specific oxygen meters in confined areas.

At present the favoured gas mixture for the MSGC detector (total volume about 0.5 m^3) does include an inflammable component (DME), however, non-inflammable gases are under study. For the final design all efforts will be made to avoid the use of inflammable gases, even in small volumes.

6.5.2 shielding considerations

The expected radiation environment in the LHC experimental areas, see Chapter 7, sets strict limits on the minimum thickness of shielding walls and access to parts close to the vacuum chamber.

The proposed underground caverns and chicanes for services and electronics, as well as the shielding plug in the main access shaft, have been designed following the guidelines of the CERN TIS Divison.

The shielding arrangements to protect personnel during access periods from the induced radioactivity have not yet been studied in detail. It is, however, foreseen to move the forward calorimeters and the shielding protection for the low-β quadrupoles into a shielded area during maintenance work on the end-caps.

Maintenance work on the central inner detectors is limited to short interventions, see Section 7.4; longer repair work may require the removal of the inner tracking detectors to some shielded work area.

6.6 Detector Alignment

Given the stringent requirements on spatial precision and stability for the different detector parts and the overall size and complexity of the proposed detector, alignment considerations will play a major role in the design of the detector.

Fully automated monitoring systems and high-precision alignment techniques will be employed on-line to measure the absolute dimensions and geometries of the detectors elements, their relative positions to each other, and their absolute positions with respect to the beam line.

For the measurement of the locations of reference points on the outside of the detector, close-range photogrammetry techniques offer an interesting possibility. Precisions of 1/250 000 and better can be reached. Cameras and photo scanners, using CCD techniques, with an accuracy of better than 1 μm, are commercially available.

The crustal movements of the cavern can be monitored using clinometers, installed close to the detector, together with reference points embedded deep into the bed rock.

References

[1] Freysinet/EDF-CLI, CERN Manutentions Lourdes, DGC/BL/CK/674-92 (1992)

[2] See CERN civil-engineering group drawing LHC/ES1/2000-0611/B

[3] See CERN vacuum group drawing: 06/LHC/VXEYA/0001/B

[4] Minutes from meeting on Safety aspects of the LHC Experimental Areas held on 18 October 1991

7 Radiation Environment

Detailed estimates of the radiation environment for the proposed detector are essential for choosing suitable technologies for the various subdetectors. A study of the radiation levels expected for the ATLAS detector has been performed over the last two years: the most important figures are shown in the following, for a complete description the reader may refer to [1, 2, 3] and references therein.

7.1 Description of the Simulations

An assumption on the particle multiplicities and spectra arising from minimum bias collisions is the starting point for any realistic simulation. For the present study the code DTUJET [4] has been used; details about the code, physics and its performance when compared with currently available collider data can be found in [5] . The uncertainties in these predictions are discussed in [2, 6]: they are as large as 50% and represent one of the largest sources of the systematic error for the radiation estimates presented below.

The latest version of the FLUKA code [2] has been used to follow particle interactions inside the detector. This code is widely employed when simulating the interaction of high-energy beams with accelerator and detector components. It contains a detailed model for low-energy neutron interaction and transport based on a standard multigroup approach. A special cross-section library has been produced for this task [7]. A detailed description of the code features and its benchmarks can be found in [1, 2, 3].

The following components of the radiation field have been calculated assuming a yearly integrated luminosity of 10^5 pb^{-1} and an inelastic cross-section for pp events, single diffraction excluded, of 60 mb:
a) Absorbed doses in the detector;
b) Neutron fluxes;
c) Induced radioactivity and residual dose rates;
d) Neutral particle punch-through.

The detector set-up used in the simulations is sketched in Fig. 7.1. It represents a situation where the LAr technique is used for both the electromagnetic and hadronic calorimeter and the forward calorimeter is made of lead-liquid scintillator with a 5:1 volume ratio. The sensitivity of the results given here to the specific detector configuration is discussed in [2].

7.2 Total Absorbed Dose

The predicted maximum absorbed dose per year of operation in different parts of the detector is given in Table 7.1 and in Fig. 7.1. The dose levels include the contributions of all components of the radiation field.

7.3 Neutron Flux

Certain detector components (e.g. electronic devices) are sensitive to damage by low-energy neutrons. Since, in complex detector configurations, the number of low-energy neutrons is not necessarily proportional to the absorbed dose, separate assessments of cascade development in the detector have been performed. The maximum fluxes of neutrons with energies $\geq$100 keV, averaged typically over 20 cm in r or z, are presented in Table 7.1.

Hydrogenated materials are very effective in reducing neutron fluxes, especially for the component due to backscattering from the calorimeters into the central cavity [2]. The effect of a 5 cm thick polyethylene layer at the entrance face of the calorimeters, as foreseen in the ATLAS detector, is shown in Table 7.1.

7.4 Induced Radioactivity and Residual Dose Rates

The induced radioactivity is a major concern for the detector design, in particular in view of planning safety and maintenance operations. A precise assessment of the produced isotopes can hardly be performed without the detailed knowledge of the structure and composition of all detector components and therefore, at the moment, no full quantitative estimate can be given. Nevertheless, calculations have been performed, e.g. to assess the risk associated with an incident in the cryogenic system of the LAr calorimeter and the release of the argon into the atmosphere (see Chapter 6.5). The production of two isotopes has been considered: ^{41}Ar and ^{3}H, the latter being mainly produced in the bulk material of the calorimeters. The isotope ^{41}Ar ($T_{1/2}$ = 1.83 h) is mainly produced via thermal neutron capture and it is the major source of LAr radioactivation. The production cross-section is well known, but the thermal flux is strongly affected by small amounts of absorbing isotopes or hydrogen and therefore the numbers quoted in Table 7.1 can change substantially for different detector configurations. On the other hand, ^{3}H ($T_{1/2}$ = 12.4 y) is a spallation product whose production rate does not depend too much on the details of the calorimeters for a given absorber material. The numbers quoted in Table 7.1 are the activities accumulated after one fill for ^{41}Ar (numbers in brackets have been computed without the moderating layer) and after 10 years of operation for ^{3}H. Even though it is expected that the argon radioactivation will be

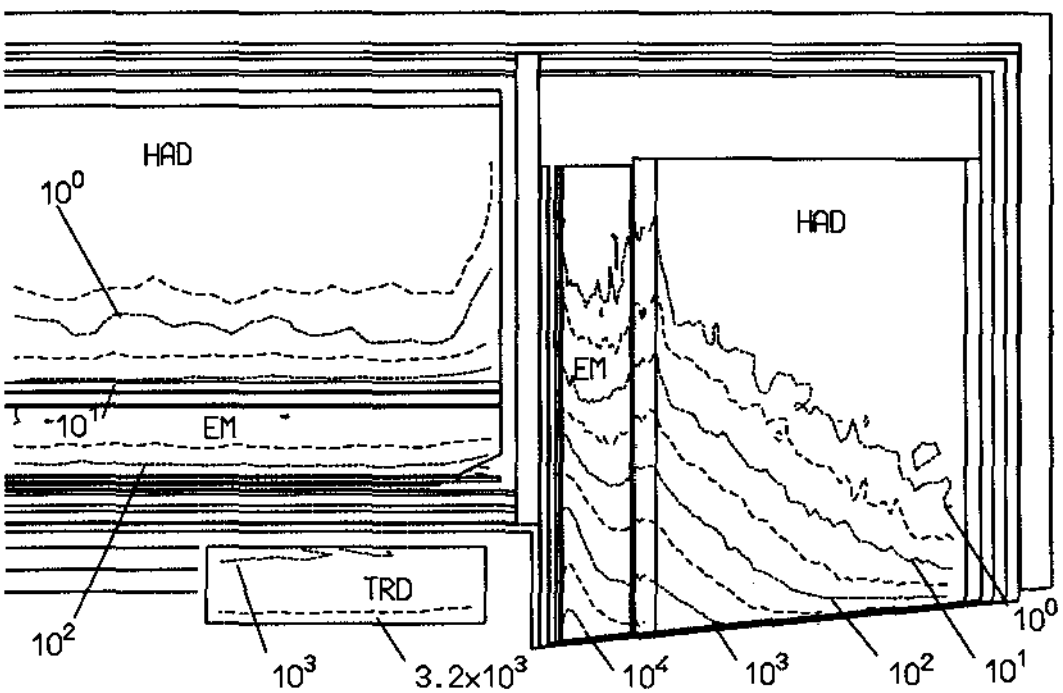

Figure 7.1: *Lines of constant radiation doses in* Gy*/year for a yearly integrated luminosity of* 10^5 pb^{-1}

Table 7.1: *Peak neutron fluxes and doses, and activation of the ATLAS detector components with and without the moderator*

Detector Component	Dose	Neutron Flux		Activity	
	(kGy y^{-1})	with mod. (cm^{-2} y^{-1})	no mod. (cm^{-2} y^{-1})	^{3}H (GBq)	^{41}Ar (GBq)
SITV	28	6.0×10^{12}	2.5×10^{13}		
SIT	1.6	1.9×10^{12}	1.9×10^{13}		
End-cap TRDs	4.0	3.4×10^{12}	2.8×10^{13}		
Barrel *em* calorimeter	0.4	6.8×10^{12}	1.7×10^{13}	0.5	20 (50)
Barrel hadron calorimeter	0.02	1.0×10^{12}	1.4×10^{12}	0.1	0.5 (1)
End-cap *em* calorimeter	21	8.2×10^{13}	9.1×10^{13}	2	50 (50)
End-cap hadron calorimeter	4.0	4.0×10^{13}	5.1×10^{13}	2	2 (2)
Forward calorimeter	830	1.1×10^{15}		100	

dominated by ^{41}Ar, it must be stressed that many other isotopes will be produced.

The dose rates of concern for maintenance work due to induced radioactivity can be calculated using established methods, independent of the detailed knowledge of the produced isotopes [1]. The rate of high-energy inelastic hadron interactions ('star' production), averaged over the outer 5 cm of a large object, can be converted into the contact dose rate by means of the so-called ω-factors. The resulting dose rates are presented in Fig. 7.2 for the customary conditions of 30 day irradiation time and 1 day of cool-down time.

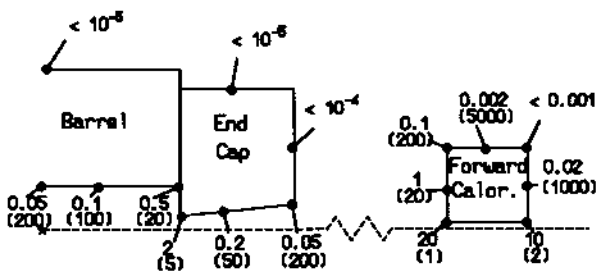

Figure 7.2: *Expected radiation levels after 1 day cool-down time (mSv/h); in parentheses the maximum allowed annual access time in hours (see text).*

The maximum number of hours that a person could work without exceeding the CERN annual reference level (15 mSv/y) is given in parentheses. It must be stressed that the quoted numbers give only an indication of the order of magnitude of the problem. They have been computed with a detector layout corresponding roughly to 12 and 14 λin the barrel and end-caps respectively. While the dose rates close to the inner surfaces are not affected by different calorimeter thicknesses, proper scaling factors have to be applied to the numbers quoted for the outer surfaces in case the calorimeter thickness changes.

7.5 Neutral Particle Punch-through

The amount of neutron and photon punch-through in the barrel and in the end-caps has been estimated using the geometry as shown in Fig. 7.1, for a luminosity of $\mathcal{L} = 2 \cdot 10^{34}$ cm^{-2}s^{-1}. Table 7.2 shows the resulting fluxes at the outer surface of the iron yoke, averaged over the indicated pseudorapidity ranges.

The neutron flux includes thermal neutrons to account for background from neutron capture. For photons a threshold of 300 keV has been applied. The same considerations as in the previous section apply when scaling to different calorimeter thicknesses.

Table 7.2: *Neutral particle punch-through*

η	Punch-through (cm^{-2}s^{-1})	
Barrel	n	γ
0-0.7	74	15
0.7-1.2	230	38
End-cap	n	γ
1.2-1.44	27	4
1.44-2.3	620	120
2.3-2.9	27000	5500

References

[1] A. Ferrari et al., The radiation environment for the ATLAS detector, ATLAS note in preparation.

[2] A. Ferrari et al. in *Proceedings of the Second International Conference on Calorimetry in High Energy Physics*, edited by A. Ereditato, (Capri, Italy, 14–18 October 1991), p. 101.

[3] G.R. Stevenson et al., CERN Divisional Report TIS/RP/92-07/CF.

[4] J. Ranft and K. Hahn, CERN Divisional Report TIS-RP/21 (1988).

[5] P. Aurenche et al., Phys Rev. **D45** (1992) 92.

[6] D.Petermann, J. Ranft and F.W. Bopp, Hadron Production at Supercolliders in the Two Component Dual Parton Model and the Small x Behaviour of the Structure Functions, Report UL-92-04 (1992).

[7] E. Cuccoli et al., A group library from JEF 1.1 for flux calculations in the LHC machine detectors, JEF-DOC-340 (1991).

8 Physics Performance

8.1 Introduction

In this section we review the performance of the ATLAS detector for a variety of physics processes. It is impossible to give credit for all the detailed and extensive work done over the past few years, nor is it possible to cover the full range of physics to be expected at LHC. We rather use a set of benchmark processes, most of which are sensitive to the detector performance, in order to illustrate the capabilities of the ATLAS detector. We thus hope to demonstrate that it will be able to cope with possible as yet unexpected new physics.

In the following, the ATLAS detector performance is usually simulated using the relevant acceptance figures, and parametrizations of the calorimeter energy and muon momentum resolutions (see Section 1). Wherever relevant, more detailed simulations are discussed; a few examples are:
- a detailed study of the photon identification power of the barrel calorimeter, in order to understand jet backgrounds to H $\rightarrow \gamma\gamma$ decays;
- a realistic simulation of the tracking and calorimetry performance to study backgrounds from radiative Z decays to H $\rightarrow \gamma\gamma$ decays;
- a study of lepton isolation using a full detector simulation to estimate the backgrounds from heavy quarks to a possible signal from H$\rightarrow$ ZZ* $\rightarrow$ 4-lepton decays.

Unless otherwise specified, the results shown correspond to integrated luminosities of 10^5 pb^{-1}, as expected for one year of high-luminosity running at LHC. The observation of a given physics signal will be declared possible if a statistical significance of 5 σ can be achieved. Lepton reconstruction efficiencies are assumed to be 90%. This includes trigger efficiencies, calorimetric and track reconstruction for electrons, and inner/outer track reconstruction and matching for muons. Effects of pile-up and possible isolation cuts are included separately wherever relevant.

If not explicitly stated otherwise, physics processes, including initial- and final-state radiation, hadronisation and pile-up of minimum bias events, were generated using the PYTHIA [6] Monte Carlo program [1]. Whenever better or more appropriate theoretical calculations were available, the production cross-sections from PYTHIA were suitably renormalized.

[6] We are deeply indebted to T. Sjöstrand, who has been of great help to us throughout this work on physics simulations.

8.2 Higgs Sector

We first discuss the search for a Standard Model neutral Higgs boson (H) over a mass range from 80 GeV to 1000 GeV. We then extend the discussion to a search for Higgs bosons in the framework of the minimal supersymmetric extension of the Standard Model (MSSM), and finally briefly describe the search for other possible scenarios for electroweak symmetry breaking.

8.2.1 Search for the Higgs boson in H $\rightarrow \gamma\gamma$ decays

This channel seems to be the only way to observe a possible signal from Higgs boson production at LHC in the mass range $80 < m_H < 130$ GeV. The observation of the signal requires good electromagnetic calorimeter resolution and very efficient rejection of jet backgrounds, in particular of isolated π^0's, which may simulate isolated photon signatures. In addition, for the direct H $\rightarrow \gamma\gamma$ signal, an accurate measurement of the photon directions with the calorimeter is needed in order to achieve the desired mass resolution. A quantitative discussion of how these parameters affect the significance of the observed signal can be found in [3].

The following analysis is based on the expected performance of the ATLAS em calorimeter + preshower system. These performance figures are the results of extensive simulation work, most of which has been verified by test-beam data (see also Section 2.3.2).

8.2.1.1 Direct production (pp$\rightarrow$ H $\rightarrow \gamma\gamma$)

This study [4] can be summarized in two parts:
- Observability of the signal above the irreducible background from photon pairs.
- Rejection of other backgrounds.

Table 8.1 summarizes, for a range of Higgs masses, the most relevant numbers used to extract the expected signal and background rates. The photon identification efficiency is assumed to be 80%, as discussed below. The acceptances include the effect of the kinematic cuts, which require two photons with $p_T^1 > 40$ GeV and $p_T^2 > 25$ GeV within $|\eta| < 2.5$ (but excluding the region spanning the crack between barrel and endcap calorimeters). An additional cut, $p_T^1/(p_T^1 + p_T^2) < 0.7$, combined with the isolation cuts described below, significantly reduces the background from quark bremsstrahlung ($qg \rightarrow q\gamma \rightarrow q\gamma\gamma$) [5]. After cuts this background is about 50% of the $\gamma\gamma$ background ($q\bar{q} \rightarrow \gamma\gamma$ and $gg \rightarrow \gamma\gamma$). Consequently the differential cross-section $d\sigma/dm$ for $\gamma\gamma$ production after cuts was multiplied by a factor 1.5 to account for the remaining quark bremsstrahlung. Con-

Table 8.1: *Observability of* $H \rightarrow \gamma\gamma$ *(direct and associated H production). The event numbers include the losses due to photon efficiency and bin width.*

	$H \rightarrow \gamma\gamma$ direct production					WH, $t\bar{t}$ H $\rightarrow \ell\gamma\gamma$+X			
Higgs mass (GeV)	80	90	110	130	150	80 WH	80 $t\bar{t}$ H	110 WH	110 $t\bar{t}$ H
$\sigma \times$BR (fb)	51	57	68	70	35	0.82	0.80	0.74	0.71
Acceptance (%)	23	30	41	46	51	15	21	23	32
Mass resolution (%)	1.45	1.40	1.22	1.19	1.12	1.45		1.22	
N_S (signal in mass bin)	600	876	1430	1650	915	14		18	
N_B (bgd in mass bin)	36000	34000	25000	20000	13500	11		7	
Stat. significance	3.2	4.8	9.0	11.7	7.9	4.2		6.8	

servatively the K-factor, taking into account QCD corrections to gg$\rightarrow$ H production [6], was not included in the signal cross-sections quoted in Table 8.1. The statistical significances were computed as the ratios $N_S/\sqrt{N_B}$, where the signal and background event rates were summed over mass bins approximately 2.5 times larger than the expected mass resolutions.

The significances of the signal vary approximately as the square root of the pseudorapidity coverage of photon detection. The mass resolutions quoted in Table 8.1 are dominated by the electromagnetic calorimeter sampling and constant terms, as shown in Fig. 2.24. Figure 8.1 shows, for m_H= 110 GeV, the expected result of a single experiment[7], where the signal is seen above the irreducible $\gamma\gamma$ background in the measured $m_{\gamma\gamma}$ spectrum.

Two other backgrounds to the Higgs signal are:

1) γ-jet and jet-jet events where one or two jets are misidentified as γ's. Figure 8.2 shows the ratios between these backgrounds and the irreducible $\gamma\gamma$ background, after kinematical cuts, as a function of the rejection power of the photon identification cuts against hadronic jets, R. To allow for the uncertainties in the overall rates of jet backgrounds and in the estimation of R (fragmentation, correlations etc.) we demand that the sum of these backgrounds (solid line in Fig. 8.2) be $\leq$ 20% of the irreducible background. This leads to a requirement of $R \geq 10^4$.

An estimate of R for the barrel em calorimeter was obtained through a 'fast' GEANT simulation of a sample of 10^5 hadronic jets, with transverse energy above 40 GeV at $\eta \sim 0$. A simplified geometrical description of the calorimeter and preshower detector was adopted, using a set of em and hadronic shower libraries. Two series of cuts were applied to estimate R:

- Calorimeter cuts, requiring an em energy deposition above 35 GeV in an area corresponding to $\Delta\eta \times \Delta\phi = 0.06 \times 0.06$, an electromagnetic energy of less than 5 GeV in 0.18×0.18 around the trigger cluster, excluding the cluster energy, a total hadronic energy of less than 5 GeV in 0.18×0.18, and a shower shape matching that expected from isolated em showers. The overall efficiency of these cuts, including pile-up effects and calorimeter noise, is 90% for isolated photons, while R is about 3000. Most of the remaining jets consist of isolated π^0's, a result in agreement with previous simulations performed at particle level without using GEANT [3].

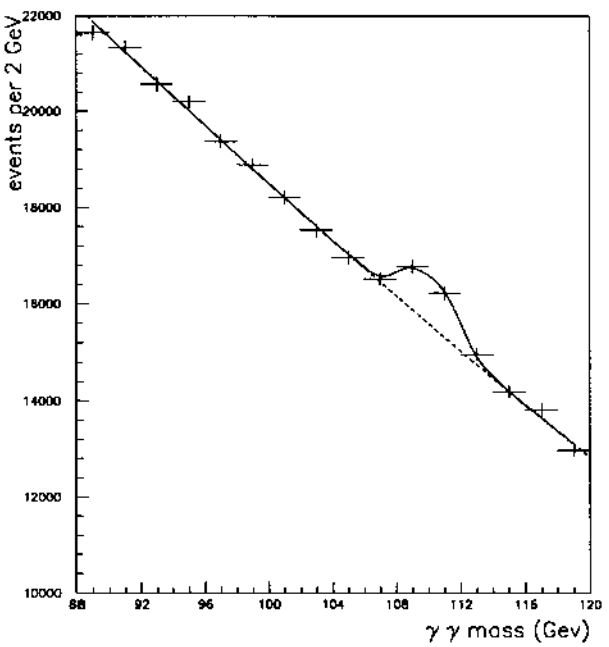

Figure 8.1: *Expected* $m_{\gamma\gamma}$ *spectrum for* $H \rightarrow \gamma\gamma$ *signal above irreducible* $\gamma\gamma$ *background for* m_H = *110 GeV and* 10^5 pb^{-1}

[7] Monte Carlo simulation with expected bin-by-bin statistical fluctuations.

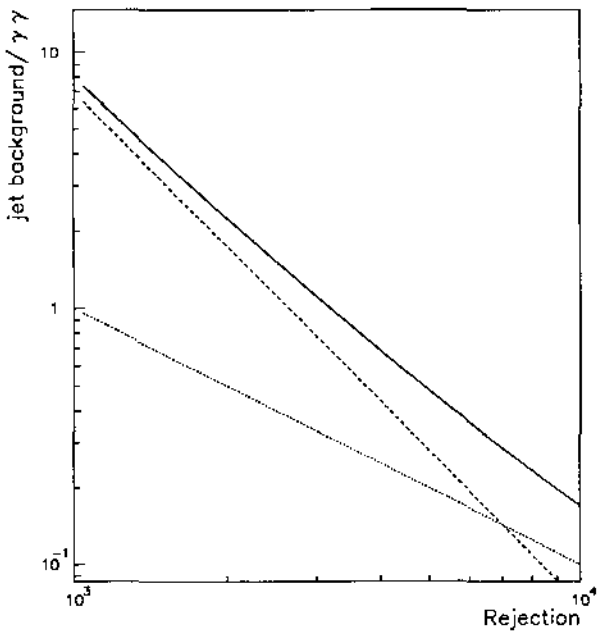

Figure 8.2: *Expected ratio of jet-jet to $\gamma\gamma$ (dashed) and γ-jet to $\gamma\gamma$ (dotted) rates versus rejection of photon identification cuts against jets*

• The additional factor 3 needed in rejection per jet is obtained by using the preshower information, as mentioned in Section 2.3.2. The simulation results and the test-beam measurements are in good agreement, yielding an estimated photon efficiency of 90%, which includes the photon conversion probability, for a rejection of ~ 3.5. The preshower rejection decreases strongly for π^0 energies above 100 GeV.

This study clearly demonstrates the ability of the detector to reach the desired goal in terms of photon identification.

2) Another potentially dangerous background arises from $Z \rightarrow e^+e^-$ decays, where both electrons may be misidentified as photons. For the worst case, $m_H = m_Z$, the very high rate of $Z \rightarrow e^+e^-$ decays results in a required veto efficiency of 99.8% per electron, in order to bring this rate below 10% of the expected Higgs signal rate. A complete simulation of radiative Z decays, including bremsstrahlung in the material of the inner tracking detector has been performed. Preliminary results show that a track veto, based on reconstructed track segments in the individual tracking subdetectors (see Section 3.5), achieves a rejection of 500 against electrons from $Z \rightarrow e^+e^-$ decays and of better than 100 against photons from $Z \rightarrow ee\gamma$ decays. The desired performance to reject this background can therefore be achieved, but the efficiency of the veto cuts for the $H \rightarrow \gamma\gamma$ signal, taking into account pile-up and photon conversions, is still under study.

From Table 8.1 we conclude that a signal from $H \rightarrow \gamma\gamma$ can be seen above the irreducible $\gamma\gamma$ background over most of the mass range studied. For $m_H < 90$ GeV, several years of running may be needed to obtain a convincing signal.

8.2.1.2 Associated production This channel, WH, $t\bar{t}H \rightarrow \ell\gamma\gamma+X$, differs substantially from direct $H \rightarrow \gamma\gamma$ production: the expected rates are a factor of 50 lower, the vertex position can be unambiguously defined by the lepton charged track, and there are many different sources of reducible and irreducible backgrounds. A study of known background sources has been performed [4], and only a short summary can be given here:

• Photon identification cuts have been shown above to reject jets by more than a factor 3000; the dominant background sources are therefore the irreducible $W\gamma\gamma$ and $t\bar{t}\,\gamma\gamma$.

• Large potential backgrounds from misidentified leptons are also present from Z, W, and $t\bar{t}$ leptonic decays accompanied by hard photons. They can be reduced to a level below that of the irreducible backgrounds, if the charged track veto efficiency is 99%.

• The expected rates of signal and background events (see Table 8.1) are similar in magnitude and small ($\sim$ 10 to 20 events per year). Therefore a very good understanding of the background shape will be needed before a convincing signal can be established.

8.2.2 Search for the Higgs boson in $H \rightarrow ZZ^* \rightarrow \ell\ell\ell\ell$ decays

This mode is the most promising one to search for a Higgs boson with mass between 120 and 180 GeV. In this mass range the Higgs boson width remains quite narrow. The reducible backgrounds, containing non-isolated leptons, are large, as shown in previous studies [7]. Good lepton identification at large rapidities and at as-low-as-possible transverse momenta plays a major role in the experimental sensitivity to this channel.

An analysis similar to the one reported in [7] has been performed, with emphasis on three aspects:

• Expected precision of Higgs mass reconstruction.

• Realistic estimate of rejection of non-isolated leptons from b-quark decays, using calorimetry and tracking information.

• Reconstruction of signal above background with full detector simulation.

The selection cuts applied are roughly adapted to the geometrical acceptance and expected electron energy and muon momentum resolutions of the ATLAS detector, and require:

- Two leptons with p_T> 20 GeV within $|\eta| < 2.5$.
- Two other leptons with p_T> 10 GeV within $|\eta| < 2.5$.
- One dilepton mass combination within ±6 GeV of the Z boson mass.
- The other dilepton mass above 12 GeV.

Table 8.2 shows, for various values of m_H, the expected rates of reconstructed signal events, where the 4-lepton mass is required to be within $\pm 2\sigma$ of m_H. The acceptances quoted include the effect of kinematic cuts, fiducial cuts (estimated to retain 90% of the events), and lepton selection efficiency (assumed to be 90% per lepton). If the geometrical acceptance were increased to $|\eta| < 3$ for all leptons with $p_T > 10$ GeV, the expected signal rate would increase by ~ 16% independently of m_H. If leptons

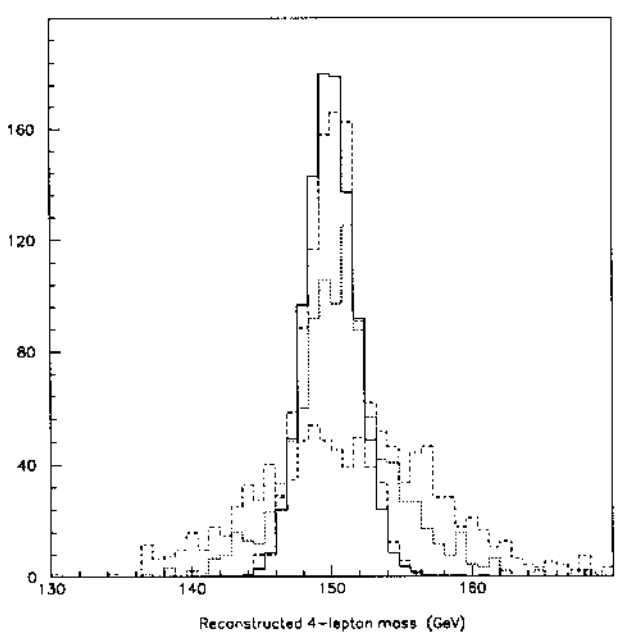

Figure 8.3: *Higgs mass resolution (m_H= 150 GeV) obtained for 4-lepton decays in various detector configurations (see text)*

with $p_T > 7$ GeV could be efficiently identified and measured, the expected rate would increase by 55% (17%) for m_H = 120 (150) GeV. Figure 8.3 shows the distributions of reconstructed 4-lepton masses in four different cases for m_H = 150 GeV. The expected resolution for the 4-electron mass (solid histogram) is ~ 1.8 GeV, before bremsstrahlung effects are taken into account. For the 4-muon mass reconstruction, Fig. 8.3 shows three cases, using parametrized resolution functions for different stand-alone muon magnet configurations, from a full air-core toroid (dashed histogram with σ = 1.9 GeV), to a barrel air-core with warm iron-core endcaps (dotted histogram with σ = 3.4 GeV), and to a full iron-core system (dash-dotted histogram with σ = 6.3 GeV). A Z mass constraint, applied to the reconstructed momenta of the relevant muon pair, improves the 4-muon mass resolution from 3.9 to 3.4 GeV and 9.6 to 6.3 GeV in the last two cases, where the detector resolution on the reconstructed dilepton mass is significantly larger than the natural Z width. If the inner tracking detector measurement is combined with any of the muon measurements discussed above, the 4-muon mass resolution is found to be similar to that obtained with the full air-core stand-alone system.

Also shown in Table 8.2 are the contributions from the three dominant background sources to the Higgs signal in this channel. The largest arises from $t\bar{t}$ events containing four leptons in the final state. This non-resonant background is reduced by demanding one dilepton mass combination compatible with the Z boson mass. It was simulated forcing both W and b-quark decays to leptons. Until a completely unbiased Monte-Carlo generation is available, we assume that the increase in rate due to 4-lepton events from $t\bar{t}$ production which do not all arise from direct W boson and b-quark decay is small after kinematical cuts [8]. After selection cuts, the non-resonant $t\bar{t}$ background is still the dominant one. We note that the $Zb\bar{b}$ background, simulated using PYTHIA or ISAJET through $gb \rightarrow Zb$, is underestimated by a large factor, as explained in [7]. We have used an exact calculation of $gg \rightarrow Zb\bar{b}$ [9], interfaced to PYTHIA, to correctly evaluate this background. Most events containing leptons from cascade b-decays are rejected by the kinematic cuts. The much smaller irreducible background from continuum Z^*Z or γ^*Z production has been increased by a factor 1.3 compared to the PYTHIA $q\bar{q} \rightarrow Z^*Z$ generation, to account also for $gg \rightarrow Z^*Z$ production [10]. Figure 8.4 (a) shows the expected Higgs signal, using all 4-lepton channels for m_H= 130, 150 and 170 GeV, above the sum of all backgrounds, for one experiment with an integrated luminosity of 10^5 pb^{-1}. Figure 8.4 (b) shows the same signal after the following lepton isolation cuts (applied after full GEANT simulation):

- less than 12 GeV excess energy measured in the calorimeter over ΔR <0.2 around the lepton direction [8]. For electrons, an area of 25 cells in the em

[8] ΔR is defined by $\Delta R = \sqrt{(\Delta\eta)^2 + (\Delta\phi)^2}$.

calorimeter ($\Delta\eta \times \Delta\phi = 0.10 \times 0.10$) is excluded from the isolation cone;
• no additional track with $p_T > 1.5$ GeV is reconstructed within $\Delta R < 0.15$.
Both particle-level studies and GEANT simulations of the calorimeter response show that the rejection against electrons from b-quark decays increases rapidly with the p_T of the electron. With the cuts given above, the $t\bar{t}$ ($Zb\bar{b}$) events are rejected by a factor $\gtrsim 25$ (15) and the efficiency for the Higgs signal is found to be $\sim 50\%$.

Table 8.2: *The observability of* $H \rightarrow Z^*Z \rightarrow \ell\ell\ell\ell$

m_H(GeV)	120	130	150	170	180
$\sigma\times$ BR (fb)	1.4	4.1	8.2	2.1	5.8
Acceptance (%)	6.8	13.7	22.4	28.2	32.5
$\sigma(m_H)$ (GeV)	1.6	1.8	2.0	2.2	2.4
No Isolation:					
N_S (mass bin)	9.5	56.3	184	59.3	189
N_B (mass bin)	282	570	836	740	616
$t\bar{t}$	267	501	720	633	523
$Zb\bar{b}$	11	61	106	96	81
Z^*Z	4	8	10	11	12
Stat. sign.	0.6	2.4	6.4	2.2	7.6
With Isolation:					
N_S (mass bin)	4.8	28.1	91.9	29.7	94.3
N_B (mass bin)	13.1	26.5	38.0	34.7	30.2
Stat. sign.	1.3	5.5	14.9	5.0	17.2

From these results and the expected significances quoted in Table 8.2, we conclude that the discovery of a Higgs signal, for $130 < m_H < 180$ GeV, will be possible in this channel, at the full design luminosity, by combining the electron and muon signatures. At luminosities of 10^{33} cm^{-2}s^{-1}, it might be possible to detect a Higgs boson signal in a narrow interval around m_H= 150 GeV. A muon system with an air-core magnet in the barrel region would be able to discover or confirm a Higgs signal in the muon channel alone, with a precision comparable to that of the calorimeter for electrons, for $m_H = 150$ GeV but not over the full mass range studied here. Any type of muon measurement which would use the inner tracking detector would also display such a capability.

8.2.3 Search for a heavy Higgs boson, $180 < m_H < 1000$ GeV

Although most of the possible decay modes have been studied in the past [11], more realistic detector simulations have been performed since. Here we briefly

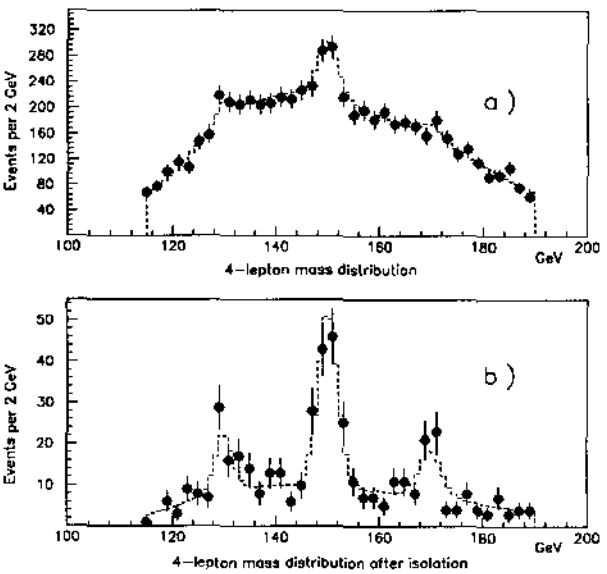

Figure 8.4: *Reconstructed 4-lepton invariant mass above background, without (a) and with (b) isolation cuts, for* m_H *= 130, 150, 170 GeV. The dashed histogram represents the expected summed signal plus background and the dots show the result of a single experiment with an integrated luminosity of* 10^5 pb^{-1}

summarize the results most relevant to the detector design :
• For $180 < m_H < 800$ GeV, the most promising channel remains the 4-lepton channel, even though the rate is very limited at the high end of the mass range. Here the Higgs width grows rapidly, as do the momenta of the leptons to be detected. Therefore the observation of a possible Higgs signal in this channel depends more on the luminosity than on detector performance. Previous studies, using the most recent theoretical calculations [12], showed that a Higgs boson with $m_H \leq 800$ (500) GeV should be detected in this channel for an integrated luminosity of 10^5 (10^4) pb^{-1}. Figure 8.5 shows the reconstructed 4-lepton mass distribution for $m_H = 800$ GeV together with the dominant background from ZZ continuum production, through $q\bar{q}$ or gg fusion. Shown are the expected distributions for a set of cuts which steadily improve the significance of the Higgs signal. In particular, the cuts imposing the presence of one or two reconstructed tag jets in $2 < |\eta| < 5$ with $p_T > 20$ GeV, improve the significance of the signal, although the number of events is quite small. We will come back to jet tagging in the discussion of $H \rightarrow WW$ decays. At lower masses the signal rates are high, such that with an integrated luminosity of 10^4 pb^{-1} a Higgs boson with mass between 200 and

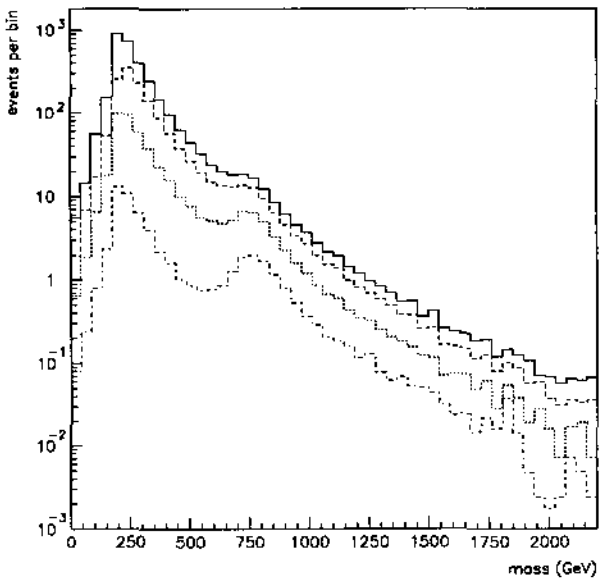

Figure 8.5: *Expected* $H \rightarrow ZZ \rightarrow 4\ell$ *signal above continuum background for* $m_H = 800$ *GeV, with a succession of cuts applied (see text): all events in acceptance (solid); events with Z transverse momentum larger than* $m_{ZZ}/4$ *(dashed); events with one reconstructed tag jet (dotted); events with two reconstructed tag jets (dot-dashed)*

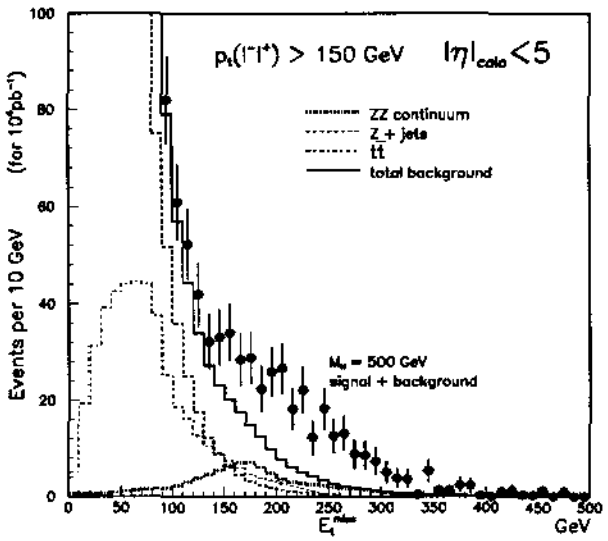

Figure 8.6: *Expected* E_T^{miss} *spectrum for the* $H \rightarrow ZZ \rightarrow \ell\ell\nu\bar{\nu}$ *signal above various backgrounds: Z+jet events (dashed), ZZ continuum (dotted) and* $t\bar{t}$ *(dash-dotted). The full histogram corresponds to the summed background, and the expected signal from one experiment, for* $m_H = 500$ *GeV and* 10^4 pb^{-1} *is shown above this background*

300 GeV may be detected separately in the 4-muon and 4-electron channels.

• For Higgs masses larger than the reach accessible to the 4-charged-lepton channel, the $H \rightarrow ZZ \rightarrow \ell\ell\nu\bar{\nu}$ channel may be considered. This channel benefits from six times more rate, but the decay cannot be completely reconstructed because of the escaping neutrinos. The expected spectrum of missing transverse energy, E_T^{miss}, is shown for $m_H = 500$ GeV and one year of running at 10^{33} cm^{-2}s^{-1}, in Fig. 8.6 and for $m_H = 700$ GeV and an integrated luminosity of 10^5 pb^{-1} in Fig. 8.7. The background below the signal is dominated by the irreducible $ZZ \rightarrow \ell\ell\nu\nu$ continuum, with smaller contributions from Z+jet, $t\bar{t}$ and WZ production [13]. The potentially very dangerous Z+jet background dominates for $E_T^{miss} < 150$ GeV. It may arise from Z+jet events, where one jet (or more) either escapes the detector acceptance (see Fig. 2.3 in Section 2.2.3) or is mismeasured in the calorimeter due to cracks (see Fig. 2.25 in Section 2.7). Using a parton-level simulation, it was found that such events occur with a probability of $\sim$ 20% (0.5%) for the barrel/endcap (endcap/forward) cracks. The simulated single particle responses in the vicinity of these cracks were used to estimate the non-Gaussian tails in the E_T^{miss} resolution for Z+jet events. For E_T^{miss} values larger than 100 GeV, such effects are found to result in a less than 10% increase of the E_T^{miss} rate. Even when detector effects are accounted for, the dominant contribution to the Z+jet background arises from high-p_T neutrinos from semi-leptonic decays of b-quarks produced in association with a Z boson, provided that the active calorimeter coverage extends to $|\eta| \geq 4.5$. Also shown in Fig. 8.7 is the expected E_T^{miss} spectrum from minimum bias pile-up. This background is dominant for E_T^{miss} values below $\sim$ 50 GeV but is negligible for E_T^{miss} values larger than 100 GeV. Pile-up from rarer processes, such as $b\bar{b}$ events with true E_T^{miss}, is found to be negligible.

Even though the statistical significance of the Higgs signals shown in Figs. 8.6 and 8.7 is large, these signals are very broad and the backgrounds will not be perfectly known. Recent calculations [14] of QCD corrections to ZZ and WZ continuum production show that these corrections increase the rate of high-p_T bosons (i.e. of large E_T^{miss} for $Z \rightarrow \nu\bar{\nu}$ or $W \rightarrow \tau\nu$ decays) in such events. If applied to the distributions shown in Figs. 8.6 and 8.7 these corrections would increase the ZZ continuum rate at large E_T^{miss} by approximately a factor 2, and the WZ continuum rate by approximately a factor 5, bringing it

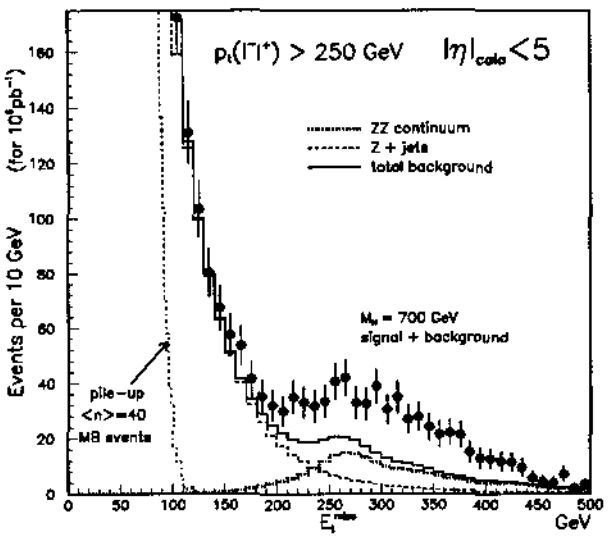

Figure 8.7: *Expected E_T^{miss} spectrum for the $H \rightarrow ZZ \rightarrow \ell\ell\nu\bar{\nu}$ signal above various backgrounds: Z+jet events (dashed), ZZ continuum (dotted) and minimum bias pile-up (dash-dotted). The full histogram corresponds to the summed background, and the expected signal from one experiment, for m_H = 700 GeV and 10^5 pb^{-1} is shown above this background*

to $\sim$ 40% of the ZZ continuum.

Until more detailed studies are available, we tentatively conclude that a Higgs boson may be discovered in this channel, for $500 \leq m_H \leq 800$ GeV. We note (see below) that jet tagging may reject most of the dominant backgrounds, which are still significant at large E_T^{miss}.

• We conclude this overview of the Higgs sector by some remarks on the non-purely-leptonic decay modes of the Higgs boson, i.e. $H \rightarrow WW \rightarrow \ell\nu jj$ (and similarly $H \rightarrow ZZ \rightarrow \ell\ell jj$) decays. The expected rates for $H \rightarrow WW \rightarrow \ell\nu jj$ decays are quite large, $\sim$ 3000 events from qq $\rightarrow$ qqH production alone for m_H = 1 TeV and an integrated luminosity of 10^5 pb^{-1}. Unfortunately the background rates are much larger, with approximately equal contributions from $t\bar{t}$ and W+jet events.
In the following we describe a study of the $H \rightarrow WW \rightarrow \ell\nu jj$ channel, for m_H = 1 TeV [15]. This study aimed at understanding the required calorimeter performance in terms of reconstructing $W \rightarrow jj$ final states from high-p_T W decay in the central region ($|\eta| < 2$), and of tagging the outgoing quark jets in the forward region ($2 < |\eta| < 5$). The Higgs signal is compared to the $t\bar{t}$ background, which was shown to be the most dangerous one in a previous study [16].

In the central region, the following algorithm is used to reconstruct $W \rightarrow jj$ decays: in a first step at least two jets are required, with $p_T > 50$ GeV within a cone of $\Delta R < 0.2$. A granularity of 0.10 × 0.10 in $\Delta\eta \times \Delta\phi$ was assumed for both the electromagnetic and hadronic calorimeters. The dijet mass was computed using all cells with $E_T > 3$ GeV within $\Delta R < 0.5$ around the centre of gravity of the two jets. This algorithm optimizes the dijet mass resolution, while remaining almost insensitive to pile-up effects. After kinematical cuts, $m_{jj} = m_W \pm 15$ GeV, $p_T^{\ell,\nu} > 100$ GeV and $p_T(W \rightarrow jj$ and $W \rightarrow \ell\nu) > 350$ GeV, the efficiency is 22% for the Higgs signal and $\sim 3 \cdot 10^{-4}$ for $t\bar{t}$ events. The efficiency for reconstructing the $W \rightarrow jj$ signal is sensitive to the calorimeter granularity, which, if increased (decreased) to 0.15 × 0.15 (0.05 × 0.05), leads to a loss (gain) of 32% (23%) of the events. We expect a hadron calorimeter granularity of 0.10 × 0.10 to be adequate, given the much finer granularity of the electromagnetic calorimeter. The expected resolution on the reconstructed W mass is 5.7 GeV, increasing to 7.4 GeV without the 3 GeV cell threshold and decreasing to 4.7 GeV in the absence of pile-up.

Jet tagging [17] is expected to considerably improve the significance of a possible signal produced through WW or ZZ fusion. In order to minimise pile-up effects, a tag jet is defined as a jet cluster, reconstructed within $\Delta R < 0.5$, for cells with $E_T > 3$ GeV, and $2 < |\eta| < 5$, with $p_T^j > 25$ GeV. The optimum cut on the tag jet energy, E^j, is around 600 GeV.

Table 8.3: *Expected rates for $H \rightarrow WW \rightarrow \ell\nu jj$ signal (m_H = 1 TeV) and $t\bar{t}$ background, using jet tagging cuts (see text)*

	Signal	$t\bar{t}$ background
Central cuts and reconstruction	640	24000
Single jet tag $E^j > 600$ GeV $p_T^j > 25$ GeV	390	4500
Double jet tag $E^j > 600$ GeV $p_T^j > 25$ GeV	90	200

Table 8.3 shows that the signal significance is improved by jet tagging cuts. The contribution from pile-up is small: 12% (5%) of the single (double) tag $t\bar{t}$ background events. Most of these pile-up tags arise from QCD jets produced at large rapidity. The jet tagging performance is not sensitive to variations of the forward calorimeter performance around its

baseline design values. In addition to the $t\bar{t}$ background, we expect an equally large contribution from $W \rightarrow \ell\nu$ events, accompanied by two hard jets with mass within ± 15 GeV of the W mass. This background has been shown to be more easily rejected by jet tagging cuts than the $t\bar{t}$ background [16]. We note however, that, as in the $H \rightarrow ZZ \rightarrow \ell\ell\nu\overline{\nu}$ case, the shape of the m_{WW} distribution of the backgrounds may not be known well enough to convincingly extract a possible Higgs signal in this channel for an integrated luminosity of 10^5 pb^{-1}.
Jet tagging will be a very useful experimental signature for isolating WW fusion processes, even in the absence of a Higgs boson signal.

8.2.4 Higgs sector in the Minimal Supersymmetric Standard Model

As discussed in detail in recent work [18], two Higgs doublets are required in the MSSM, resulting in five physical states, two charged (H^+, H^-) and three neutral, referred to as h (lighter scalar with mass m_h), H (heavier scalar with mass m_H), and A (pseudoscalar with mass m_A). At tree level all the masses in the MSSM Higgs sector can be computed in terms of two parameters, usually chosen to be m_A and $\tan\beta$, the ratio of the vacuum expectation values of the two Higgs doublets. Radiative corrections to the Higgs boson masses have been computed and are quite large, in particular in the case of m_h, for large values of the top quark mass, m_t [19].

We summarise the potential of the ATLAS detector in the MSSM Higgs sector [9] in Fig. 8.8. Shown are contours, corresponding to a discovery with 5 standard deviation significance, in the (m_A, $\tan\beta$) plane, for various possible Higgs boson signatures and for $m_t = 140$ GeV [4, 20]:

- A large region in the parameter space, shown to the right of curve a and inside curve b, can be explored through a search for $h \rightarrow \gamma\gamma$ (and to a lesser extent $H \rightarrow \gamma\gamma$) decays. These are in general suppressed in rate compared to the Standard Model $H \rightarrow \gamma\gamma$ decays discussed in Section 8.2.1, and can only be detected at the highest LHC luminosities.
- At these luminosities the region in parameter space inside curve c, can be explored through a search for $H \rightarrow ZZ \rightarrow 4\ell$ decays. The region is quite small since this decay is strongly suppressed for large values of $\tan\beta$ or when the decay channel $H \rightarrow t\bar{t}$ is kinematically allowed.
- The region to the left of curve d, where $m_A < 100$ GeV, can be explored through the search

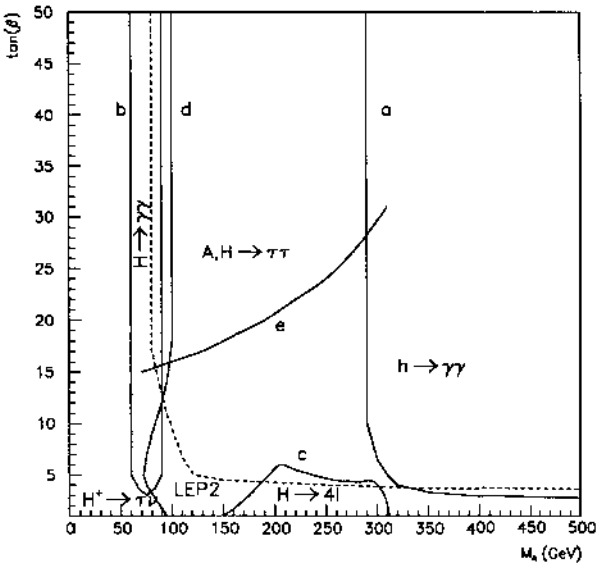

Figure 8.8: *Discovery contour curves (5σ) in the (m_A, $\tan\beta$) plane for various Higgs signals in the MSSM (see text)*

for charged Higgs bosons in top-quark decays, as described in Section 8.3.2. For larger values of m_t, the contour shown for this channel is displaced towards larger values of m_A (for example the region $m_A < 150$ GeV would be explored for $m_t = 200$ GeV).
- Finally a large fraction of the remaining parameter space, above curve e, can be explored through $A \rightarrow \tau\tau$ and $H \rightarrow \tau\tau$ decays, where at least one of the τ's decays leptonically [20]. This requirement strongly suppresses purely hadronic backgrounds and provides for a straightforward trigger. As discussed, however, in studies of Standard Model $H \rightarrow \tau\tau$ decays [21], such a signal can only be well reconstructed kinematically at moderate luminosities and with good calorimeter coverage, which together allow for a precise reconstruction of missing transverse energy and therefore of the invariant mass of the tau lepton pair.

Also shown in Fig. 8.8 is the sensitivity to the MSSM Higgs sector expected at LEP II for an integrated luminosity of 500 pb^{-1} and at 190 GeV centre-of-mass energy [22]. We stress that, as in the case of the Standard Model Higgs boson, we did not include the K-factor of ~ 1.7 for the signal in this study.

In conclusion, a large region of the MSSM parameter space can be explored in the Higgs sector even at moderate LHC luminosities. This is an important aspect of physics at LHC and it involves a variety of channels, which require precise and efficient reconstruction of photons, electrons, and muons at high

[9] Higgs boson decays to supersymmetric particles are assumed to be kinematically forbidden

luminosity, and of tau leptons, missing transverse energy and also b-quark secondary decay vertices (see Section 8.3.2.1) at moderate luminosities.

8.2.5 Gauge boson pairs at high mass

If no Higgs boson is found below $\sim$ 1 TeV, an important goal of the LHC will be the exploration of alternative mechanisms for restoring unitarity in gauge boson scattering, such as dynamical symmetry breaking scenarios. Some technicolour models [23] predict longitudinal gauge boson pair resonances such as the techni-rho (ρ_{tc}), a composite vector boson decaying into gauge boson pairs, or more general vector isotriplets ($V^{\pm}$, V^0) as in the BESS model [24]. In general these models predict resonant signals in the production of pairs of longitudinal gauge bosons (W_LW_L, Z_LZ_L, and W_LZ_L).

Here we study the W_LZ_L resonance, corresponding to the techni-rho, ρ_{tc}, and the techni-omega, ω_{tc}, of isospin 0, which decays into $Z_L\gamma$. In the following only leptonic final states are considered.

8.2.5.1 W_LZ_L resonance The signal production cross-section is $\sim$ 40 fb, resulting from a combination of $W_LZ_L \rightarrow W_LZ_L$ scattering and of direct $q\bar{q}' \rightarrow W_LZ_L$ production. The dominant background sources are:

- $t\bar{t}$ decays with three charged leptons in the final state and one dilepton combination with mass close to m_Z;
- Continuum $q\bar{q}' \rightarrow WZ$;
- Continuum $WZ \rightarrow WZ$ production, with one or both of the gauge bosons transversely polarized;
- $\gamma W \rightarrow WZ$ production.

The last two backgrounds have not been simulated, but they are accounted for by increasing the other contributions by 50% [25]. After energy smearing, E_T^{miss} was computed from the momentum vectors of all particles observable in the detector. A W mass constraint was applied to the lepton-neutrino pair in order to reconstruct the total invariant mass of the WZ system. Isolation cuts are very effective at reducing the large $t\bar{t}$ background, for the high lepton momenta expected here. After simple kinematic cuts and this last cut, the $t\bar{t}$ background is negligible. Figure 8.9a displays the reconstructed WZ mass for the expected signal and the summed background, in the case of a ρ_{tc} of mass 1.0 TeV and width 220 GeV.

8.2.5.2 $Z_L\gamma$ resonance This resonance [26] can easily be reconstructed in final states with Z decays to charged leptons. The dominant sources of backgrounds are continuum $Z\gamma$ production and Z+jet production where one jet fakes an isolated photon. A rejection R against jets of $\sim$ 1000 is sufficient to reduce this last background to a negligible level. Figure 8.9b shows the reconstructed $Z\gamma$ mass distribution for the expected signal and the summed background, in the case of an ω_{tc} of mass 1.5 TeV and width 120 GeV. The production cross-section is 50 fb for this ω_{tc} mass.

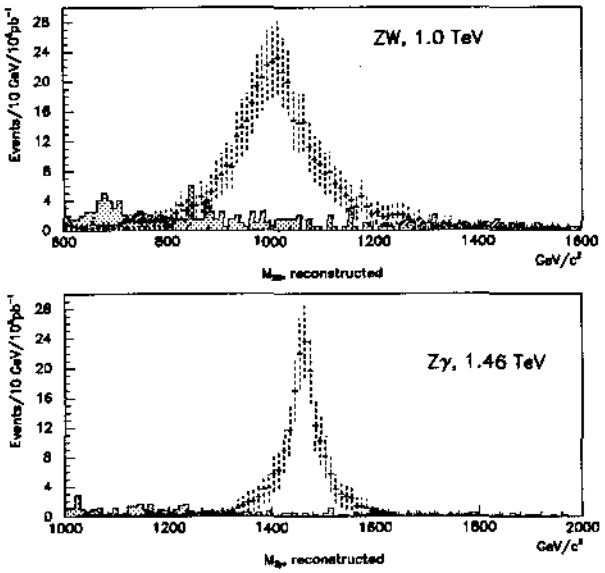

Figure 8.9: *Reconstructed masses for high mass resonances decaying into gauge boson pairs : (a) a 1 TeV ρ_{tc} to WZ to 3-lepton decays; (b) 1.5 TeV ω_{tc} to $Z\gamma$ with Z to 2-lepton decays*

From these studies we conclude that WZ and $Z\gamma$ resonances with masses below $\sim$ 2.0 TeV may be observed at the LHC in purely leptonic decay modes.

8.3 Top-quark Physics

A combined analysis of existing electroweak data suggests that the most probable value of m_t is around 140 GeV and that m_t cannot be much larger than 200 GeV [27]. Experiments at Fermilab may therefore discover the top quark during the coming years. Precise measurements of m_t and studies of top-quark decays will, however, not be possible before LHC, where copious production of $t\bar{t}$ events ($\sigma_{t\bar{t}} = 3$ nb for $m_t = 140$ GeV) will yield $\sim$ 25000 events per day even at luminosities as low as 10^{32} cm^{-2}s^{-1}. Purely hadronic final states from $t\bar{t}$ production are swamped by QCD multijet backgrounds. In the following we consider only final states containing at least one high-p_T isolated charged lepton (electron or muon), which

will allow a rather clean tagging of $t\bar{t}$ events and provide for a straightforward trigger.

8.3.1 Measurement of m_t

The top-quark mass is an important parameter in the Standard Model, and may not be known to better than $\sim$ 10 GeV at the start-up of LHC. Electroweak measurements at LEP, combined with a precise measurement of m_t, may ultimately set limits on m_H. The uncertainty on m_H would then have equal contributions from LEP errors and a 5 GeV error on m_t [28]. This sets the scale for the precision needed for a measurement of m_t at LHC.

8.3.1.1 Measurement of m_t in hadronic top-quark decays This is the only channel for which a complete reconstruction of m_t can be performed. A lepton, with $p_T > 40$ GeV, is required from one of the top-quark decays, in association with at least three reconstructed jets within $|\eta|< 2$ and with $p_T^1 >50$ GeV and $p_T^{2,3} > 40$ GeV in the hemisphere opposite to the lepton. Two of these jets are required to have an invariant mass within $\pm$20 GeV of the W mass.

Figure 8.10 shows, for the cuts described above and for $m_t = 130$ and 200 GeV, the reconstructed 2-jet and 3-jet invariant mass distributions. The shaded (white) distribution corresponds to $t\bar{t}$ events reconstructed with (without) b-tagging. A jet is tagged as a b-jet if it contains one associated charged track with $p_T> 2$ GeV and an impact parameter greater than 200 μm (see Section 3.5.5). Events are retained in the shaded histogram for the 3-jet mass, if the 2-jet combination corresponds to jets not tagged as b-jets and if the third jet is tagged as a b-jet. The background shown in Fig. 8.10 corresponds only to the combinatorial background from jets in $t\bar{t}$ events. The signal to background ratio in the 3-jet mass peak is improved by a factor 4 with the chosen b-tagging cuts, at the expense of losing $\sim$ 30% of the signal. Larger improvements can be obtained by requiring the presence of a second b-jet, which would reduce to a negligible level most of the other potential backgrounds to the $t\bar{t}$ signal:

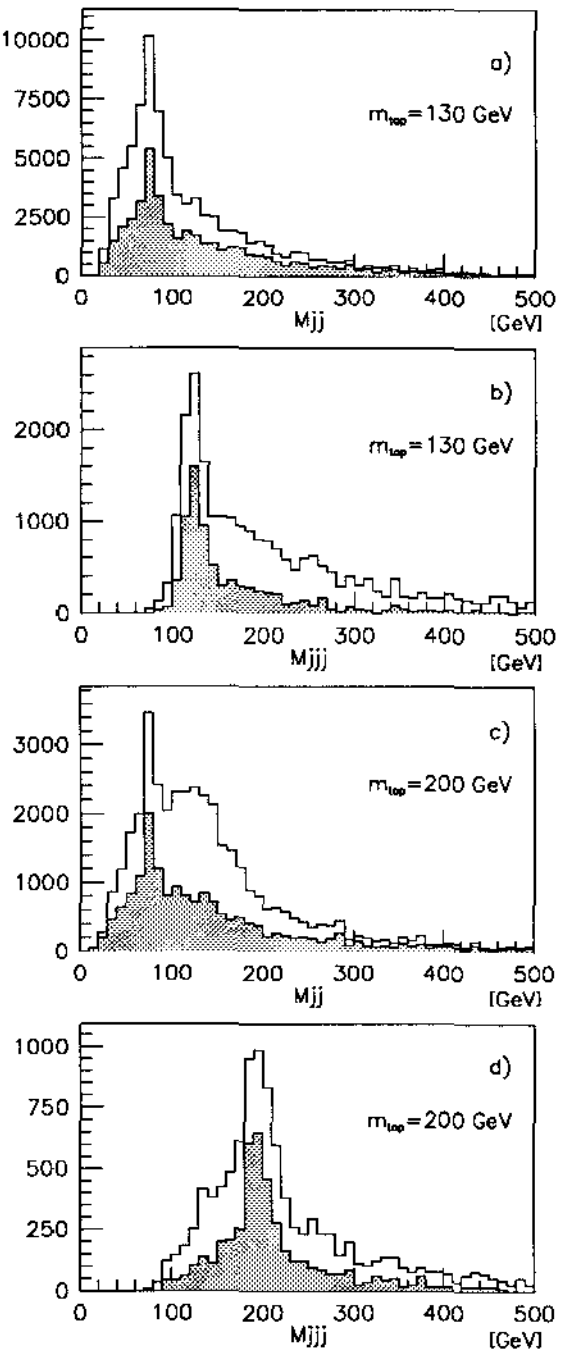

Figure 8.10: *Reconstructed 2-jet and 3-jet masses, with and without b-tagging, above combinatorial background (see text), for m_t=130 GeV (a) and b)), and m_t=200 GeV (c) and d)).*

- W+jet events, which after cuts appear at a rate comparable to the combinatorial background shown in Fig. 8.10;
- $b\bar{b}$ +jet events, which can be reduced to a negligible level with lepton isolation cuts and, if needed, by requiring $E_T^{miss} > 50$ GeV;
- multijet events, where one jet is misidentified as an

electron. A combined rejection, from electron identification cuts and, if needed, the E_T^{miss} cut quoted above, of $\sim 10^5$ would reduce such backgrounds to a negligible level.

The top signal can be extracted in this channel for an integrated luminosity smaller than 30 pb^{-1}. For 10^3 pb^{-1} the statistical error on m_t is $\sim$ 1 GeV. The systematic error is expected to be larger, even when using the reconstructed 2-jet mass peak to calibrate the hadronic calorimeter energy response. It is difficult to estimate precisely its value before inspecting real data. The error is estimated in a conservative way as the sum of the effects of uncertainties on b-fragmentation (Δm_t = 3 GeV), on the calorimeter response to low energy hadrons (Δm_t = 4 GeV), and on the jet definition (Δm_t = 3 GeV) [29]. This gives a total error of $\pm$6 GeV, which would decrease with a good understanding of the calorimeter response and of b-jet fragmentation.

8.3.1.2 Measurement of m_t in multilepton channels Multilepton channels (especially the isolated eμ channel) can be used to extract a very clean top quark signal. The dominant background to the eμ channel is expected to be $b\bar{b}$ production followed by b and $\bar{b}$ decays to electron and muon. Other background sources (WW $\rightarrow$ eμ, Z $\rightarrow \tau\tau \rightarrow$ eμ and Wb$\bar{b} \rightarrow$ eμ) are found to be negligible. A clean signal, with good acceptance ($\sim$ 10% for m_t = 200 GeV), can be obtained for $p_T^{e,\mu} > 50$ GeV and $20° < \Delta\phi(e\mu) < 160°$. Using lepton isolation cuts, even a moderate rejection of $\sim$ 10, for $p_T > 50$ GeV, against leptons from b-quark decay reduces the $b\bar{b}$ background to two orders of magnitude below the signal. The expected observable cross sections after these cuts, varies from $\sim$ 5 to 1.5 pb for m_t from 130 to 200 GeV, which gives a clean top signal with only a few pb^{-1} of integrated luminosity.

The best measurement of m_t can then be obtained by considering events where one b decays to a muon. The invariant mass of this muon and the isolated lepton with the opposite sign, coming from the same top-quark decay, is sensitive to m_t [30]. This method will provide the most accurate measurement of m_t, but requires integrated luminosities larger than 10^4 pb^{-1}. We refer the reader to Ref. [29] for details and summarize the main results here. For m_t = 140 (200) GeV, one expects 5000 (2900) events for 10^4 pb^{-1} . This leads to an expected statistical error on m_t of 1.2 (1.9) GeV with a systematic error of 4.0 (5.0) GeV. In this channel we expect the experimental systematic errors to be negligible, so the systematic error is essentially of a theoretical nature:
- Uncertainty on p_T^{top}. There is a small dependence of the dilepton mass on the p_T of the top quark at production. The resulting uncertainty on m_t is estimated to be $\sim \pm 2$ GeV.
- Uncertainty in b fragmentation. The relative error on m_t is $\sim$ 0.5 $\times \sigma(x_B)/x_B$ (where x_B is the fraction of the b quark energy taken by the B hadron). The fragmentation of b quarks is now measured by LEP with an error of $\sim$ 1.5% [31], but this cannot be naively extrapolated to top decay at this level of precision because the environments are different. Therefore, we conservatively quote an error of $\sim$ 2.2% on m_t, which will probably be reduced in the future.

8.3.2 Study of top-quark decays

In extensions of the Standard Model with charged Higgs bosons, H^+, as for example in the MSSM (see 8.2.4), the decay t $\rightarrow$ bH^+, if kinematically allowed, can compete with the standard t $\rightarrow$ bW decay. The H^+ decays to $\tau\nu_\tau$ or $c\bar{s}$ depending on $\tan\beta$. For a given m_t, the branching ratios relevant for t $\rightarrow$ bH^+ searches (neglecting the decay $H^+ \rightarrow$ Wh) can be computed from m_{H^+} and $\tan\beta$. In the range $1 < \tan\beta < 50$, the t$\rightarrow$ bH^+ branching ratio varies from 50% to 4%. Over most of this range, $H^+ \rightarrow \tau\nu_\tau$ is the dominant decay mode and $H^+ \rightarrow c\bar{s}$ dominates only for $\tan\beta < 1.5$.

Before discussing direct searches of t$\rightarrow$ bH^+, we note that an inclusive measurement of BR(t $\rightarrow$ bW) can be obtained by comparing the observed rates in the single isolated lepton channel and in the two isolated lepton channel. An accuracy of $\sim$ 5%, limited by the uncertainty on the background in the single isolated lepton channel, can be achieved [29].

8.3.2.1 Search for t$\rightarrow$ bH^+, $H^+ \rightarrow \tau\nu_\tau$ A clean sample of $t\bar{t}$ events is selected by requiring an isolated high-p_T lepton (e or μ). In this sample the decay t $\rightarrow$ bH^+ will give an excess of events with one isolated τ compared to events with an additional lepton [32]. The best sensitivity to this channel is obtained by considering hadronic τ decays [33].

Top events are selected by requiring an isolated lepton with $p_T > 40$ GeV within $|\eta| < 2$. Two jets, tagged as b-jets as descibed above, with $E_T >$ 40 GeV and $|\eta| < 2$ are also required. With these cuts, the non-$t\bar{t}$ background is greatly reduced, as discussed in Section 8.3.1.1 . At a luminosity of 10^{33} $cm^{-2}s^{-1}$ hadronic τ-decays can be selected by the following cuts, aimed at rejecting backgrounds from QCD jets:
- E_T(calorimeter cluster) >30 GeV
- $\{E_T(\Delta R < 0.3) - E_T(\Delta R < 0.1)\} < 3$ GeV
- p_T of leading track pointing to cluster > 30 GeV

- E_T of cluster consistent with measured p_T
- no other track with $p_T > 5$ GeV within $\Delta R < 0.3$

These cuts enhance the right-handed τ signal from H^+ decays and tend to select $\tau \rightarrow \pi\nu$ and $K\nu$ decays because of the tracking cuts. Using particle-level simulations, a rejection against light-quark jets of ~ 500 is obtained, with $\sim 10\%$ efficiency for τ's (the simulation of the calorimeter cuts has been cross-checked using a full GEANT simulation). The number of events with an additional lepton is then compared to that with an additional τ, and the excess of τ's is calculated, after subtracting the background (coming mainly from $t\bar{t}$ events where one jet fakes a τ). Uncertainties on the τ excess arise from the limited statistics and also from the systematic error on the τ efficiency and on the number of fake τ's (assumed to be 3% each). The resulting significance of the τ

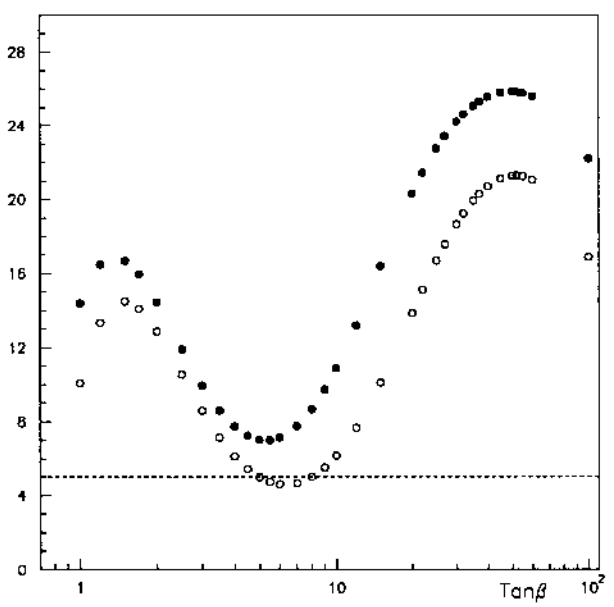

Figure 8.11: *Statistical significance of expected excess of tau leptons from charged Higgs decay in $t\bar{t}$ events versus* $\tan\beta$, *for* m_{H^+} *=100 GeV,* m_t *= 140 GeV (full circles) and 200 GeV (open circles) and an integrated luminosity of* 10^4 pb^{-1}

excess is shown in Fig. 8.11 as a function of $\tan\beta$, for $m_{H^+} = 100$ GeV, $m_t = 140$ and 200 GeV, and for an integrated luminosity of 10^4 pb^{-1}. An excess of ~ 400 τ's is expected from a charged Higgs signal, for $m_t = 140$ GeV and $\tan\beta = 6$, above 400 τ's from W decay and a residual background of 900 fake τ's. The systematic errors are the dominant source of uncertainty. Most of the $\tan\beta$ range can be covered with a significance larger than 5.

8.3.2.2 Search for $t \rightarrow bH^+$, $H^+ \rightarrow c\bar{s}$ The top events are selected as above by the presence of an isolated lepton and the H^+ mass peak is searched for in the 2-jet mass distribution. Over most of the parameter space, both the H^+ and W mass peaks can be seen, but a good jet energy resolution is useful to separate them, if m_{H^+} is not much larger than the W mass. As in Section 8.3.2.1, b-tagging can be used to reduce the combinatorial background, by vetoing b-jets in this case. Figure 8.12 displays the expected reconstructed dijet mass distributions, for $m_t = 200$ GeV, $m_{H^+} = 130$ GeV, $\tan\beta = 1.0$, and an integrated luminosity of 100 pb^{-1}. With a larger integrated luminosity of 10^4 pb^{-1}, the range $\tan\beta < 2$ can be covered for $m_{H^+} < (m_t - 20$ GeV).

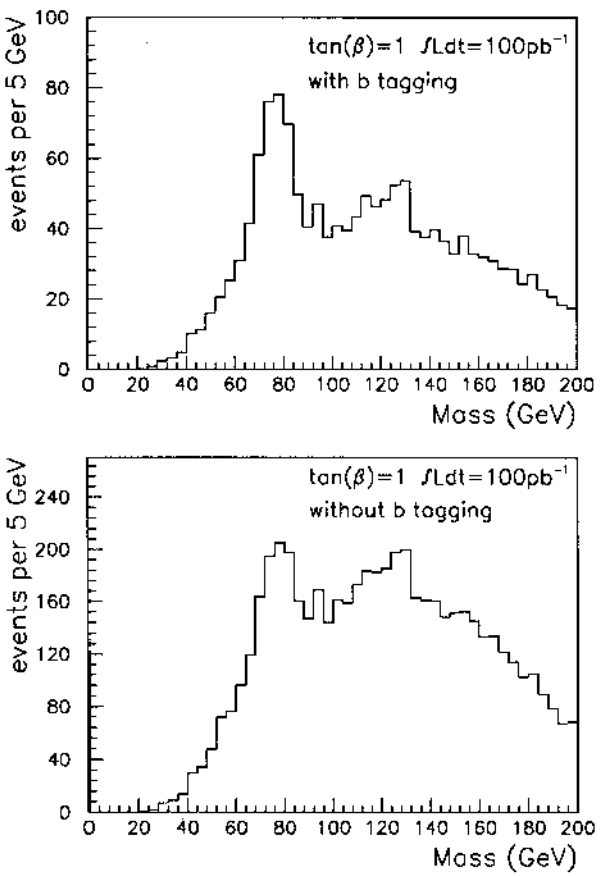

Figure 8.12: *Distribution of reconstructed 2-jet mass for charged Higgs decay to $c\bar{s}$ with m_{H^+} = 130 GeV, above the combinatorial background from $t\bar{t}$ events*

8.3.2.3 Toponium decay to $\gamma\gamma$ It has been suggested in [34] that, if $m_t < 120$ GeV, the 0^{-+} toponium state can be seen in the $\gamma\gamma$ channel. For larger values of m_t, the top-quark width becomes too

large and toponium does not exist. We use the cross-section and branching ratio estimates of [34], which however suffer from large uncertainties since the rate for this process is proportional to a large power of the strong coupling constant. Under the same assumptions as for the $H \rightarrow \gamma\gamma$ search, we conclude that the signal can be seen, for $90 < m_t < 110$ GeV, with an integrated luminosity of 10^5 pb^{-1}. This may allow a very precise measurement of the toponium mass (better than 1 GeV), and, with additional theoretical input, a very good determination of m_t.

8.3.3 Conclusions

The two most important aspects of top-quark physics at LHC will be:

- The top-quark mass measurements, for which various independent methods can be used, and an error at the level of $\lesssim 5$ GeV can be achieved, limited by theoretical uncertainties which may decrease in the future.
- The search for $t \rightarrow bH^+$ decays to investigate models with two Higgs doublets. If this decay is kinematically allowed, most of the parameter space can be covered, mainly using τ detection, but also using 2-jet invariant mass distributions.

Most of this field can be studied at low luminosity (10^{32} or 10^{33} cm^{-2}s^{-1}). To exploit it fully, it is important to measure electrons, muons, jets, E_T^{miss}, and to identify hadronic b-quark and τ decays.

8.4 Measurement of CP-violation in B-decays

B-mesons offer a possibility to test whether CP-violation is correctly described by the three-generation quark mixing matrix (CKM matrix) [35]. As an example, the decay channel $B_d^0 \rightarrow J/\psi K_S^0$ has been studied in a preliminary way. At LHC, the expected production cross-section for b-quarks is very large, 0.1 to 0.7 mb [36]. B-events can be tagged by an inclusive single muon trigger, with $p_T > 20$ GeV and $|\eta| < 2$. Given the total combined branching fraction, $Br(b \rightarrow B_d^0) \times Br(B_d^0 \rightarrow J/\psi K_S^0) \times Br(J/\psi \rightarrow \ell^+\ell^-) \times Br(K_S^0 \rightarrow \pi^+\pi^-)$ of $\sim 10^{-5}$ [37], we expect to collect about 12000 $b\bar{b}$ pairs per year, with a muon tag [10] on one side and a $B_d^0 \rightarrow J/\psi K_S^0$ decay on the other.

A first estimate of the B_d^0 reconstruction efficiency was performed using a simple simulation with the following cuts [38]:

- all four final-state particles are within the tracking volume with $p_T > 1$ GeV;
- the K_S^0 decay length in the transverse plane is between 1 cm and 30 cm;
- the transverse momentum of the J/ψ is larger than 10 GeV;
- the angle between the K_S^0 and the $J/\psi < 45°$.

The lepton identification efficiency is assumed to be 80%, and the overall track-finding efficiency to be 95%. Table 8.4 shows the reconstruction efficiencies, ϵ_{rec}, and expected rates of reconstructed events, N_{rec}, for various η-coverages of the tracking detector and for an integrated luminosity of 10^4 pb^{-1}, corresponding to one year of running at 10^{33} cm^{-2}s^{-1}. The expected rates for reconstructed events could be increased substantially by lowering the muon p_T threshold to 6–12 GeV (depending on the magnet system), but dilution effects, reconstruction efficiencies and backgrounds are expected to be worse.

Table 8.4: *Number of reconstructed events* $B_d^0 \rightarrow J/\psi K_S^0 \rightarrow \ell^+\ell^-\pi^+\pi^-$.

	$\lvert\eta\rvert \leq 1.5$	$\lvert\eta\rvert \leq 2.0$	$\lvert\eta\rvert \leq 2.5$
ϵ_{rec}	0.08	0.10	0.13
N_{rec}	920	1150	1490

The identity (correct tag) of the reconstructed B-meson is determined from the charge of the trigger muon. Dilution effects (mistags) are caused by cascade decays of the b, misidentified muons (π, K-decays, punchthrough), and $B^0 - \bar{B}^0$ oscillations. For the trigger thresholds considered here, we expect the rate of misidentified muons to be negligible. With a muon p_T trigger threshold of 20 GeV, the fraction of wrong-sign muons is found to be 11.5%. Defining the dilution factor D without oscillation as

$$D = \frac{N(correct\ tags) - N(mistags)}{N(correct\ tags) + N(mistags)}$$

we obtain $D = 0.77$. Including the $B^0 - \bar{B}^0$ oscillations of the tag, the final dilution factor D' is 0.6. The time-integrated observed asymmetry has the form

$$A \equiv \frac{N_{rec}^{\mu^+} - N_{rec}^{\mu^-}}{N_{rec}^{\mu^+} + N_{rec}^{\mu^-}} = \sin 2\beta \cdot D' \cdot \frac{x_d}{1 + x_d^2}$$

where β is one of the angles of the CKM matrix unitarity triangle, $x_d = \Delta m/\Gamma$ with Δm being the mass difference between the weak eigenstates and Γ their average width. The statistical error on $\sin 2\beta$ is $(\frac{x_d}{1+x_d^2} \cdot D' \cdot \sqrt{N_{rec}})^{-1}$. With one year of running and a tracking coverage over $|\eta| < 2$, we expect to measure the value of $\sin 2\beta$ with an accuracy of ± 0.10.

[10] electrons from b-decay are not expected to be efficiently triggered on with the level-1 calorimeter algorithm and are therefore not included in the expected rates.

The feasibility of using the ATLAS vertex detector for a time-dependent asymmetry measurement is under study. Such a measurement could improve the accuracy, due to the reduction of the extra dilution factor coming from the time-integration.

This preliminary result is encouraging and more detailed simulations are under way to evaluate more accurately the expected potential of the ATLAS detector to reconstruct efficiently $B_d^0 \rightarrow J/\psi K_S^0$.

8.5 Supersymmetry

In this section we discuss the potential of the ATLAS detector to detect the production and decay of supersymmetric particles. We work entirely within the MSSM, as introduced in Section 8.2.4. Unless explicitly stated otherwise we set $\tan\beta = 2$, $m_{H^+} = 500$ GeV, and $\mu = -440$ GeV. In general, we use $m_{\tilde{q}} = 2 \cdot m_{\tilde{g}}$ and $m_t = 140$ GeV.
The supersymmetry signal in the strongly interacting sector has been generated using the ISASUSY Monte Carlo [39]. For a given set of MSSM parameters, this program computes masses and decay patterns of the supersymmetric particles. The cascade decays of gluinos and squarks are fully accounted for.

8.5.1 Multijet + E_T^{miss} signature

Even after including the effects of cascade decays the multijet+E_T^{miss} signature remains promising for the detection of gluinos and squarks. It is largely insensitive to the values of $\tan\beta$ and μ. The irreducible background, already extensively studied in [40], has been reevaluated within the ATLAS simulation framework. It consists mainly of $t\bar{t}$ and W+jet production followed by leptonic W-decay and Z+jet production followed by $Z \rightarrow \nu\bar{\nu}$.

To isolate the signal from the background we use two sets of cuts, optimized for different mass ranges:
Cut 1: Three jets with $p_T > 200$ GeV, a fourth jet with $p_T > 100$ GeV, sphericity in the transverse plane, $S_T > 0.2$ and $E_T^{miss} \gtrsim 300$ GeV.
Cut 2: As Cut 1, except $E_T^{miss} > 600$ GeV.
The main potential source of instrumental background is 4-jet production where one jet falls in the transition region between the end-cap and forward calorimeters and is severely mis-measured. A detailed simulation of the response to jets falling in the transition region is underway using a shower library technique. However, for the high E_T^{miss} cuts used in this analysis, this background does not pose a serious problem. Figure 8.13 shows, after all cuts except the one on E_T^{miss}, the expected E_T^{miss} distribution for squarks and gluinos of equal mass of 1.5 TeV (histogram), the Standard Model (S.M.) background (open circles) and the cross-section for 4-jet production from [41] with three jets with $p_T > 200$ GeV and the fourth jet, having $p_T > 100$ GeV, falling in the transition region (black squares). These latter points are plotted against the p_T of the fourth jet. Clearly, even in the extreme case where *all* the energy of the fourth jet is lost, the fake E_T^{miss} rate would be below the S.M. background for $E_T^{miss} \gtrsim 300$ GeV.

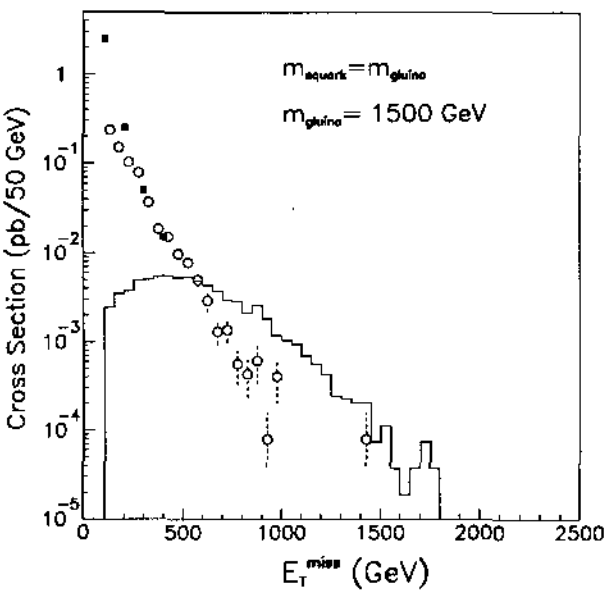

Figure 8.13: *Cross-section for the signal, in the case of* $m_{\tilde{q}} = m_{\tilde{g}}$ *of 1.5 TeV (histogram), for the total background (open circles) and for production of 4-jets with one jet in the transition region between end-cap and forward calorimetry (black squares), see text*

Figure 8.14 shows the cross-section for signal and background after the cuts described above as a function of the common mass for the case $m_{\tilde{g}} = m_{\tilde{q}}$. In the case of approximately equal masses (both for $m_{\tilde{q}} > m_{\tilde{g}}$, and $m_{\tilde{g}} > m_{\tilde{q}}$) squarks and gluinos could be discovered with the ATLAS detector up to masses of 1.6/2.0/2.3 TeV for integrated luminosities of 10^3/ 10^4/ 10^5 pb^{-1} respectively. In particular, for a mass of 1.5 TeV the significance of the signal will be ~ 9 for 10^3 pb^{-1}. For the case $m_{\tilde{g}} = 2 \cdot m_{\tilde{q}}$, the discovery range for squarks extends to 0.75/1.0/1.2 TeV for 10^3/ 10^4/ 10^5 pb^{-1} respectively. Similarly the gluino can be observed up to 1.0/1.25/1.4 TeV for the three luminosity ranges in the case of $m_{\tilde{q}} = 2 \cdot m_{\tilde{g}}$.
For the three cases of mass relations studied, a gluino or squark with mass of 300 GeV can be discovered easily for integrated luminosities larger than 10^3 pb^{-1}.

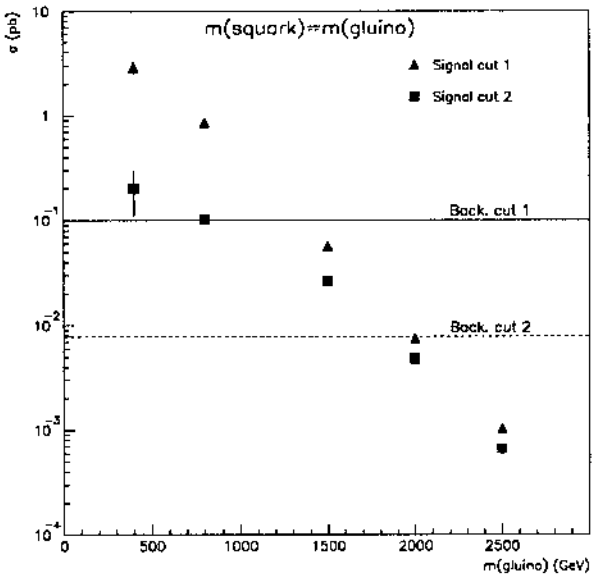

Figure 8.14: *Cross-section of the signal, in the case of* $m_{\tilde{q}} \sim m_{\tilde{g}}$, *and sum of backgrounds, see text*

8.5.2 Same-sign dilepton signature

Same-sign dileptons are a distinctive signature of gluino decays. They can arise from two same-sign W-bosons produced from the decay of a gluino pair, since the gluino is a Majorana particle. The relevant cross-sections and decay branching fractions are not very sensitive to the input SUSY parameters.

Physics rates of same-sign isolated dileptons have been shown to be low in [42]. On the other hand dileptons from $t\bar{t}$ production, where one lepton charge is mis-measured, are likely to produce a significant background. A complete study of systematics in the tracking which might produce mismeasurement of charge even at low momenta has not yet been performed [11], we therefore quote results in terms of the probability of an incorrect charge assignment.

To extract the signal the following criteria were used:

- the event is required to have at least one isolated [12] same-sign dilepton, where both leptons have $p_T > 30$ GeV and $|\eta| < 2.5$.
- $E_T^{miss} > 100$ GeV
- In the high gluino mass region a better signal to background ratio is achieved by increasing the cut on p_T of the leptons to 50 GeV.

The total cross-section after cuts as a function of $m_{\tilde{g}}$ is plotted in Fig. 8.15, for signal after cutting at lepton p_T larger than 30 GeV (triangles) and 50 GeV (squares). Also indicated in Fig. 8.15 is the background level of $t\bar{t}$ contribution with true same-sign dileptons for the cut at 30 (dashed) and 50 GeV (dotted) [13]. For the 30 GeV cut the background from charge misidentification equals the true same-sign background for misidentification probabilities larger than $4 \cdot 10^{-4}$, while for the harder cut the corresponding probability is $7 \cdot 10^{-5}$. The final observ-

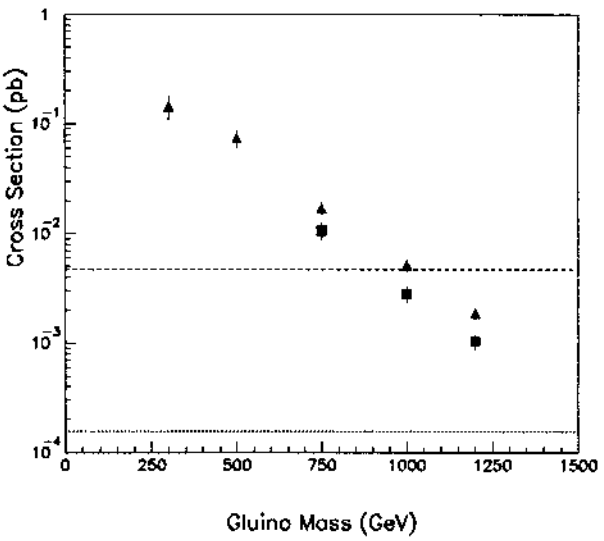

Figure 8.15: *Cross-section of the signal for* $p_T^\ell > 30$ *GeV (triangles) and 50 GeV (squares). Also shown is the remaining* $t\bar{t}$ *background, for* $p_T^\ell > 30$ *GeV (dashed) and 50 GeV (dotted)*

able cross-section is not very sensitive to the SUSY parameter μ, choosing $\mu = -150$ GeV or -300 GeV results in observed cross-sections 2–3 times larger than the ones shown here.

We conclude that it is possible to observe gluino pair production with the ATLAS detector by searching for same-sign isolated dileptons from their cascade decay, up to gluino masses of 1 (1.3) TeV, for integrated luminosities of 10^4 (10^5) pb^{-1}, if the charge misassignment probability for an isolated lepton is less than $10^{-3}(10^{-4})$.

8.5.3 Multiple-Z signature

Cascade decays of heavy gluinos include neutralino and chargino decays, where multiple Z's can be produced. This leads to a possible signature for supersymmetry, which consists of four high-p_T leptons,

[11] We note however that the background introduced by charge misidentification due to the finite momentum resolution is at a negligible level.

[12] The efficiency and rejection of isolation criteria are discussed in Section 8.2.2

[13] This represents the 68% c.l. upper limit for this background since no background events pass the 50 GeV cut.

from the decay of two Z's, several hard jets and E_T^{miss}. The main backgrounds to this signal will be ZZ continuum production, followed by leptonic decays of the Z bosons, and $t\bar{t}$ production followed by semileptonic decays of the t and b quarks.
The inclusive branching ratio for $\tilde{g} \rightarrow Z + X$ strongly depends on the exact choice of the SUSY parameters. To study the efficiency to detect the 4-lepton signature with the ATLAS detector we have chosen $\tan\beta = 2$, $\mu = -200$ GeV, $M_{\tilde{g}} = 800$ GeV and $M_{\tilde{q}} = 1.6$ TeV. For these parameter values the production cross-section of gluino-pairs is 2.35 pb, while the branching ratio for $\tilde{g}\tilde{g} \rightarrow ZZ + X$ is 4%. For an integrated luminosity of 10^5 pb^{-1} , we expect 40 events in the 4-e, 4-μ and 2e2μ channels. To separate the signal from the background the following cuts were applied:
• four jets, with $p_T^1 > 200$ GeV, $p_T^2 > 100$ GeV and $p_T^{3,4} > 50$ GeV;
• four isolated leptons with $p_T^{1,2} > 20$ GeV and $p_T^{3,4} > 10$ GeV;
• at least two ee or $\mu\mu$ mass combinations with $|m_{\ell\ell} - m_Z| < 6$ GeV;
• $E_T^{miss} > 100$ GeV.
After these cuts,, ten signal events survive over a background of less than one event. We conclude that for favourable sets of SUSY parameters a signal could be seen in the ATLAS detector. The exact range of parameters accessible is under study, but generally the rate for this process is largest for $|\mu| < 200$ and $m_{\tilde{g}} < 700$ GeV, and for large $|\mu|$ and 700 GeV $< m_{\tilde{g}} <$ 950 GeV. Given the varied and complicated signatures of SUSY, this channel could provide a valuable consistency check on SUSY signals detected in other channels.

8.5.4 Direct production of charginos and neutralinos

Charginos and neutralinos can be pair-produced via Drell–Yan processes. If particles heavier than $\tilde{\chi}_1^0$ are produced they decay via cascade chains giving intermediate vector bosons and lighter charginos/neutralinos.

These events give a clean signature in purely leptonic channels when all the vector bosons decay into electrons or muons. Since $t\bar{t}$ events will produce isolated dileptons at high rates, present studies concentrate on final states with three or more leptons. An earlier study [43] has investigated several sets of cuts on lepton momenta and isolation indicating that an excess of signal events could be observed for a region of parameter space. In this region the charginos and neutralinos are beyond the reach of LEP II. It is also complementary to the region where gluino and scalar-quark masses are relatively large and easily detectable with the ATLAS detector.

Simulation work using the generator of [43] to optimize cuts for the ATLAS detector, and to evaluate the feasibility of the hadronic veto is now in progress.

8.5.5 Slepton production

Pair-production of sleptons has a low cross-section, typically 10^{-6} of the cross-section for strongly interacting sparticles of equal mass. The signature would be a high-mass pair of opposite-sign leptons and E_T^{miss}, in combination with small hadronic activity.
We have inserted the matrix elements from [44] in PYTHIA and generated the signal for 200 GeV slepton mass, assuming a 100% branching ratio for sleptons to lepton-photino. After requiring two isolated leptons with $p_T > 20$ GeV, the top background is at least one order of magnitude larger than the signal, even at large values of E_T^{miss}. Increasing the cut to 80 GeV and vetoing events with additional hadronic jets yields roughly equal signal and background cross-sections of $\sim$ 1 fb, for $E_T^{miss} > 200$ GeV. Detailed simulation work is in progress to include the effect of cascade decays, to evaluate possible additional cuts and also to estimate how accurately the top background can be measured in other channels.

8.6 Search for New Vector Bosons

In this section we discuss the capability of the ATLAS detector to observe new (neutral or charged) vector gauge bosons. These occur naturally in several models, e.g. some minimal extensions of the Standard Model [47] and models for electroweak symmetry breaking through compositeness [48].

8.6.1 Search for Z′ in the two-lepton channel

In Fig. 8.16, the reconstructed dilepton mass spectra from $Z' \rightarrow e^+e^-$ and $Z' \rightarrow \mu^+\mu^-$ decays, plotted for both muon magnet systems, is shown for $m_Z' = 4.5$ TeV, using the Extended Gauge Model of Ref. [47], above the small background, which arises mainly from Drell-Yan production. In this lepton energy range, the observability of a Z′ peak is clearly more straightforward in the electron channel, where calorimeter cuts alone may be sufficient to extract the signal.

The Z′ forward-backward asymmetry is a quantity sensitive to the specific model used. As an example Fig. 8.17 shows the expected measured electron forward-backward asymmetries, for $m_{Z'} = 3$ TeV.

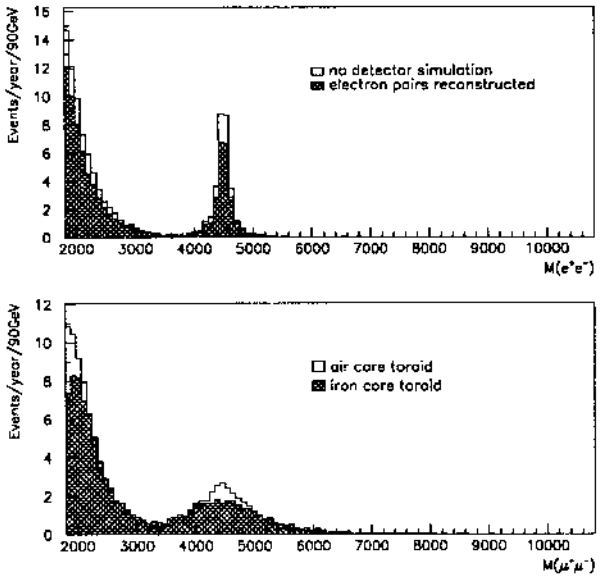

Figure 8.16: *Reconstructed dilepton mass for $Z' \rightarrow ee$ and $\mu\mu$ decays, with $m_{Z'} = 4.5$ TeV*

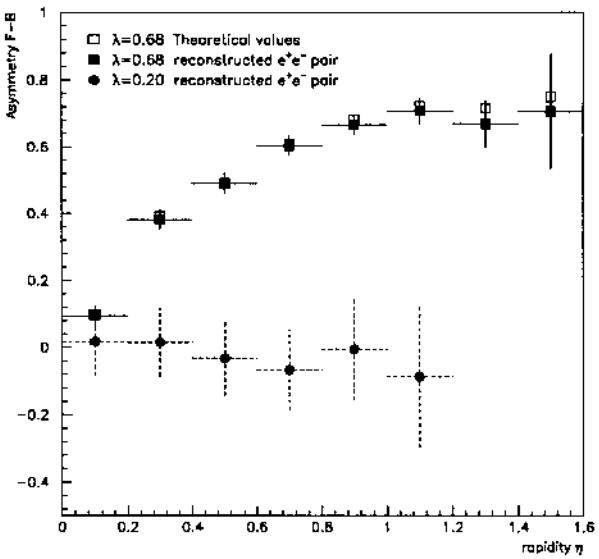

Figure 8.17: *Rapidity dependence of forward-backward asymmetry for $m_{Z'} = 3$ TeV and two values of λ (see text)*

In this case the model of Ref. [48] was used, with two values of the mixing parameter, $\lambda = 0.20$, giving ~ 400 reconstructed events per year and no observable asymmetry, and $\lambda = 0.68$, giving ~ 5200 reconstructed events per year and a very large observable asymmetry. The distortion of the asymmetry due to charge misassignment is small and minimized by changing the sign of the appropriate electron for events with like-sign pairs. This distortion is expected to be negligible in the case of a measurement in the dimuon channel.

8.6.2 Search for Z′ in the two-jet channel

A study of this channel for the ATLAS detector is described in [49]. The selection requires 2 jets with $|\eta| < 1$ and $p_T > 300$ GeV. The rapidity cut substantially improves the signal to background (S/B) ratio. The expected rates in this channel are much larger than for the two-lepton channel, but much smaller than those for continuum QCD production [50]. Owing to the very low $S/B \simeq 10^{-3}$, it is important to have a precise and unbiased knowledge of the background over a large mass range around the Z′ peak. The p_T threshold must therefore be chosen well below the signal region. Jets are reconstructed in a cone of $\Delta R < 0.7$, where the cone size is not a sensitive parameter in this analysis, since pile-up effects are small for these high-p_T jets. Table 8.5 displays the contribution of the calorimeter jet resolution (effects from pile-up are included) on the Z′ mass resolution, as well as the statistical significance of the detected signal. These numbers are computed for $m_{Z'} = 2$ TeV and an integrated luminosity of 10^5 pb^{-1}. From these numbers, we conclude that the dominant effect clearly comes from the constant term, and that a calorimeter, with a jet resolution of $50\%/\sqrt{E} \oplus 3\%$, is adequate for this channel.

Table 8.5: *Expected dijet mass resolution and statistical significance of signal, for $m_{Z'} = 2$ TeV and for various stochastic and constant terms in the calorimeter jet resolution*

$\sigma_E/E = a/\sqrt{E} \oplus b$		$\frac{\sigma_M}{M}$(%)	$\frac{S}{\sqrt{B}}$
a(%)	b(%)		
0	0	2.6	7.6
30	1	3.0	7.5
50	2	3.4	7.4
50	3	4.5	6.8
50	4	5.4	6.1
100	2	3.8	7.2
100	4	5.1	6.0

The signal was generated using a minimal extension of the Standard Model (Extended Gauge Model) [47]. Table 8.6 shows the statistical significance for the observation of a Z′ as a function of its mass, for a hadronic jet resolution of $50\%/\sqrt{E} \oplus 2\%$. The width of the mass window used to define the sig-

nal was chosen to be approximately $\pm$ 2 $\Gamma_{Z'}$. From these numbers we conclude that it is possible to observe a Z' in the 2-jet decay mode in this model, for an integrated luminosity of 10^5 pb^{-1}and masses between 1 and 2.5 TeV. For $m_{Z'}$ = 1 TeV, the dijet-p_T trigger threshold would have to be lowered to $\sim$ 150 GeV, requiring a special trigger scheme at high luminosity. If a W' were produced with about the same mass, the signal would then be increased by a factor 3, with the same background, increasing the sensitivity up to 4 TeV. In Figure 8.18 we show the expected two-jet mass spectrum for an integrated luminosity of 10^5 pb^{-1} in the presence of a Z' signal, with $m_{Z'}$ = 2 TeV and $\Gamma_{Z'}$ = 63 GeV, after subtraction of the background, which is fitted in the mass range from 1 to 2.5 TeV.

Table 8.6: *Expected statistical significances for the observation of a Z' $\rightarrow$ jj signal*

$m_{Z'}$ (TeV)	$\Gamma_{Z'}$ (GeV)	$\sigma \times B$ (pb)	$S/\sqrt{B}$ (10^5 pb^{-1})
1.0	32	13.9	17.9
1.5	47	3.6	13.0
2	63	0.71	7.4
3	95	$7.3 \cdot 10^{-2}$	3.7
4	127	$1.0 \cdot 10^{-2}$	1.6

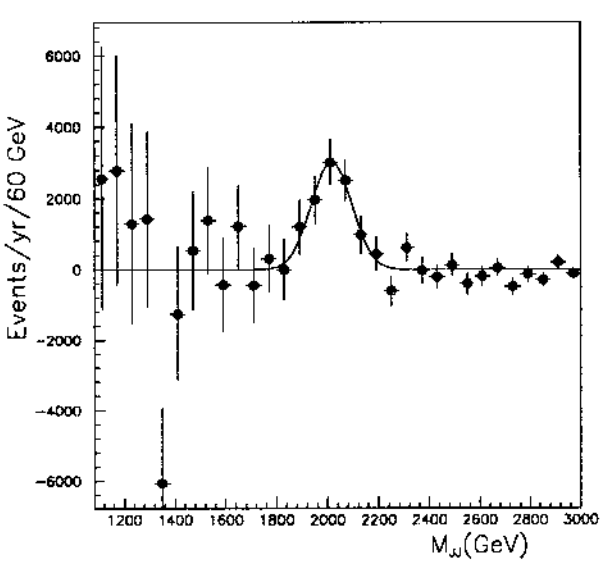

Figure 8.18: *Observed dijet mass spectrum after background subtraction, for $m_{Z'}$ = 2 TeV*

8.6.3 Conclusions

The sensitivity to a possible signal from new neutral gauge bosons is presented in Fig 8.19. Shown are 5σ limits, separately for Z' decays to electron pairs, muon pairs and jet pairs, as a function of the Z' mass and the ratio of the expected rate to the corresponding one for standard couplings ($\Gamma_{Z'}$ is assumed to increase linearly with $m_{Z'}$). The best sensitivity is

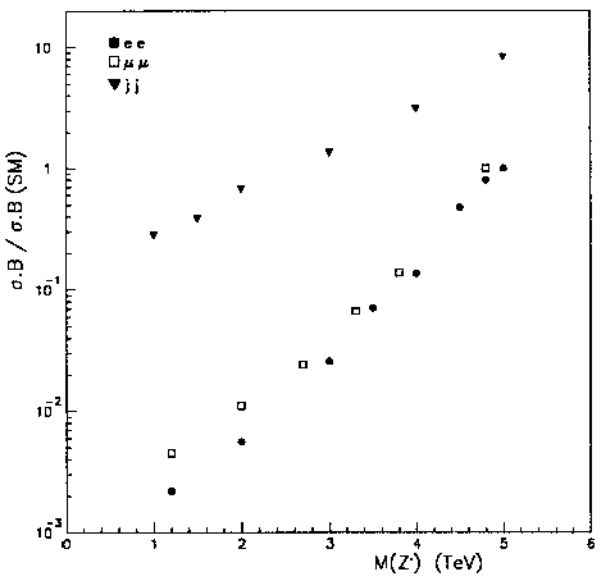

Figure 8.19: *Discovery mass limits for Z' $\rightarrow$ee, $\mu\mu$ and jj (see text)*

achieved through the Z' $\rightarrow$ ee channel. The other channels, if observed, will provide useful information on the Z' couplings and possibly asymmetries.

8.7 Search for Quark Substructure

The hypothesis of a parton substructure can be tested by measuring the inclusive jet cross-section. A composite nature of quarks would show up as deviations from the standard QCD expectations at high transverse momenta, where valence quark scattering dominates. Figure 8.20 shows the deviations of the cross-section from QCD for different values of the compositeness scale (Λ_c). Also indicated is the statistical accuracy which can be reached with integrated luminosities of 10^4 pb^{-1}and 10^5 pb^{-1}. The result will depend on the quality of the measurement as well as on the theoretical knowledge of the expected cross-section. Systematic uncertainties on the linearity, resolution and overall response of the calorimeter may enhance the measured rates for the higher p_T values, thus faking the presence of a contact interaction. Typical systematic effects at a fixed p_T of 4 TeV

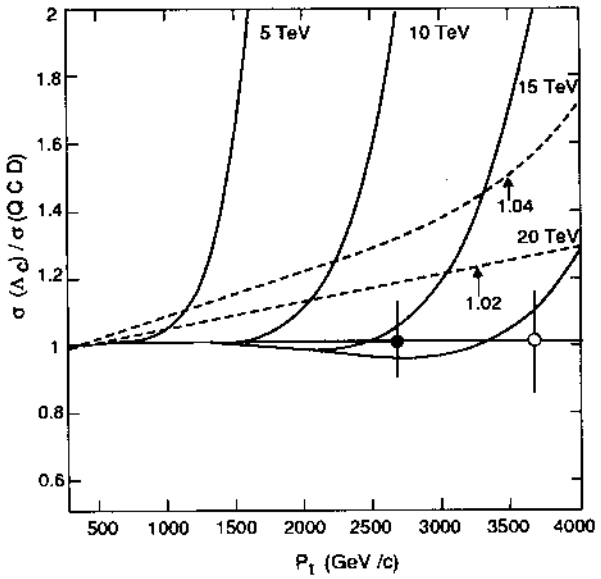

Figure 8.20: *Deviation from QCD for different Λ_c values. The dashed lines show the effect of possible systematics error as described in Table 8.7. The statistical sensitivities for 10^4 pb^{-1} (full circle) and 10^5 pb^{-1} (open circle) are also shown*

are listed in Table 8.7. While non-Gaussian tails in the energy spectrum and a wide range of values of the $1/\sqrt{E}$ scaling term are not critical, the constant term in the resolution is somewhat more important. The biggest systematic effect is caused by non-linearities in the calorimeter response. If an uncorrected non-linearity of 4% subsists between 500 GeV and 4 TeV, it will fake a compositeness signal with $\Lambda_c \sim$ 15 TeV. All these contributions strongly depend on the energy scale calibration, its monitoring and extrapolation to the highest p_T values. In particular, for a non-compensating calorimeter, the accuracy of the jet energy calibration, which will be extracted from test beam measurement on single hadrons, will depend on the knowledge of the charged to neutral particle ratio in the fragmentation. The calculations also rely on a good knowledge of the parton densities in the proton, the jet fragmentation properties and higher-order contributions to the cross-section.

Table 8.7: *Systematic effects on inclusive jet spectrum at fixed p_T of 4 TeV*

Effect (p_T = 4 TeV)	$\sigma_{meas.}/\sigma_{QCD}$
$\frac{\sigma}{E} = 70\%/\sqrt{E}$	1.1
$\frac{\sigma}{E} = 50\%/\sqrt{E} + 5\%$	1.25
Non-Gaussian tails	1.15
4% non-linearity	1.7

8.8 Gauge Boson Pair Production

Gauge boson pair production provides an essential test of the three vector-boson coupling. The gauge cancellations predicted by the Standard Model can be studied and possible anomalous couplings detected. Under some very general assumptions such anomalies can be described by two parameters κ and λ (the Standard Model values are $\kappa = 1$ and $\lambda = 0$). As an example the Wγ channel can be studied using leptonic W decays. In this channel, the photon transverse momentum distribution is very sensitive to possible anomalous couplings, especially at large p_T^γ (see Fig. 8.21). The main backgrounds arise from $t\bar{t}\,\gamma$ and $b\bar{b}\,\gamma$, but also from W+jets, $b\bar{b}$ and $t\bar{t} \rightarrow$ lepton+jets, where a jet is misidentified as a photon. We assume photon identification cuts with a rejection of 10^4 against jets (see Section 8.2.1) and lepton isolation cuts similar to those discussed in Section 8.2.2. For p_T^l >25 GeV, p_T^γ > 100 GeV and $|\eta|^{l,\gamma} < 2.5$, we expect to observe $\sim$ 17000 Wγ pairs above a background of $\sim$ 10000 events, for an integrated luminosity of 10^5 pb^{-1}. A significant excess of 160 events, with p_T^γ > 300 GeV, above the expected Standard Model rate of $\sim$ 700 events, would be observed for $\kappa = 1.1$.

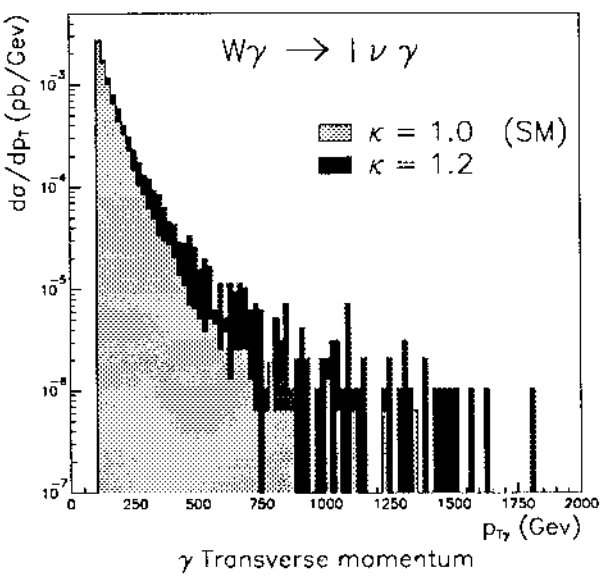

Figure 8.21: *Transverse momentun of γ in Wγ events for κ = 1.0 (light grey) and 1.2 (dark grey).*

8.9 Heavy-ion Collisions

Heavy ion collisions constitute an attractive addition to the pp physics programme. Very high energy density and temperature of nuclear matter may be reached in Pb-Pb collisions at LHC, which could lead to a phase transition and the creation of a Quark Gluon Plasma (QGP).

The ATLAS detector may be complementary to a dedicated heavy ion experiment in the search for some rare processes considered as possible signatures of the QGP. The study of heavy quarkonium states ($c\bar{c}$ and $b\bar{b}$) is of particular interest. Such studies will concentrate mainly on bottonium rather than charmonium production, since J/ψ production will arise dominantly from B-meson decay at LHC (except at very low p_T).

In order to extract a possible signal from the QGP, it is necessary to measure the production rates of the interesting bottonium states as a function of global variables related to the energy density and to the geometry of the collision, but also of more specific observables, where the behaviour of the various Υ states is not predicted to be the same [51]. For instance no suppression due to Debye colour screening is expected for the first directly produced Υ state as a function of p_T^{Υ}.

The ATLAS performance in terms of momentum resolution is adequate to separate the various Υ states, only if the inner tracking detector can be used. In this case the expected relative mass resolution is $\sim$ 1%, but would be $\sim$ 3.5% using only the outer muon measurement. Obviously detailed simulations of Pb-Pb collisions are needed in order to understand the tracking detector performance in these much more difficult conditions. In an environment with charged particle multiplicities at least ten times higher than for high luminosity pp collisions, an upgrade of the inner tracking detector may be needed to achieve adequate pattern recognition and electron identification.

A trigger on electron pairs with $p_T^e > 5$ GeV and on muon pairs with $p_T^{\mu} > 6$ (12) GeV, in the air-core (iron-core) option, should be feasible at the luminosities foreseen for Pb-Pb collisions, and would therefore result in an unbiased measurement of Υ production as a function of p_T^{Υ}, down to small enough values of p_T^{Υ}. A trigger on central collisions (and energy density) would be easy to implement using both the electromagnetic and hadronic calorimetry. Significant variations of the energy density could be achieved by performing measurements with different projectiles.

References

[1] H.U.Bengtsson and T.Sjöstrand, PYTHIA, Comput. Phys. Commun. 46 (1987) 43;
T.Sjöstrand, CERN-TH.6488/92.

[2] *Proceedings of the Large Hadron Collider Workshop*, edited by G. Jarlskog and D. Rein (Aachen, 4-9 October 1990) CERN 90-10/ECFA 90-133.

[3] C.Seez and J.Virdee in [2], Vol. II, p. 474.

[4] L.Fayard and G.Unal, EAGLE note PHYS-NO-001, with add. 1 & 2.

[5] P.Aurenche et al., Ref. [2], Vol. II, p. 83.

[6] S.Dawson, Nucl. Phys. **B359** (1991) 283;
A.Djouadi, M.Spira and P.Zerwas, Phys. Lett. **B264** (1991) 440.

[7] M.Della Negra et al., Ref. [2], Vol. II, p. 509.

[8] A.Nisati Ref. [2], Vol. II, p. 492.

[9] B.van Eijk and R.Kleiss, Ref. [2], Vol. II, p. 183.

[10] E.W.N.Glover and J.J. van der Bij, Phys. Lett. **B219** (1991) 488

[11] D.Froidevaux, in Proc. of the Workshop on Physics at Future Accelerators, La Thuile, Jan. 1987, CERN 87-07, Vol. 1, p. 61.

[12] U.Baur and E.W.N.Glover, Ref. [2], Vol. II, p. 570.

[13] I.Zuckerman et al., ATLAS note, PHYS-NO-007.

[14] J. Ohnemus and J.F. Owens, Phys. Rev. **D43** (1991) 3626;
B. Mele et al., Nucl. Phys. **B357** (1991) 409;
J. Ohnemus, Phys. Rev. **D44** (1991) 3477.

[15] A.Erdogan et al., ATLAS note, PHYS-NO-008.

[16] M.H.Seymour, Ref. [2], Vol. II, p. 557.

[17] R.H.Cahn et al., Phys. Rev. **D35** (1987) 1626

[18] Z.Kunszt and F.Zwirner, CERN preprint, CERN-TH.6150/91.

[19] Y.Okada, M.Yamaguchi and T.Yaganida, Prog. Theor. Phys. Lett. 85(1991)1;
J.Ellis, G.Ridolfi and F.Zwirner, Phys. Lett. **B262** (1991) 447;
H.E.Haber and R.Hempfling, Phys. Rev. Lett. **66** (1991) 1815;

R.Barbieri, M.Frigeni and F.Carcaglio, Phys. Lett. **B258** (1991) 167;
R.Barbieri and M.Frigeni, Phys. Lett. **B258** (1991) 395.

[20] G.Unal et al., EAGLE note, PHYS-NO-005.

[21] R.K. Ellis et al., Nucl. Phys. **B297** (1988) 221;
L. DiLella, Ref. [2], Vol. II, p. 530;
K. Bos, F. Anselmo and B. van Eijk, Ref. [2], Vol. II, p. 538.

[22] P. Janot, LAL Preprint, LAL 92-27.

[23] A. Dobado and M.J. Herrero, Phys. Lett. **B228** (1989) 495
J. F. Donoghue and C. Ramirez, Phys. Lett. **B234** (1990) 361;
A. Dobado, M.J. Herrero and J. Terron, Ref. [2], Vol. II, p. 768.

[24] R. Casalbuoni et al., Phys. Lett. **B155** (1985) 95; Nucl. Phys. **B282** (1987) 235; Nucl. Phys. **B310** (1988) 181; Ref. [2], Vol. II, p. 786.

[25] A. Dobado, M.J. Herrero and J. Terron, Ref. [2], Vol. II, p. 770.

[26] R.S. Chivukula and M. Golden, Phys. Rev. **D41** (1990) 2795.

[27] The LEP Collaborations, Phys. Lett. **B276** (1992) 257.

[28] A. Blondel, F.M.Renard and C.Verzegnassi, Phys. Lett. **B269** (1991) 419.

[29] G.Unal and L.Fayard, Ref. [2], Vol. II, p.360.

[30] K. Foley et al., in Expts, Detectors and Experimental areas for the Supercollider, Berkeley, 1987, World Scientific (R. Donaldson and M.G.D. Gilchriese eds.), p.701.

[31] P. Roudeau in Proc. of the Joint Int. Symp. & Europhysics Conference on HEP, Geneva, July 1991, World Scientific (S. Hegarty et al., eds.), Vol.2, p.301.

[32] M. Felcini, Ref. [2], Vol.II, p.414.

[33] G.Battistoni et al., EAGLE note, PHYS-NO-003.

[34] G. Pancheri, J-P. Revol and C. Rubbia, Phys. Lett. **B277** (1992) 518.

[35] A. Carter and A.I. Sanda, Phys. Rev. Lett. **45** (1980) 952; Phys. Rev. **D23** (1981) 1567;
I.I. Bigi and A.I. Sanda, Nucl. Phys. **B193** (1981) 85;
I.Dunietz, Ann. Phys. **184** (1988) 350;
M. Botlo et al., SSCL and SLAC Preprint, SSCL-538, SLAC-PUB-5795 (1992).

[36] J.P.Guillet, P.Nason and H.Plothow-Besch, Ref. [2], Vol. II, p. 116.

[37] Particle Data Group, Phys. Rev. **D11** (1992) 1.

[38] P.Eerola, ATLAS note, PHYS-NO-009.

[39] ISASUSY 1.0, written by H.Baer, F.E. Paige, S.D. Protopopescu, and X.Tata.

[40] C.Albajar et al., Ref. [2], Vol. II, p. 608.

[41] J.G.M. Kuijf, *Multiparton Production at Hadron Colliders*, PhD. thesis, Leiden University (1991).

[42] H.Baer et al., Phys. Lett. **B161** (1985) 175;
G.Gamberini, Z. Phys. **C20** (1986) 605.

[43] R.Barbieri et al., Nucl. Phys. **B367** (1991) 28.

[44] S.Dawson, E.Eichten and C.Quigg, Phys. Rev. **D31** (1985) 1581.

[45] F.delAguila and Ll.Ametller, UAB-FT-243/90.

[46] B.Mansoulié, Proceedings of the Workshop on Physics at Future Accelerators, La Thuile 7-13 Jan. 1987, CERN 87-07, Vol. 2, p. 126.

[47] N.G. Deshpande, J.A. Grifolds and A. Mendez, Phys. Lett. **B208** (1988) 141;
F. Feruglio, L. Maiani and A. Masiero, Phys. Lett. **B233** (1989) 512.

[48] J.L. Kneur and G. Moultaka, Ref. [2], Vol. II, p. 737.

[49] A.Henriques and L.Poggioli, ATLAS note, PHYS-NO-010.

[50] F. del Aguila et al., Ref. [2], Vol. II, p. 686.

[51] F. Karsch and H. Satz, CERN Preprint, CERN-TH.5900/90.

9 R&D, Costs, and Sharing of Responsibilities

9.1 R&D Summary

At this early stage of preparation for an LHC experiment it is not yet possible to make a definite selection of the technology for many of the detector subsystems. One key element in the decision process are results and extrapolations from R&D and pre-prototype test activities. Only realistic large scale tests can demonstrate the feasibility of a given technology and its potential to fulfil, in a cost-effective way, the essential physics requirements.

Many members of the ATLAS Collaboration are therefore involved in detector R&D and pre-prototype projects. The activities of particular interest to ATLAS are summarized in Table 9.1 which also includes for each project an indication of its relevance to the future detector design. We request that these projects be supported with high priority.

Technical R&D efforts are also required to study and optimize further the magnet options in order to arrive at a selection before the Technical Proposal.

9.2 Costs and Schedules

The detector concept presented in this Letter of Intent has been guided so far primarily by the physics requirements and not by a strict cost target. The ATLAS Collaboration is therefore still at an early stage of cost estimates and of detector optimization with respect to costs. At the moment engineering and industrial cost estimates are available only for part of the components of the detector. It is particularly difficult to estimate electronics and DAQ costs, and large extrapolations have to be made from today's costs. This is even more so for the inner detector and possibly the calorimeter front-end electronics which have to be radiation hard. Therefore it must be stressed that present estimates are to be considered preliminary and indicative only.

Whenever possible, experience from the R&D projects has been used in the estimates which are summarized in Table 9.2 for the baseline design (or baseline options) of all detector subsystems. As guiding principle all manpower for industrial products as well as for industrial support is included in the material costs, but no explicit contingencies are included at this stage. It has to be noted that the cost estimates of various baseline options for a given detector subsystem do not always assume the same level of industrial involvement. In addition, very substantial laboratory support manpower (engineers and technicians) will be needed to construct, test, and install the detector. A first estimate amounts to a total of at least 1500 man-years. Every effort will be made to find them within the collaborating institutions.

The choices of technologies still left open at this stage introduce another element of uncertainty in the overall detector cost estimate which is reflected in Table 9.2.

The preliminary cost estimate given in Table 9.2 refers to the complete detector, and amounts to 370–450 MCHF depending on the final choices of the muon magnet system and detector subsystem options. It is recognized by the ATLAS Collaboration that further optimization work on the detector concept is required with the goal of reducing costs while maintaining the physics objectives. Staging could be introduced only at the price of reduced physics performance. Several scenarios with deferred installation of parts of detector subsystems will have to be evaluated carefully should financial or time constraints impose a need for it. Such possibilities are, for example, a deferred installation of the end toroid muon spectrometers at the price of a very significantly reduced acceptance or only a progressive completion of the read-out electronics or of other detector subsystems. In the case of the superconducting air-core muon magnet, an alternative cost saving would be achieved by replacing, in the end-caps, the air-core by warm iron-core toroids.

First order construction schedules have been worked out for some of the most critical large components as well as for the installation of the detector in the experimental area (see 6). In brief, the design and construction time is dominated by the muon magnets (see 4) and the calorimetry (see 2) which may both require as much as 5 to 6 years including tests at the surface. A period of 1.5 to 2 years, partially overlapping with the testing time, is estimated for the installation in the experimental cavern.

9.3 Collaboration Structure

The organizational structure of the collaboration has been kept as simple as possible for the phase of the preparation of this Letter of Intent (LoI). Questions of detector optimization are discussed within appropriate Working Groups comprising all necessary expertise from the collaboration. The Working Groups prepare the general discussions in the Plenary Meetings and in the LoI Board with nominated members responsible to represent all physics, detector and logistics aspects. The LoI Board meetings, open to all members of the collaboration, have been steering the work towards the detector concept and the experi-

mental programme presented in this LoI.

The decision-making body is the assembly of one representative from each collaborating institution (Collaboration Board). This body acts after discussion in a Plenary Meeting. The overall co-ordination is the responsibility of F. Dydak and P. Jenni acting as co-spokespersons.

The organizational structure for the phase after approval by the LHC Committee to proceed towards a Technical Proposal has not yet been defined. It is expected that it will be based on similar working bodies and that it will maintain the present open spirit of the collaboration, although with the addition of a more formal definition of responsibilities corresponding to the commitments to be taken for the Technical Proposal.

9.4 Construction Responsibilities

The construction responsibilities can only be established once final choices and definite commitments are taken for the detector concept to be presented in a Technical Proposal. At this stage only an indication can be given in terms of areas of interest expressed by the collaborating institutions.

The areas of interests of the different groups for the detector construction are listed in Table 9.3 for those where this is known already. CERN, with its dual role as host laboratory and collaboration partner, is not listed explicitly at this stage. CERN is expected to contribute to infrastructure, overall engineering, and other general co-ordination efforts such as DAQ and offline analysis tools, as well as to one or two major detector subsystems. The first indications from Table 9.3 are that the interests and potential construction capabilities of the collaboration are spread over all aspects of the detector subsystems.

Table 9.1: *Detector R&D and pre-prototype activities with ATLAS involvement*

Detector Subsystem	R&D and Pre-prototype Activity	Comments
Inner detector - vertexing and innermost tracking	RD19 Si pixel detectors RD20 Si micro-strip detectors RD8 GaAs detectors	All are part of the baseline design, and R&D is needed to optimize integrated design
- outer tracking and electron identif.	RD2 Si strip and pad detectors RD6 TRD straw detectors RD28 micro-strip gas counters	All are part of the baseline design, and R&D is needed to optimize integrated design
	RD7 scintillating fibres	Alternative, R&D is needed to confirm the feasibility of the scheme
Em calorimeter and preshower detector	RD3 LAr Accordion	Baseline barrel, baseline option end-cap R&D is needed to optimize design
	P44 LAr TGT	Alternative barrel, baseline option end-cap R&D is needed to demonstrate feasibility
	RD1 scintillating fibres	Alternative, only reduced R&D is needed
Hadronic calorimeter	RD1 scintillating fibres RD3 LAr Accordion P44 LAr TGT Scintillator tiles pre-prototype	All are baseline options, and R&D is required to arrive at a decision before the Technical Proposal
Forward calorimeter	Liquid scintillator and High pressure gas pre-prototypes	Both are baseline options, and R&D is required to arrive at a decision before the Technical Proposal
Muon system - tracking detectors	RD5 honeycomb strip chambers High pressure drift tubes Jet cell drift chambers	All are baseline options, and R&D is required to arrive at a decision before the Technical Proposal
- trigger detectors	RD5 resistive plate chambers	Same comment as above
- general aspects	RD5 punch through, em showers etc	
Trigger - level 1	RD5 muon triggers RD27 calorimeter triggers, system aspects	
- level 2	RD2 and RD6 electron track triggers RD11 EAST general architectures	
- level 3	RD13 general architectures	
FE electronics	RD12 general read-out systems RD16 FERMI digital calor. FE/read-out RD29 DMILL radiation hard electronics (detector specific FE electronics R&D is included in the corresponding projects)	
DAQ system	RD13 general DAQ and readout RD23 optoelectronic signal transfer	

Table 9.2: *Preliminary cost estimates (in MCHF)*

Detector subsystem (baseline or baseline option)	Material cost mechanics or system	Material cost electronics	Total subsystem material cost
Inner detector			74
- SITV	15.0	10.0	
- GaAs	1.5	1.5	
- SIT	9.5	9.5	
- MSGC	3.0	10.0	
- TRD/T	8.0	5.0	
- moderator and supports	1.0		
Superconducting solenoid	8.0		8–13
Flux return yoke (if separate)	4.5		
Em calorimeter barrel and end-cap			49
LAr Accordion (including preshower)	30.0	19.0	
Hadronic calorimeter			27–43
- LAr Accordion	38.5	4.5	
- scintillating fibres	27.5	10.0	
- scintillator tiles	14.0	13.0–21.5	
Cryostat and cryogenics			30–45
- em and hadronic LAr calorimeter	45.0		
- em LAr calorimeter only	30.0		
Forward calorimeter			9–10
- liquid scintillator	6.0	3.0	
- pressurized gas	5.5	4.0	
Muon toroid magnet			72–115
- superconducting air-core	110.0		
- cryogenics	5.0		
- warm iron-core	71.5		
Muon detectors			23–27
- high pressure drift tubes	11.5	6.5	
- honeycomb strip chambers	5.5	10.5–13.0	
- jet cell drift chambers	16.0	4.0	
- resistive plate chamber trigger	4.0	2.5	
Trigger electronics		26.0	26
Data acquisition and slow control		27.0	27
Offline computing	5.0		5
Infrastructure	18.5		19
Total detector material cost			370–450

Table 9.3: *Areas of interest for the detector construction (see text for CERN)*

Detector subsystem	Institutions interested
Inner detector	Amsterdam NIKHEF, Bern, Birmingham, Bratislava, Cambridge, Cracow INP, Cracow INPT, Dortmund, Florence, Freiburg, Geneva, Glasgow, Hamburg, Helsinski, Kosice, Lancaster, Liverpool, London QMWC, London UC, Lund, Manchester, Marseille CPPM, Melbourne, Milano, Moscow Lebedev, Moscow MEPhI, Moscow MSU, Munich MPI, Oslo, Oxford, Pisa, Prague, RAL, Sheffield, Siegen, St. Petersburg NPI, Sydney ANSTO, Tel-Aviv, Uppsala, Vienna, Weizmann, Wuppertal
Superconducting solenoid	Helsinki, RAL, Saclay DAPNIA
Calorimetry and preshower	Alberta, Alma-Ata, Annecy LAPP, Barcelona UA, British Columbia, Clermont-Ferrand, Dubna JINR, Grenoble ISN, Kosice, Lisbon, Madrid UA, Mainz, Marseille CPPM, Milano, Montreal, Munich MPI, Orsay LAL, Paris VI and VII, Pavia, Prague, Protvino IHEP, Rio de Janeiro COPPE, Saclay DAPNIA, Stockholm MSI, Victoria
Forward calorimetry	Moscow ITEP, Protvino IHEP
Muon magnet	Helsinki, RAL, Saclay DAPNIA
Muon detectors	Amsterdam NIKHEF, Athens NTU, Bratislava, Cosenza, Dubna JINR, Frascati, Freiburg, Kobe, Mainz, Manchester, Moscow MSU, Munich LMU, Munich MPI, Nijmegen (KUN, NIKHEF), Pisa, Prague, Protvino IHEP, Rome I and II, Saclay DAPNIA, Saratov, St. Petersburg IFMO, Tel-Aviv, Tokyo, Weizmann
Trigger	Amsterdam NIKHEF, Annecy LAPP, Birmingham, Copenhagen NBI, Cracow INP, Dubna JINR, Frascati, Heidelberg IHEP, Jena, London QMWC, London RHBNC, Lund, Mannheim, Orsay LAL, Oslo, Paris VI and VII, Prague, Protvino IHEP, RAL, Rome I and II, Saclay DAPNIA, Sheffield, Stockholm, Stockholm MSI, Tokyo, Valencia
Data acquisition	Annecy LAPP, Athens, Barcelona UA, Birmingham, Cambridge, Cracow INP, Cracow INPT, Debrecen ATOMKI, Dubna, Glasgow, Liverpool, London UC, Lund, Mainz, Manchester, Marseille CPPM, Oslo, Paris VI and VII, Pavia, RAL, Saclay DAPNIA, Stockholm MSI, St. Petersburg NPI, Tokyo